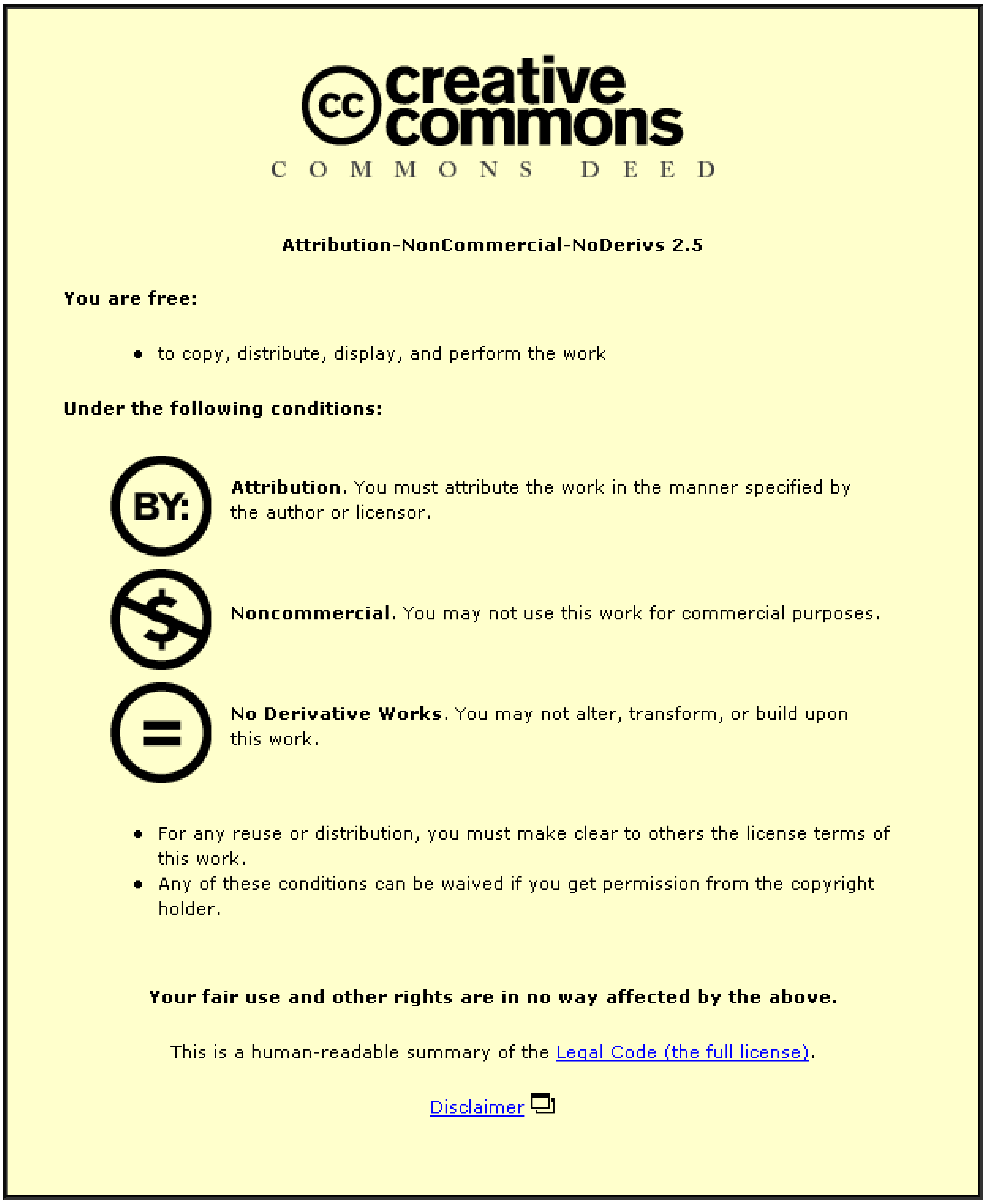

PARTICLE IMAGE VELOCIMETRY APPLIED TO INTERNAL COMBUSTION ENGINE IN-CYLINDER FLOWS

by

Mark Reeves
B.Sc. (Hons)

A Doctoral Thesis submitted in partial fulfilment of the
requirements for the award of Doctor of Philosophy
of the
Loughborough University of Technology

September 1995

LIST OF CONTENTS

NOMENCLATURE

IC	Internal Combustion
SI	Spark Ignition
CI	Compression Ignition
CFD	Computational Fluid Dynamics
TDC	Top Dead Centre
BDC	Bottom Dead Centre
IVC	Inlet Valve Closure
RPM	Revolutions Per Minute (engine crank speed)
LDV	Laser Doppler Velocimetry
PTV	Particle Tracking Velocimetry
PIV	Particle Image Velocimetry
BSR	Barrel Swirl Ratio (based on PIV in motored engine or steady flow swirl meter measurements)
TVR	Tumble Vortex Ratio in a motored engine (based on LDV measurements)
TVR_O	Estimated TVR at IVC based on LDV steady flow profiles
UV	Ultra-Violet
CW	Continuous-Wave
LSP	Laser Speckle Photography
LSV	Laser Speckle Velocimetry
CCD	Charge Coupled Device
FFT	Fast Fourier Transform
$\boldsymbol{x} = (x,y)$	Cartesian co-ordinates in flow
$\boldsymbol{X} = (X,Y)$	Cartesian co-ordinates on PIV transparency
s_i, s_o	Image and object distances
z	Distance from centre of interrogation volume
Δt	Laser pulse separation
$\mathbf{v} = (u\mathbf{i}+v\mathbf{j}+w\mathbf{k})$	Velocity vector
$\mathbf{s} = (\Delta x,\Delta y,\Delta z)$	Displacement vector in flow
$\mathbf{S} = (\Delta X,\Delta Y)$	Displacement vector on PIV transparency
M	Magnification of imaging optics
f	Focal length of imaging optics
W	Laser sheet thickness
h	Laser sheet height
L	Interrogation volume width and height in flow
D	Interrogation region size on transparency

N_p	Number of paired particle images
N_u	Number of unpaired particle images
$I(X,Y)$	Intensity distribution in interrogation region
$P(X,Y)$	Intensity distribution of single particle image
$R(\xi,\eta)$	Autocorrelation function
(ξ,η)	Cartesian co-ordinates in autocorrelation plane
$R_{dc}(\xi,\eta)$	Self correlation peak function
$R_s^+(\xi,\eta), R_s^-(\xi,\eta)$	Signal peaks in autocorrelation plane
$R_{np}(\xi,\eta)$	Spurious correlations due to paired particles
$R_{nu}(\xi,\eta)$	Spurious correlations involving unpaired particles
$R_{pp}(\xi,\eta)$	Autocorrelation of single particle image intensity distribution
d_i	Particle image diameter
N_s	Total number of spurious correlation peaks
N	Total number of particle images
$I_1(X,Y)$	Intensity distribution of interrogation region due to first exposure alone
$I_2(X,Y)$	Intensity distribution of interrogation region due to second exposure alone
$R_{cc}(\xi,\eta)$	Cross correlation of first and second intensity distributions
I_o	Illumination intensity in light sheet
λ	Wavelength of illuminating light
σ	Mie scattering coefficient
d_p	Diameter of seed particle
w_e	Energy of illuminating light pulse
ε	Mean exposure at image plane
n	Mie scattering exponent
d_a	Diameter of imaging lens aperture
N_s	Source density
C	Mean number density of particles in the flow
$f^{\#}$	Imaging lens f / number
δ_z	Imaging lens depth of focus
H_1	Signal peak height
H_2	Height of highest noise peak
S/N	Signal to noise ratio
D_r	Dynamic range
V_{max}	Maximum velocity in dynamic range
V_{min}	Minimum velocity in dynamic range
ϕ	Velocity gradient strength

P_{lens}	Power of cylindrical lens
d	Axial separation of two lenses
P_c	Power of half-cylinder in plane of curvature
n_w	Refractive index of cylinder medium
n_i	Refractive index of in-cylinder fluid
n_o	Refractive index of fluid external to cylinder
t	Thickness of cylinder wall
R_i	Internal cylinder radius
R_o	External cylinder radius
P_{system}	Net power of optical system
r_i^m	Axial distance of meridional line image from cylinder centreline -
r_i^s	Axial distance of sagittal line image from cylinder centreline
Δr_i	Axial separation of meridional and sagittal foci
X_{max}	Maximum X co-ordinate in measurement area
M_x	Magnification in X direction
M_y	Magnification in Y direction
$M_x(0)$	X magnification in centre of field
$M_y(0)$	Y magnification in centre of field
E_x	X position error due to distortion
E_y	Y position error due to distortion
d_b	Laser beam diameter
f_1, f_2	Focal lengths of sheet forming lenses
θ	Divergence of laser sheet
ω_e	Engine crank rotational speed
$\mathbf{r}$	Vector distance of velocity vector from centre of rotation

ABSTRACT

Particle Image Velocimetry (PIV) is now emerging as a powerful tool for the investigation of unsteady fluid mechanics. At the same time, the study and optimisation of in-cylinder flow processes in automotive Internal Combustion (IC) engines is of increasing importance in the design of improved combustion systems with lower emissions and favourable power and efficiency characteristics.

This thesis describes the development and application of PIV as a routine diagnostic tool for the investigation of in-cylinder flows in a production geometry single cylinder research engine exhibiting "barrel swirl" or "tumbling" in-cylinder fluid motion. The work has involved the design and installation of a complete PIV engine facility, based around a four-valve, four-stroke Rover research engine equipped with piston crown optical access and a glass cylinder liner. Novel techniques for the on-line monitoring of important experimental parameters have been developed which permit the reliable acquisition of high spatial resolution PIV data from both horizontal and vertical measurement planes within the engine cylinder.

A novel optical correction technique has been developed to control the severe particle image degradation which was experienced when imaging vertical planes within the glass cylinder. A simple means for selection of an appropriate corrective lens for this application is described, together with an experimental evaluation of the lens performance.

A representative set of PIV images and data from both horizontal and vertical planes are then presented. These have been selected from a comprehensive set of flow mapping experiments in the motored engine. The data are discussed with reference to the work of others in engines of similar geometry and have shed new light on the detailed processes involved in the formation and breakdown of barrel swirl.

Initial PIV measurements ahead of a flame under part load, skip fired conditions have also been made in the engine. This has demonstrated the possibility of investigating in-cylinder flow behaviour under conditions approaching those in a fully firing, production geometry optical engine. Finally, limitations in the PIV technique employed in this work and methods of overcoming them are described and the prospects for further work are discussed.

ACKNOWLEDGEMENTS

I would like to thank my supervisors, Dr Colin Garner and Professor Neil Halliwell and my Director of Research, Professor John Dent, for their help and encouragement during the course of my studies. Special thanks are also due to Dr Jeremy Coupland for his valuable advice.

For the preparation of photographic material my gratitude is extended to Mr Vince Scothern and Mr Ken Topley. I would also like to thank all of the technical staff in the Department of Mechanical Engineering who assisted in building the PIV engine experimental facility. In particular, I am grateful to Jim Lewis, Bob Ludlam, Brian Mace, Brian Cooper and Steve Taylor for their contributions. Steve Retter deserves a special mention for the design and build of the electronic engine timing system. Thanks are also given to Norman Cole at Spectron Lasers Ltd. and to Andrew Shand at AEA Harwell.

At Rover, many thanks are due to all those involved in the conception of the project and the design and build of the optical engine. These include Dr Jeremy Davies, Peter Parker, Stan Wallace, Dr Clive Buckberry, Graham Marshal, Adrian Fitzpatrick and Trevor Wood. Thanks are also due to Dr Dave Towers, Bob Head, Brian Taverndar and Jack Junday for their involvement in the latter stages of the project. I would also like thank both Rover and the EPSRC for their financial support.

My gratitude is also extended to all of my friends and colleagues at Loughborough and Rover who have helped, supported or entertained me during the course of this work. Special thanks are due to Chris Creasey and Mark Cole for their humour and understanding.

Finally, I would like to thank my family for their support and for tolerating my absence during the writing of this Thesis.

PUBLICATIONS ARISING FROM THIS WORK

The following written publications arose from this and related work;

"Particle Image Velocimetry Measurements of Barrel Swirl in a Production Geometry Optical IC Engine", M Reeves, C P Garner, J C Dent and N A Halliwell, SAE Congress and Exposition, SAE Paper # 940281, Detroit, Feb 1994.

"In-cylinder particle image velocimetry measurements in a four-stroke, four valve optical I C engine", M Reeves, C P Garner, J C Dent and N A Halliwell, IMechE Int. Seminar, 'Optical Methods and Data Processing in Heat and Fluid Flow', City University, April 1994.

"Study of Barrel Swirl in a Four-Valve Optical Engine Using Particle Image Velocimetry", M Reeves, C P Garner, J C Dent and N A Halliwell, COMODIA 94 Int. Symp., Yokohama, Japan, July 1994.

"Cross correlation for Particle Image Velocimetry using Polarisation Sensitive Image Labelling", M Reeves, N J Lawson, N A Halliwell, J M Coupland, Applied Optics and Optoelectronics FASIG conf. (Institute of Physics), York, England, 5-8 September, 1994.

"Particle Image Velocimetry: Image Labelling Using Encoding of the Point Spread Function by Application of a Polarisation Sensitive Pupil Mask", M Reeves, N J Lawson, N A Halliwell, J M Coupland, Applied Optics, 34[1], pp 194-200, Jan 1995.

"Particle Image Velocimetry Measurements of In-Cylinder Flow in a Multi-Valve I.C. Engine", M Reeves, C P Garner, J C Dent and N A Halliwell, Accepted for publication by IMechE Part D, Journal of Automobile Engineering, Jan 1995.

"Particle Image Velocimetry: Theory and Application of Image Labelling using a Polarisation Sensitive Pupil Mask", N J Lawson, M Reeves, N A Halliwell, J M Coupland, Submitted to Meas. Sci. Tech, November 1994.

"Particle Image Velocimetry Analysis of I.C. Engine In-Cylinder Flows", M Reeves, C P Garner, J C Dent and N A Halliwell, Submitted to Journal of Optics and Lasers In Engineering, November 1994.

"Full Field IC Engine Flow Measurement Using Particle Image Velocimetry", M Reeves, C P Garner, J C Dent and N A Halliwell, Submitted to SPIE Journal of Optical Engineering, March 1995.

"Numerical Modelling and Particle Image Velocimetry Measurement of the Laminar Flow Field Induced by an Enclosed Rotating Disc", Int. Journal for Numerical Methods in Fluids, Garner, C.P., Zhou, M., Reeves, M., accepted for publication May 1995.

CHAPTER 1

INTRODUCTION

1.1 Background

The details of fluid motion within the cylinders of automotive Spark Ignition (SI) internal combustion engines are known to profoundly affect engine performance and emissions [1.1,1.2]. Increasingly stringent emissions legislation and ever present consumer demands for improved performance and fuel economy have lead to the development of combustion systems in which the control of in-cylinder fluid mechanics through appropriate design plays a vital role. The development of three-dimensional Computational Fluid Dynamics (CFD) models for the prediction of port, valve and in-cylinder flows and combustion has provided an attractive tool for engine designers, with the promise of significant savings in engine testing and reductions in engine design cycle time. However, CFD predictions are limited in their treatment of turbulence and are sensitive to computational grid geometry and boundary conditions, so that experimental validation is always required in new applications. Therefore, in-cylinder flow visualisation and velocimetry techniques are also becoming increasingly important for the validation of CFD models, the verification of design intent and for the detailed study of fundamental in-cylinder flow processes.

The control of in-cylinder flow is achieved in production engines primarily through the design of the inlet ports, the cylinder head and piston crown geometry and through intake valve timing. Details of the inlet port and intake valve flow determine volumetric efficiency and hence power output, and can also strongly affect combustion duration through the generation of large scale, long lived fluid motion within the engine cylinder. It is believed that the large scale fluid motion, which is generated during induction, is distorted in the late stages of the compression stroke and generates an enhanced turbulent flow field which promotes rapid and stable combustion.

The two major types of in-cylinder flow pattern which are generated during induction and are known to enhance burning rates are known as "swirl" (or "axial swirl"), and "tumble" (or "barrel swirl"). These are large scale vortex structures whose axes of rotation are, respectively, parallel and perpendicular to the cylinder axis (see figures 1.1

and 1.2). Combinations of tumble and swirl give rise to vortex motion with an inclined axis of rotation. The mechanisms by which swirl and tumble lead to turbulence enhancement are believed to be different. Swirling flow can be compressed into a cylindrical cross section combustion chamber without geometrical distortion, whereas tumble is subject to high shear forces as it is compressed into an increasingly adverse clearance volume geometry near Top Dead Centre (TDC). As a result, pure swirl tends to survive throughout the compression stroke, producing a moderate turbulence enhancement due to wall shear, while tumble motion breaks down at an earlier stage, producing high turbulence intensities at the time of ignition [1.3].

Many multi-valve spark ignition engines are now designed with directed inlet ports and a pentroof combustion chamber. The pentroof geometry provides an increased valve curtain area and hence high volumetric efficiency, for high power output. Furthermore, the inlet port geometry permits strong tumble motion to be generated without recourse to valve shrouding, while the multiple inlet valves provide the potential for exploiting combinations of tumble and swirl via asymmetric valve timing or throttling strategies [1.4, 1.5, 1.6, 1.7].

The enhanced turbulence intensity and increased flame propagation rates generated in this type of engine have been shown to improve cyclic variability and tolerance to lean air/fuel ratios and exhaust gas recirculation [1.8, 1.9, 1.10]. Furthermore, it has been demonstrated that the strongly ordered in-cylinder motion responsible for turbulence enhancement may also be used to achieve significant charge stratification for extended lean operation by suppression of three dimensional cross-flow effects [1.11,1.12]. This type of engine is therefore proving important in meeting the increasingly stringent emissions legislation and consumer expectations of performance and efficiency.

The beneficial effects of tumble motion are, however, also accompanied by an increase in the velocity of bulk charge motion in the vicinity of the spark plug at the time of ignition and high turbulent strain rates during tumble breakdown. This can adversely affect the processes of the spark discharge and early flame kernel growth [1.13, 1.14]. The processes of tumble formation and breakdown and interactions of the bulk and turbulent flow with the combustion processes must therefore be fully understood if developments of this type of engine are to provide future emissions and performance improvements.

Single point velocimetry techniques such as Hot Wire Anemometry (HWA) [1.15] and Laser Doppler Velocimetry (LDV) [1.16, 1.17] have been used to study the formation and breakdown of barrel swirl and have provided much useful insight into these processes. However, the velocity fields involved are complex, unsteady and exhibit cyclic variations so that whole field visualisation and velocimetry methods are also required for full characterisation of the in-cylinder flow.

Therefore, whole field optical measurement techniques such as Streak Photography, [1.11] Particle Tracking Velocimetry (PTV) [1.18, 1.19] and Particle Image Velocimetry (PIV) [1.20, 1.21, 1.22] are finding increasing application to the study of in-cylinder flows within SI engines. These whole field velocimetry techniques provide the ability to record instantaneous, cycle resolved, two dimensional maps of velocity within extended measurement planes inside optically accessed engine cylinders and therefore provide an important complement to pointwise data and a potential means for the validation of CFD simulations. In each method, flow-following particles are introduced into the engine's intake and their progress over time is recorded using a modulated illumination source and a photographic or electronic camera. Amongst these techniques, only PIV is capable of measurements under conditions of high concentrations of flow seeding particles, giving the potential for measurements on a regular grid with high spatial resolution without recourse to significant interpolation [1.23].

Whole field imaging techniques require extensive optical access for illumination and viewing so that modified optical engines are required in these studies. Where an axial swirl motion is predominant, optical access for viewing horizontal planes may be provided by windows in the piston crown or cylinder head and horizontal laser sheets may be introduced through a transparent cylinder wall. The study of tumble motion requires optical access for vertical planes by means of a transparent cylinder. Although low spatial resolution PTV measurements have been made in vertical planes within optical cylinders [1.19, 1.24], aberrations due to refraction in the curved cylinder wall have prevented many workers from attempting the high resolution PIV measurements required for the detailed characterisation of tumble formation and breakdown. The detailed study of this type of flow using PIV has therefore required the use of unrealistic engines with square pistons and flat liners [1.25], or water analogue engines employing refraction correction by index matching, in which only the induction flow can be simulated [1.26,1.27].

This thesis reports new developments in the application of PIV to the study of in-cylinder flow fields in planes both perpendicular and parallel to the cylinder axis in a production geometry single cylinder optical engine exhibiting barrel swirl. This has involved the development of a number of innovative experimental techniques. The most significant of these is a simple means of optical correction for high resolution imaging of vertical planes within the engine's thick glass cylinder. The flow mapping experiments which were enabled by these developments have given new insights into the important processes involved in barrel swirl formation and breakdown in this type of engine.

The next section of this chapter describes the development of experimental techniques for in-cylinder flow visualisation and measurement. The current state of knowledge regarding turbulence enhancement in SI engines and, particularly, the development of the Barrel Swirl engine and the flow processes occurring within it are reviewed in section 1.3. Finally, a summary of the achievements of this work and an overview of the remainder of the thesis is given in section 1.4.

1.2 Techniques for In-Cylinder Flow Visualisation and Measurement

1.2.1 Early Techniques

The importance of in-cylinder fluid motion and the need for its visualisation and measurement has been recognised since the early days of engine research. In-cylinder flow was studied by Clerk as early as 1921 using a low speed optical engine designed by H. Ricardo [1.28]. The flow was visualised by the introduction of smoke and Clerk's qualitative observations were sufficient to confirm the turbulent nature of in-cylinder flow and to disprove Otto's earlier theory about the existence of charge stratification in this type of engine.

The introduction of discrete particles of flow-following matter was a natural progression of Clerk's technique. In 1937 a study of different types of in-cylinder fluid flow was undertaken by Lee [1.29] which employed a number of innovations. Firstly, the in-cylinder flow could be changed conveniently by shrouding different portions of the inlet valves. Secondly, pieces of feather were introduced in the flow as tracers and the motion of these was recorded using a high speed cine camera and an intense light source. By manually matching the locations of the tracers in subsequent frames, estimates of fluid velocity were made. This technique forms the basis of Particle Tracking Velocimetry in engines.

Early attempts to characterise swirl flows in motored engines used impulse type swirl meters [1.30]. Rotating vane and impulse swirl meters of this type are still used today for the comparison of different swirl and tumble inducing cylinder heads on steady flow rigs [1.19, 1.31]. However, mechanical swirl indicators of this type are extremely obtrusive and have poor frequency response so they cannot be used to study transient events within realistic engines.

Shadowgraphy and the more sensitive Schlieren Photography, have been used extensively for the qualitative visualisation of density gradients within fluid flows, fuel sprays [1.32], ignition systems [1.33] and flames [1.34]. However, the limited density gradients within large scale in-cylinder flow structures has typically restricted flow visualisation applications to valve flows during induction [1.35], crevice flows and roll-up vortex formation [1.36] during the exhaust stroke. The application of Schlieren photography requires accurate collimation of a light beam traversing the engine cylinder and has therefore largely been restricted to applications in square piston engines with flat windows, or in cases where illumination and viewing was possible via systems of flat windows and mirrors in the cylinder head and piston crown [e.g. 1.37]. Schlieren photography has recently been performed in a cylindrical bore optical engine in which the external curvature of its optical cylinder liner was modified to preserve the collimation of parallel rays passing through engine [1.38].

1.2.2 Single Point Velocimetry

The application of Hot Wire Anemometry (1.39) and later, Laser Doppler Velocimetry [1.40] to engine flow studies, permitted the detailed quantitative study of in-cylinder fluid motion. These techniques provide point measurements of velocity from which ensemble averaged velocity profiles and turbulence statistics can be estimated. A critical comparison of these techniques has been made by Witze [1.41]. Hot wire anemometry suffers from directional ambiguity, is intrusive and the fragility of the probes and calibration issues preclude their use in many conditions within realistic engines. However, the relatively low cost of HWA equipment, the high frequency response of the transducers and continuous signal ensures that HWA is still used for the measurement of turbulent length scales and in certain cold flow engine applications.

By contrast, Laser Doppler Velocimetry is non-intrusive, requiring limited engine modification in the form of optical windows. The measurement volume is readily traversed through the flow for velocity profile measurement, without interfering with the flow structure. Therefore, LDV has become the preferred technique for the measurement of velocity profiles within realistic engines under motored and fired conditions.

LDV measurements in steady flow rigs have contributed much to the knowledge of the behaviour of valve flows at different valve lifts [1.42, 1.43]. Swirl and tumble ratios have also been estimated from Hot Wire [1.44] and LDV velocity profiles measured in both steady flow rigs [1.45] and in motored engines [1.46].

The non-intrusive nature of LDV makes it the only pointwise velocity method capable of measurements under firing conditions. This has permitted measurements of the pre combustion fluid motion in firing compression ignition [1.47] and SI engines [1.48], measurements in end-gas [1.49] and studies of flow characteristics ahead and behind of a developing flame front [1.50].

Analysis of LDV data collected from a large number of engine cycles permits the estimation of ensemble averaged mean velocities and turbulence intensities [1.51]. Turbulence intensities estimated in this way may, however, be greatly overestimated due to contamination of the turbulent fluctuations by cyclic variations of the mean flow [1.52] and may vary significantly according to the particular data reduction technique which is used [1.53]. Cycle-resolved turbulence statistics can be estimated using LDV if the seeding density and hence data rate is sufficiently high to give a quasi-continuous velocity signal [1.52, 1.54]. In this case the cyclic variations do not contaminate the turbulence measurements but unsteady motion of large scale structure within an individual cycle will do so [1.53]. Nevertheless, velocity and turbulence data from LDV has contributed greatly to the understanding of in-cylinder mean and turbulent flows and their influence on combustion.

Although pointwise velocity data have provided much useful insight into in-cylinder flow processes and will undoubtedly continue to do so, the reality of flow within IC engine cylinders is complex, unsteady and transient. The process of induction creates high momentum jets of fluid which penetrate the cylinder and set up large scale, three dimensional fluid motion. During the compression process this motion is modified by the piston movement and the changing geometry of the clearance volume. The details of the mean and turbulent flow vary according to the position within the clearance volume and change in time. Therefore, a limited number of point measurements, while providing valuable time averaged data and turbulence estimates, are not sufficient to fully describe the details of the unsteady flow processes which take place.

Attempts have been made to overcome the limitations of single point measurements while avoiding the practical considerations and data reduction problems associated with whole field techniques. One such example is the development of a scanning LDV system, which allowed a cycle resolved velocity profile to be captured by rapid scanning of the measurement volume along a given line [1.55]. This system also permits turbulence length scale estimation, but is mechanically complicated and high data rates are required to give a continuous velocity signal. Another technique, known as "displaced line diagnostics" uses a UV laser to write a line of phosphorescent seeding particles in the engine flow, the distortion of which over a short period of time gives the velocity profile [1.56]. However, while this technique is conceptually and experimentally simple, it offers relatively poor accuracy and is limited in spatial and temporal resolution.

While these developments have gone some way to overcoming the limitations of single point measurements, the need for truly whole field flow visualisation and measurement for the characterisation of complex unsteady in-cylinder flows has seen an increase in the application of Particle Tracking and Particle Image Velocimetry.

1.2.3 Particle Tracking and Particle Image Velocimetry in IC Engines

Increasing confidence in the use of engines with extensive optical access, the availability of inexpensive and high quality electronic and photographic recording media and reliable high power and pulsed lasers as illumination sources has seen the increasing application of Particle Tracking Velocimetry (PTV) and Particle Image Velocimetry (PIV) to the characterisation of instantaneous whole field in-cylinder flow structure. These techniques are typically capable of providing full planar measurements of two in-plane velocity components and, through more sophisticated recording techniques, three components of velocity within thin planes or extended volumes may be estimated.

In PTV and PIV experiments, small tracer particles are introduced into the flow and subjected to intense stroboscopic illumination so that their positions may be recorded, photographically or electronically, at two or more known instants in time. In the typical measurement procedure, the recordings are digitised for automated extraction of the velocity data. In PTV, individual particles or groups of particles are identified and matched between exposures such that their displacement, and hence velocity, may be measured. In PIV, the spatial particle image distribution is correlated to give the mean displacement in each region without recourse to individual particle image recognition.

PTV has been used for the characterisation of induction-like flows in liquid analogue engines [1.26, 1.27]. The use of liquid analogues permits high resolution imaging within cylindrical test sections by means of index matching, but also limits study to the flow during induction. In addition, dynamic similarity with air flow in the real engine must be assumed if the results are to be meaningful. The liquid analogue PTV studies have allowed estimates of Swirl and Tumble ratios at inlet valve closure to be made for a variety of cylinder heads. Such measurements have produced useful correlations with known engine performance [1.27] and have also been used as initial conditions for CFD predictions of flow during compression [1.57]. In motored engine studies, PTV has been applied to the study of cyclic variability in an axial swirl flow within a motored engine [1.18] and tumble flow has also been investigated in a motored engine with PTV, allowing tumble ratios to be calculated after the point of inlet valve closure [1.19]. The spatial resolution in this latter study was, however, insufficient to provide detailed information on the process of tumble breakdown.

A variation on PTV is streak photography, which involves illuminating the flow with an intense light sheet which is modulated in pulses of finite duration so as to record streaked images of individual particles. The length and direction of an individual particle image streak yields the local velocity vector. Modulating the illumination by intensity or colour allows the beginning and end of the streaks to be identified to give the unambiguous vector direction and to discard any streaks which are truncated as they exit the light sheet. The streak photography technique has been used to visualise and quantify swirl and tumble in a water analogue rig [1.58].

The application by Kuwahara *et al* [1.13, 1.11] of streak photography in a motored engine has provided some of the most detailed flow visualisation and velocimetry data concerning tumble breakdown to-date. In this case, colour coding of streak ends allowed for higher seeding densities to be used than in any previous PTV studies, thereby avoiding the requirement for ensemble averaging or interpolation. This gave higher spatial resolution velocity measurements and, by the use of a flat cylinder head window, permitted the spatial characteristics of tumble breakdown in the combustion chamber to be quantified for the first time.

In general, the need for long illumination pulses, or long trains of rapid pulses in PTV experiments calls for the use of modulated Continuous Wave (CW) lasers or multiple pulsed white light sources. These illumination sources provide laser sheets of relatively low power density, so that large (10-100 μm) seeding particles must be used to achieve sufficient side-scattering for adequate particle imaging. The frequency response of the large flow following particles then places a lower limit to the spatial and temporal velocity scales which may be resolved. In addition, relatively low densities of tracer particles are needed to avoid the joining or cross over of streaks or particle paths and to avoid excessive computation time in identifying images of individual particles. Since the initial particle positions within the flow are random, a particle density which is sufficiently low to avoid these problems will also lead to many areas in the flow which contain no particles at all and hence no velocity information. Therefore, the velocity fields produced in the PTV work reported here, are often seen to be sparse and require significant interpolation or ensemble averaging. The advent of Particle Image Velocimetry has provided a means for achieving high spatial resolution measurements on a regular grid for the study of cycle-resolved flow fields within realistic motored engines.

In Particle Image Velocimetry, a high energy laser light sheet is pulsed two or more times to "freeze" the motion of microscopic seeding particles within a thin plane in the flow. A high resolution photographic or electronic imaging system viewing normal to the plane of the light sheet records the positions of the particles at two or more known instants in time as they move in the plane of the light sheet. The mean velocity within each small region of the recorded field is determined by performing a spatial correlation of the digitised region. The use of high energy, short pulse duration laser illumination allows micron sized seeding particles to be used which are capable of following the most rapid velocity fluctuations expected in in-cylinder IC engine flows [1.59]. Further, by using a large aperture and restricting the depth of field of the imaging system to be of the same order of the light sheet depth, particle image sizes of the order of a few of microns are possible.

The spatial correlation process used in PIV does not involve the identification of individual particle images that is required in PTV. Consequently, a sufficiently high density of seeding particles may be used that each region of the flow is likely to contain the required density of tracer particles and hence potential velocity information. The spatial resolution capability of PIV is therefore potentially higher than for the PTV and streak techniques, giving more complete and detailed velocity maps from a single instantaneous recording [1.23]. Under ideal conditions, measurement grid sizes of the order of 0.5mm are possible. The PIV technique therefore appears well suited to the study of both the formation of large scale motion within IC engine cylinders and its subsequent modification and breakdown into small scale motion during compression.

PIV was first applied to in-cylinder measurements by Reuss *et al* [1.20] in a motored engine exhibiting axial swirl. The engine was equipped with a flat window in part of the cylinder head which gave access to a limited portion of the flow. The presence of strong bulk flow across the measurement window allowed the velocity direction to be determined unambiguously using autocorrelation analysis and small scale structure was visualised by high pass filtering. The limited velocity range within the window also allowed the experimental parameters to be optimised to minimise noise, such that important spatial derivative quantities such as large scale vorticity and strain rate could be calculated. Application of the same technique in a skip fired experiment permitted velocity, vorticity and strain measurements ahead of a developing flame to be made [1.60].

The application of PIV under motored and fired conditions was further developed in a study by Nino *et al* [1.21]. In this work a large cylinder head window allowed a complete flow reversal to be resolved in a high swirl engine under both motored and fired conditions, while the use of two colour illumination and cross correlation allowed the velocity vector directions to be determined unambiguously without *a-priori* knowledge of the flow structure.

Successful motored and fired [1.61] measurements in axial (vertical) planes have also been made in square piston optical engines, although the industrial relevance of flow measurements in such unrealistic geometries is a matter for debate. Cycle-resolved measurements of compression flow in a square piston engine have been attempted using a high speed camera and a copper vapour laser as a high repetition rate pulsed illumination source [1.62]. This technique holds the potential for examining the spatial and temporal evolution of bulk and turbulent flow within measurement planes in an engine, although the low individual pulse energy inherent in these rapid pulsed lasers leads to problems with film sensitivity, spatial resolution and noise characteristics.

A bonus of PIV measurements in combusting flows is that the number density of seed particles changes across the flame front due to expansion (in the case of solid particles) or evaporation/combustion (in the case of liquid particles). This allows the flame front position and shape to be determined simultaneously with the gas velocities ahead of the flame. Work in a rapid compression machine has shown that this can allow the burning velocity of the flame to be calculated from the gas velocity and flame speed deduced from successive flame positions in a rapidly recorded sequence [1.63].

Although PIV has many potential benefits in terms of spatial and temporal resolution over alternative techniques, its successful application to any flow measurement requires careful control of several important experimental factors, which will be discussed in more detail in Chapter 2 of this Thesis. The high resolution imaging which PIV demands necessitates careful control of optical aberrations and optimisation of the imaging system. Furthermore, the flow seeding, illumination and data analysis parameters all require careful attention. The application of PIV to engine flow measurement presents additional difficulties. Levels of stray light from piston, valve, cylinder and combustion chamber surfaces can be relatively high compared to the light scattered from the seeding particles. In complex flows, out of plane particle motion and spatial velocity gradients can be sufficiently high to restrict the correlation procedure used to determine mean particle displacements, particularly during induction and the later stages of compression. For these reasons, few examples of successful PIV measurements in engines have been reported in which the flow deviated strongly from in-plane solid body motion.

This Thesis reports the application of PIV to the study of tumble formation and breakdown in a motored four valve engine which is fully representative of typical production geometries. The detailed study of this type of flow in a production geometry engine requires vertical planes to be imaged to high resolution through the cylinder wall and therefore demands a careful treatment of optical aberrations which has not been addressed in any previous work.

The significance of in-cylinder motion and turbulence enhancement in SI engines will now be discussed. A very brief overview of some of the important consequences of fluid motion in IC engines is also given to indicate some of the potential areas for application of the new whole field velocimetry techniques in engine development.

1.3 Fluid Motion and Turbulence Enhancement in SI Engines

1.3.1 Fluid motion in IC engines

The details of fluid motion within Spark Ignition (SI) and Compression Ignition (CI) engines affect many important aspects of their operation [1.1,1.2]. Fluid motion affects the volumetric efficiency of the engine via wave action in the inlet and exhaust system and the details of port and valve flow. In spark ignition engines the preparation of premixed air/fuel mixture depends upon the details of atomiser (or carburettor) flows and the fuel distribution within the cylinder is determined by the air flow through the final stages of the inlet port and within the engine cylinder itself. Bulk and turbulent motion within the cylinder affect efficiency through heat transfer and influence the operation of the ignition source and early flame development. In compression ignition (CI) engines where liquid fuel droplets are injected, directly or indirectly into the engine, the major role of bulk flow is to supply a turbulent, rapidly swirling air flow for the rapid combustion of fuel droplets. Turbulence may be enhanced in swirl flows through the use of squish or appropriate combustion bowl design. In SI engines the production of turbulence by the breakdown of large scale motion is known to have crucial influence on combustion duration and cyclic variability, thereby having a vital influence on power and emissions characteristics. Fluid motion ahead of the propagating flame affects the progress of combustion while the flame-induced motion may significantly modify the flowfield itself. During the exhaust stroke, the details of crevice flows and piston induced roll-up vortices significantly influence emissions of unburned hydrocarbons. Residual motion at the end of the exhaust stroke may modify the intake process in a subsequent cycle.

Although all of the above processes are worthy of individual discussion and could benefit from the application of the new cycle-resolved, whole field velocimetry techniques, the role of in-cylinder fluid motion in providing the conditions for rapid and stable combustion in spark ignition engines through the production of turbulence near TDC is of primary significance in this work. The importance of turbulence enhancement and the work which has lead to the current state of knowledge regarding its generation and effects are now reviewed.

1.3.2 Turbulence Enhancement in SI engines

The influence of turbulence on flame speed in combustion bombs and tubes had been known since the studies of Mallard and Le Chatalier, circa 1883, later summarised by Bone in 1927 [1.64]. These experiments showed a clear relation between increased "agitation" of a combustible mixture and the speed at which a flame would propagate through it. It is now accepted that the enhanced flame speed which is observed in turbulent flows is primarily due to an increase in flame area through convolution or "wrinkling" of the thin flame reaction sheet by small scale flow eddies [e.g. 1.65, Keck]. The turbulent, unsteady nature of the pre combustion flowfield within an IC engine was first observed in early visualisation experiments performed by Clerk [1.3]. The link between increased turbulence and enhanced flame speed in engines was subsequently proved by Clerk in an experiment in which an engine was fired several cycles after the inlet valves had been closed, such that the turbulence generated during induction could decay completely. Combustion rates in the quiescent flow were significantly reduced compared to those measured in normal engine operation, proving the enhanced combustion rate to be linked to fluid motion generated by the induction process. Bouchard subsequently observed a linear relationship between flame speed and engine speed, although an adequate explanation for this linearity remained elusive [1.66].

The application of Hot Wire Anemometry to in-cylinder turbulence measurements by Semenov confirmed these early observations [1.67], although at this stage the turbulence observed in the pre combustion flow near TDC was wrongly believed to be the remnants of turbulence produced during induction. It is now known that small scale turbulence generated during induction decays rapidly, on the timescale of one millisecond, and consequently cannot survive through to TDC [1.68]. Detailed studies of flame propagation rates and turbulence intensities measured using Hot Wire Anemometry were made by Lancaster *et al* [1.69]. These studies revealed that the ratio of the fully developed turbulent flame speed to the laminar flame speed scaled linearly with the motored engine speed and the motored turbulent intensity and, significantly, could be increased for given engine conditions by appropriately shrouding the inlet valve. The speed scaling of mean and turbulent flow were confirmed by Witze [1.70, 1977] who also observed a rise in turbulence intensity towards TDC which was attributed to compression stroke enhancement of the intake generated turbulence.

The beneficial effects of improved flame propagation rates in production engines were reviewed by Mattavi [1.71] and included reduced cyclic variability and enhanced tolerance to high compression ratio operation, exhaust gas recirculation and lean mixtures. Significant reductions in combustion duration could be achieved through fluid motion enhancement, particularly using swirl and squish flows, and by means of suitable geometrical combustion chamber design for the maximisation of flame frontal area and minimisation of flame travel distances. While moderate turbulence enhancement had been observed in swirl flows in disc shaped combustion spaces, it appeared that the TDC turbulence intensities were limited in these cases to approximately half of the mean piston speed [1.72]. However, in an attempt by Witze *et al* to create a quiescent flow with zero swirl in a flat head engine, a rolling vortex was generated which was found to give rise to an increased turbulence intensity prior to TDC [1.48]. The mechanism proposed for the turbulence enhancement was the breakdown of the bulk rolling flow due to its distortion in the latter stages of the compression stroke.

Subsequently, Gosman *et al* studied the effects of strong tumbling motion which was generated by shrouding a portion of the inlet valve, in an experimental and computational study of in-cylinder flow [1.73]. This work showed that turbulence intensities of over twice the levels measured in swirl flows could be generated from the distortion of large scale tumbling motion during the latter stages of compression. This was confirmed by Kyriakides and Glover [1.16] in correlations of air motion and turbulence intensities at the spark plug for a variety of shrouded valve configurations. Work by Vafidis [1.74, 1987] showed that similar levels of turbulence enhancement could be achieved without recourse to valve shrouding, by reorientation of the inlet port. This gave the opportunity to achieve practically the turbulence levels required for high burning rates without compromising volumetric efficiency. A detailed LDV study of the mechanism of turbulence enhancement [1.3] in a flat head motored engine showed that the rotation rate of the tumbling vortex could increase during compression due to conservation of angular momentum, the tumble vortex breaking down well before TDC. Both the CFD [1.73] and phenomenological models [1.75] of tumble vortex spin up and breakdown show that the combination of spin-up followed by the rapid distortion of the tumbling vortex near TDC generates high fluid shear stresses which cause the release of turbulent kinetic energy and eventual tumble breakdown into multiple eddies. This process is indicated in figure (1.3).

The increasing use of multivalve pentroof combustion chamber engines gave the opportunity for increased control of in-cylinder motion as well as an increased valve curtain area for high volumetric efficiency. The open chamber geometry and central spark location in this type of engine further optimised combustion duration and stability. The favourable geometry of the combustion chamber was also found to accommodate the tumble vortex to a later stage in compression, thereby promoting enhanced tumble spin-up and increasing the energy available for turbulence enhancement during combustion. Increasing the tumble ratio was found to further increase the turbulence levels and also to delay the breakdown of large scale motion, generating maximum turbulence levels towards the end of the compression stroke [1.76] and, in some cases, after TDC [1.31].

The improved combustion stability afforded by turbulence enhancement in this type of engine was found to give additional performance benefits in terms of higher compression ratio operation and increased tolerance to lean air fuel ratios and exhaust gas recirculation for emissions control [1.9, 1.77, 1.78]. Correlations of intake generated flow observed and measured using particle tracking techniques in water analogue rigs and motored optical engines have shown that both the strength and inclination axis of the tumble vortex at BDC correlate with combustion duration [1.27]. This has been verified in LDV studies [1.79], flame speed measurements [1.80] and classical burn rate diagnostics using steady flow swirl meters to characterise cylinder head activity [1.6].

The use of tumble for turbulence enhancement after TDC is accompanied by remaining large scale motion at the time of ignition, and this has been confirmed with detailed LDV [1.81] and particle tracking studies [1.82]. It is known that high bulk velocities can disrupt the spark discharge [1.33] and adversely influence flame development through convection towards combustion chamber surfaces [1.83], while excessive turbulence intensities during combustion can lead to flame quenching [1.14]. These problems cause misfire and incomplete combustion and can lead to unacceptable driveability and hydrocarbon emissions, particularly under lean burn conditions.

Reduction of the bulk flow at the central ignition site in a high tumble engine was achieved by Kuwahara *et al* [1.82] through modification of the piston face shape, where charge stratification was also employed to assist stable lean operation. In this case the application of quantitative streak photography was instrumental in characterising the large scale flow structure and verifying the effects of the final piston design. The use of asymmetric inlet conditions to incline the tumble axis is also believed to stabilise the conditions for ignition and early flame growth for engines with central ignition by reducing the bulk velocity and cyclic variability of flow direction at the spark location [1.84].

The variety of flow control opportunities afforded by multivalve cylinder heads and the clear requirement to optimise the in-cylinder flow structure throughout the combustion event has lead to increased application of three dimensional CFD flow modelling for the prediction of port and in-cylinder bulk flows and turbulence [refer for example to: 1.12, Baritaud; 1.85, Henriot; 1.86, Haworth; 1.87, Le Coz; 1.88, Tatschl]. While such CFD predictions have been able to replicate the trends in experimentally observed features of bulk and turbulent flow, the magnitude and precise spatial structure of both bulk and turbulent motion have often not been accurately represented.

Although much is now known about the mechanisms for turbulence enhancement in SI engines and its effects on combustion, there is still little consensus as to the ideal flow conditions required at each phase in the initiation and combustion process, less still on how these can best be achieved in practical engines. CFD is gaining in popularity as a practical engine design tool which promises the rapid evaluation of new experimental flow strategies, but detailed experimental validation is always required when CFD is applied to new engine geometries. While the pointwise velocimetry techniques can provide detailed measurements at limited numbers of selected points within in-cylinder flows, whole field flow visualisation and measurement is also required in the study of the complex, unsteady flows upon which modern engines rely. The whole field velocimetry techniques such as PIV are therefore beginning to play a vital role in the validation and further development of CFD codes, the study of flow and combustion interaction and the fundamental study of the formation and breakdown of large scale motion within realistic engine configurations.

1.4 Present Contribution and Thesis Outline

1.4.1 Contributions from this Work

Controlling the combustion process in SI engines via fluid motion is a complex undertaking which requires a detailed understanding of the whole flow field and its effects on combustion throughout the entire initiation and burning event. Particle Image Velocimetry (PIV) provides an important new tool for the investigation of in-cylinder flow and its effects on combustion.

This Thesis is concerned with the development of PIV for the characterisation of in-cylinder flows in a four valve four stroke spark ignition engine exhibiting tumble, although the techniques described have equal applicability in high axial swirl spark ignition and compression ignition (diesel) engine research.

In PIV, the laser light sheet and photographic camera must be considered as forming a multi point anemometer in which every point within the measurement plane must have the correct focal distance, seeding concentration and optical aberration characteristics. Additional experimental difficulties can be expected when applying PIV in the conditions of a motored or firing IC engine. A major achievement of this work has been the design and development of a PIV engine facility which permits the routine acquisition of PIV data in the demanding geometry and hostile environment of a realistic optical IC engine.

In order to study the evolution and breakdown of tumble using PIV, it has been necessary to record high resolution images from axial planes within the cylinder through the curved cylinder wall. This has been achieved by means of a single optical element to correct for severe astigmatism introduced by the glass cylinder, which now permits PIV measurements to be performed to a spatial resolution approaching that achieved by other workers through flat windows. The optical correction method used in this work will potentially permit the extension to higher spatial resolution of many other techniques requiring whole field in-cylinder imaging. Methods for optimising the focusing of the imaging system and the calibration of remaining field distortion are presented. It is hoped that in the future the single element corrective lens can be further developed using computational finite ray tracing, to provide improved aberration correction over wider fields with reduced distortion.

The complete PIV engine facility and experimental techniques developed during this work have now been replicated in a research laboratory of the industrial sponsor, Rover, where it will be used as a routine tool in the development process of new engines and the validation of CFD models.

Although the prime aim of this work has been the development of PIV for engine applications, new insight into the evolution and breakdown of tumble motion has also resulted from a systematic set of flow mapping experiments in the engine. Important flow processes which govern the formation and breakdown of barrel swirl have been identified. These are the impingement of counter rotating vortices during early induction, and stagnation of impinging flow on the piston crown mid way through the compression stroke. It was demonstrated that both effects can be reduced by increasing the degree of barrel swirl motion during induction. Large scale bulk motion is shown to be present during ignition and to persist until several tens of degrees after TDC in the motored flow. This confirms concern for possible adverse effects on initiation and early flame growth.

Initial measurements of the flow ahead of a developing flame in the engine have also been made which, although providing little new insight into flame development, confirms that useful measurements can be made routinely under fired conditions.

1.4.2 Overview of the Thesis

Chapter 2 describes in detail the PIV technique and the effects of the important experimental parameters involved in its optimisation for in-cylinder applications.

Chapter 3 describes refractive methods for the correction of aberrations when performing imaging through the transparent walls of cylindrical test sections. Correction for retaining the collimation of transilluminating beams is distinct from that of imaging planes within the cylinder and is reviewed in Section 3.2. The development and application of a corrective lens for high resolution imaging of finite conjugate planes within the engine cylinder is enumerated in Section 3.3.

The PIV engine facility which was designed and installed in the first stages of this work is described in Chapter 4. The pulsed Nd:YAG laser specification, the Rover single cylinder optical engine design and the light sheet formation and imaging optics are described in Section 4.2. Details of specific experimental techniques which were found essential for the routine acquisition of high quality PIV images from the facility are given in Section 4.3. Descriptions of the interrogation system and procedure are given Section 4.4 and Section 4.5 details the measurement conditions for motored and fired PIV experiments.

PIV measurements from the engine are presented in Chapter 5. Typical PIV images and their characteristics are presented in Section 5.2. Motored, cold flow results are presented in section 5.3. These represent velocity maps from a variety of horizontal and vertical planes, under conditions of moderate and high swirl and different engine speeds. Comparisons of the PIV results with data from other sources are given in Section 5.4. The ability to record useful PIV images under firing conditions is demonstrated in section 5.5.

Chapter 6 is devoted to a discussion of the practical and fundamental limitations to the current measurement technique and potential methods for their improvement. Important practical limitations are discussed in Section 6.2, together with suggestions for improvements. The fundamental limitations inherent in autocorrelation analysis are discussed in Section 6.3 and possible methods for overcoming these by implementing cross-correlation interrogation are presented.

The thesis is closed in Chapter 7, with conclusions in section 7.1, and suggestions for further development of PIV techniques and their applications in in-cylinder engine research in Section 7.2.

CHAPTER 2

PARTICLE IMAGE VELOCIMETRY AND ITS OPTIMISATION

2.1 Introduction

Particle Image Velocimetry has its origins in Laser Speckle Photography (LSP), a surface metrology technique for the measurement of in-plane displacement of solids. In LSP an optically rough solid surface is illuminated with coherent light and the resulting speckle pattern is recorded, before and after surface deformation, on the same piece of photographic film. Given that the speckle pattern does not significantly change between the two exposures, the displacement of individual speckles in each small region of the double exposed recording gives a measure of the local surface displacement. The speckle pattern within each region is dense and complex, so the mean speckle displacement in each region cannot be determined readily by locating and matching individual speckles. Burch and Tokarski [2.1] showed that the mean speckle displacement could be recovered from speckle photographs by interrogating each region of the transparency with a narrow laser beam. This generated a Young's fringe pattern in which the orientation and spacing of the fringes were simply related to the direction and magnitude of the surface displacement in the interrogation region. The magnitude and angle of the displacement vector could therefore be measured at each location in the transparency, subject to a 180 degree directional ambiguity. Barker and Fourney extended the technique to the measurement of interior displacements in laser illuminated planes within solid transparent models [2.2]. The speckle pattern caused by side scattered light from the measurement plane was recorded with a photographic camera viewing orthogonal to the illuminated plane.

Laser Speckle Velocimetry (LSV) was adapted from LSP for the measurement of velocity fields within low speed, laminar fluid flows. In the first applications of LSV, fluids were heavily seeded with flow following particles to produce the required speckle effect e.g. Dudderar and Simpkins [2.3], Grousson and Mallick [2.4] and Barker and Fourney [2.5]. The formation of coherent speckles in LSV required that extremely high seeding densities be used, such that the light scattered from individual particle images could interfere at the image plane of the recording device. This condition was readily achieved in low speed, recirculating fluid flows. However, in early applications of laser speckle velocimetry to unsteady gas flows, it was noted that velocity data could still be extracted using the Young's fringe method, although the recordings actually consisted of well defined images of individual particle pairs instead of the expected random speckle effect [see Meynart, 2.6]. The effects of reduced seeding densities on the interrogation process were subsequently discussed by Pickering and Halliwell [2.7] and Adrian [2.8] and, in the particle imaging regime where speckle is absent, the LSV technique became known as Particle Image Velocimetry (PIV). The relaxed seeding requirement in PIV means that adequate seed densities can be achieved in a variety of high speed gas flows of practical interest, while the absence of speckle gives greater tolerance to decorrelation by out of plane fluid motion.

The Young's fringe processing techniques which were prevalent in early LSP and PIV work used a variety of data reduction techniques, including in some cases user input, to determine the fringe orientation and spacing. Typical approaches included fringe integration along a user-defined fringe direction to reduce speckle noise, followed by conventional fringe counting or Fourier Transform techniques for determining fringe spacing. Alternative approaches determined the fringe direction without manual intervention by correlating a small number of intensity profiles taken through the fringe pattern at different locations. However, in the general case, the fringe pattern is the superposition of a number of sets of Young's fringes of different orientation and visibility, which correspond to each possible particle pairing within the interrogation region. The most dominant set of fringes is most likely to correspond to the mean particle displacement. However, this is not necessarily easily identified by the operator or by algorithms which use a limited portion of the available fringe information. Further to this, many practical PIV experiments require large interrogation grids consisting of up to 100x100 individual regions, so that fully automated, reliable and rapid transparency analysis is essential. A quantitative comparison of different fringe processing algorithms for speckle photography was made by Huntley [2.9]. The most accurate and reliable approach was to calculate the full two dimensional Fourier transform of the digitised fringe pattern and hence generate the two dimensional spatial autocorrelation of the original double-exposed image distribution on the transparency. The most likely displacement vector could then found by locating the centroid of the most dominant non-central peak in the autocorrelation plane, the result being subject to a 180 degree directional ambiguity.

The most intensive part of the autocorrelation process is the calculation of the two dimensional Fourier transform of the fringe pattern. The need to compute this Fourier transform can be avoided by presenting the fringe pattern to a second optical Fourier transforming system. This requires a spatial light modulator to convert the intensity distribution of the Fringe pattern into an amplitude distribution which can modulate a second coherent light beam. The all-optical autocorrelation process may be performed extremely rapidly in this manner and, if the remaining processing bottlenecks of transparency scanning and autocorrelation peak location are removed, interrogation rates of the order of thousands of regions per second may be achieved [e.g. 2.10]. Unfortunately, high speed spatial light modulators are at present expensive and unreliable, although slower, electronically addressed liquid crystal devices have been used in practical interrogation systems [2.11].

The approach now taken by the majority of workers is to digitise the interrogation region using a CCD camera equipped with a microscope objective and to perform a fully digital computation of the two dimensional autocorrelation function of the original particle image field. This completely eliminates the requirement for coherent optical processing. The digital interrogation process is consequently relatively immune to phase noise, which is a significant source of fringe degradation in Young's fringe processing systems [2.7]. All-digital interrogation also enables modified interrogation algorithms to be applied flexibly, permitting pre-processing of the particle image fields for noise reduction purposes and enabling on-line PIV recording and interrogation using electronic imaging devices. With digital systems of modest cost, interrogation rates of a few interrogation regions per second are commonly achieved, while fully optimised digital systems based on parallel processors achieve rates of several hundred regions per second and above [2.12]. The interrogation procedure used in the work presented in this Thesis was based on a commercially available, purely digital autocorrelation system and the discussion which follows will be restricted to this method of interrogation, although many parallels with all or part optical interrogation systems may be drawn.

The past decade has seen the development of PIV from a technique confined mainly to low speed, well controlled flows in liquids to a viable research tool for the study of turbulent, reversing, reacting and even transonic flows in gases. Excellent reviews of the evolution of PIV and recent advances are available in the literature [e.g. 2.13, 2.14, 2.15]. A significant recent advance has been the development of all-digital integrated PIV systems in which high resolution CCD cameras are used to replace the photographic recording process [2.16, 2.17, 2.18]. CCD arrays of 2k and 4k square are now available, but despite the benefits of low noise, grey level imaging afforded by CCD technology, the spatial resolution of the cameras still falls short of that of high resolution photographic emulsions. These are still required whenever high spatial resolution PIV measurements are required over extended areas of flow field.

Theoretical analyses and the practical experience of experimentalists have shown that the successful application of PIV demands a careful compromise between many experimental parameters. For example, at the image recording stage, the characteristics of the light sheet, seeding particle number density and the particle image size and shape all affect measurement accuracy and validity. The height of the signal peaks relative to the spurious correlation peaks in the autocorrelation is affected by flow parameters such as velocity gradients and in-plane and out-of-plane particle movement. Random film noise in the PIV recordings or structured fogging caused by stray illumination can also significantly degrade the autocorrelation and lead to increased proportions of erroneous measurements. In what follows, the basic requirements for PIV recording and interrogation techniques are described and the theoretical and experimental considerations involved in designing a successful PIV experiment are discussed.

2.2 The Basic PIV Technique

2.2.1 PIV Recording

In its simplest form, the PIV technique requires the formation of a thin, double-pulsed laser light sheet within the fluid, in which the positions of a large number of flow following particles are recorded at two instants in time by means of a photographic or electronic camera viewing normal to the light sheet plane (Fig 2.1). In the interrogation process, the photographic recording is subdivided into a regular grid, which may contain of the order of 100x100 individual interrogation regions, each of which contains typically 5 to 20 particle image pairs. The interrogation region is typically a square of side *D*, which relates to an interrogation volume in the flow of side *L* and depth *W*, as shown in figure (2.2). The interrogation region size must be chosen carefully according to the considerations given in section 2.4. The finite laser sheet thickness defines the interrogation volume depth, *W*, and is chosen to be less than or equal to *L* so as to accommodate finite out-of-plane velocity components.

The particle distribution in the flow area is imaged onto the film with a lens of focal length f whose optical axis is perpendicular to the measurement and image planes. Using the notation of Adrian [2.13], where $\mathbf{x} = (x,y,z)$ represent the flow co-ordinates and $\mathbf{X} = (X,Y)$ represent film plane co-ordinates, then in the absence of field distortions the co-ordinates are related by;

$$\mathbf{X} = \frac{s_i}{s_0 - z}(x\mathbf{i} + y\mathbf{j}) \tag{2.1}$$

where **i** and **j** are unit vectors in the x and y directions, s_i is the image distance, s_o is the object distance and z is measured from the centre of the interrogation volume. Sign changes due to inversion of the image have been neglected. The mean particle displacement vector in the flow during the pulse interval Δt, due to the velocity vector $\mathbf{v} = (u\mathbf{i}+v\mathbf{j}+w\mathbf{k})$ is in general three dimensional and is given by

$$\mathbf{s} = \Delta t\,(u\mathbf{i} + v\mathbf{j} + w\mathbf{k}) \tag{2.2}$$

The imaging process projects the displacement vector **s** onto a plane with a nominal magnification $M=s_i/s_o$. If perspective effects are included, the two dimensional displacement vector $\mathbf{S}=(\Delta X\mathbf{i}+\Delta Y\mathbf{j})$ in the film plane is given by

$$\mathbf{S} = M\Delta t(u\mathbf{i} + v\mathbf{j}) + M\frac{(x\mathbf{i} + y\mathbf{j})}{s_0 - z}w\Delta t \tag{2.3}$$

In high spatial resolution PIV experiments the light sheet thickness, W, is usually sufficiently small to ensure that $z \ll s_o$, so that

$$\mathbf{S} = M\Delta t(u\mathbf{i} + v\mathbf{j}) + M\frac{(x\mathbf{i} + y\mathbf{j})}{s_0}w\Delta t \tag{2.4}$$

Therefore, in the general case, the true in-plane displacement is contaminated by perspective effects which increase with the out of plane displacement and the angle between the measurement region and the optical axis. In the limit of paraxial recording, where $|\mathbf{x}|/s_O \ll 1$, the effects of perspective can be neglected and equation (2.4) is further simplified to

$$\mathbf{S} = M\Delta t(u\mathbf{i} + v\mathbf{j}) \tag{2.5}$$

The measurement of the in-plane velocity components is then reduced to the measurement of the components of the mean displacement vector, given that the camera magnification and laser pulse separation are known. The displacement vector is determined by the correlation process which is described below and the in-plane velocity components are given by

$$u = \Delta X / M\Delta t \tag{2.6a}$$

$$v = \Delta Y / M\Delta t \tag{2.6b}$$

It is instructive to estimate the error in the displacement vector estimate due to perspective in a typical PIV arrangement, since this is often neglected in discussions of measurement accuracy. Consider an imaging system with an 80mm focal length lens operating at magnification of unity such that $s_O = s_i = 160$mm, and an out of plane displacement of $w\Delta t = 0.2$mm. The sheet thickness, W, is normally of the order of <1mm so that the effect of z may be neglected. At a position in the flow which is 20 mm from the optical axis the perspective contamination of the in-plane displacement given by the second term in equation (2.3) is equal to 0.025 mm. For a typical in-plane particle displacement of 0.2 mm this represents a 12.5% error in the displacement vector. This error is a systematic function of position but is also a function of the unknown out-of-plane displacement. In the measurements presented here, a magnification of 0.4 was used with an 80mm macro lens so that $s_O = 280$mm. This limits the perspective error at the same flow position to 0.0056 mm on the film or 0.014 mm in the flow. The measurement error has therefore been reduced to 7%. The perspective error diminishes in proportion to the out-of-plane displacement and can be reduced significantly in the case of two dimensional flows, if the light sheet is oriented with the predominant flow direction. Therefore, in the measurements of predominantly in-plane tumbling flow which is the subject of this work, the typical perspective error can be reduced to the level of the random measurement error and for the purposes of flow mapping in this work was neglected.

In flows of practical interest, finite spatial and temporal velocity gradients are clearly present, i.e. u,v and w are functions of both time and space [2.19]. This introduces a small error into the estimate of the Eulerian velocity vector which is a function of the spatial and temporal flow characteristics and the distance the particle is permitted to move between exposures. However, by limiting the laser pulse separation and the interrogation region size to be much less than the time and length scales in the flow field, the errors in the Eulerian velocity estimate may be restricted to be less than the random measurement error and adequate estimates of the velocity vector can be made. More work is required to quantify the effects of this bias in highly turbulent unsteady flows.

2.2.2 PIV Interrogation

The process of measuring the mean particle displacement vector within each small region of the flow transparency is known as interrogation. The transparency is divided into a large number of square interrogation regions whose centres are located on a regular grid. For simple double exposed PIV transparencies the displacement vector within the interrogation region is determined by calculating the digital autocorrelation of the double exposed particle image field. This is typically carried out by illuminating the transparency and digitising each small region in turn using a microscope objective and CCD camera coupled to frame grabber under the control of a digital computer (Fig 2.3). The autocorrelation is calculated from the digitised particle image distribution by performing a two dimensional real-to-complex FFT. The squared modulus of each pixel is then calculated to give the power spectrum, which is analogous to the Young's fringe pattern in optical systems. A second FFT is then performed on the power spectrum, which, according to the Wiener Kintchine Theorem, produces the autocorrelation of the original particle image distribution.

Each interrogation region contains a number, N_p, of paired particle images which are separated by the mean displacement vector, S, and also a number of unpaired particles, N_u. The unpaired particles are caused by truncation of paired images by the interrogation region boundaries and their numbers increase in proportion with the mean in-plane particle displacement and out of plane fluid motion. In the absence of film noise, with uniform illumination, identical particle images and a uniform displacement across the region (i.e. no velocity gradient), the intensity distribution of the interrogation region can be modelled as

$$I(X,Y) \propto P(X,Y) * \sum_{i=1}^{N_p} \{\delta(X - X_i, Y - Y_i) + \delta(X - [X_i + \Delta X], Y - [Y_i + \Delta Y])\ \}$$
$$+ P(X,Y) * \sum_{k=1}^{N_u} \delta(X - X_k, Y - Y_k) \tag{2.7}$$

where $\delta(X,Y)$ is the delta function and $P(X,Y)$ is the particle image function and * represents convolution.

The autocorrelation $R(\xi, \eta)$, of the intensity distribution $I(X,Y)$ is defined by

$$R(\xi,\eta) = \int\int_{-\infty}^{+\infty} I(X,Y) I(X-\xi, Y-\eta) dX dY \tag{2.8}$$

It can be shown [e.g. 2.20] that the autocorrelation of the particle field intensity distribution in equation (2.6) can be expressed as

$$R(\xi,\eta) \propto R_{dc}(\xi,\eta) + R_s^+(\xi,\eta) + R_s^-(\xi,\eta) + R_{np}(\xi,\eta) + R_{nu}(\xi,\eta) \tag{2.9}$$

The individual terms on the right hand side of equation (2.9) correspond to correlations between individual features in the intensity distribution function as follows:

a)	$R_{dc}(\xi,\eta)$	central, self correlation function of the intensity distribution
b)	$R_s^+(\xi,\eta) + R_s^-(\xi,\eta)$	signal peaks located at +/- $(\Delta X, \Delta Y)$
c)	$R_{np}(\xi,\eta)$	noise peaks due to correlations between paired particles
d)	$R_{nu}(\xi,\eta)$	noise peaks due to correlations involving unpaired particles

The spurious peaks R_{np} and R_{nu} form a random noise floor from which the signal peaks must be distinguished for a valid displacement estimate. An experimentally simulated particle image field is shown in figure (2.4). This was produced by Lawson, by photographing scattering particles set in optical epoxy with a diffraction limited lens and optimally processed film and represents an ideal PIV experimental result [2.19]. The digital autocorrelation of the region is shown in figure (2.5), with the peaks R_{dc}, R_S and the noise floor structure $(R_{np}+R_{nu})$ indicated. The signal peak is located in practice by defining a mask to obscure the self correlation peak. The signal peak co-ordinates are then found to the nearest pixel by locating the highest pixel value in the remaining unmasked area. The estimate of the peak location is then refined to sub-pixel accuracy using a local interpolation or centroid calculation. The distance between the centre of the autocorrelation plane and the estimated peak location is the expected mean displacement vector.

The central self correlation peak, $R_{dc}(\xi,\eta)$ and the signal peak $R_S(\xi,\eta)$ have profiles which are proportional to the autocorrelation $R_{pp}(\xi,\eta)$ of the particle image function $P(X,Y)$. For a Gaussian particle image having a 1/e diameter equal to d_i, $R_{pp}(\xi,\eta)$ is a Gaussian having a 1/e diameter equal to $\sqrt{2}\, d_i$. The height of the self correlation peak is proportional to $(2N_p+N_u)$ and is at least twice as high as the signal peak.

The signal peak function, $R_S(\xi,\eta)$ is repeated in opposite quadrants in the autocorrelation plane such that its centroid co-ordinates are located at $(\Delta X,\Delta Y)$ and $(-\Delta X,-\Delta Y)$. The duplication of the signal peak arises from the inability to identify the particle images corresponding to the first and second exposures in a conventional double exposed recording. The resulting directional ambiguity may be a serious limitation in the study of complex, reversing flow fields and can only be resolved by employing more sophisticated recording and interrogation techniques, which will be described later. The height of the signal peak in the ideal case is proportional to the number of paired particle images, N_p, and the signal peak is normally the highest non-central peak in the autocorrelation plane. The height of the signal peak compared to that of spurious correlation peaks is an important indication of measurement confidence. The signal peak must be distinct from the self correlation peak and higher than the largest noise peak for a valid velocity measurement to result.

Each spurious correlation produces a particle correlation function $R_{pp}(\xi,\eta)$ whose height is proportional to the number of spurious particle pairings which contribute at each displacement vector. The total number of spurious correlation peaks is given by

$$N_S = 4N(N-1) + N_u(N_u-1) + 4NN_u \qquad (2.10)$$

and these form a random noise floor from which the signal peak must be distinguished for a successful determination of the displacement vector. As the number of particle images in a region increases, the likelihood of a number of spurious correlation peaks coinciding to give a spurious peak of significant height increases, whereas the signal peak height is always limited to a maximum value which is proportional to $2N_p$. As a consequence, increasing the number of particle images in a region initially gives improved measurement performance, but there is a maximum particle image density above which no further improvement occurs. The spurious noise peaks are randomly distributed across the correlation plane and may therefore distort the signal peak shape, thereby introducing a random error into the velocity estimate. In simulations of double exposed interrogation regions, the total random error due to the noise floor is typically less than 1% of full scale velocity (2.18,2.20). In practical applications, correlated film and CCD noise and irregular particle images increase the random error further. Prasad *et al* report typical errors of the order of 1.5% of full scale velocity in the relatively ideal experimental case of turbulent channel flow [2.22].

A particularly important case arises when there are only two particle image pairs in an interrogation region, as indicated in figure (2.6). The signal peak is then the same height as the largest spurious correlation peak, so that each of the two indicated displacement vectors appear equally likely. In such a case the correct peak choice can only be made if flow continuity criteria or *a-priori* knowledge of flow direction is used. It is therefore important with autocorrelation analysis to use a sufficiently high mean seed density to reduce the probability of finding just two pairs in a region to an acceptable value.

Since the largest non central peak is not always the true displacement peak, it is customary to store the co-ordinates of the largest two or three signal peaks for use in post processing refinement of the velocity vector map. Post processing procedures typically include the removal of spurious vectors which are discontinuous with their neighbours. Missing vectors may be replaced with a vector determined from a suitable second or third candidate peak. Where no continuous vector choice is available the vector may be interpolated with a value calculated from its valid neighbours.

The directional ambiguity which arises in autocorrelation analysis may prove a serious limitation to the measurement of complex fluid flows. In the measurements presented in this Thesis the directional ambiguity problem has been addressed only in the sense that existing LDV data at a number of crank angles, and flow visualisation have been used to infer the bulk flow directions within the engine cylinder. Subsequent flow directions were inferred from flow continuity considerations. In general this approach is clearly unsatisfactory, since in flows of arbitrary complexity such additional flow direction information may be unavailable. Several techniques exist for resolving the ambiguity problem which do not require *a-priori* knowledge of the flow structure. These include image shifting and image labelling, together with cross-correlation of the first and second particle image fields.

Image shifting involves the introduction at the image recording stage of a known spatial shift of the entire particle image relative to the recording medium between the two exposures. With photographic recording, the shift may be introduced by a rotating mirror, film translation or polarising devices and is chosen to be greater than the most negative image displacement expected from fluid motion. The result of autocorrelation interrogation will then always yield a positive vector from which the vector shift can be subtracted to give the unambiguous displacement vector [2.23]. If the image shift or bulk flow is sufficiently large to move the second exposure particle field onto a different interrogation region, the two regions can be cross-correlated to give the unambiguous velocity vector [2.24]. Finally, by labelling the first and second particle images using, for example, colour [2.25], or by recording the separate exposures on different portions of film, the two separate images may be cross-correlated without recourse to image shifting.

For two separated image fields having equal and uniform intensity profiles and uniform particle displacements, the first and second intensity distributions I_1 and I_2 may be modelled as

$$I_1(X,Y) \propto P(X,Y) * \sum_{i=1}^{N} \{\delta[X - X_i, Y - Y_i]\} \qquad (2.11)$$

$$I_2(X,Y) \propto P(X,Y) * \sum_{i=1}^{N} \{\delta[X - (X_i + \Delta X), Y - (Y_i + \Delta Y)]\} \qquad (2.12)$$

The cross-correlation function is then defined as

$$R_{cc}(\xi, \eta) = \int \int_{-\infty}^{+\infty} I_1(X,Y) I_2(X - \xi, Y - \eta) dXdY \qquad (2.13)$$

The cross-correlation of the first and second particle image fields can be expressed as [2.19]

$$R_{cc}(\xi,\eta) \propto R_s(\xi,\eta) + R_n(\xi,\eta) \qquad (2.14)$$

the individual terms of which correspond to;

1)	$R_s(\xi,\eta)$	a single signal peak located at the unambiguous displacement vector
2)	$R_n(\xi,\eta)$	a random noise structure due to spurious correlations

A typical result of a cross-correlation of two particle image fields, separated by a polarisation sensitive labelling technique [Reeves *et al*, 2.26] is shown in figure (2.7). This shows the characteristic single signal peak which unambiguously locates the displacement vector, thereby eliminating directional ambiguity.

The cross-correlation of uniquely identified first and second particle images offers further advantages over conventional autocorrelation analysis. Most significantly, there is no self correlation peak, so that displacements approaching zero may be measured, thus expanding the measurement dynamic range. The number of spurious correlation peaks in the cross-correlation plane is reduced by a factor of approximately four compared to an autocorrelation with the same particle image density. This increases the probability of correct signal peak detection and also permits the use of higher seeding densities. Further, the restriction of avoiding the condition of two particle image pairs is lifted, so that lower mean seeding densities may also be used. The reduced sensitivity of cross-correlation interrogation to seed density may be useful whenever large changes in seed density occur in the flow due to expansion, or in conditions where accurate seed density control is difficult.

Despite the clear advantages of image shifting and cross-correlation, limitations of experimental complexity and cost restricted the engine experimentation presented in this Thesis to simple double exposed PIV recording and analysis. A detailed discussion of the available techniques for directional ambiguity removal is included in Chapter 6 and further work in this important area is planned.

2.3 PIV Recording Considerations

2.3.1 Particle Seeding Requirements

The practical success of any PIV experiment is highly dependent on achieving appropriate particle flow seeding characteristics. The important seeding parameters which must be considered are;

1) Particle flow-following characteristics
2) Particle light-scattering characteristics
3) Particle number density in the flow
4) Tendency of particles to foul optical windows
5) Tendency of particles to abrade cylinder surfaces
6) Ability of particles to withstand experimental conditions

The flow-following and light-scattering properties of small seed particles are both strong functions of particle size. Smaller particles follow the flow more accurately, but scatter light less efficiently than larger particles of the same material. In order to select an appropriate seed material it is first necessary to decide the degree of flow following that is required in the experiment and then to ensure that sufficient side scattered signal is available to record the particle image on the chosen detector.

2.3.1.1 Flow-following characteristics

The flow-following ability of a particular particle may be expressed as the percentage accuracy to which the true amplitude of a flow oscillating at a known angular frequency can be followed. This figure therefore gives an indication of the minimum flow timescale which can be resolved by a given particle.

If relatively low frequency flow fluctuations are of primary interest, for example the large scale flow structures which exist in IC engine in-cylinder flows prior to their breakdown, relatively large flow seeding particles may be used if their mean density is low. Their high scattering efficiency then allows the use of relatively lower power illumination. In turn this reduces experimental difficulties with stray illumination or "flare" and allows high rates of PIV image recording through the use of rapidly pulsed or modulated lasers. For example, hollow glass microballoons with a diameter of 40 μm are able to follow large scale flow structures with fluctuation frequencies of 250 Hz to 90% amplitude accuracy [2.27]. Particles of this nature scatter light very efficiently and have permitted chopped CW laser illumination to be used for cycle-resolved streak photography velocity measurements in a motored engine [2.28]. However, the limited flow following ability precludes the use of such particles for studies of high frequency turbulent structures.

If high frequency flow fluctuations are of interest, severe restrictions are placed on the particle diameter. Much work has been performed on the characterisation of flow following properties of microscopic particles for LDV turbulence measurements. Haghooie *et al* investigated the flow following characteristics of a number of different seed particles for LDV measurements of in-cylinder turbulence [2.29]. It was shown that alumina particles of 1μm diameter with a density of 4.0 g/cm^3 are capable of following 10 kHz sinusoidal velocity fluctuations to an amplitude accuracy of 90%. Durst *et al* give figures for particle diameters giving 99% amplitude following at turbulent frequencies of 2 kHz and 10 kHz for a variety of seed materials in air and other flows [2.30]. For example, silicone oil droplets of 0.8μm diameter are able to follow 10 kHz oscillations to 99% amplitude accuracy. Nino *et al* used 0.3-0.7 μm boron nitride particles for PIV measurements with an estimated frequency response of 20 kHz at 97% amplitude fidelity [2.31]. The most accurate practical flow followers reported to date are "white carbon" particles with a diameter of 1.3 μm and a very low density of 0.12 g/cm^3, giving a frequency response of several hundred kHz with good light scattering properties [2.27].

The majority of turbulent kinetic energy within in-cylinder IC engine flows is contained in flow frequencies less than the order of several kHz [2.29]. Tabaczynski gives typical values for integral timescales of 0.3-1.0 ms and micro timescales of 0.1-0.3ms for a variety of motored engines at speeds up to 3500 RPM [2.32]. The corresponding integral lengthscales are typically 2-10 mm with Taylor microscales in the range 0.2-1.0mm. Therefore, flow seeding particles commonly used for LDV turbulence measurements may be used in PIV measurements to visualise flow structures as small as the Taylor microscale at TDC. The spatial resolution of the PIV measurements is then limited by interrogation considerations alone.

2.3.1.2 Scattering characteristics

In the case of conventional PIV experiments, the light scattered from the seed particles is collected by an imaging lens whose optical axis is perpendicular to the light sheet. The side scattering efficiency of microscopic particles is poor, so that large aperture imaging is required in conjunction with a recording medium of suitable sensitivity. The intensity of light which is scattered into a solid angle Ω , given an illumination intensity I_O, is given by

$$I_0 \int_{\Omega} \frac{\lambda^2 |\sigma|^2}{4\pi^2} d\Omega \tag{2.15}$$

where σ is the Mie scattering coefficient and λ is the illuminating wavelength. In the case of side scatter from microscopic particles, the scattering coefficient, σ, is a strong function of the ratio of the particle diameter, d_p, to the illuminating wavelength. In the Rayleigh scattering regime, where $d_p < \lambda$ the scattering efficiency increases in proportion to $(d_p/\lambda)^4$, with erratic behaviour about this mean trend due to interference effects. In the geometric scattering regime, where $d_p >> \lambda$, the dependency is proportional to $(d_p/\lambda)^2$ and between the two regimes the dependency may be approximated as cubic. In the case of micron sized particles and conventional imaging optics, the particle image diameter, d_i is much larger than the particle diameter. An approximation given by Adrian [2.13] for the mean exposure, ε, averaged over a particle image is approximated by

$$\bar{\varepsilon} = \frac{W_e d_p^n d_a^4}{2.44^2 \lambda^4 s_0^2 s_i^2 h W} \quad \text{J/m}^2 \tag{2.16}$$

where n is the power law appropriate to the particle size range, W_e is the energy of the light pulse, d_a is the diameter of the lens aperture, s_o and s_i are the object and image distances, W is the sheet thickness and h is the height of the light sheet as shown in figure (2.2).

In the present work, medium format Kodak Technical Pan film was used for recording PIV images over extended regions within the engine cylinder. This film is a fine grain, panchromatic, low noise emulsion giving a resolution of approximately 200 line pairs per mm at a sensitivity of 1mJ/m^2. In the engine experiments, oil droplets of approximately 0.5 micron minimum diameter were illuminated with Nd:YAG laser light at a wavelength of 532nm. A medium format camera equipped with an f=80mm lens was operated at a magnification of 0.4 and a nominal f/number of 5.6. Accordingly, the object and image distances were 280mm and 112mm and the aperture diameter was approximately 14mm. The sheet thickness, *W*, was approximately 600μm and the height of the light sheet was 50mm. Assuming an exponent $n=4$ for Rayleigh scattering, the pulse energy required to give an exposure of 1mJ/m^3 for 0.5 μm particles given by equation (2.16) is approximately 58mJ. This compares with an experimental pulse energy of 100-120 mJ. Pulse energies of this order are readily achieved using reliable pulsed Nd:YAG laser technology.

Exposure calculations are highly sensitive to the particle diameter, so that pulse energy requirements calculated in this way are only crude estimates. For accurate estimates of illumination requirements, full Mie scattering theory must be applied in conjunction with accurate knowledge of the particle diameter. The sensitivity of the scattered intensity to the particle diameter favours the recording of larger particles in a given size distribution. It is therefore preferable to work with monodisperse particle size distributions where possible.

The use of microscopic solid seed particles or liquid droplets is common in LDV and PIV experiments. However, the compromise between light scattering and flow following presents a major restriction to choice of particle image diameter. For example, increasing the diameter of alumina particles from 1 to 2 μm would be expected to give an order of magnitude increase in side scatter but the 90% amplitude flow-following would fall from 10kHz to 2kHz [2.29]. Recently, specially developed hollow monodisperse SiO_2 spheres of approximately 3μm diameter have been reported for LDV studies in combusting flows [2.34]. Owing to their reduced density and hence increased size, these are expected to offer approximately an order of magnitude improvement in side scattered intensity compared with liquid oil droplets of the same flow following fidelity. These are now available commercially and offer an attractive compromise between flow-following and light scattering characteristics in situations where solid particles may be used.

2.3.1.3 Particle seeding number density

As noted previously, it is important to achieve the correct number density of seeding particles within the flow. Several workers have addressed the effect of seed density on measurement confidence, using Monte-Carlo simulations of the PIV recording and interrogation processes. Coupland and Pickering have recommended an optimum number of seven seed particles per interrogation volume for adequate signal to noise ratio under conditions of low velocity gradients [2.35]. Keane and Adrian recommended a minimum of ten particles per interrogation region [2.21] and Lawson reported little improvement for seed densities exceeding 12 [2.19]. Since the seed particles are distributed randomly in space, the probability of achieving N particles in a volume V given a mean seed density of N_i particles per interrogation volume in the flow is approximated by Poisson statistics as given in [2.13]

$$\text{Prob}(N_i \text{ particles in } V) = \frac{(NV)^{N_i}}{N_i!} e^{-N_i V} \qquad (2.17)$$

Using this formula, it is found that a mean seed density of at least 6 particle pairs per region satisfies the condition of avoiding having exactly two particle image pairs in each region in over 95% of the total number of regions. This condition is automatically met if the seed densities recommended from Monte-Carlo studies are achieved.

If Lawson's recommendation of 12 particles per region is followed, seed densities of the order of 2.4 x 10^{10} m^{-3} are required in the flow assuming interrogation volumes of 0.5 mm^3. These seed densities have been achieved in many LDV studies in non-reacting gas flows [2.30]. However, consideration must be given when seeding flows in which the gas density undergoes significant changes or where reactions such as combustion modify or destroy the seed particles.

An upper limit of seed density is reached above which decorrelation occurs due to speckle formation. This occurs with coherent imaging when the seed density is such that there is a considerable chance of two or more particle images from the same exposure overlapping at the film plane. Adrian describes a "source density", which is equal to the mean number of particles found in a cylindrical flow volume whose depth, *W*, is equal to that of the light sheet and whose diameter is equal to that of a particle image diameter when projected back into the flow. If C is the mean number of particles per unit volume in the flow and the camera magnification is M, the source density is given by

$$N_s = CW\frac{\pi d_i^2}{4M^2} \tag{2.18}$$

With reference to equation (2.17), values of N_S much smaller than unity imply low proportions of overlapping particles and hence the particle imaging regime, whereas a source density significantly higher than unity implies the speckle regime. With a typical particle density, C, of $2.4\text{x}10^{10}$ particles per cubic metre, the speckle regime is avoided for particle images of diameter significantly less than 130 μm. Therefore, in the case of typical particle image diameters of the order of 10-20μm, the adverse effects speckle are entirely avoided in practice. However, with certain imaging geometries, aberrations may degrade particle images to the extent that high source density speckle may become problematic.

2.3.1.4 Additional seeding considerations

Having selected the correct particle size for flow following and scattering, the remaining considerations regarding the suitability of the particles for the given experimental conditions must be made. In high speed motored engine studies at realistic compression ratios, temperatures of up to 500°C may be achieved near TDC. Therefore the flow seeding must be able to withstand this temperature without combustion, decomposition or significant evaporation. This is the case for most common solid seed particles. However, window fouling by solid flow seeding material is a major experimental concern, since optical windows must be kept scrupulously clean for low flare illumination and high resolution imaging. In addition, abrasion damage to optical windows and piston rings must be minimised to prolong engine life. Therefore, liquid droplets are preferred for motored engine work and measurements ahead of flame fronts in fired engines, so long as their vapour pressure is sufficiently low to resist evaporation. This precludes the use of water droplets as seed material in motored engines with realistic compression ratios, despite their excellent characteristics in terms of window cleanliness [2.36].

Therefore, high vapour pressure liquid droplets such as silicone oil aerosols are preferred for prolonged seeding in motored engines. Silicone oil has been used by Armstrong in a square piston engine [2.36] and by Lecordier *et al* in a rapid compression combustion bomb [2.37] for PIV measurements ahead of developing flames. In these cases the oil droplets survived to within 0.3mm of the flame front location and could therefore be used as accurate flame front markers. Liquid oils are atomised easily to form seed aerosols of the required mean diameter using conventional atomiser technology and may be dispersed rapidly with little agglomeration or fouling of solid surfaces.

Velocity measurements behind flame fronts require the use of refractory seed particles. Witze and Baritaud have compared a variety of refractory seed particles for LDV measurements in engines [2.38]. Aside from considerations of abrasion and window soiling, the particle aerodynamics and light scattering properties of typical seed materials were shown to alter after passage through a flame front. In particular, sub-micron TiO_2 and Al_2O_3 are excellent seed materials for motored engine studies, but give reduced scattering after passage through the flame. Both ZrF_4 and ZrO_2 appear to survive the flame front with minimum reduction in flow-following or light-scattering ability. Unfortunately, ZrF_4 produces hydrofluoric acid *in situ* and is therefore unsuitable for in-cylinder use. ZrO_2 is more benign, but has severe abrasive properties in sizes over one micron. Reuss *et al* used boron nitride for successful PIV measurements in a fired engine. This has the advantage of being a soft seeding material, but significant window fouling was experienced [2.39]. The hollow SiO_2 spheres developed by Ikeda *et al* [2.34] are reported to give excellent scattering properties even after passage through flame fronts. Another promising alternative to the common refractory seed materials is 1μm molybdenum disulphide, which has been used for LDV measurements in an unlubricated motored diesel engine at speeds up to 3000 RPM [2.40]. These particles are reported to survive combustion intact and also have the benefit of lubricant qualities, although no PIV measurements have been reported using this material to-date.

2.3.2 Particle Imaging Requirements

The light scattered from the each flow seeding particle is collected by the imaging optics and focused down, ideally, to a diffraction limited spot. In typical PIV experiments using microscopic seed particles, the particle image diameter is much larger than the diameter of the seed particle. In this case, the diameter of the diffraction limited particle image is an Airy function whose diameter is a function of the particle size, illumination wavelength, camera magnification and f/ number (denoted $f^{\#}$) as follows [2.13]

$$d_i = 2.44(1+M)f^{\#}\lambda \tag{2.19}$$

The particle image size is an important parameter in the optimisation of the interrogation process, since it determines the minimum measurable particle displacement. Consequently, the ratio of the interrogation region size on the film to the particle image size is proportional to the measurement dynamic range. In reality the particle image size may not be diffraction limited. The particle image size and shape will then be determined by aberrations in the camera lens, or more likely, aberrations introduced into the imaging system by optical windows, or image degradation by multiple reflections or contamination of optical surfaces.

The depth of field of the imaging system determines the accuracy to which the camera lens must be focused and aligned with respect to the measurement plane. According to [2.13], the depth of field within which the diffraction limited image of a point source varies in diameter by less than 20% is given by

$$\delta_z = 4(1+M^{-1})^2 f^{\#2}\lambda \tag{2.20}$$

For maximum use of the available side-scattered light, the depth of field of the imaging system can be constrained to be approximately equal to the light sheet thickness, W. This then determines the recommended f/ number.

For the author's case the light sheet thickness was approximately 0.6mm, with a magnification M of 0.4 and a wavelength of 532 nm. The optimum f/ number from equation (2.20) is then 4.8. In practice, the aperture was set to $f^{\#} = 5.6$ to reduce the effects of aberrations of the lens and optical windows. The diffraction limited particle diameter given by equation (2.19) was then 10.0 μm. In practice the typical particle image diameters observed on recorded PIV images were in the range 15 to 20μm.

The recording medium itself must have sufficient spatial resolution to resolve the particle images accurately, have sufficient area to record the region of interest in the flow and have suitable noise characteristics. A sensible criterion for maximising the use of the recording medium resolution is that each resolvable element on the film should correspond to the order of one pixel in the digitised interrogation region. Experimental and Monte-Carlo simulations of interrogation regions have shown that interrogation resolutions of 128 x 128 or 256 x 256 are required for optimal autocorrelation, with particle images of at least 2 pixels and ideally 4 pixels in diameter [2.22]. The Kodak Technical Pan film used in the engine measurements here was measured to give a spatial resolution of approximately 200 line pairs/mm. Therefore the film had a spatial resolution of approximately 2.5μm, which is more than sufficient to resolve particle images at a diameter of 15 μm and above. With a camera magnification of 0.4, each interrogation region occupied approximately 0.45mm on the film. Therefore, each interrogation region contained approximately 180 x 180 resolvable elements on the film, hence satisfying the minimum resolution criterion of 128 x 128 digitised elements, with particle images of a diameter of approximately four pixels. Using the central 45mm of medium format film, approximately 100 x 100 non-overlapping interrogations regions could be resolved.

A useful comparison can be made with electronic recording media at this stage. At present, CCD imaging arrays of up to 4000 x 4000 pixels are commercially available, although very expensive. With a 4k x 4k array, only 31 x 31 non-overlapping regions are available if an interrogation resolution of 128 x 128 is used. However, electronic media do not suffer from the requirement for wet processing and have further advantages in terms of on-line monitoring of image quality, and the potential for digital noise reduction techniques. CCD technology also potentially offers improved noise and dynamic range qualities compared to photographic emulsions and this may allow smaller interrogation region sizes than 128 x 128 to be used [e.g. 2.16]. At present, however, further improvements are required before the full area-bandwidth product of film can be matched by that of CCD imaging technology.

The noise characteristics of a variety of photographic emulsions for PIV recording were investigated by Pickering and Halliwell [2.41] with regard to Young's fringe processing. The most important source of film noise in the case of coherent optical processing was found to be phase noise due to emulsion thickness variations. However, with digital interrogation using incoherent illumination of the transparency, the effects of phase noise may be neglected and amplitude noise due to random grain distribution and fogging is more significant. Under ideal recording and processing conditions, Prasad *et al* showed that the effect of film noise on digital autocorrelation may also be neglected [2.22]. This is not the case in many practical PIV applications and experimentalists will be aware that film fogging due to stray illumination introduces noise into the particle image recordings over a range of spatial frequencies. This noise may severely affect measurement accuracy and valid data rates. The adverse effects of such noise can be mitigated by pre-processing of each interrogation region by binarisation or more complex morphological filtering, at the cost of increased computational effort [e.g. 2.42].

2.4 Interrogation Considerations

2.4.1 Optimisation Criteria for PIV

The ability of the autocorrelation process to give the true mean particle displacement may be measured in several ways. These include accuracy, signal to noise ratio and valid data rate. The accuracy of the velocity measurement in realistic conditions depends on the details of the autocorrelation procedure and the quality of particle images. Lawson gives a typical accuracy of 1-2% of full scale velocity due to random error in the location of the signal peak centroid [2.19]. However, this value is dependent on the correct identification of the true signal peak from the random spurious correlations which constitute the noise floor. When a spurious noise peak is incorrectly chosen as the signal peak, extremely large measurement errors result. Coupland and Pickering [2.35] proposed a confidence criterion based upon a signal to noise ratio defined as the ratio of the signal peak height, H_1 to that of the next highest noise peak, H_2, in the correlation plane as follows;

$$S/N = 20\log_{10}(H_1/H_2) \quad \text{dB} \tag{2.21}$$

A signal to noise ratio of zero means that the signal peak is indistinguishable from a spurious correlation peak. Keane used instead the concept of a valid data yield, which is the proportion of detected vectors in a given experiment or simulation which satisfy a given validity criterion. The validity criterion may be a minimum allowable value of H_1/H_2 or, when the flow structure is known, a maximum measurement error. The valid data yield and S/N ratio are affected by the following parameters which have been investigated in simulated interrogations;

1 The interrogation resolution
2 The particle image size compared to the pixel size
3 The spread in particle displacements within a region due to velocity gradients

4 The ratio of the interrogation region size to the particle image size D/d_i
5 The number of particle images, N_i, per interrogation region
6 The proportion of lost of particle pairs due to in-plane and out-of-plane movement

In addition, sources of correlation noise such as structured and random film noise due to illumination flare and digitisation noise are of known to be of practical importance, but have not been studied systematically in terms of correlation degradation.

Since the initial locations of the particle images are random, a large number of realisations of individual interrogations are required to estimate the statistical effects of each important parameter. Therefore, investigations of the systematic and random errors involved in PIV measurements and analysis of the effects of the above parameters have typically used Monte Carlo simulations of PIV recordings or idealised experimental simulations in which each important parameter can be controlled individually [e.g. 2.19, 2.21, 2.22, 2.35].

A set of general recommendations resulting from this work, which serve as useful approximate optimisation criteria, is as follows:

1 Use an interrogation resolution of at least 128 x 128. Larger resolutions are required in conditions of high velocity gradients.
2 Ensure that each digitised particle image is at least four pixels in diameter
3 Choose the interrogation region size, D, and the pulse separation, Δt, to restrict changes in particle pair displacements due to velocity gradients to be less than the particle image diameter, d_i
4 Achieve the smallest possible particle image size compatible with (3)
5 Ensure that the particle image density exceeds 10 pairs per interrogation region
6 Restrict out of plane movement and in-plane movement in the flow to $0.25D$ to limit loss of pairs.

Recent work by Lawson has lead to the formulation of a systematic and elegant optimisation procedure based on results from extensive Monte-Carlo simulations and idealised photographic particle image recordings [2.19]. This work showed that the signal to noise ratio is maximised for particle image densities of at least 12 per interrogation region. Given particle image densities of this value, the maximum possible signal to noise ratio (referred to as the "baseline" S/N ratio) was shown to be function of the ratio of the interrogation region size to the particle image diameter D/d_i in a given experiment. S/N loss functions were modelled for in and out of plane movements and were subtracted from the baseline value to give a residual S/N ratio. The residual S/N ratio was then used to determine the maximum allowable value for the product of the velocity gradient and the dynamic range. If S/N loss estimates can be made for the additional experimental sources of correlation noise, this procedure would be an extremely valuable aid to assessing the likely success of a PIV experiment under given flow conditions.

Implications of the above optimisation criteria for the measurement dynamic range and velocity gradient tolerance will now be discussed.

2.4.2 Measurement Dynamic Range

The measurement dynamic range, D_r, may be defined as the ratio of the maximum measurable velocity to the minimum measurable velocity, that is

$$D_r = \frac{V_{\max}}{V_{\min}} \tag{2.22}$$

The minimum particle displacement which can be measured occurs when the signal peak is just resolved from the central self correlation peak in the autocorrelation plane. The spatial extent of the central self correlation peak and the signal peak are determined by the autocorrelation of the two dimensional particle image intensity profile. In the ideal case of diffraction limited imaging where the size of the seed particle is a small fraction of the diffraction limited particle image size, the particle image is the point spread function of the camera aperture. This is an Airy disc, which for simplicity may be approximated by a Gaussian intensity profile with a 1/e diameter of d_i. The corresponding particle self correlation function R_{pp} is a Gaussian function with a 1/e diameter of approximately $\sqrt{2}d_i$ [2.19]. The signal peak height is at most half of the self correlation peak height, so that the self correlation and signal peaks have profiles proportional to $2R_{pp}$ and R_{pp} respectively. Figures (2.8a to 2.8c) show graphically that the signal peak becomes undetectable when the true displacement vector has a length less than d_i. Therefore the minimum resolvable velocity is given by

$$V_{min} = d_i/M\Delta t \tag{2.23}$$

The interrogation region size is selected to give the data on a regular grid of sufficient resolution to reveal the length scales of interest in the flow. However, the correlation process is most effective when the particle image distribution exhibits a precise spatial repeat, without rotation or shear. The interrogation region size must therefore also be chosen to restrict the effects of spatial velocity gradients on the correlation, as will be discussed later. Once the spatial resolution has been chosen, the upper end of the useful particle displacement range is selected to restrict the loss of pairs due particle motion out of the interrogation region volume. The relative in-plane and out-of-plane movements are subject to the same restriction. Keane recommends an upper limit for the particle displacement of one quarter of the interrogation region length [2.21]. In Lawson's *S/N* loss model, an in-plane displacement of 0.25*D* corresponds to a *S/N* loss of approximately 2dB [2.19]. The maximum velocity which can be measured given this restriction is therefore

$$V_{max} = 0.25D/M\Delta t \tag{2.24}$$

The dynamic range can then be expressed as a simple ratio of these two quantities i.e.

$$D_r = V_{max}/V_{min} = 0.25D/d_i \tag{2.25}$$

For the engine measurements reported here, d_i~15 μm and D=0.448mm, giving a measurement dynamic range of 7.46. In engine flows, this limited measurement range prevents the simultaneous measurement of high and low velocity regions. For example, during induction maximum velocities of the order of 100m/s are expected close to the valve curtain, while lower velocity recirculation regions with vortex centres of zero velocity are induced beneath the inlet valves. In such cases, therefore, erroneous velocity measurements can be expected in regions of the flow which fall outside the measurement range and these will have to be removed in a systematic validation procedure. In practice, the already limited dynamic range may be restricted further by irregular particle image shapes and sizes and DC peak broadening by film and CCD noise, all of which occur in real PIV experiments. In particular, severe particle image degradation may be expected when imaging vertical planes within the engine through thick cylindrical windows.

Figure (2.9) shows typical particle images in an interrogation region recorded through the flat piston crown window under conditions of low velocity gradients, together with the autocorrelation of the region. Particle image diameters are the order of 15 μm. Figure (2.10) shows typical particle image pairs and their autocorrelation after recording a PIV image through the cylindrical glass cylinder at the same magnification and f/number. Aberrations have severely degraded the particle image diameter to a value of approximately 100μm. This has several important consequences for PIV recording and interrogation. Firstly, the enlarged particle images give rise to a much reduced mean exposure at the film plane, ε, so that higher illumination energies are required with the consequence of increased flare levels and potential laser damage to optical windows. Secondly, the self correlation and signal peaks in the autocorrelation are significantly broadened and distorted, giving a reduced dynamic range and poor accuracy in terms of signal peak centroid location. Finally, the source density is increased by virtue of the enlarged particle image diameter, so that the formation of speckle becomes increasingly likely. Control of the particle image diameter is therefore essential if meaningful measurements are to be made through curved windows of the nature required for realistic optical IC engines.

At the lower end of the measurement dynamic range, velocity estimates are subject to increasing error, the random measurement error being a constant proportion of the full scale velocity. The signal peak centroid estimate suffers additional error at low displacements as the signal peak structure becomes modified by the self correlation peak structure. It is clear that removal of the self correlation peak would expand the velocity dynamic range and reduce measurement errors at the low velocity end of the dynamic range. This requires the application of more sophisticated recording techniques such that the first and second particle image fields can be uniquely addressed and subsequently cross-correlated.

It is interesting to examine equations (2.19) and (2.20) with regard to the theoretical measurement dynamic range, given diffraction limited imaging of point sources. If the depth of focus is constrained to exactly equal the light sheet thickness, then for a cubic interrogation volume we have

$$L=W=\delta_z=D/M \qquad (2.26)$$

Equations (2.19) and (2.20) then give the result

$$D_r \propto \frac{D}{d_i} = \frac{1}{1.22}\sqrt{\frac{L}{\lambda}} \qquad (2.27)$$

The measurement dynamic range is then a function of the interrogation volume size and the illuminating wavelength alone. With autocorrelation PIV there is therefore little opportunity within the constraints of physical imaging considerations to improve measurement dynamic range. However, this result also shows that the measurement dynamic range is independent of the imaging system magnification, assuming diffraction limited imaging. This has several useful implications for the design of a PIV experiment. Firstly, so long as the recording medium is able to sufficiently resolve the particle images, the magnification can be reduced to allow a larger area of flow to be recorded, without compromising dynamic range. Secondly, commonly available, inexpensive 35mm and medium format macro lenses are typically optimised for near diffraction-limited imaging at magnifications less than unity. The lens may therefore be operated at its optimised conjugate ratio without compromising dynamic range. Finally, so long as the mean exposure given by equation (2.16) is sufficient, the larger object distances allow the imaging system to be placed further from the measurement section. This minimises perspective errors and relieves geometrical restrictions on experimental design by allowing the camera to be placed further from a hostile flow environment.

2.4.3 Effects of Spatial Velocity Gradients

The presence of spatial velocity gradients in the flow of interest imposes severe restrictions on the optimisation of autocorrelation PIV experiments. Unfortunately for PIV measurements, IC engine flows exhibit very high spatial velocity gradients in the form of both deterministic and random small scale motion, particularly during induction and in the turbulence enhancement phase during compression. In poorly optimised experiments, not even the integral length scales in the flow can be resolved and all the potential benefits of PIV over particle tracking methods may be lost. It is therefore essential to understand the velocity gradient limitations and to design the PIV experiment accordingly.

For the purposes of PIV optimisation, it is convenient to define a velocity gradient srength, ϕ, expressed as a ratio of the maximum change in velocity across an interrogation region divided by the full scale velocity;

$$\phi = \frac{|\Delta V|}{V_{\max}} = \frac{|\Delta V|}{0.25D/\Delta t} \tag{2.28}$$

The practical consequence of finite velocity gradients is to smear out the signal peak, increasing its spatial extent and reducing its height. This is because individual particle image pairs within an interrogation region experience slightly different flow velocities, so that the particle image distribution does not exhibit a precise spatial repeat. As the velocity gradient increases, the finite range of particle pair displacements reduces the signal peak height from its theoretical maximum value, thereby increasing the probability of erroneous velocity measurements. High velocity gradients will completely splinter the signal peak if the spread in particle displacements exceeds twice the diameter of an individual particle image. Keane and Adrian report significant correlation deterioration for velocity changes somewhat lower than this extreme case and recommend a maximum spread in particle image displacements of one particle image diameter within an interrogation region [2.21]. If the pulse separation is Δt, this criterion can be expressed as

$$|\Delta V| = d_i/\Delta t \tag{2.29}$$

Substituting the limiting value of $|\Delta V|$ in equation (2.28) gives a maximum recommended velocity gradient strength as follows;

$$\phi = \frac{d_i}{0.25D} = D_r^{-1} \tag{2.30}$$

or, alternatively

$$\phi D_r = 1 \tag{2.31}$$

This useful rule of thumb embodies the most significant compromise in autocorrelation interrogation; the maximum velocity gradient strength which can be tolerated is the inverse of the measurement dynamic range. Lawson introduced the product ϕD_r as an optimisation parameter which could be related systematically to the residual *S/N* ratio in a given PIV experiment [2.19]. The recommendation of Keane and Adrian, that ϕD_r should be limited to be less than unity in practical experiments is consistent with the optimisation procedure of Lawson. Following Lawson's prescription, for a typical value of $D/d_i = 25$ and a particle image density of 12 per region, the baseline *S/N* ratio is 10.2dB. From this must be subtracted *S/N* losses as follows: an in-plane *S/N* loss of 2dB for a maximum in-plane displacement of $0.25D$; an out-of-plane *S/N* loss of 2dB; and an estimated *S/N* loss due to film and camera noise of a further 3dB. This gives a residual *S/N* ratio of 3.2dB. Using Lawson's data relating signal to noise ratio loss against the product ϕD_r, this residual *S/N* ratio corresponds approximately to a maximum value of ϕD_r of 1, which is in accord with Keane and Adrian's recommendation.

It is instructive to estimate the number of complete flow reversals spanning the dynamic range which can be resolved using the constraint $\phi D_r = 1$. In the case of a simple shear flow which spans the dynamic range from zero to V_{max}, the number of end-to-end interrogation regions required to limit ϕ is equal to the numerical value of the dynamic range itself. For example, with the experimental value of D/d_i=30, the measurement dynamic range is approximately 7.5 and consequently 7.5 interrogation regions are required to appropriately limit the velocity change within in each region. A solid body rotation includes two complete flow reversals so that 15 regions are required to resolve a vortex with adequate *S/N* ratio. If, as in the engine measurements reported here, each interrogation region is 1.12mm when projected into the flow, then the minimum vortex size which can be resolved is approximately 16.8mm. This clearly has important implications for PIV engine measurements in terms of spatial resolution and estimates of derivative flow quantities.

For example, given a dynamic range of 7.5, a maximum velocity of 10 m/s and an interrogation region size of 1.0mm in the flow, the maximum permitted value of $|\Delta V|$ is 10/7.5=1.33m/s, corresponding to a maximum tolerable strain rate of 1.33×10^3 s^{-1}. Strain rates in excess of this value are known to have significant effects on IC engine combustion, but happen to be at the very limits of strain rates accessible by PIV measurements using autocorrelation analysis. The integral length scale in typical TDC engine flows, which contains the significant energy containing structures, is the order of 2-10 mm [2.32], so the velocity gradient restriction is likely to lead to high data dropout even at the integral scale unless the pulse separation can be restricted to reduce the already limited dynamic range. It is clear that, while micron sized seed particles are able to follow and visualise flow structures at the Taylor microscale, limitations inherent in the autocorrelation process prevent velocity measurements at this scale. Figure (2.11) is a detail from a typical PIV image recorded in the four-valve engine during mid-compression. This shows clearly the combination of large scale structure at the integral scale and small scale random turbulent motion which can be expected in PIV measurements in realistic engine geometries. The tumble flow structure differs significantly from the near solid body rotation which existed in the measurements of Reuss *et al* [2.39] and Nino *et al* [2.31]. Much of the fine detail of the flow will be lost during the interrogation process due to velocity gradient peak splintering or by the smoothing effect of calculating mean velocities within individual interrogation regions.

Despite these limitations, PIV measurements of large scale flow structure are still extremely valuable, particularly as there are at present no proven alternative methods of achieving similar whole field measurements of suitable spatial resolution and accuracy. Measurements of large scale structure are sufficient to give new insight into the whole field flow structure for the validation of CFD models and for the fundamental study of the effects of large scale flow properties on combustion [e.g. 2.31, 2.39].

Cross-correlation is again seen to have significant advantages over autocorrelation analysis in terms of velocity gradient tolerance. The absence of the self correlation peak means that the velocity gradient tolerance may be increased by restricting the maximum permitted particle displacement, while maintaining a useful measurement dynamic range. Since velocities approaching zero can theoretically be measured with cross-correlation, the minimum measurable velocity is limited by measurement accuracy alone. Assuming a minimum measurable velocity corresponding to one tenth of the particle image diameter, then minimum measurable displacement for $D/d_i=30$ will be 0.0033 D. If the dynamic range is fixed at the value of 7.5 used in the autocorrelation example, the maximum required displacement is $0.025D$. This gives an increase in velocity gradient tolerance of a factor of 10 when compared with the autocorrelation case. In this case the spatial resolution of the measurements would then be limited in practice by the interrogation grid spacing. In reality it would be desirable to achieve a sensible compromise between expanding the dynamic range and improving spatial resolution. If practical methods for cross-correlation can be developed and measurements are rigorously optimised according to the procedure outlined by Lawson [2.19], spatial resolutions of the order of the Taylor microscale should in future become possible.

The fundamental limitations of autocorrelation and cross-correlation PIV under conditions of significant velocity gradients have been discussed in recent work by Huang *et al* [2.43]. Alternative interrogation schemes have been proposed by Huang *et al* [2.44] and Jambunathan *et al* [2.45]. These methods use estimates of velocity gradients resulting from a conventional cross-correlation interrogation to artificially distort the first particle image field in regions which gave poor signal peak height. The distorted first particle image field is then cross-correlated with the second field to give a correlation with an increased signal peak height. The process is repeated iteratively until all interrogation regions give peaks above a certain height. Although the process is extremely intensive computationally, the improvement in data yield under conditions of high velocity gradients appears impressive. In addition, the process yields an estimate of the local small scale velocity gradients through the distortion factors which are applied to the first image field. It should be noted that the iterative procedure can only be applied if sufficient valid data is generated in the initial conventional correlation to allow the gradients in regions of data dropout to be estimated. It is likely that new methods such as these will give the potential for direct estimation of small scale velocity gradients in cases where the velocity gradients would prevent meaningful velocity measurements using conventional PIV techniques.

2.5 Closure

The important experimental parameters involved in the optimisation of PIV experiments have been discussed. The successful application of autocorrelation PIV demands close control of all of the optimisation parameters and some restrictive compromises must be made in the case of flows which exhibit small scale motion of significant amplitude. The velocity length and time scales determine the choice of seeding material and size, which in turn determines the choice of recording medium and imaging lens requirements. The most significant compromise forces the dynamic range to be restricted in order to give sufficient tolerance to the velocity gradients expected within the flow of interest. Regions containing excessive velocity gradients will give erroneous, or at best poor accuracy velocity estimates. Interrogation regions which contain particle displacements outside of the restricted dynamic range will also give additional erroneous velocity measurements, which will need to be filtered out in a post processing procedure. Further data dropout will occur due to random measurement error, but most significantly due to contamination of the particle image recording by stray illumination or "flare".

The existence of an optimum seed density in the flow demands close control of the flow seeding. In IC engines the seed density will vary from BDC to TDC by a factor equal to the compression ratio, so that some method for on-line evaluation of in-cylinder seed density is desirable. The measurement dynamic range is controlled through the ratio of the interrogation region size to the particle image size. Considerations of film sensitivity require that large aperture imaging is necessary at the PIV recording stage. This then implies a small depth of focus, so that careful camera focusing and precise relative orientation of the light sheet and camera axes is required. The details of a variety of experimental techniques designed to meet the above conditions and hence permit the routine acquisition of high quality PIV images from within IC engine cylinders are presented in Chapter 4.

A fundamental obstacle to the application of autocorrelation PIV within cylindrical test sections is particle image degradation by window aberrations. Close control of window aberrations must be implemented if successful autocorrelation PIV is to be applied with a useful velocity dynamic range. The techniques used to achieve high quality particle images when imaging through the thick wall of the glass cylinder will be described in the following chapter.

CHAPTER 3

OPTICAL CORRECTION FOR IMAGING THROUGH CYLINDRICAL WINDOWS

3.1 Introduction

The measurement of representative flows within optical IC engines requires that the engine geometry and all aspects of its operation are as realistic as possible. Certain experiments involving optical diagnostics require a line of sight through the cylinder volume and others require planes within the cylinder to be imaged through the cylinder wall. If production engine geometries are to be maintained, transparent cylinders are clearly required to provide optical access without significantly modifying the in-cylinder flow processes. Optical cylinders and piston bowls made from materials such as fused silica, sapphire and perspex have been demonstrated to survive prolonged motored operation and even skip-fired operation in a variety of research engines [e.g. 3.1, 3.2, 3.3, 3.4]. The use of engines with cylindrical windows has permitted a variety of through-cylinder optical diagnostics to be performed in research engines of realistic geometry. The application of optical flow and combustion diagnostics is providing a valuable source of knowledge of in-cylinder flow and combustion processes which is proving increasingly important in the optimisation of new engine concepts.

The use of thick cylindrical windows, however, has serious implications for image quality in high resolution imaging applications, where refraction of light rays which pass through the walls of the cylinder may cause significant image distortion and pointwise image aberrations. For the purposes of further discussion, "distortion" refers to a change in local magnification with position in the field of view, whereas "aberrations" refer to the deviation of point images from their diffraction limited form.

In many of the above techniques, the effects of pointwise aberrations may be neglected. For example, in many Laser Induced Fluorescence, Mie scattering, flow visualisation and particle tracking experiments, the spatial resolution of the measurements is typically limited by the use of relatively low resolution electronic imaging devices. In these cases, pointwise aberrations may be insufficient to affect the spatial resolution of the measurements. However, the remaining geometrical distortions may require correction so that each measured quantity may be correctly located in space. Geometrical image distortions may be measured from the image of a regular grid placed within the cylindrical test section, as is common practice in photogrammetry [e.g. 3.5]. The distortion calibration may then be used to correct the experimental images computationally.

In point velocity measurements such as crossed-beam LDV, the effects of refraction on a limited number of rays passing through the cylinder may have to be considered in order to correctly locate the cross-over point in space and to determine accurately the angle between the beams. This is achieved by modelling the passage of individual light rays through the cylinder using geometrical ray tracing [e.g. 3.6, 3.7]. The aberrations suffered by scattered light exiting the cylinder can be neglected in LDV, since the light scattered from each incident beam suffers precisely the same aberrations and velocity measurements are due only to differential signal characteristics.

Visualisation techniques such as shadowgraphy, certain holographic and tomographic techniques and particularly Schlieren photography, require that bundles of parallel rays (i.e. a collimated beam) pass through the engine cylinder, and remain accurately parallel within the cylinder volume. This problem has been reviewed by Vikram [3.8] with regard to holographic imaging within cylinders. A solution to the collimation problem may be achieved by calculating the power of the optical cylinder in the plane of curvature using the well known Thick Lens Formula and neutralising this generally small, negative power, by refractive index matching or the use of additional refracting surfaces. The latter technique was implemented by Fujikawa *et al* in a specially designed Schlieren engine using a non-concentric outer surface to the cylindrical windows [3.9]. The same effect could be achieved by a suitably selected positive lens placed at the appropriate distance from the cylinder [3.8].

For techniques in which planes within the cylinder must be imaged at a finite conjugate ratio the solution is not conceptually so straightforward. In liquid analogue engine flows, a high degree of correction can be achieved by index matching the refractive indices of the fluid with the cylinder material and surrounding the cylinder in a matched liquid gate. This technique has been used successfully for particle tracking velocity measurements in water analogue engines [e.g. 3.10] and is commonly applied in LDV measurements in liquid flows within cylindrical sections [e.g. 3.11]. However, PIV measurements of tumbling gas flow in a realistic engine require high resolution imaging of extended planes within optical cylinders where index matching is precluded. In order to form particle images of the size and uniformity required for PIV measurements, the refraction of each of many rays within conical ray bundles scattered from each object point in the measured flow must be suitably controlled.

An example of aberrated particle images recorded from within the Rover engine cylinder is shown in figure (2.10). The effects of such aberrations are to severely limit the measurement dynamic range, reduce measurement accuracy and increase the occurrence of speckle, as discussed in the previous chapter. These effects have to-date limited the application of high resolution PIV in engines to measurements of axial swirl flows through flat piston crown windows, or to velocity measurements within unrealistic square piston engines in which flat optical windows and square pistons are used [3.12]. Others have used conventional piston designs, but have modified cylinder heads to accept small, flat windows, so that the compression ratio and clearance volume shape are compromised [3.13]. Two proposed solutions to high spatial resolution whole field velocimetry within cylinders involve holographic image recording as opposed to photographic imaging. These techniques also give the potential for estimating three components of velocity within extended flow volumes. Barnhart *et al* have demonstrated a holographic PIV imaging system which is capable of significantly reducing image aberrations by means of phase conjugate reconstruction through the image recording optics [3.14]. Coupland and Halliwell propose holographic recording of three dimensional particle image fields followed by optical correlation techniques offering immunity to phase aberrations [3.15]. While these holographic techniques may potentially provide aberration immunity over large fields of view within cylindrical test sections, many experimental difficulties must be overcome before they are likely to become accepted as routine measurement tools.

In this chapter, a new and simple strategy is presented for determining the power and orientation of cylindrical corrective optics for the control of aberrations which are encountered when imaging through thick cylindrical optical windows. The corrective lens requirements for first order aberration control can be estimated without recourse to computer aided finite ray tracing. It is demonstrated that in the current PIV application, a useful degree of correction can be achieved over extended measurement planes within an optical engine cylinder using a single corrective lens. The degree of correction achieved has enabled, for the first time, imaging of sufficient resolution for autocorrelation PIV measurements of tumbling motion within the glass cylinder of a fully production geometry optical research IC engine. Future improvements in corrective lens performance are to be expected by using the author's solution as the starting point for design optimisation using finite ray tracing techniques.

Firstly, the related problem of maintaining accurate collimation of beams traversing the cylinder will be reviewed. The more general problem of imaging an object plane within the cylinder is then discussed and a systematic means for calculating the required corrective lens properties is presented. The performance of the corrective lens used in this work is demonstrated with examples of images of resolution charts and point objects imaged within the cylinder using a well corrected medium format photographic camera. Some of the limitations of the current approach are discussed and a preliminary assessment of systematic errors arising from remaining field distortion is presented.

3.2 Correction for Collimation of Transilluminating Beams

Before discussing correction for finite conjugate imaging, the simpler case of achieving a degree of collimation of a transilluminating beam passing through a cylindrical test section will be discussed. This has relevance to optical engine diagnostics requiring collimated illumination, such as Schlieren photography, as well as to a variety of industrial and medical flow visualisation and holographic imaging applications [see 3.8]. There are also important differences in the approach required for optical correction for collimation and for finite conjugate imaging, which will be illustrated in what follows.

In the general case of experiments involving cylindrical test sections, the optical window or cylinder and the internal and external media will have arbitrary refractive indices. The remaining important parameters are the inner and outer diameters and hence the cylinder wall thickness. The general cylinder geometry and refractive index nomenclature is illustrated in figure (3.1).

To simplify discussion, it will be assumed that the cylinder axis is always vertical. The optical axis lies in a horizontal plane which is perpendicular to the cylinder axis. Rays which are incident upon the cylinder surface in a horizontal plane are known as sagittal, rays incident in the orthogonal vertical plane are known as meridional. Collimated incident meridional rays pass through the cylinder without deviation by refraction. However, sagittal rays are refracted due to their finite angles of incidence with the curved cylinder cross section and are deflected such that they are no longer parallel. As a first approximation, the problem of maintaining the collimation of an incident beam within the cylinder reduces to determining the effective optical power, P_C, of a half cylinder in the plane of its curvature [3.8, 3.9]. The power in the sagittal plane can then be neutralised by one of several techniques: index matching; modification of the curvature of the outer cylinder surface; or the use of cylindrical lenses placed some distance from the cylinder walls. The use of index matching is discussed in references [3.8 and 3.11] with regard to liquid flows, but is not feasible for air flows where there will always be a large refractive index difference between the wall and the in-cylinder gas. Collimation by modification of the outer cylinder wall curvature has been implemented in a Schlieren engine [3.9], but the cost of machining a modified optical quality cylinder is high. The following discussion is therefore limited to collimation by means of external cylindrical lenses.

Figure (3.2) shows the geometry for maintaining collimation of sagittal rays using a single cylindrical lens of power P_{lens} placed a distance d from the cylinder centreline. The power of a half cylinder in its plane of curvature, can be estimated from the thick lens formula [3.16]

$$P_c = \frac{(n_w - n_0)}{R_o} + \frac{(n_i - n_w)}{R_i} - \frac{(n_w - n_0)(n_i - n_w)t}{n_w R_o R_i} \qquad \mathrm{m}^{-1} \qquad (3.1)$$

where n_W is the refractive index of the window material, n_i is the refractive index of the fluid inside the cylinder, n_O is the external fluid refractive index and R_i and R_O are the inner and outer radii, giving a wall thickness $t = R_O - R_i$.

In the case of air inside and outside the cylinder, $n_i = n_O = 1.0$ and the power of the cylinder, P_C is always negative. To retain collimation of light within the cylinder, the overall system power for each half-cylinder must be neutralised using a positive cylindrical lens of the correct power, placed with its plane of curvature parallel to the cylinder's plane of curvature. If the corrective cylindrical lens has power P_{lens} and is separated by a distance d from the first principal point of the half cylinder, the total power of the half system is given by

$$P_{system} = P_c + P_{lens} - dP_c P_{lens} \qquad \mathrm{m}^{-1} \qquad (3.2)$$

For net zero power the required cylindrical lens is of power

$$P_{lens} = \frac{P_c}{dP_c - 1} \qquad \text{m}^{-1} \qquad (3.3)$$

The principal points of the cylinder half lens and corrective lens can be calculated to achieve the correct spacing, *d*. In general, the power of the cylinder will be low so that the required corrective cylindrical lens is likely to be relatively thin. A reasonable estimate for the first principal point of thin components is the mid-point of the lens on-axis, whereas the first principal point of any cylinder is on its centreline. Once the power of the required correcting lens has been selected, fine tuning of collimation may then achieved by varying the distance *d* until optimum collimation is achieved.

The fused silica engine cylinder used in this work had the dimensions and properties listed in table 3.1 below.

Internal Radius R_i	42.225 mm
External Radius R_o	55.0 mm
Wall thickness t	12.775 mm
Refractive index n_w	1.46071 (at λ=532nm)
Cylinder height (not used in calculations)	90mm

Table 3.1 Properties of fused silica engine cylinder

Using the above values for the engine cylinder, the power of the half-cylinder as given by equation (3.1) is -1.734 m^{-1}, so that the half cylinder acts as a weak negative lens of focal length -576.6 mm. If a single corrective lens is to be placed 10mm from the outer cylinder wall, then $d = (R_o+10)$ mm from the cylinder centreline. The required power, P_{lens} given by equation (3.3) is approximately +1.558 /m. In other words, a single positive cylindrical lens of focal length f = 642mm is required if it is to be placed 10mm from the outer cylinder wall. The lens must be placed with its plane of curvature parallel with that of the cylinder, as indicated in figure (3.2).

3.3 Aberration Control for Finite Conjugate Imaging

3.3.1 Introduction

In the case of imaging planes within the cylindrical test section, it is necessary to consider refraction effects on conical ray bundles emanating from point objects within the cylinder. Rays propagating in both the sagittal plane and the meridional plane undergo deviations due to their finite incidence angles with the walls of the cylinder. The geometry encountered by sagittal and meridional rays is, however, completely different; meridional rays from on-axis object points encounter a flat cross section wall of thickness t, whereas sagittal rays encounter circular window surfaces. The situation for general skew rays and for off-axis points in the object field is more complex.

The complexity of the geometry suggests that the problem appears suited to computer based finite ray tracing methods. It is certainly the case that improved solutions for optical correction could result from a full treatment of the problem using such techniques. However, the author's experience is that a great deal may be achieved by the application of extremely simple paraxial ray tracing, that is, relatively simple geometrical ray tracing formulae which assume small angles of incidence for rays close to the optical axis. It will then be shown experimentally that, if optical correction is achieved close to the axis, then adequate off-axis performance may also be achieved for cylinder geometries typically used in optical engines.

3.3.2 Examples of Aberrated Images from the Engine Cylinder

For measurements of tumble flow within the optical engine cylinder, three distinct planes parallel with the cylinder axis were of primary importance. These planes were the plane bisecting the engine cylinder (plane 2) and passing through the symmetry plane of the four-valve cylinder head, and two equivalent planes, plane 1 and plane 3, parallel to plane 2 but passing through the centrelines of an inlet and exhaust valve, as indicated in figure (3.3). Typical particle images were recorded from the centre of plane 2 using a photographic camera lens and a CCD microscope viewing the camera film plane and are shown in figures (3.4a to 3.4c). These were recorded by operating the camera lens at a fixed nominal camera lens magnification of 0.4 and an *f*/number of 5.6 and translating the camera assembly to three different positions along the optical axis. It can be considered that the camera lens is sampling planes of the aberrated virtual particle images which are produced within the engine cylinder. The images clearly demonstrate severe astigmatism resulting from the cylindrical window geometry. Figure 3.4b shows the particle images at the position of best focus (or "circle of least confusion"), located at an axial position approximately equidistant from the two astigmatic line foci. The two orthogonal line foci (figs 3.4a and 3.4c) are separated by an axial distance of approximately 4.0mm within the cylinder. The vertical line focus is due to sharp focusing of sagittal rays alone and will be termed the "sagittal focus", whereas the horizontal line focus is formed by sharp focusing of meridional rays alone and is the "meridional focus". The aberrations deteriorate even further from the "ideal" case of figure (3.4) for off-axis object positions. It can be considered that cylinder produces aberrated virtual images of the particles, which can then be imaged by a camera lens or any other imaging system. For the purpose of further discussion, it is assumed that aberrations due to the camera lens may be neglected compared to the aberrations in the virtual images due to the cylinder and that the camera lens affects the final real image characteristics only through magnification and f/number considerations.

At the plane of best focus, where the particle images are at least approximately circular, their diameter is approximately 100 μm. The length of the astigmatised line images is typically 150 μm. With reference to equation (2.25), the measurement dynamic range in autocorrelation PIV is inversely proportional to the particle image diameter, so that degraded images of this nature are entirely inappropriate for autocorrelation based PIV. The enlargement of the particle images also reduces the mean exposure at the film plane by a factor proportional to the square of the particle diameter, so that much higher illumination energies are required. In fact, to record the images in figs (3.4a-c), the full laser energy of 350mJ per pulse was required. This gave rise to a great deal of stray illumination or "flare" and laser power densities in the light sheet were close to the damage threshold of the engine's optical windows.

It is conceivable, given a sufficient exposure and with cross-correlation analysis, that PIV measurements could be made with the "best focus" aberrated particle images, so long as the source density is limited to avoid speckle effects. Velocity measurements using autocorrelation could also be made with the line focus images, so long as measurements were restricted to that velocity component which is perpendicular to elongated line images. However, given the restrictions of autocorrelation analysis and the complex, reversing flows encountered within engine cylinders, improvements in particle image quality are essential.

3.3.3 Experimental Determination of Corrective Lens Requirements

The characteristic through-focus behaviour seen in figures (3.4a-3.4c) indicates a severe, first order astigmatism. This is distinct from, and far more severe than, the classic third order aberration of astigmatism which is associated with rotationally symmetric lens systems. As with astigmatism of the human eye, it should be possible to perform a first order correction by means of a cylindrical lens of the appropriate power and orientation, such that the sagittal and meridional foci can be made to coincide at the same point on the optical axis. To make the discussion which follows independent of the camera lens characteristics, this condition can be restated as follows; the cylindrical corrective lens must operate on the virtual sagittal and meridional images within the cylinder to form a corrected virtual point image. This corrected image can then be imaged by any external optical system. It will then remain to demonstrate whether higher order aberrations may be tolerated in the otherwise corrected particle images.

The experimental value of the axial separation of the two orthogonal virtual line foci can be used to immediately estimate the required corrective lens properties. The sagittal and meridional line foci are formed at the virtual image locations indicated in figure (3.5). Applying the Gaussian lens formula, if the axial distances of these positions from the cylinder centreline plane are r_i^m and r_i^s then a weak, positive cylindrical lens of focal length f, should force the meridional and sagittal foci to coincide at the same axial location as the sagittal focus, so long as

$$\frac{1}{f} = \frac{1}{-v + \Delta r_i} + \frac{1}{v} \tag{3.3}$$

where

$$\Delta r_i = r_i^m - r_i^s \tag{3.4}$$

and the sign convention for r_i is that locations to the right of the cylinder centreline in figure (3.5) are negative. For example, consider that we wish to place the corrective lens at least 150mm from the meridional image plane, then referring to figure (3.5) we have $v \sim 150$ mm and experimentally, $|\Delta r_i| \sim -4.0$ mm. The required cylindrical lens then has a focal length of 4.65 m. In practice, a meniscus cylindrical lens of approximately 4m focal length was the closest available off-the-shelf optic, and this had to be placed a little closer to the object point than the 150mm used in this example.

Meniscus lenses of this type are formed by polishing one spherical lens surface and then neutralising the power of the lens in one direction by polishing the other surface as a toroidal section. Since toroids can be polished in a quasi-random process, the resulting lenses can be made cheaply without significant systematic scratching or surface deviations. The additional benefit is that the resulting lenses are only of the order of a few millimeters thick and therefore can be used in the control of astigmatism without introducing significant additional aberrations.

Figure (3.6) shows corrected particle images from the centre of plane 2. The particle image diameter is approximately 12μm. It is significant to note that the lens required for finite conjugate correction is much weaker than that required for collimation and must also be oriented with its plane of curvature *perpendicular* to that of the cylinder. This is in direct conflict with the orientation required for the collimation of transilluminating beams and illustrates the different approaches required for correction at different conjugate ratios.

3.3.4 Theoretical Calculation of the Corrective Lens Requirements

It has been shown that the experimental value for the axial separation of the two line foci may be used to estimate simply the required corrective lens power. However, it is also of general value to model the astigmatic axial separation for general cylindrical geometries, materials and axial measurement plane locations, in order that some general rules for lens selection, and for choice of window material and thickness can be found.

The separation of the astigmatic line foci, Δr_i, will in general depend on the cylinder geometry, the location of the measurement plane and the refractive indices of the cylindrical window and the internal and external media. Due to the need to correct for beam positions and beam angles in LDV measurements in cylindrical test sections, equations for focal shifts suffered by meridional and sagittal paraxial rays entering thick walled cylinders have already been developed [e.g. 3.6, 3.7]. The simplest of these are in fact little more than modified thick lens formulae. In what follows, the existing LDV equations have been reinterpreted to give the approximate axial locations of virtual sagittal and meridional line foci due to object points on the optical axis within the engine cylinder. This then allows the required cylindrical lens power to be calculated from equations (3.3) and (3.4).

With reference to figure (3.7), meridional rays experience, in effect, a flat optical plate of thickness *t*. Refraction at the plate surfaces causes the virtual image to suffer a first order focal shift along the optical axis [3.6]. In the case of paraxial imaging, where incidence angles are small, the magnitude of the focal shift is given by

$$r_i^m = \frac{n_i}{n_o} r_o - \left(\frac{n_i}{n_o} - \frac{n_i}{n_w}\right)t + \left(\frac{n_i}{n_o} - 1\right)R_o \qquad (3.5)$$

where r_O is the true axial location of the object point. However, if the internal and external media are air ($n = 1.0$) this reduces to

$$r_i^m = r_o - \left(1 - \frac{1}{n_w}\right)t \qquad (3.6)$$

It is apparent that the virtual image is always shifted towards the observer by a distance which is independent of the object position and proportional to the window thickness. Typical window materials will give a shift of between 0.315*t* (for fused silica) to 0.444*t* (for sapphire). The 12.775 mm thick fused silica window used in the PIV experiments gives a fixed focal shift of 4.03mm toward the camera.

Bicen [3.6] and Boadway and Karahan [3.7] give equations for the axial shift of the cross-over point of two sagittal, paraxial LDV beams entering a thick cylinder in terms of their intended cross-over point. This is the reverse case of calculating the axial shift of the virtual image for sagittal rays emerging from an axial point object. If their equations are rearranged, with careful attention to sign conventions, to reverse the object and image positions, the following expression for the position of the sagittal virtual image is achieved;

$$r_i^s = r_o\left[1 - n_o \frac{r_o}{R_o}\left(\frac{R_o}{R_i}\left(\frac{1}{n_w} - \frac{1}{n_i}\right) + \left(\frac{1}{n_o} - \frac{1}{n_w}\right)\right)\right]^{-1} \qquad (3.7)$$

The sign convention is the same as previously, with negative values of r_o representing points to the right of the cylinder's centreline as shown in figure (3.8). In fact it can be shown that equation (3.7) is just an expression of the well known thick lens formula [e.g. 3.16] in which the object and image distances are measured from the principal point of the cylinder (i.e. its centreline).

For the present case for air flow where $n_i = n_o = 1$ this expression reduces to

$$r_i' = r_o\left[1- \frac{r_o}{R_o}\left(1-\frac{R_o}{R_i}\right)\left(1-\frac{1}{n_w}\right)\right]^{-1} \tag{3.8}$$

We see again that the virtual sagittal image position is always closer to the viewer than the object position, regardless of the magnitude or sign of r_o except for the case where $r_o = 0$. In this case, $r_i = r_o = 0$, which corresponds to the trivial case of an object position on the cylinder centreline. Each sagittal ray strikes the inner and outer cylinder surfaces at right angles and suffers no refraction, so the object and image positions coincide.

Combining equations (3.6) and (3.8) gives the axial separation of the two orthogonal virtual images as follows

$$\Delta r_i = r_o - \left(1-\frac{1}{n_w}\right)t - r_o\left[1- \frac{r_o}{R_o}\left(1-\frac{R_o}{R_i}\right)\left(1-\frac{1}{n_w}\right)\right]^{-1} \tag{3.9}$$

A negative value of the separation of the two orthogonal astigmatic foci Δr_i, indicates that the virtual meridional image is closer to the viewer than the sagittal image. The relative locations of the object position and the two orthogonal virtual line images are shown in figure (3.9). Once the value of Δr_i is known, it is a simple matter to calculate, using equation (3.3), the focal length of the cylindrical lens needed to achieve coincidence of the sagittal and meridional images and thereby correct the first order astigmatism. The cylindrical corrective lens must have the correct focal length, f, and orientation to shift one of the virtual images by the required amount at a useful working distance, v. The working distance needs to be chosen so that the corrective lens is placed sufficiently close the imaging lens that the field of view is not clipped. There should also be sufficient space to adjust the corrective lens position to permit fine adjustment and correction for all of the required axial object positions.

For an object on the engine cylinder centreline, the calculated focal separation Δr_i is approximately -4.03mm. This is in excellent agreement with the experimental value for the focal separation and in practice leads to the same choice of corrective lens.

The sagittal and meridional virtual image positions have been calculated for the whole range of axial object positions within the engine cylinder and are shown in figure (3.10). The axial distances between the two line foci were also measured experimentally by translating the photographic camera at fixed focus on a graduated slide and noting the relative axial positions of the sharp astigmatic line foci. Figure (3.11) shows a comparison between the calculated and experimental focal separations, with excellent agreement between the two. It is seen that the value of the focal separation varies from approximately -4.0mm on the cylinder centreline (plane 2) to approximately -3.5mm on the parallel plane 18mm from this (plane 1). This small change in focal separation is easily accommodated by adjusting the axial position of the $f = 4.0$m cylindrical lens.

The performance of the optical correction in the engine application will now be described and finally, the limitations of the method and future prospects for achieving further improvements in image quality will be discussed.

3.3.5 On-axis Performance of Corrective Lens

The meniscus cylindrical lens was placed between a Mamiya 645 medium format camera and the cylindrical test section as shown in figure (3.12). The camera was equipped with a Mamiya Sekor 80mm macro lens, which was optimised for a magnification of approximately 0.5. For the purposes of the tests and for PIV measurements, the lens was operated at a magnification of 0.4 in order to record the complete in-cylinder measurement area on standard format film. An *f*/number of 5.6 was used throughout the evaluation and PIV experiments. A variety of test objects could be placed inside the glass cylinder in the planes of interest and the real images which were formed in the film plane of the camera were observed using a CCD microscope assembly. The microscope was focused accurately on the camera film plane and could be translated so as to view any portion of film plane. The CCD microscope and photographic camera were mounted on a common base and could be translated along the optical axis for fine focusing. The corrective lens was oriented parallel to the camera lens in a mount which allow a rotational movement about the optical axis in addition to translation along the optical axis.

To optimise the positions and orientations of the imaging components, a finely ground glass slide was first placed inside the cylinder in the plane of interest. This was illuminated with white light to provide an extended image consisting of a large number of point sources. With the corrective lens removed, the photographic camera assembly was then translated along the optical axis, with the CCD camera focused at the film plane centre, until a series of sharp vertical line foci were observed. The corrective lens was then placed on the optical axis and translated to achieve the maximum degree of correction, i.e. the sharpest possible point images. Following this, the image was further optimised by adjusting the rotation of the corrective lens and the relative axial positions of the corrective lens and camera assembly in an iterative fashion. The appearance of a 0.4mm high region of the film plane following this procedure is shown in figure (3.13).

The extent of the on-axis optical correction for plane 1 was quantified by imaging a standard USAF resolution slide placed within the optical cylinder. Figure (3.14) shows an image of the central portion of the resolution chart when imaged with the camera and CCD microscope in the absence of the glass cylinder. The original image indicated a camera lens resolution of between 10 and 20 μm. Images were recorded of the resolution chart placed within the cylinder, without optical correction. Figure (3.15) shows the astigmatised image at the plane of best focus. Finally, with the corrective lens in place and optimised, the USAF resolution chart image is as shown in figure (3.16). For points close to the optical axis, the full camera lens resolution of approximately 10-20μm is recovered.

Introducing a pulsed laser light sheet into the cylinder and seeding the cylinder volume with sub-micron olive oil droplets gave an indication of the particle image quality which could be expected in PIV recordings. A multiple exposed PIV image of particles moving in a low speed, convective flow within the cylinder in plane 1 is shown in figure (3.17). The laser sheet was ~0.6 mm thick and 40mm wide, using an 80mJ pulse at a wavelength of 532 nm from a Nd:YAG laser. The figure indicates that particle images of suitable quality for PIV measurements are formed even in regions far from the optical axis.

The maximum on-axis resolution which could be achieved was found to be almost independent of the distance of the object plane from the cylinder centre. However, the off-axis behaviour of the point images was strongly dependent on the location of the measurement plane. The behaviour of off-axis object points cannot be modelled using the simplifying assumptions of paraxial imaging and a finite ray tracing approach is required.

This was beyond the scope of the current work. However, the off-axis performance of the imaging system was investigated experimentally to reveal some useful rules for optimising the experimental arrangement and corrective system.

3.3.6 Off-axis Performance of Optical Correction

Optimal optical correction was achieved only for object points close to the optical axis. It was found that the images of off-axis points deteriorated rapidly as the measurement plane approached the camera. This is because the incidence angles experienced by a fan of sagittal rays from an off-axis object point increase rapidly as the cylinder wall closest to the camera is approached and higher order effects become important. In practice, it is found that the meridional focal surface remains planar, whereas the sagittal focal surface becomes curved. The axial separation of the two focal surfaces therefore increases for off-axis objects, so that a simple first order optical correction cannot work optimally over the whole field.

Measurements of the meridional and sagittal focal surfaces without optical correction were made for the three planes by translating camera at fixed focus and locating the axial positions of the two line images for a planar object for a number of off-axis points in the image plane. The results are shown in figure (3.18) for the bore centreline (plane 2) and the two "equivalent" planes, 1 and 3. Within the experimental error, the meridional surfaces for each measurement plane were indeed planar. However, the curvature of the sagittal focal surfaces was significant and depended strongly on the axial object position. For plane 1, which is the most distant from the camera, the meridional and sagittal focal surfaces were parallel to within 2mm, so that good correction was achieved to within a few mm of the cylinder wall. Planes 2 and 3 exhibited increasingly curved sagittal focal surfaces and the off-axis correction achieved by the cylindrical lens deteriorated rapidly. Near-wall measurements will only be possible for these planes if the corrective optic is optimised for the larger focal separation at the expense of losing resolution close to the axis. It is of practical importance to note that imaging plane 3 can always be avoided by imaging the more distant equivalent plane, if optical access from opposite sides of the engine is available. This should be taken into consideration at an early stage in the design of an optical engine. For the purposes of further discussion, the worst practical case for off-axis imaging will be taken as the cylinder centreline plane.

Using the 4m corrective focal length lens, with its position fixed to optimise on-axis point images, the shapes of the resulting best focal surfaces were measured. The focal surfaces were found to be non-planar. As expected, plane 1 was the flattest and plane 3 the most severely curved (see figure 3.19). Since imaging plane 3 can always be avoided, the most severe practical case was the cylinder centreline, plane 2. Here, the axial location of the best virtual image near the wall was up to 4mm from the object plane. In order to achieve a large area of reasonably corrected imaging, it was necessary to defocus the imaging system for on-axis points to minimise the separation of the curved best focal surface from the measurement plane. This increased the size of on-axis particle images but achieved a better overall off-axis performance. The amount of defocus required depends on the size of the field of view and the axial location of the measurement plane. For measurements in plane 1, a maximum defocus of 0.5mm is needed if the full area from wall to wall is required. For measurements in plane 2 a defocus of up to 2.5 mm may be required to cover the complete measurement plane. In practice, the measurement area in this work was limited by the size of the piston crown window, which limited the extent of the light sheet, so that a maximum defocus of approximately 1.0mm was required when imaging plane 2.

Typical particle images recorded with the CCD microscope in the worst-case bore centreline plane are shown in figure (3.20). A defocus of 1.0mm was used to achieve a suitable compromise between on-axis and off-axis performance. In photographic PIV recordings, the fine detail shown in the individual particle images is lost due to film noise. Particle images of a size range of 12-25 μm were achieved over the full horizontal and vertical extent of the sheet. Somewhat better correction was achieved in plane 1.

Having demonstrated that suitable particle images may be formed using the corrective lens, it remains to assess the change in magnification across the field of view. Any significant change in magnification with position will give a systematic velocity measurement error, which may need to be corrected after PIV processing. A position error will also arise due to the integrated effect of magnification changes. If the position error is significant, the translation stage movement during PIV interrogation will also require correction.

A preliminary investigation into changes in magnification with position was carried out by photographing an accurately square grid which was placed inside the cylinder in planes 1 and 2. The camera and corrective optic positions were optimised for each measurement plane as described earlier, with a nominal camera magnification of 0.4. The nominal magnification was set using a 1mm scale oriented vertically within the measurement plane. Errors in manually adjusting the lens magnification resulted in a true magnification in the vertical direction of approximately 0.39 in each measurement plane for locations close to the optical axis. The square calibration grid was made by twice contact printing a 100 lines per inch Ronchi ruling onto holographic film, rotating the ruling through 90^o between exposures. The local horizontal and vertical grid spacings were then measured from the photographic recording along a series of horizontal profiles. This was achieved automatically by interrogating the grid photographs by autocorrelation, as if they were PIV recordings, using a translation stage, CCD microscope camera and frame store.

The x (horizontal) and y (vertical) magnifications, M_x and M_y along three horizontal profiles were measured in this way. The three profiles were located at the positions indicated in figure (3.21) and were selected to test the image distortion at the extremes of the field of view within the cylinder. Figures (3.22a) and(3.22b) show the estimated y and x magnification as functions of position on the photographic transparency, for the worst-case bore centreline plane (plane 2). The most extreme measurement location required for PIV measurements is indicated 'X_{max}'. Variations in the y magnification are negligible within the measurement error, except at the very edges of the field and toward the cylinder head. It is for this reason that a vertical scale is chosen for defining the nominal camera magnification. The profile of x magnification (figure 3.22b) shows a significant reduction in magnification toward the cylinder walls. However, within the PIV measurement region defined by the maximum light sheet dimensions, the change in magnification is limited to a maximum of approximately 5% of the nominal magnification, with substantially lower deviations close to the centre of the field. Figures (3.23a) and (3.23b) show the y and x magnification profiles for measurement plane 1. Changes in y magnification with both horizontal and vertical position in the field are again negligible. Changes in x magnification with position become significant only for positions further than approximately 9mm from the centreline. This corresponds to a distance in the engine of approximately 22.5 mm from the centreline, which is the maximum width of light sheet used in the PIV experiments. Therefore, to retain experimental simplicity, no correction for magnification changes has been made in the velocity measurements presented in this work. It should be borne in mind, however, that near-wall measurements will be subject to large errors which will require correction for distortion. It is significant to note that in plane 2, the x magnification at the centre of the field, $M_x(0)$, is approximately 2.5% higher than the vertical magnification $M_y(0)$. For plane 1, using the same corrective lens, $M_x(0)$ is approximately 2.0% less than $M_y(0)$. This is a further indication of the complexity of the optical correction problem and the need for caution in assessing experimental errors in each new measurement application.

While the change of x magnification with position may be neglected in terms of velocity measurement, the position error which results from the integrated effect of the magnification change may be substantial. In PIV interrogation, the recorded PIV transparency is typically interrogated by translating the illuminated image using a fixed translation increment and estimating the velocity within each small interrogation region. If significant distortion is present, the use of a fixed translation increment leads to an error in the spatial location of the resulting measurement. In the case of in-cylinder imaging where the magnification decreases towards the edge of the field, the location in the flow is underestimated by an increasing amount as the extremes of the transparency area are approached. If the translation stage increment is D, and the y magnification measured at the centre of the field $M_y(0)$, is taken as the nominal magnification, then the x position error, E_x, in the flow accumulated after N translation increments is approximately given by

$$E_x = \sum_{i}^{N} D\left(\frac{1}{M_y(0)} - \frac{1}{M_x(i)}\right) \tag{3.10}$$

where $M_x(i)$ is the magnification in the i^{th} interrogation region.

Figure (3.24a) shows the magnitude of the position error in the flow which arises by interrogating the photograph from plane 2 using a fixed translation stage increment of 0.4mm (nominally 1.0mm in the flow). Moving out from the centre of the field, the error is first positive, indicating that $M_x(0) > M_y(0)$. As the extremes of the field of view are approached, the accumulated position error decreases and becomes negative as the local magnification is diminished. Measurements were not possible within 2mm of the walls due to extreme aberrations and reflections of the grid in the cylinder wall. However, within the PIV measurement area the position error is limited to less than 0.4mm. This is less than half of the typical interrogation region size in the flow. The magnitude of the position errors arising in plane 1 are a little higher, and are always negative, as shown in figure (3.24b). However, within the area of interest for the current PIV measurements, the position error is again less than half of the interrogation region size in the flow. Owing to the small position errors which accumulate within the measurement areas, their effects were neglected in the PIV measurements in this work. However, further work would be required to assess and correct for the effects of distortion should near-wall measurements be attempted.

3.4 Closure

A simple method for selecting a corrective lens for the correction of on-axis first order astigmatism of particle images within the optical engine cylinder has been presented. The experimental performance of a lens selected using this prescription has been demonstrated to give particle images which are of sufficiently small diameter to permit PIV measurements using autocorrelation. On the cylinder axis, corrected particle images are close to the diffraction-limited diameter afforded by the camera lens. However, off-axis aberrations are more severe, so that a compromise defocus is required to enable large fields of view to be imaged in certain measurement planes. Planes closer to the camera than the cylinder centreline give unacceptable off-axis aberrations and should be avoided in preference to planes more distant than the centreline.

A preliminary attempt has been made to assess the effects of distortion on in-cylinder PIV measurements. Within the area limited by the light sheet geometry, such effects can be neglected.

The off-axis performance of the optical correction could potentially be improved by performing a systematic finite ray tracing design optimisation, which would typically require a multiple optical element solution. A first guess improvement would use a cylindrical field flattener placed close to the film plane to reduce the defocus requirement. This approach is analogous to distorting the film plane so that each off-axis point is optimally focused. However, a different field flattening lens would be required for each measurement plane within the engine.

The initial degree of astigmatism introduced by the cylinder could be reduced for both on and off-axis object points by manipulation of the cylinder properties. With reference to equation (3.9) the axial astigmatic focal separation can be reduced by reduction of the wall thickness, t. This will also improve off-axis aberrations, although this should be confirmed by ray tracing. Therefore, the minimum wall thickness should be used which is compatible with mechanical integrity considerations. Sapphire cylinders 3mm thick have been demonstrated to survive continuously fired operation in an optical engine [3.2]. The on-axis focal separation Δr_i at the centreline of such a cylinder, given by equation (3.9) is only -1.33mm compared with -4.03 mm for the fused silica cylinder used in this work. While sapphire is expensive to machine, its combination of high tensile strength and good thermal conductivity gives resistance to mechanical and thermal stresses and wear. Despite the machining difficulties reported in [3.2] with regard to polishing sapphire cylinders to the required optical finish, it is perhaps time to reconsider sapphire optical engines given improved optical fabrication technology.

The development of suitable optical correction is a significant contribution towards the application of PIV in realistic IC engine cylinders. The advances reported here are of potential significance for many optical in-cylinder IC engine diagnostics and a variety of additional imaging applications of interest to industry and medicine may be envisaged. However, it is acknowledged that the developments reported here represent a relatively crude first-order solution to a complex optical problem. It is therefore hoped that the initial solution can be used as a starting point for a more rigorous analytical treatment of the generic problem of imaging within cylindrical test sections. Finally, it should be noted that the achievement of suitable particle image quality through the application of optical correction, while important, is only one of a number of experimental parameters which need to be considered when making PIV measurements in the transient and hostile environment of a research engine cylinder. The following chapter describes the remainder of the PIV engine facility, with particular emphasis on the experimental design and procedures required to achieve routine in-cylinder PIV measurements.

CHAPTER 4

EXPERIMENTAL

4.1 Introduction

The work presented in this Thesis had three chief aims. The first was to develop a PIV engine facility and a robust set of experimental tools for the routine application of PIV to in-cylinder flow measurement. The second was to perform PIV measurements on a production geometry engine under motored conditions for comparison with existing data. The final aim was to perform preliminary PIV measurements ahead of a flame front under skip-fired conditions.

The need to achieve routine PIV measurements arose from the requirement of the industrial sponsors to develop an in-house capability for whole-field in-cylinder flow mapping. As many PIV experimentalists have discovered, the successful recording of a PIV image suitable for interrogation requires the close control of a number of experimental parameters, even in simple steady flow conditions. The application of in-cylinder PIV requires additional care. For example, seed densities vary throughout the engine cycle and the complicated geometry demands careful orientation of the light sheets. The high frequency fluctuations expected in the flow require that microscopic seed particles are used. Therefore, high laser pulse energies are required in conjunction with large aperture imaging. The requirement for mapping the flow over large areas within the engine cylinder and the small depth of field of the camera lens means that the camera axis must be very accurately aligned with the light sheet. Other considerations include the need to accurately synchronise the PIV recording to the engine crank angle and the minimisation of stray illumination or 'flare'.

In what follows, the PIV facility which was designed and installed in the early stages of this work is described. Details of the important experimental techniques which were developed to permit routine PIV recording are then presented. The commercial PIV interrogation system which was used to process the recorded PIV images is briefly described. Finally, the range of measurement conditions which were investigated in both motored and fired PIV experiments is given.

4.2 The PIV Engine Facility

4.2.1 Overview

The PIV set up can be considered as a combination of a number of individual systems. A schematic of the complete PIV engine facility is shown in figure (4.1). The optical engine, its drive and services provide the flow to be measured. The pulsed laser provides a collimated pulsed beam for illumination. An electronic synchronisation system fires the laser at the appropriate engine crank angle and a system of cylindrical optics converts the laser beam into an intense, thin light sheet which is introduced into the optical engine cylinder. The flow is seeded using an aerosol generator and the corrective lens and camera form an imaging system which is used to record the PIV images. The important characteristics of each of the separate facility components is now described.

4.2.2 The Rover Optical Engine

The engine to be studied was a single cylinder, four-stroke, four-valve pentroof SI research engine, which was designed and built entirely by Rover Group's Advanced Power Train Technology Department. A schematic of the optical engine is shown in figure (4.2). The engine was based around a Ricardo single cylinder crankcase, with a purpose-designed barrel containing the optical cylinder and an elongated piston. The Rover engine has much in common with other optical research engines, with the exception of optical access over the complete piston stroke via a transparent bore combined with a production cylinder head geometry. The cylinder head was a development version of the T-16 tumble head which was designed to generate an ordered in-cylinder tumbling flow via the geometry of the directed inlet ports and the pentroof combustion chamber. A section through cylinder head showing the pentroof combustion chamber geometry is shown in figure (4.3a). Figure (4.3b) shows the combustion chamber as viewed through the piston crown, with the flat squish bands and the spark plug location indicated. The tumble activity of this and similar cylinder heads has been evaluated using a variety of techniques. The Barrel Swirl Ratio (BSR) has been determined by steady flow measurements using impulse swirl meters [4.1]. Velocity profiles have also been measured using LDV in steady flow rigs and used to validate the impulse swirl meter measurements [4.2]. Details of the in-cylinder flow have also been studied under motored conditions in a single cylinder engine using LDV [4.3].

With reference to figure (4.2), optical access through the crown of the extended piston was provided by a flat window of 'Suprasil' fused silica. This permitted the introduction of vertical light sheets and the viewing of horizontal planes, via a fixed mirror which was mounted within the engine barrel. The piston's lower end was provided with a conventional load bearing ring set, which moved within a water-cooled cylinder liner in the barrel casting. A set of three plastic and composite sealing rings at the upper end of the piston moved within a 'Suprasil' fused silica cylinder, which provided optical access over the complete piston stroke. The purpose of this upper ring set was to bear piston side forces on the silica cylinder and to provide effective sealing at engine speeds up to 2000 RPM, without damaging the cylinder surface.

The optical cylinder, which had an internal radius of 42.225mm and a wall thickness of 12.775mm, was of imaging quality and was finished to within 2λ of true cylindrical surface form. Precision gaskets of compliant silicone rubber located the optical cylinder within the engine barrel. The cylinder head was located on the barrel top face using dowels and was fixed to the engine barrel using long through-bolts which were readily accessible via the cam box. Tightening the through-bolts to mate the barrel top face with the cylinder head face automatically ensured correct preload of the silicone rubber gaskets. The assembled optical engine showing the inlet and exhaust systems is shown in figure (4.4).

The use of the through-bolt system allowed the engine to be dismantled rapidly for cleaning of optical windows and subsequent reassembly. This process typically had to be performed after an accumulated running time of approximately 10 minutes with flow seeding, and could be completed within one hour. However, the through-bolt system also prevented oil lubrication of the cam box, which instead was packed with high temperature molybdenum grease. An early engine failure resulting from inadequate lubrication of the cam bearings led to their replacement with-sealed-for-life needle roller bearings, after which many hours of motored engine running time at high speeds has been successfully accumulated.

The important engine characteristics are summarised in table (4.1). The piston stroke, bore and compression ratio are typical of current pentroof four-valve spark-ignition engines of production geometry. The nominal Barrel Swirl Ratio (BSR) as measured on a Rover steady flow rig using the technique outlined in reference [4.1] is 1.2. That is to say that the angular rotation rate of the bulk in-cylinder flow about a horizontal axis perpendicular to the crank axis is 1.2 times higher than the angular rotation rate of the engine crank. The BSR could be increased to a nominal value of 1.8 by modifying the inlet port face using an inlet port face inducer gasket as shown in figure (4.5). Cylinder pressure measurements indicated that the use of the port face gasket achieved the increased BSR without reducing the induced mass at the operating speeds of interest. The induced air or charge was drawn through a manifold mounted to the inlet port face. This connected to an intake plenum which was equipped with a standard air filter, to prevent ingress of large particles. In motored studies, the exhaust was discharged to the outside atmosphere via the shortest possible length of flexible hose. For skip-fired combustion studies, the exhaust was diluted with excess air and discharged via a metal hose to an external ventilation stack.

BORE	mm	84.45
STROKE	mm	89.0
SWEPT VOLUME	cc	500 nominal
COMPRESSION RATIO		10.5:1
VALVE LIFT	mm	10.16
INLET VALVE PEAK LIFT	/degrees crank angle	70° Before TDC
EXHAUST VALVE PEAK LIFT	/degrees crank angle	70° After TDC
CAM PERIOD	/degrees crank angle	240°
ENGINE SPEED RANGE	RPM	200-2000
PISTON/HEAD FACE CLEARANCE AT TDC	mm	1.3
CONNECTING ROD LENGTH	mm	155.4

Table 4.1 Engine Configuration

The engine was motored using a 7.5kW three phase Flux Vector motor and controller. The engine speed could be set manually to an accuracy of +/- 2RPM at a speed of 1000 RPM, which was the maximum engine speed used for routine PIV measurements. The optical engine, motor and services were mounted on a common baseplate, which was itself mounted to the floor via four Metallastic vibration dampers as shown in figure (4.6). All the optical components were mounted on a stiff table, which was rigidly fixed directly to the floor. This prevented vibration of optical components and eliminated the risk of damage to the photographic camera. Accelerometer measurements showed that the effects of velocity measurement error due to relative motion between the camera and engine were negligible compared to in-cylinder gas velocities at typical operating speeds. The pulsed laser was located on a separate, rigidly fixed table approximately 1m from the optical engine.

4.2.3 Pulsed Laser Specification

A Spectron Nd:YAG twin-oscillator, twin-amplifier frequency doubled laser was used as the illumination source for the laser light sheet. The flashlamp-pumped laser gave Q-switched pulse energies of up to 350 mJ, with individual pulse durations of approximately 8ns. At typical in-cylinder flow velocities of $10ms^{-1}$ this pulse duration was sufficient to freeze the particle locations in space to within 0.08 µm. The wavelength of the frequency doubled emission was 532nm. This gave enhanced Rayleigh scattering and smaller diffraction limited particle image sizes compared to competing Ruby laser technology. This permitted lower pulse energies to be used, with reduced problems of flare and laser damage to optics in the illumination path.

Each of the two oscillators and amplifiers could be triggered separately, thus allowing infinite control of the laser pulse separations and simple control of the individual pulse energy. A schematic of the laser internal layout is given in figure 4.7. One disadvantage of the twin cavity system was the need to maintain accurate co-alignment of the two separate outputs. The laser was also provided with an injection seeder common to the two oscillator cavities, for future holographic PIV studies requiring coherent output. The Pockels cell delay for each oscillator cavity was the order of 140 µs. This corresponds to a crank angle delay of 0.84 degrees at an engine speed of 1000 RPM.

The pulsed laser energy requirements were estimated using the equations for photographic exposure given in Chapter 2, together with the prior practical experience of Reuss et al [4.4]. Assuming 0.5µm diameter seeding particles and a light sheet thickness of 0.6mm, the minimum pulse energy requirement was estimated at 58mJ. Typical pulse energies of 80-120 mJ were used in this work. The oscillator cavity optics were optimised for a pulse repetition rate of 1Hz. This is much lower than the free-running 25-50Hz repetition rates which are typical of Nd:YAG lasers, but allowed the laser to be fired in a single-shot mode, on demand, with good pulse energy and beam pointing stability.

The laser was equipped with a programmable delay generator, which could be adjusted rapidly to give precise laser pulse separations accurate to +/-0.1% of the full scale setting. For a typical pulse separation of 20 μs this gave an accuracy of +/- 50ns, or a maximum Δt error of 0.25%. This was negligible compared with other velocity measurement errors described previously. However, in order to achieve this accuracy in practice, the Pockels cell delays on the laser had to be regularly checked and adjusted to avoid offset errors in the pulse timing.

4.2.4 Laser/Engine Synchronisation System

The laser was synchronised with the required measurement crank angle using a purpose-built electronic timing unit, shown in figure (4.8). This was specified at an early stage in the project and was designed and built in the Department of Mechanical Engineering electronic workshop at Loughborough. The unit allowed the laser firing to be synchronised to any crank angle within the four-stroke engine cycle, to resolution of 0.1 degrees crank angle. An AVL optical crank encoder (type 360B/600) provided a 5 pulses per degree crank angle square waveform TTL output, giving 10 pulse edges per degree for input to the timing unit's counter module. The cam position was sensed by a Hall effect transducer and a ferrous encoder disc. The cam encoder pulse was used to reset the counter every 720 crank angle degrees, so that any crank angle within this range could be selected unambiguously. For the purposes of optical alignment and for calibrating the engine timing system, the laser could be fired repetitively at the same point in every engine cycle. For recording PIV images, the timing system was switched to a one-shot mode and was armed and triggered manually in conjunction with manual operation of the camera shutter.

4.2.5 Beam Delivery and Light Sheet Optics

The pulsed output from the Nd:YAG laser was steered using a system of dielectric coated mirrors toward the sheet forming optics as shown in figure (4.9). A beam-steering periscope allowed the beam height and orientation to be adjusted according to the measurement plane of interest. The distance between the laser and engine was kept to a minimum (less than 1m) to reduce the sensitivity of the illumination system to any pointing instabilities in the laser.

The pulsed laser output was in the form of a collimated beam with a diameter, d_b, of approximately 6mm. This was transformed into a light sheet of diverging width and collimated thickness using a combination of a positive cylindrical lens of focal length f_1 and a negative spherical lens of focal length f_2 in a Galilean telescope arrangement as shown in figure (4.10). The two lenses are placed a distance $f_1 + f_2$ apart, giving a beam contraction ratio of $-f_1/f_2$. The light sheet thickness, W, is then given by

$$W = -df_2 / f_1 \qquad [4.1]$$

The divergence half angle, θ, in the orthogonal plane is given by

$$\theta = \tan^{-1}(-d/2f_2) \qquad [4.2]$$

This arrangement contracts and then collimates the laser beam in one direction and diverges the beam in an orthogonal direction. The individual lens focal lengths are chosen to provide the desired sheet thickness and divergence. For the engine PIV measurements, the cylindrical lens had a focal length of 200 mm and negative spherical lens had a focal length of -25mm. This gave a contraction ratio of 8, so giving an estimated sheet thickness of approximately 0.75mm and a divergence angle of approximately 6.8 degrees. This optical arrangement has several advantages over alternative sheeting optics. Firstly, the region of highest optical power density occurs close to the negative spherical lens. This protects the expensive optical windows from potential laser damage due to accidental misfocus. Secondly, the light sheet thickness is collimated over an extended region, so that the measurement plane thickness is uniform and well defined. This reduces the incidence of unwanted out of focus particle images at the extreme ends of the measurement area and places limits on the out-of-plane velocity gradient effects and perspective errors.

The light sheet could be oriented for measurements in horizontal or vertical planes by rotation of the cylindrical lens in its mount. For horizontal plane measurements the sheet was passed through the cylinder walls. For measurements in vertical planes, the sheet was reflected off a high energy dielectric mirror mounted at 45° within the engine barrel, and passed through the fused silica piston crown window. The width of the in-cylinder measurement region was therefore limited by the light sheet divergence and the clear aperture of the piston crown window. Introducing vertical light sheets through the cylinder wall was found to be unsatisfactory due to high levels of stray illumination or 'flare' caused by multiple reflections within the cylinder.

4.2.6 Flow Seeding

Liquid oil flow seeding was used for both motored and fired engine studies. An aerosol of microscopic oil droplets was generated using a Laskin atomiser of the design used by Kompenhans in reference [4.5]. The atomiser was of simple construction and is shown in figure (4.11). Air at a gauge pressure of up to 70 kPa is fed down a central tube and exits at high speed through a series of 1mm diameter holes immersed in the oil. Atomisation takes place as the air jets emerge into the oil and as bubbles burst on the oil surface. Large droplets are removed by the disc-shaped baffle which is seen toward the top of the atomiser. The resulting mist of fine droplets was passed through a simple separator to further remove larger droplets. The remaining seed mist was distributed within the engine intake plenum and was thoroughly mixed with intake air upon reaching the inlet valves. The seed density was set for a given engine speed by adjusting the supply pressure by means of a precision regulator as shown in figure (4.12).

Initially, olive oil was used as the seed material. This has been shown to generate oil droplets smaller than 1.0 μm in diameter in previous PIV studies [4.5] and has a relatively high vapour pressure and dissociation temperature, thus resisting evaporation at the elevated temperatures expected near TDC compression. However, evaporation loss of seed near TDC was problematic under part throttle motored conditions, possibly owing to the reduced intake and in-cylinder pressures. Therefore, the olive oil was replaced with Dow Corning 550 high temperature Silicone fluid. This had approximately the same viscosity and density as olive oil and was expected to give particles of similar size range. The vapour pressure was sufficiently low to eliminate evaporation losses at part throttle and the seed survived throughout the complete four-stroke cycle, as reported previously by Armstrong [4.6].

4.2.7 Imaging Optics

The combination of the engine optical windows, the cylindrical corrective lens and photographic camera, together formed the imaging system. This had to be carefully focused and optimised as described in the preceding chapter, for each vertical measurement plane. The camera was a medium format Mamiya 645 camera having a film format of 6cm by 4.5cm. A Mamiya Sekor f80 macro lens was operated at a fixed nominal magnification of 0.4, close to its design magnification of 0.5. This enabled a large in-cylinder region, from the piston crown surface at BDC to the spark electrode, to be imaged onto the film. The camera lens centreline was located half way down the piston stroke, to allow maximum optical access into the combustion chamber. The camera aperture was set at a nominal f/number of 5.6, giving a depth of focus of approximately 0.8mm. This was closely matched to the light sheet thickness. The theoretical diffraction-limited particle image size was approximately 10µm, although typical particle image sizes recorded through the thick optical windows were between 15 µm and 25µm in diameter. To provide some degree of rejection of ambient light and thus allow safe room lit operation of the engine, a Balzer's additive dichroic filter (type 'DT green', bandpass 520-580nm) was mounted to the front of the camera lens. This allowed the camera shutter to be operated manually on a 'B' setting for periods up to one second with negligible film fogging. The same filter provided excellent rejection of combustion emission during fired experiments. Kodak Technical Pan 2415 film was used to record the PIV images. This was push processed with D-19 developer to give an effective film speed of approximately 100 ASA with an estimated spatial resolution of approximately 200 line pairs per mm.

The camera was fixed to a fine translation stage via a tilt adjustable mount. The translation stage allowed precise focusing at a fixed camera lens magnification. To the same stage was mounted a detachable CCD microscope assembly. The microscope could be translated to focus on any area of the film plane to assess and optimise particle image quality prior to PIV recording. Figure (4.13) shows the camera and CCD microscope assembly on its translation stage and optical rail carrier. The fine translation stage was itself mounted to an optical rail, which also carried the cylindrical corrective optic when necessary. The rail was aligned to be accurately perpendicular to machined engine datum faces. The complete imaging system could then be systematically optimised for focus and alignment with respect to the light sheet. Figure (4.14) shows the imaging system, complete with corrective lens, set up for imaging a vertical plane within the engine cylinder. Figure (4.15) shows the system, without the corrective optic, set up for imaging horizontal planes via the piston crown window.

4.3 Experimental Techniques

4.3.1 Overview

A range of experimental techniques were developed to ensure that, once the engine and optics were set up, successful PIV images could be reliably recorded. In order to achieve the same seed density at each measurement crank angle, a means was devised to estimate and control the seed density during an engine run. The formation of accurately co-aligned laser light sheets was also necessary and the twin light sheet had to be oriented accurately with respect to the desired measurement plane. The laser sheet also had to be accurately parallel with the camera film plane to maintain focus over the field of view. Errors in the timing system due to the encoder datum and fixed delays in the timing system were also considered and finally, the photographic recording and developing procedures were systematically controlled.

4.3.2 Seeding Control

Lawson [4.7] and Keane and Adrian [4.8] recommended minimum seed densities of approximately 12 particle image pairs within each interrogation region, or higher levels if out of plane motion or velocity gradients were significant. In the engine studies, a seed density of 20-30 particle image pairs per interrogation region was sought. The interrogation regions were of the order of 1mm square and 0.6mm deep, so that a seed density of at least 3×10^{10} particles/m^3 was required. A series of photographic PIV recordings taken at engine speeds of up to 2000RPM showed that the single Laskin atomiser was capable of supplying the required seed density over the complete range of engine operating speeds. The remaining problem was to ensure that the correct seed density was achieved during induction to give the target seed density at the measurement crank angle, despite seed density increases due to compression.

Figure (4.16) shows the instantaneous compression factor as a function of compression crank angle for the PIV engine. At TDC the instantaneous compression factor is equal to the compression ratio of 10.5. The seed density at any crank angle during compression is approximately equal to the initial seed density at Inlet Valve Closure (IVC) multiplied by the instantaneous compression factor, so that an initial density of 20 particles per region gives a TDC seed density of the order of 210 particles per region. Therefore, if PIV measurements are required at a number of different compression crank angles in a single engine run, an on-line means of monitoring and adjusting the seed density is required. If multiple identical atomiser systems are available, the initial IVC seed level can be optimised by turning off the appropriate number of atomiser nozzles. The approach taken in this work with a single atomiser was to obtain a measure of the seed density at IVC within the engine and to adjust this value via the atomiser supply pressure to compensate for seed density increases due to compression.

The seed density was estimated for a fixed light sheet geometry and laser pulse energy by means of a 100mm^2 silicon photovoltaic cell which was mounted in the camera viewfinder as shown in figure (4.17). The detector collected the light scattered from seed particles which occupied a central circular region in the flow having a radius of approximately 14mm. As the laser light sheet was pulsed, the integrated voltage output from the detector was displayed on a storage oscilloscope, the amplitude of the voltage pulse being proportional to the integrated light intensity collected during each 8ns pulse. This included a small offset level due to flare, which was measured by firing the laser at IVC with the seed generator turned off.

A steady seed level was first achieved by running the engine at constant speed and setting the seeder supply pressure to a fixed value. The linearity of the detector was estimated by varying the laser pulse energy in a vertical light sheet introduced in the engine, and noting the integrated seed monitor voltage output at IVC on a storage oscilloscope. The detector output was found to be approximately linear over the range 20-180 mV as shown in figure (4.18). The detector output was then calibrated against the density of particle images measured in PIV recordings taken at IVC, for a range of atomiser supply pressures. For the purposes of calibration, the camera magnification and f/number were identical to those used in all subsequent PIV recordings, as were the mean light sheet intensity and film processing procedure. The apparent seed density in the flow in particles per square millimeter was measured over a central region of the transparency by digitising the region, thresholding at a fixed value and manually counting distinct particle images. At least 100 particle image counts were made for each measurement. The calibration graph of apparent particle density against photodetector output is shown in figure (4.19) and shows excellent linearity over the range 0-80 particles per mm^2. This implies that the particle density is a function of the atomiser supply pressure, whereas the particle size distribution is independent of supply pressure over the useful operating range. The intercept at approximately 10mV corresponded to the level of stray illumination in the centre of the field of view at the IVC crank angle.

During a PIV experiment, The seed level was adjusted to give a typical seed monitor output of approximately 70mJ at IVC, thus achieving seed levels of 20-30 particles $/\text{mm}^2$ in the flow. If measurements were required at later crank angles, the atomiser supply pressure was reduced to reduce the IVC photodetector voltage by the appropriate compression factor shown in figure (4.16). It was found that this procedure allowed a range of crank angles to be recorded reliably during a single engine run, from IVC to 338° before TDC, giving particle image densities typically no more than a factor of 2 from the intended value.

The use of the viewfinder photodetector had the additional advantage of allowing the level of stray laser illumination to be estimated. This was found to be particularly useful during the alignment of horizontal measurement planes, where minimum flare levels occurred when the horizontal light sheet was accurately perpendicular to the cylinder axis.

4.3.3 Laser Light Sheet Orientation

The use of thin laser sheets required that the output beams from the two laser amplifiers were accurately co-aligned. For reasons of safety, major beam alignments were carried out using low power, non Q-switched pulses, so that the paths of the beams were additionally required to be independent of pulse power. Thermal lensing effects within the Nd:YAG laser rods means that this condition is not generally guaranteed, so a series of experiments were performed to assess beam alignment characteristics. The small depth of field of the imaging optics also required that the laser sheets be oriented accurately with respect to the camera film plane.

Beam profile measurements were performed using an unbiased general purpose photodiode, which was first tested for linearity against the laser's own calibrated energy monitor. A 25μm pinhole and diffuser were mounted in front of the photodiode and the assembly was fixed to a 5μm resolution micrometer stage as shown in figure (4.20). The laser was fired at a repetition rate of 1Hz and the amplitude of the integrated voltage output on a storage oscilloscope was taken as a measure of beam intensity averaged over the 25μm pinhole aperture. Profiles of beam intensity were built up by translating the photodiode assembly perpendicular to the plane of the light sheet. In the following experiments, aspects of beam alignment were investigated using the sheet forming optics described previously.

Figure (4.21) shows the beam profiles of the laser sheets on the optical axis, for both open-lase and Q-switched laser pulses from one oscillator and amplifier combination. The pulse energy for the Q-switched pulse was 80mJ. The centres of the two beams coincide to within 100 µm. at the waist of the laser sheet. Since the individual light sheet thickness at the 1/e intensity point is approximately 500µm, the low power open-lase beams can therefore be used for safe and reliable alignment of the full power laser sheets used in PIV measurements. Figure (4.22) shows beam profiles for the two individual 80mJ light sheets at the sheet waist, following careful beam alignment. The beams are accurately co-aligned, but the individual beam profiles are significantly different. Beam 1 shows an almost Gaussian profile, while beam 2 displays a bimodal intensity distribution. Variations in beam quality of this nature are typical of cavity-to-cavity build variations in commercial high power Nd:YAG lasers. For PIV recording, identical square profile light sheets are ideally required. Figure (4.23) shows three laser sheet profiles taken at three positions along the optical axis for a 100mJ light sheet formed from beam 1. The beam centres are shifted relative to each other due to small errors in the initial positioning of the photodiode assembly from profile to profile. The sheet thickness shows a negligible variation over the 100mm measurement region.

The twin pulsed light sheets were aligned accurately with respect to machined engine datum faces in order to simplify camera alignment and focusing. For horizontal light sheets, the open-lase beams were aligned to be accurately parallel to the piston crown face at the required position on the cylinder axis. For vertical measurement planes a datum plate was located on the barrel's viewing port, on which was scribed a series of fine vertical lines corresponding to individual measurement planes. With the cylinder head removed, a similarly marked, translucent datum plate was mounted to the location face on the top of the engine barrel. The laser sheets were aligned to coincide with the relevant datum marks on each of the two datum plates. The parallelism of the camera film plane with the light sheet was checked by introducing seed into the cylinder and translating the camera's CCD microscope over the entire field of view to assess particle image focus. Great care was then taken to ensure that laser sheet optics were not disturbed during engine rebuild. Following engine rebuild the camera film plane could be used as a datum so that any light sheet drift could be compensated for if necessary by minor readjustments of the light sheet optics.

4.3.4 Timing System Calibration

The laser Q-switch delay and systematic error in the orientation of the cam encoder disc introduced slight errors in the timing system datum. The Q-switch delay was of the order of 140 μs and gave a speed-dependent error in the crank angle at which the laser fired. The cam encoder orientation gave a further fixed crank angle error. Therefore, the crank angle which was selected on the electronic laser timing unit was not necessarily the crank angle at which the laser fired. In order to calibrate this error, the engine flywheel was marked with pointers indicating the intended measurement crank angles. A small portion of the laser output was then used to strobe the flywheel, so that for a given engine speed, the total crank angle offset could be measured and taken into account when selecting the measurement crank angle. In this way, the full resolution and accuracy of the timing system was used and the uncertainty in the measurement angle was of the same order as the uncertainty due to the finite laser pulse separation time used for the PIV measurements.

4.3.5 Photographic Techniques

The alignment and focusing procedure for the camera and corrective lens system were carried out as described in the previous chapter. The use of the CCD microscope to monitor particle images in the camera film plane was essential for this purpose. It was found that camera alignment with respect to the light sheet was equally important for both vertical and horizontal measurement planes, due to aberration and depth of focus considerations. In the case of horizontal planes, the camera viewed the light sheet via the 45° mirror and piston crown window. Significant image degradation occurred due to coma introduced by relative tilt of the ~25mm thick window to the camera lens axis. This was eliminated by careful adjustment of the mirror and camera orientation, using the CCD microscope to optimise image quality over the entire field of view.

The camera magnification was set to a nominal value of 0.4 using a 10mm reticule in the film plane and a 1mm scale placed in the measurement plane. For measurements in vertical planes, the scale was placed vertically to set the nominal magnification, since the magnification in the vertical direction was constant over the central portion of the field of view. The optical correction was optimised iteratively as described in the previous chapter, with the additional requirement of achieving the correct nominal magnification. Typical errors in the magnification setting were less than 1%.

The PIV images were recorded on Kodak Technical Pan 2415 film. This was developed in D-19 for 6.5 minutes at room temperature, giving an effective film speed of approximately 100 ASA at a resolution of 200 line pairs per millimetre. The film was quickly rinsed and immediately fixed in Agfa-Gevaert Structurix G127 (1 part fixer to 3 parts water) for 4 minutes, rinsed for 5-10 minutes and then dried. The individual frames were then mounted in medium format glass slide mounts for protection.

4.3.6 Typical PIV Recording Procedure

In order to minimise engine running time and seed throughput, a systematic procedure for recording PIV data was implemented. This also gave a high degree of confidence that the majority of PIV images within an engine run would provide useful flow visualisation and velocity data, once developed. This was particularly important given the number of PIV images required for flow mapping and the investment of time required in setting up the optical engine and developing the images for each engine experiment. Starting with the dismantled engine, the following procedure was followed for all the PIV measurements presented here ;

Clean optical windows and piston rings+ replace
Align light sheets
Align and focus camera
Optimise corrective optic if required + check magnification
Check beam energies using laser energy monitor
Check seed images using CCD microscope
Rebuild engine carefully with particular regard to the seating of sealing gaskets
Recheck camera focus and sheet alignment + readjust light sheet if necessary
Check window cleanliness
Remove CCD microscope and replace with film cassette
Run engine at speed and check timing datum
Take PIV measurements as follows:

(Set crank angle
Set laser pulse separation
Check seed level using photodetector and adjust if necessary
Arm laser timing system
Open camera shutter
Trigger laser timing system
Wait for laser pulse
Close camera shutter
Wind on camera)

It was possible to record 15 PIV images over a range of crank angles within a single engine run lasting under 5 minutes. A maximum of two engine runs at 1000 RPM could be made before the accumulation of seed material on the optical windows necessitated dismantling of the engine for cleaning of the optical surfaces. Optical windows were scrupulously cleaned using methanol, the window cleanliness having a significant effect on particle image quality. The time between engine cleaning operations was a function of seed throughput alone. Window fouling was more problematic when measurements in the combustion chamber were of interest. This was due to a band of seed material deposited at the top of the piston stroke by the upper piston ring, which accumulated rapidly during an engine run. Therefore, crank angles close to TDC were always recorded in the first stages of a PIV experiment and crank angles near BDC were recorded last.

The required laser pulse separation was estimated from a series of preliminary PIV experiments in which PIV images were recorded at range of pulse separations for a range of extreme measurement crank angles. With typical in-cylinder velocities of 10ms^{-1}, pulse separations of the order of 25µs gave maximum particle displacements in the flow of 0.25mm; approximately one quarter of the interrogation region size. In motored work, for a given inlet configuration and measurement plane, it was found that the same pulse separation could be used for all crank angles between Inlet Valve Closure and 40° before TDC. After this point, the pulse separation was first reduced to accommodate squish-induced velocity increases and then increased after TDC due to the breakdown of large scale motion into small scale turbulence. In practice, the pulse separation could not be optimised perfectly without repeating each measurement using an excessive number of different pulse separations. The interrogation region size therefore had to be adjusted in some cases at the interrogation stage to accommodate the maximum particle displacements which were present.

4.4 Interrogation of PIV Images

4.4.1 Interrogation System

A commercially available interrogation system using digital autocorrelation was used to process all of the PIV images resulting from this work. The PC based 'VISIFLOW' PIV interrogation system was supplied by AEA technology. The PIV transparencies were mounted on a two axis Time and Precision translation stage and translated in front of a CCD microscope camera for digitisation of the individual interrogation regions. A white light source and diffuser illuminated the transparency, a small region of which was imaged onto the Sony XC-77RR-CE CCD camera array using a 25mm microscope objective and extension tubes. The imaged region was digitised with a Data Translation DT2855 frame grabber. The 768x512 image was subdivided into a 4x3 grid of 256x256 pixel regions, with a 50% overlap between neighbouring regions as shown in figure (4.24). Each 256x256 pixel area represented one interrogation region. The calculation of the mean particle image displacement within each region was performed on a S.M.I.S. array processor. This was performed using FFT based calculation of the digital autocorrelation of each region. During the initial signal peak search, the co-ordinates of the brightest non-central pixel in the autocorrelation were located as the first approximation to the displacement vector. The central self correlation peak was excluded from the signal peak search by applying a 'DC peak mask' of user-defined radius. The position estimate of the signal peak was then refined to sub-pixel accuracy by performing a signal peak centroid calculation using neighbouring pixels within a user-defined radius. The signal peak was then masked off using a 'signal peak mask' of equal radius to that used for the centroid determination. The process was repeated to locate the highest three candidate signal peaks in each region, in rank order of height. The interrogation process typically took 15 seconds per region at the 256x256 FFT resolution. For each interrogation region the co-ordinates of the highest three non-central signal peak candidates were located. Velocity data was stored as a list of three pairs of velocity angles (subject to a 180° ambiguity) and magnitudes.

Interrogation regions sizes typically used in the engine measurements were a little over 1mm in the flow, or 0.4mm on the transparency. The largest in-cylinder measurement areas required up to 100x150 interrogation regions, giving 15000 individual velocity measurements. Film noise, velocity gradients, out of plane particle motion and particle motion outside the measurement dynamic range gave rise to erroneous vectors which accounted for at least 10-15% of the velocity measurements, depending on the flow conditions and image flare at the measurement crank angle. Erroneous vectors were removed in a systematic post-processing procedure using the AEA Technology PIV analysis and display software [4.9]. This included removal of vectors lying outside of user-defined velocity limits and those vectors showing gross discontinuity from their neighbours. Remaining gaps in the velocity field could be filled by interpolation from neighbouring validated measurements.

4.4.2 Interrogation Procedure

The interrogation size was chosen according to the requirements of dynamic range and velocity gradient considerations, as discussed in chapter 2. For all the measurements in vertical planes, the interrogation region size was 1.12mm in the flow, or 0.448mm on the transparency. For 15μm particle images, this gave a theoretical useful dynamic range of approximately 7.5. For measurements in horizontal planes, the interrogation region size was 1.422 mm in the flow or 0.569 mm on the transparency, giving a theoretical measurement dynamic range of approximately 9.5. The difference in the measurement grid size was due to the slightly higher flow velocities encountered in the horizontal measurement plane. The CCD microscope magnification was adjusted by means of interchangeable extension tubes. The framestore pixel size was then calibrated by placing a regular 0.5mm grid in place of the PIV transparency and manually locating the centre of grid lines in a digitised image of the grid using a cursor. In this way, the relation between pixel displacements and flow displacements was determined and used as a calibration factor for input to the PIV interrogation software.

The PIV transparency was then mounted in front of the CCD microscope and illuminated with the white light source. The lower left corner of the interrogation area was then located and used as the starting point for interrogation. Where the piston crown window was visible in the PIV recordings, the intersection of the light sheet with the piston window edge was used as the datum point. For many of the measurements, no reliable datum point was present and the resulting vector maps are not precisely located with respect to the cylinder axis or piston crown.

The DC peak mask radius was determined by trial and error on a few typical interrogation regions. Typical radii of 14-16 pixels were used, corresponding to a minimum measurable displacement of 28-32 μm. This is somewhat larger than the typical particle image diameter and reduced the measurement dynamic range still further from the theoretical value. The need for a larger DC peak mask arises due to broadening of the self correlation peak due to non-uniform particle image sizes and, particularly, by correlated film noise caused by flare. The radius defined for the signal peak centroid calculation and signal peak mask was typically 8 pixels. The diameter of the signal peak mask was therefore approximately twice the typical particle image diameter. This was necessary to achieve accurate centroid estimates from the broadened signal peaks which are expected in conditions of high velocity gradients.

4.4.3 Post Processing Procedure

The large number of spurious velocity measurements resulting from the interrogation process required that a systematic post processing procedure be applied to remove them from the data set. The post processing procedure consisted of the following steps;

1) Removal of vectors lying outside upper and lower limits defined by the operator
2) Removal of vectors lying within +/- 3° of the horizontal or vertical
3) User-definition of unambiguous vector directions
4) Removal of vectors with more than 30% deviation from their nearest neighbours

At each stage, the removed vector was replaced with a second or third candidate peak if this satisfied the previous validation criteria. Careful comparison of the vector map with the original PIV image was carried out after each stage to avoid introducing false detail into the vector map. The removal of vectors very close to the horizontal and vertical was found to significantly improve the vector fields. The occurrence of spurious vectors close to the horizontal and vertical arises due to structured fogging in these directions and, in the absence of strong particle images toward the edges of the light sheets, due to correlated CCD camera noise or FFT artefacts.

Finally, gaps in the vector field were filled by interpolation using a weighted average of neighbouring velocity values within a radius of 5 data points. An inverse-square weighting factor was applied to data points according to their distance from the interpolated region. Figures (4.25a to 4.25e) show the results of each stage of the validation procedure for a typical vector map from the engine. The proportion of invalid data was typical of that for PIV measurements, with significant data loss due to film fogging and excessive velocity gradients.

Ideally, the proportion of invalid data should be minimised by application of more reliable PIV recording and interrogation techniques. However, given the conditions of high velocity gradients and the limitation of autocorrelation analysis, the post-processing and interpolation procedures were required to give continuous vector maps for the calculation of macroscopic flow characteristics and suitable flow visualisation.

4.5 Measurement Conditions

4.5.1 Engine Conditions

The majority of the experiments conducted on the engine related to the characterisation of the cold flow under motored conditions. A preliminary proof-of-principle investigation of the combustion flow field was also conducted under part throttle, skip-fired conditions.

4.5.1.1 Conditions for motored flow experiments

Owing to the lengthy interrogation time required using the available interrogation system, PIV images were recorded at a limited number of engine conditions. A single engine speed of 1000 RPM was used with a wide open throttle (WOT) for all the measurements presented here, with the exception of the fired results, where the throttle was adjusted to limit peak cylinder pressures.

For measurements of cold flow in the motored engine, air alone was fed to the intake. The in-cylinder flow field was studied for two different nominal Barrel Swirl Ratios (BSR). The BSR was changed from a 'low' value of 1.2 to a 'high' value of 1.8 by means of the port face inducer gasket described earlier. The gasket increased the BSR by obstructing the lower portion of the inlet port face, thereby directing a greater proportion of the flow over the upper portion of each inlet valve. Figure (2.46) shows typical cylinder pressure traces for each BSR inlet configuration. The similarity of the two pressure traces show that the induced mass at each BSR is almost identical, despite the reduced cross-sectional area of the inlet port in the high BSR configuration. A corollary of this is that this particular inlet port is not optimised for mass flow in the standard BSR configuration.

4.5.1.2 Conditions for fired PIV experiments

After the complete set of motored PIV measurements had been made, the engine intake was modified to permit skip-fired operation with an air-propane mixture at a part throttle condition. A limited number of preliminary PIV images were then recorded in a horizontal plane close to the cylinder head face. The purpose of this work was to test the engine design for integrity under firing conditions and to confirm the possibility of making PIV measurements ahead of a developing flame under realistic engine conditions.

The fused silica cylinder was designed to withstand maximum pressures of 2200 kPa with a safety factor of approximately two. Therefore, the firing engine conditions were carefully controlled to limit cylinder peak pressures. The inlet manifold was modified to accept a commercial gas carburettor between the plenum and port face flange, as shown in figure (4.27). The gas carburettor was supplied with propane at a little over atmospheric pressure via a low pressure regulator and cut-off valve. To avoid excessive firing cylinder pressures during the setting up procedure, the carburettor mixture was first adjusted by transferring the complete optical engine's inlet onto a Ricardo E6 single cylinder engine having similar bore dimensions to the optical engine. The compression ratio was set to a value of 10.5:1 and the carburettor mixture set screw was adjusted to give smooth engine running at 1000RPM, with silicone oil seeding at the level required for PIV recording at TDC. During this process, the engine exhaust was monitored using a Ricardo Oliver Multigas exhaust gas analyser and the carburettor was fine adjusted to give an air/fuel mixture slightly lean of stoichiometric. Once the approximate desired mixture had been achieved, the inlet and carburettor throttle plates, mixture set screw and ignition delay were adjusted iteratively to limit the peak firing pressure to approximately 1000 kPa under continuous firing operation. With the same settings and a motored engine speed of 1000RPM, single-shot ignition firing produced higher peak pressures of approximately 2000 kPa, due to the lack of exhaust gas residuals. Since the optical engine was designed only for skip-fired operation, the expected maximum peak pressure was therefore of the order of 2000 kPa.

The inlet system was then transferred back to the Rover optical engine. A flexible, air-purged steel exhaust was fitted to the engine. A standard spark plug and electronic ignition unit were triggered in a single-shot mode under control of the laser/engine timing unit, with an ignition timing of 5^o before TDC. The engine was motored at 1000 RPM with seeding appropriate for TDC images. With perspex guards placed over the engine windows, the propane supply was turned on and the engine was manually skip-fired several times. The carburettor setting was adjusted to give a clean, blue flame. Typical motored and fired pressure traces from the optical engine are shown in figure (4.28). Typical cylinder pressures of up to 1600 kPa were recorded with single-shot ignition. Occasionally, unusually high peak pressures of up to 3000 kPa were recorded with single shot firing. The engine was fired a total of approximately 50 times and suffered no damage to either optical surfaces or sealing gaskets. Very minor sooting of optical windows was observed, this being negligible compared to fouling of the windows by seed material during motored operation.

PIV images were recorded for a range of crank angles from the ignition crank angle to 40° after TDC. The gas supply was turned off immediately after acquiring the PIV images and the engine was then allowed to run for a short period of time to completely purge the engine and exhaust system of air/fuel mixture.

4.5.2 Measurement Locations and Crank Angles

4.5.2.1 Motored measurement locations and crank angles

Three planes were of immediate interest in the characterisation of the in-cylinder flow. The single horizontal measurement plane and two parallel vertical measurement planes are shown in figure (4.29). Plane A-A was a vertical plane which passed through the centres of an inlet and exhaust valve and was of interest due to the expected strong in-plane tumbling motion. Plane B-B was a vertical plane parallel to plane A-A, and was located on the cylinder head symmetry plane. This was of interest since previous LDV, Hot Wire Anemometry and CFD velocity data have been acquired in this plane by other workers in similar engine geometries.

Plane H-H was a horizontal measurement plane, located 3mm down from the cylinder head face. At most engine crank angles, the flow was expected to be strongly out of this plane and measurements were therefore limited to only to crank angles at which significant in-plane motion was present. This included motored measurements close to TDC and particularly the fired PIV measurements after TDC.

The maximum extent of the measurement areas is indicated by the shaded regions in figure (4.29). For planes A-A and B-B, the width of the measurement areas was limited by the piston crown window dimensions as indicated. The pulse energy used for plane B-B measurements was approximately 120mJ, compared with 80mJ for plane A-A. The increased pulse energy was to compensate for the increased laser sheet width required for measurements in plane B-B. In some of the early PIV measurements, the width of the measurement area was typically less than the maximum allowed by the piston crown access. This was due to a reduction in light sheet intensity towards its edges and imprecise laser sheet orientation.

The centreline of the camera lens was optimised at a single position to provide maximum access into the combustion chamber volume, so that velocity measurements close to the spark location could be made. For plane B-B the lower face of the spark electrode was just in the field of view. It should be noted that the edge of the camera field is subject to the worst aberrations as well as the largest perspective errors. Therefore, if future measurements are required in the combustion chamber, optical access should ideally be provided in the combustion chamber wall. As the piston position passes the centreline of the camera lens, the region of the flow directly above the piston becomes progressively obscured. This limits the lower extent of the measurement area and creates difficulties in locating a spatial datum for the velocity measurements.

For measurements in plane H-H, the only measurement crank angle of interest which provided sufficient in-plane motion was at the nominal wide open throttle ignition point of 22° before TDC. Although images were recorded at other crank angles the degree of out- of-plane-motion in plane H-H was generally too high to permit successful PIV interrogation.

The measurement crank angles recorded for vertical planes were chosen to characterise the formation and breakdown of large scale tumbling motion throughout the induction and compression strokes. Images were recorded in planes A-A and B-B for both the standard and high BSR inlet configurations at the crank angles listed in table 4.2 below.

CRANK ANGLE	SIGNIFICANCE
45° After TDC	Example of Induction Flow
222° After TDC	Inlet Valve Closure
260° After TDC	Intermediate Point
300° After TDC	Expected Tumble Breakdown
320° After TDC	Intermediate Point
338° After TDC	Nominal WOT Ignition Timing

Table 4.2 Measurement crank angles for vertical planes

4.5.2.2 Firing measurement locations and crank angles

For the firing experiments, the horizontal plane H-H alone was recorded. This was due to the limited access afforded into the combustion chamber when imaging through the engine cylinder. The ignition crank angle was 5° before TDC and images were recorded at 12, 25 and 38° after TDC. To compare the combustion induced flow field with the motored flow field under the same conditions, the fired measurements were repeated with the same inlet conditions without ignition. Of the 12 fired images recorded, only one example of a fired PIV image was interrogated, together with the baseline image without ignition. This was the 25° after TDC image, which provided a clear cross section through the flame with a predominant in-plane unburned gas motion.

4.6 Closure

A description of the PIV engine facility which was developed in this work and its constituent systems has been given. This has included the development of number of special techniques for ensuring the routine acquisition of high quality PIV data in the demanding application of in-cylinder velocimetry. The measurement conditions and locations for a series of motored and fired PIV studies have been described. In the following chapter, representative PIV images from the engine at a variety of these measurement locations and crank angles will be shown. PIV vector maps resulting from the extensive motored PIV experiments and the preliminary fired study will then be presented and discussed with reference to the work of others in optically accessed engines.

CHAPTER 5

PIV RESULTS

5.1 Introduction

The PIV images which were recorded at the conditions outlined in the previous chapter provided immediate, high spatial resolution flow visualisation in addition to quantitative flow data. In this chapter, examples of representative PIV images from each measurement plane are given and the complete set of PIV vector maps from successfully interrogated images is presented. The majority of the results relate to a motored engine speed of 1000 RPM with a wide open throttle. Preliminary results from the firing experiments are also presented.

Velocity profiles from the PIV data are compared with LDV velocity profiles from a previously published study in a Rover engine of similar geometry. The large scale flow features in the PIV measurements are also compared to the observations of other workers in related studies. A preliminary qualitative comparison of the PIV data with CFD simulations of the in-cylinder flow is made. Dynamic Barrel Swirl Ratios have also been estimated from the PIV velocity data. The PIV-based BSR values have been used for comparison with prior BSR estimates from steady flow rigs and motored LDV data.

Firstly, some typical PIV images will be presented and their important characteristics with regard to suitability for subsequent interrogation are discussed.

5.2 Typical PIV Image Characteristics

The important image characteristics which affect the interrogation process are: particle image size and shape; film noise caused by flare; and velocity gradients due to the flow structure. The characteristics of the PIV images may change significantly with measurement location and crank angle. The result of an autocorrelation on a typical interrogation region will now be presented to indicate the typical conditions under which the velocity data were extracted. A series of PIV images from both vertical and horizontal planes will then be presented and discussed to indicate the special difficulties encountered at different measurement locations and crank angles.

5.2.1 Typical Autocorrelation under Experimental Conditions

A typical interrogation region from a PIV image under realistic experimental conditions is shown in Figure (5.1a). This region displays moderate film noise and the flow condition corresponds to a velocity gradient strength-dynamic range product of approximately $\phi D_r = 1$. The effects of correlation noise on the autocorrelation are shown in figures (5.2a and 5.2b). This can be compared to figures (2.4 and 2.5) for an ideal photographic PIV recording with zero velocity gradient.

Velocity gradient signal peak broadening is clearly seen in figures (5.2a and 5.2b). The self correlation and signal peaks are also broadened by non-uniform particle image sizes. In addition, the presence of a low spatial frequency intensity variation in the image due to flare, has significantly increased the spatial extent of the central self-correlation peak, thus restricting the useful measurement dynamic range. The presence of high spatial frequency noise, caused by high levels of flare and the film grain structure has also raised the level of the noise floor in the autocorrelation. It should be noted that this result is typical of a successful PIV recording on low noise Kodak Technical Pan film, in which camera focusing, window cleanliness and flare were closely controlled. Significant data dropout can be expected under such conditions, requiring that post-interrogation validation and interpolation be applied.

The spatial velocity gradient within the example interrogation region is the order of 2000/s, which is of the same order of the maximum values of large scale strain rate measured by Reuss *et al* in a high swirl engine [5.1]. However, specific areas of typical PIV recordings were seen to contain flow structure with strain rates far in excess of this value and gave rise to high levels of local data dropout. The loss of PIV data in highly turbulent regions of flow prevents estimation of the small scale flow characteristics which are of particular interest for correlation with combustion parameters. Given the nature of velocity gradient data loss, the caution expressed by Reuss *et al* [5.1] relating to the interpretation of length scales and strain rates measured using PIV therefore appears justified. Methods of increasing the proportion of valid data and reducing the correlation sensitivity to velocity gradients will be discussed in chapter 6.

5.2.2 PIV Images from Vertical Planes A-A and B-B

The location of the two vertical measurement planes, A-A and B-B, was shown in Figure (4.29). Plane A-A is a vertical plane which bisects an inlet and exhaust valve, and is expected to show a predominantly in-plane tumbling flow. Plane B-B is coincident with the symmetry plane of the cylinder head and is parallel to A-A. Examples of PIV images which were recorded in these planes at a range of crank angles throughout the induction and compression strokes are now presented.

5.2.2.1 PIV images from plane A-A

Significant in-plane motion was observed in plane A-A for both the standard and high barrel swirl inlet configurations, over a wide range of crank angles throughout the induction and compression strokes. The conditions of flare were found to vary with the measurement crank angle. Problems of flare were most acute for the induction crank angle, at which the laser-illuminated inlet valve protruded into the engine cylinder. Flare was also a significant problem for crank angles approaching TDC, where the proximity of the piston window to the cylinder head caused increased levels of stray illumination.

Figures (5.2a and 5.2b) are typical PIV images recorded during induction at 45° after TDC in the 1.2 and 1.8 BSR configurations. Recirculating flow patterns beneath the inlet and exhaust valves can be seen with careful examination, although flare has caused some areas in which distinct particle images are not readily observed. There is also no evidence of the expected high velocity jet flows at the cylinder walls. This is expected, since the laser pulse separation was chosen to reveal the lower velocity vortex structures beneath the valves. In addition to data losses caused by flare and dynamic range considerations, the high turbulence levels and strong shear flows which are known to exist during induction are also likely to give further data dropout during interrogation due to excessive velocity gradients.

Figure (5.3) shows a typical PIV image at IVC (222° after TDC) for the 1.2 BSR inlet configuration. Here, flare is at a minimum and large areas of flow are available for interrogation. Much of the high velocity, small scale motion seen at the induction crank angle has decayed, so that velocity gradient data dropout will be reduced at this condition. Areas of remaining flare are seen close to the cylinder head and at the piston crown surface. The cylinder head flare comes from two sources. The brightest source of flare is the intersection of the light sheet with the valve heads and reveals the pentroof combustion chamber shape. This prevents PIV measurements within several millimetres of the combustion chamber walls. The second significant source of flare is the cylinder head gasket, which gives rise to a series of irregular, curved bands of fogging beneath the cylinder head face.

Figures (5.4a and 5.4b) are PIV images recorded at 320° after TDC for the low and high BSR conditions respectively. This is close to the crank angle of maximum compressive strain. Therefore, velocity gradients during this phase are high as the flow structure is compressed into an increasingly adverse clearance geometry. The rapidly changing aspect ratio of the clearance volume may also give rise to significant out-of-plane motion and cause loss of pairs at this condition. This is particularly observed in the region beneath the exhaust valve in figure (5.4a), where no discernible particle pairs can be seen.

Finally, figures (5.6a and 5.6b) show PIV images at 338° after TDC, which is the nominal wide open throttle ignition crank angle. The proximity of the piston crown with the combustion chamber surfaces has given rise to high levels of flare. Also, the obstruction of the camera view by the piston surface and the cylinder head face has restricted the field of view to a thin slice of the flow field part way between the combustion chamber apex and the piston crown. The imaging system is operating at the edges of the camera and corrective lens fields. Furthermore, the images are being recorded through a region of the cylinder which is fouled by material left by the piston rings at the top of the piston stroke. While limited flow visualisation was provided at this crank angle by the PIV images, reliable quantitative measurements were restricted to the earlier crank angles during compression.

5.2.2.2 PIV images from plane B-B

PIV images from plane B-B showed many similar characteristics with those from plane A-A. However, the details of the flare structure were different, causing problem 'hot spots' in additional locations. Images at 45° induction showed little evidence of in-plane flow and were therefore eliminated from the study. Figure (5.7) shows a typical image taken at 300° crank angle at the low BSR condition. There is some flare due to the cylinder head gasket, although this is less serious than in plane A-A. However, flare from the combustion chamber walls is significant and two additional hot spots are seen toward either side of the light sheet above the centre of the measurement region. The spark plug lower electrode surface is just in the field of view at the top of the measurement area.

Figures (5.8a and b) show the high degree of flare experienced at the 338° after TDC condition. This was a potentially important measurement condition, giving evidence of the flow field adjacent to the spark electrode at the time of ignition. However, high velocity gradients and flare due to the proximity of the piston crown, combustion chamber and spark plug surfaces prevented useful interrogation of the images. In spite of this, the images did provide useful flow visualisation and velocity estimates were possible by manually matching particle image pairs.

5.2.3 PIV Images from Horizontal Plane H-H

Plane H-H was a horizontal plane located 3mm down from the cylinder head face, or approximately 10mm below the spark plug electrode's lower surface. Illumination of this plane required that the light sheet be introduced close to the cylinder head gasket. Furthermore, the laser sheet had to be introduced through the region of fouled cylinder at the top of the piston ring travel, so that light sheets were often of a striated nature. Therefore, images in plane H-H had to be recorded during the first minutes of engine running. A high light sheet divergence was also required to completely illuminate the region which could be viewed through the piston crown window. This reduced the light sheet intensity and increased the striation widths in the side of the image furthest from the illumination source. For the majority of engine crank angles throughout induction and compression, the flow had a large velocity component perpendicular to plane H-H. Therefore, attention was restricted to measurements close to TDC, where the proximity of the piston crown forced a predominantly in-plane flow. This included the fired PIV condition and also the motored condition at 338° after TDC.

Figure (5.9) shows a PIV image recorded at a crank angle of 338° before TDC, for the 1.8 BSR inlet configuration. The striated illumination is clearly seen. This prevented useful measurements in the half of the cylinder furthest from the illumination source. Owing to the symmetrical nature of the flow about the cylinder head symmetry plane, only the cylinder half-plane with the better illumination characteristics was interrogated. The horizontal plane images exhibited high degrees of flare distributed over the entire field of view. This was due to the proximity of the laser light sheet to the cylinder head face and gasket, which caused illumination of combustion chamber surfaces. The out of focus outlines of the inlet, exhaust valves and spark plug are clearly seen in figure (5.9) Debris carried by the piston crown window was also illuminated and gave rise to further image degradation. Careful cleaning of the piston crown surface and rapid engine reassembly was required to minimise the accumulation of air-borne lint and dust on the piston crown surface.

5.3 PIV Vector Maps From Motored Experiments

In the PIV measurements which follow, the velocity data have been subject to the post processing and interpolation procedures which were described in the previous chapter. The interrogation region dimensions were chosen to give a compromise between dynamic range and velocity gradients. For planes A-A and B-B, an interrogation region size of 1.12 mm in the flow was chosen. PIV images in plane H-H exhibited higher velocity bulk flow than the vertical planes for the same pulse separation and a larger interrogation region size of 1.422 mm was consequently used.

Each measurement was repeated for both the 1.2 and 1.8 BSR inlet conditions to investigate the effect of the initial Barrel Swirl Ratio on the development and breakdown of large scale motion through the induction and compression strokes. The pulse energy used for pane A-A was 80mJ. Pulse energies were increased to 120mJ to account for the increased beam widths in planes B-B and H-H. In general, the maximum flow velocities in the centreline plane B-B were several ms^{-1} higher than in plane A-A, particularly at the high BSR condition for which laser pulse separations of 20μs were used. The highest velocities were encountered in plane A-A at the 45^{o} induction crank angle, requiring pulse separations of 10 to 15μs. For the remaining conditions, the same pulse separation of 25μs was used for all measurement crank angles during the compression stroke.

In the vector maps which follow, all of the individual velocity vectors have been assigned a user-defined direction. The original measurements were subject to the 180^{o} directional ambiguity which is inherent in autocorrelation analysis. The initial flow directions during induction and the early stages of compression were added with reference to existing LDV data and flow visualisation. Subsequent flow directions have been assumed from flow continuity considerations, although the directions of velocity vectors within small scale reversing flow structures are unknown. Clearly, the measurement of unambiguous velocity measurements would be a major step forward in the application of in-cylinder particle image velocimetry and potential methods for achieving this will be discussed in the following chapter.

All velocity measurements within 2mm of solid surfaces are generally unreliable due to flare. In these regions, the autocorrelation typically produces a spurious vector which is approximately perpendicular to the mean background intensity gradient due to fogging. The spurious vectors close to surfaces therefore appear to give vectors of random length which are approximately perpendicular to the surface normal.

The typical proportion of data dropout for the velocity maps was of the order of 15-20%. Data dropout was much higher for the 45° inlet condition, at up to 50%. This was due to the combination of high velocity range in the flow, high velocity gradients and strong flare. The 320° crank angle for the low BSR plane B-B measurement had a large area of complete data loss due to out-of-plane motion. For measurements in planes A-A and B-B at the 338° after TDC rank angle, the data dropout due to flare and velocity gradients was too great to allow meaningful interpretation of the velocity data without reference to the original PIV images. Further developments in the PIV recording and interrogation methods are required to reduce data loss in the raw PIV data.

Further work is also required to develop a means for providing an accurate datum for the in-cylinder measurements in cases where the piston crown or spark electrode are not in view. Variations in the width of the measurement area seen in the results which follow are due to variations in the light sheet intensity profiles and alignment as the experimental technique was successively refined during the course of the study. The maximum possible extent of a collimated light sheet, as limited by the piston crown clear aperture, is indicated in each vector plot. The position of the horizontal piston face at the measurement crank angle is also indicated.

5.3.1 Vertical Planes A-A and B-B

5.3.1.1 Plane A-A

At the 45° crank angle condition shown in figures (5.10 and 5.11), the flow appears to issue from either side of the inlet valve, generating a pair of large scale counter-rotating vortices. The velocity magnitudes and velocity gradients are both high. This gave a great deal of data dropout, of the order of 50%. As a consequence, the vector maps at this crank angle are heavily interpolated. Owing to the tumble design of the cylinder head, the majority of the flow issues over the upper lip of the inlet valve, so the more dominant vortex appears toward the exhaust side of the clearance volume. With the high BSR inlet (figure 5.11), the left hand vortex dominates more strongly than in the low BSR case (figure 5.10), and the impingement region where the two vortices meet to form an unsteady upward 'fountain' flow is pushed toward the inlet side.

The flow fields at IVC (222° after TDC) gave significantly less data dropout. Much of the small scale motion introduced by the induction process has by this stage decayed to give a relatively ordered flow with much reduced velocity gradients. Figures (5.12) and (5.13) show the flow fields for the 1.2 and 1.8 BSR inlet conditions respectively. In the low BSR case in figure (5.12), the flow is disordered, with many small scale changes in flow direction. In the high BSR case, the flow appears as single ordered vortex with a clear centre of rotation as shown in figure (5.13). The difference between the two cases may be attributed to the relative strengths of the pair of opposing vortices observed during induction. For the high BSR case the main tumble vortex dominates the flow at an earlier stage to produce a more ordered tumbling motion having a higher rotation rate.

At 260° after TDC in the 1.2 BSR flow (figure 5.14), a strong upward motion is observed from the piston face near the cylinder centreline. The centre of rotation of the vortex flow is seen in the upper portion of the flow field. The flow is again far from being a solid body rotation, with irregular regions of high and low velocity gas. At this crank angle, the highest velocity gas, or "swirl tongue", appears to be exiting the pentroof combustion chamber from right to left. The high BSR condition shown in figure (5.15) produces a significantly different flow structure. The early domination of the flow field by a single inlet vortex has given rise to a single, highly ordered rotation whose centre is close to the geometrical centre of the measurement area. Maximum flow velocities are higher than for the low BSR case. The swirl tongue is seen to have completed one circuit of the cylinder and is leaving the piston surface close to the cylinder centreline.

Differences in the flow for the two inlet conditions become greater at 300° after TDC as shown in figures (5.16) and (5.17). The piston motion has an increasing effect on the flow at the piston face and compressive and shear forces increase as the flow is forced into an increasingly adverse clearance volume. In the low BSR case (figure 5.16), the flow toward the left of the piston face has stagnated and shows signs of a complete reversal. The tongue of high velocity gas is now seen toward the inlet side of the cylinder and is leaving the piston face almost perpendicular the piston surface. The high BSR flow field at this condition is significantly different to the low BSR flow, as shown in figure (5.17). The flow still appears as a relatively ordered rotational motion with an obvious centre of rotation. Typical flow velocities are now approximately twice those for the low BSR case. This indicates that the simple vortex flow has conserved a greater proportion of its initial kinetic energy. The reason for this is that the clearance volume geometry is able to sustain an ordered tumbling motion with minimal distortion, the vortex being able to move into the apex of the combustion chamber. This implies that more energy will be available for the generation of turbulence enhancement later during compression.

At 320° after TDC the low BSR flow has become rather complex, as seen in figure (5.18). The shaded area in figure indicates a large region in which no paired particle images were present. The most likely explanation for this is that the flow in this region has turned predominantly out of the plane of the light sheet, i.e. the flow has become significantly three-dimensional as seen in the original PIV image of figure (5.4). The swirl tongue now appears to have coiled into a small vortex beneath the inlet valve. Maximum flow velocities have dropped further, indicating that much of the energy in the large scale structure has been dissipated. At the high BSR case shown in figure (5.19), a single ordered vortex is still seen, although flow velocities have dropped by approximately one third from the previous crank angle. The flow has a clear centre of rotation and appears to have a solid body-like core which rotates at a greater rate than extreme edges of the flow field. In the core flow, high velocity patches of flow are seen with lower velocity patches in between. A similar situation was reported by Reuss *et al* in a high swirl engine (5.1), who proposed that the distance between such patches could be identified with the turbulence integral length scale. If this is so then the apparent separation of the high velocity patches in figure (5.19) of 2-3mm correlates well with the expected integral length scale for crank angles approaching TDC.

Figures (5.20) and (5.21) show the low and high BSR flow fields respectively at the nominal Wide Open Throttle ignition crank angle of 338° after TDC. The assumed velocity directions have been added with careful reference to the original PIV images. The velocity maps at this crank angle are subject to a high degree of uncertainty due to flare from the cylinder head and high velocity gradients. However, it is clear that maximum flow velocities have increased for both BSR configurations compared to the previous crank angle of 320° after TDC. Maximum flow velocities for the low BSR case are approximately 10 ms^{-1}, whereas maximum velocities approaching 15ms^{-1} are seen in the high BSR flow. It is likely that these increases are due to squish-induced flows which emanate from beneath the inlet and exhaust valves. Without improved optical access into the combustion chamber region, the prospects for gaining improved insight into the complex flow conditions which exist towards TDC are poor.

5.3.1.2 Plane B-B

In the high BSR condition, the trends for the evolution of the in-cylinder flow in plane B-B were similar to those for plane A-A. A single ordered vertical vortex was generated by 260° after TDC and this persisted to the maximum useful measurement angle of 320° after TDC. However, in the low barrel swirl case, there was little evidence of flow recirculating in plane B-B after IVC and the flow appeared as a simple bulk flow from the piston face toward the cylinder head.

Figures (5.22) and (5.23) show the IVC flow fields at the low and high BSR conditions respectively. The high BSR flow is more ordered and displays less of the small scale flow structure which is prevalent in the low BSR flow. The low BSR flow field also displays a long, vertical shear-type flow which is located close to the cylinder axis.

At 260° after TDC in the low BSR flow, the dominant flow feature is an upward and undulating bulk flow as shown in figure (5.24). The region of highest velocity is seen close to the spark plug. Although a low velocity recirculation region is seen to the left of the centreline beneath the spark plug, there is no evidence of a large scale recirculation of the high velocity gas within the measurement plane. Continuity considerations would suggest that the flow must exit the combustion chamber out of the plane of the light sheet. The high BSR flow at this condition is much simpler, as shown in figure (5.25). A single barrel vortex is seen with its centre of rotation close to the centre of the cylinder volume. It is clear that such a flow can move more readily into the clearance volume during compression than the bulk translational motion seen at the low BSR condition.

At 300° after TDC the low BSR flow is still dominated by convective motion toward the combustion chamber (figure 5.26). Here, however, the highest velocity gas is found near the piston crown. By contrast, the high BSR flow, shown in figure (5.27), is dominated by a single barrel vortex whose centre has moved to the inlet side of the cylinder centreline.

This trend is continued at the 320° condition, with the low BSR configuration displaying a simple convective motion toward the cylinder head with no evidence of in-plane recirculation (figure 5.28). In the high BSR flow shown in figure (5.29), the barrel vortex is still present, giving velocities close to the spark electrode of approximately $12ms^{-1}$. The patches of high and low velocity gas are again seen separated by distances of 2-3mm at this condition.

Whole field velocity measurements at the 338° crank angle were not possible from the plane B-B images. This was due to excessive flare, together with large velocity gradients due to small scale variations in flow direction. However, the original PIV images shown in figures (5.8a) and (5.8b) did provide useful flow visualisation, indicating a simple bulk flow across the spark electrode. Velocities close to the spark plug at the nominal ignition crank angle were estimated by manual matching of particle image pairs. Figures (5.30) and (5.31) show digitised regions close to the spark electrode taken from the original PIV images. These images were enhanced by optimising the offset and gain of the framegrabber for the small area close to the spark plug lower electrode surface. Both images were recorded with the same pulse separation of 20µs. For the low BSR flow, estimated velocities close to the spark electrode were approximately 8-10 ms^{-1}. velocities close to the spark electrode for the high BSR case were higher, as is shown in figure (5.31), at $12\text{-}14ms^{-1}$.

The spark plug velocities observed in the PIV engine were in good agreement with the velocities measured with LDV in a similar geometry engine [5.2]. Even at the crank speed of 1000 RPM, these velocities are far in excess of the $3\text{-}5ms^{-1}$ spark plug velocity of value recommended by Pischinger and Heywood [5.3] for stable lean operation. It is interesting to note that if the velocity scales with engine speed, then velocities in excess of $25ms^{-1}$ are to be expected at operating speeds of 2000-3000 RPM. It is known that convective flows of this magnitude can adversely affect flame initiation through disruption of the spark discharge [5.4] or by convection of the early flame toward combustion chamber walls.

5.3.2 Horizontal Plane H-H

Figure (5.32a) indicates the geometry of the cylinder head, piston position and laser light sheet for plane H-H at the measurement crank angle of 338° after TDC. The low and high BSR flow fields are shown in figures (5.32b) and (5.32c) respectively. The original PIV image for the 1.8 BSR condition flow in this plane was given in figure (5.9). In the low BSR velocity vector map shown in figure (5.32b), the flow is predominantly in-plane and left to right, with several small scale changes in flow direction. There is evidence of a recirculating region beneath the exhaust valve. In the high BSR case shown in figure (5.32c), the flow appears to consist of an in-plane recirculating pattern which is similar to the so-called "wing-vortex" structure reported in a similar engine by Ando *et al* [5.5]. Typical flow velocities in the high BSR flow are twice those in the low BSR flow at this crank angle. It is clear that significant large scale motion is present in both BSR cases and that the flow has not completely broken down into small scale turbulent eddy motion at this stage.

5.4 Discussion of Motored PIV Results

The whole-field flow visualisation and velocity data revealed in the motored PIV experiments has provided new insight into the formation and breakdown of in-cylinder tumbling motion. The evolution of the barrel vortex was seen to be transient and to depend on the initial flow conditions during induction. In the high BSR case, the ordered tumbling motion was seen to survive until late into the compression stroke. This provides greater rotational kinetic energy for subsequent conversion into turbulence generation for combustion enhancement. However, the long-lived barrel vortex also generates high velocity bulk flows at the time of ignition.

The similarity of the flow structure on planes A-A and B-B in the high BSR flow is an indication that three-dimensional motion may be suppressed at this condition. The two-dimensional nature of high BSR flows has been exploited in the work of Ando *et al*, who achieved significant charge stratification by introducing air/fuel mixture into a single inlet valve in a symmetrical four-valve high tumble engine [5.5]. This method of charge stratification was subsequently confirmed by Baritaud *et al* [5.6]. The barrel stratification method was later refined by Ando *et al* to confine the charge to a central annulus of flow rotating in the symmetry plane of the cylinder head [5.7]. This permitted extended lean operation without major changes in engine design from current four-valve technology. The achievement of practical, stable lean burn engines is of current importance due to increasingly stringent emissions standards. However, high flow velocities close to the spark at the time of ignition were also observed in the studies of Ando *et al* [5.7] and control of this strong convective flow through modification of the piston face was required to stabilise ignition in this engine [5.7].

The existence of high velocity flows in the pent roof combustion chamber apex of four valve engines has also been confirmed in LDV measurements by Hu [5.2]. It therefore appears that the full details of the in-cylinder flow structure throughout the late stages of compression are required for the purpose of optimising combustion chamber design. Whole field velocity data from the PIV experiments is a new source of information which is of value in providing a cycle-resolved description of the instantaneous flow structure within extended planar regions, which is complementary to data from pointwise velocity measurements. The potential also exists for the validation of CFD predictions of in-cylinder flow, which are becoming increasingly important in the design of advanced combustion systems.

In an initial attempt to verify the validity of the PIV measurements, some comparisons of the PIV results with prior studies in engines of similar geometry will now be made. In many cases the details of the engine geometry used for the other experimental and CFD studies were not exactly matched in the PIV optical engine. However, certain qualitative comparisons can be made which give confidence in the PIV measurements and highlight the strengths and weaknesses in the different experimental and computational techniques. In what follows, it should be pointed out that the PIV measurements are not ensemble averaged, so that the present comparisons are subject to uncertainty caused by cycle to cycle variations in the flow and the presence of random, small scale flow structure.

5.4.1 Comparison with LDV Velocity Profiles

Velocity profiles from a similar four valve engine have been made in extensive studies presented by Hu [5.2]. The LDV measurements were performed on a Rover optical engine having a pentroof combustion chamber. Two different steady flow BSR values of 0.4 and 1.7 were achieved in the same cylinder head by remodelling the inlet port floor and ceilings. Therefore, comparisons of the 1.8 BSR results from the PIV experiments may be made with the 1.7 BSR LDV measurements, although these must be treated with some caution owing to the different inlet port details in the two engines.

The LDV measurements were made only in plane B-B. Profiles of the vertical velocity component, w, and the in-plane horizontal velocity component, u, were measured for a variety of crank angles after IVC. Useful comparisons of both velocity components could only be made at the 300° crank angle. Figures (5.33a and 5.33b) show the PIV and LDV profiles of w for the high BSR inlet conditions. The PIV and LDV profiles of u are shown in figures (5.34a and 5.34b). There is good agreement between the two sets of measurements, both sets of profiles indicating an ordered tumbling motion with similar velocity magnitudes and trends. However, the cycle-resolved PIV profiles are less smooth than the ensemble-averaged LDV measurements. This is because the random small scale structure is frozen in a single PIV recording. A rigorous comparison of PIV and LDV data would require the averaging of many PIV data sets. This would be prohibitively time-consuming considering the speed of the interrogation system used in this work.

Further comparisons between LDV and PIV data require that the PIV measurement conditions are accurately matched with LDV conditions with an identical cylinder head. The general conclusions arising from Hu's LDV measurements also reinforce some specific observations from the PIV studies. These are that large scale structure exists up to and beyond the ignition point for the high BSR configuration and that velocities in the vicinity of the spark location in excess of twice the mean piston speed exist close to the time of ignition.

5.4.2 Comparison with Large Scale Flow Structure in other Engine Studies

The large scale flow structure seen in the PIV images may be compared visually with the results of flow visualisation or measurement in similar engine geometries. Omori *et al* [5.8] applied a variety of in-cylinder diagnostics to the characterisation and development of a lean burn tumble engine. This included multi-point LDV measurements and a quantitative streak velocimetry technique for detailed flow visualisation and measurement. The maximum velocity magnitudes measured using LDV in their high tumble engine at a crank speed of 1000 RPM were of the order of $13ms^{-1}$. The trends in the development of the large scale flow structure revealed by the LDV measurements compared well with the PIV observations. Specifically, as the piston speed increased towards its maximum value during the early stages of compression, the flow above the piston was stagnated to the exhaust valve side and turned upward at an increasing angle to the horizontal on the inlet side. The streak velocimetry measurements also showed similar trends to the PIV data, with the characteristic "wing" vortices observed in a horizontal plane close to the cylinder head at 345° after TDC. The observation of a single ordered vertical vortex in the clearance space at 45° before TDC is also in agreement with the high BSR PIV results at 40° before TDC.

Limited particle tracking velocimetry measurements in a four valve tumble engine were reported by Linna *et al* [5.9]. Low resolution velocity maps at a compression crank angle of 240° after TDC also indicated an ordered tumble motion, which also displayed the characteristic piston-induced stagnation and acceleration of the flow at opposite sides of the piston face.

Water analogue flow visualisation and particle tracking velocimetry measurements further support the formation of ordered in-cylinder tumbling motion and appear to give qualitatively similar flow structures for crank angles up to IVC. In particular, the intake flow development reported by Khalighi [5.10] using a four-valve cylinder head shows several common features with the PIV results. These include the generation of competing vortices during induction for low tumble configurations and the formation of an almost solid body rotation at BDC for a high tumble configuration. Kent *et al* have used a transient water analogue engine for the routine characterisation of cylinder head designs using 3D particle tracking velocimetry [5.11]. Again, similarities exist between the flow fields observed in the water analogue studies at BDC and the large scale flow structure revealed by PIV at IVC. However, the water analogue engines cannot simulate compression flow and back-to-back comparisons of water analogue PTV and PIV measurements in a real engine are ideally required to confirm the relevance of water analogue flowfield measurements to actual in-cylinder flow characterisation.

5.4.3 Comparison with CFD Simulations

Recently, much effort has been expended in the computational modelling of barrel swirl formation and breakdown. A preliminary comparison of CFD and PIV data for the Rover engine have been presented by Das and Dent [5.12]. Jones and Junday [5.13] compared their CFD simulations with hot wire anemometry and LDV data. The IVC barrel swirl ratio in the study by Das and Dent was 0.7. However, the simulated flow structure corresponded more closely to the 1.8 BSR PIV results than the 1.2 BSR experimental vector maps. Figure 5.35 shows a sample of the CFD predictions. The 45° inlet flow field in pane A-A is seen to be simpler than the twin vortex structure which was revealed in the PIV results. This is due to simplified inlet valve curtain conditions based on hot wire anemometry measurements and the use of valve masking to obtain a tumble motion with the "correct" BSR at IVC. The agreement with the high BSR PIV flow field is reasonably close for the 260° after TDC crank angle, although the centre of rotation of the barrel vortex is lower than in the corresponding PIV measurement. The large scale structure within the pent roof at 338° after TDC is also in accord with the strong cross-flow revealed in the PIV images at this condition.

CFD predictions in the plane B-B by Jones and Junday in [5.13] were not presented at precisely the same crank angles as the PIV measurements. However, the high BSR flow structure at 270° after TDC shown in figure (5.36) is in close agreement with the PIV measurement at 260° after TDC. The strong cross-flow in the combustion chamber apex at 15° before TDC in is also in agreement with the flow structure seen in the PIV images in figures (5.8b) and (5.31). However, the velocity magnitudes at this crank angle are significantly under-predicted.

The inlet conditions at the valve in both CFD studies were based on the same experimental valve curtain velocity profiles. In order to gain closer agreement with the IVC flow, it will be necessary to refine the CFD computations to give closer agreement with the experimentally determined induction flow structure. In turn, this should improve the prospects for modelling the details of piston/flow interaction, which appear to be sensitive to the relative velocity of the flow field and piston face during compression. This may require the details of the inlet port to be modelled, as was found by Le Coz *et al* [5.14], Tatschl *et al* [5.15], and the use of a finer computational grid structure in the cylinder clearance space. A consequence of these modifications will be a significantly increased computational effort.

The emergence of PIV as a practical tool for the characterisation of in-cylinder flow fields in realistic four valve engines provides an opportunity for refining and validating the CFD predictions of large scale flow structure. However, further work is required to provide the PIV data in a form suitable for direct and quantitative comparison with CFD data and to extend in-cylinder optical access to enable validation of the flow fields close to TDC.

5.4.4 Comparison of Barrel Swirl Ratios

The Barrel Swirl Ratio (BSR) is widely used as an index of cylinder head activity in the case of engines employing barrel swirl. The Barrel Swirl Ratio (BSR) is the ratio of the mean rotation rate of the barrel vortex about its horizontal axis to that of the engine crankshaft.

For a general rotating flow field, the barrel swirl ratio from planar velocity data is estimated by summation of the angular momentum of each velocity vector about the centre of rotation of the flow. This is then divided by the moment of inertia of the flow to give the equivalent solid body rotation rate. Dividing this by the engine's crank rotation rate then gives the dynamic BSR as follows;

$$BSR = \frac{\sum_{i}^{N} \mathbf{v}_i \wedge \mathbf{r}_i}{\omega_e \sum_{i}^{N} \mathbf{r}_i . \mathbf{r}_i} \qquad (5.1)$$

where i is the i^{th} data point in the vector map, ω_e is the angular rotation speed of the crank shaft and **r** is the vector distance of the measurement point from the centre of rotation of the flow as shown in figure (5.37). This definition assumes that the gas density is uniform over the entire flow field. In the PIV-based calculations of the dynamic BSR, the co-ordinates of the centre of rotation were defined by locating its position subjectively. Where no clear centre of rotation was present, the BSR ratio for each measurement plane was calculated using the centre of the measurement plane as the origin. The overall dynamic BSR for a given engine crank angle was then calculated by taking the mean of the BSR values from planes A-A and B-B.

The PIV-based dynamic BSR values could be compared to equivalent measures of cylinder head activity based on LDV or impulse swirl meter measurements. Hu [5.2] calculated dynamic "Tumble Vortex Ratio" (TVR) values for a range of motored crank angles for the nominal 1.2 BSR configuration, using LDV velocity data collected on two orthogonal lines within plane B-B. Initial TVR values at IVC were also estimated from steady flow rig LDV measurements in this work. The estimated IVC steady flow TVR was denoted TVR_0. The dynamic TVR value at IVC should ideally coincide with the steady flow value of TVR_0. Steady flow BSR values were also estimated for the two PIV engine inlet configurations, from impulse swirl meter steady flow measurements at a variety of valve lifts. These were performed at Rover, following the prescription in reference [5.16]. These measurements were used to define the nominal BSR values of 1.2 and 1.8 for the PIV engine.

The BSR was calculated from the PIV data for planes A-A and B-B for crank angles in the range 222-320° after TDC and for each of the two nominal BSR conditions of 1.2 and 1.8. The results for the low and high BSR conditions are shown in figures (5.38) and (5.39) respectively.

In the case of the low BSR head the behaviour of the BSR with crank angle is strongly dependent on the measurement plane as shown in figure (5.38). The mean BSR value at IVC is 1.2, this being equal to the nominal steady flow BSR value based on impulse swirl meter measurements. Plane B-B first demonstrates a higher BSR than plane A-A and this position is reversed after the 260° crank angle. With reference to the original PIV velocity maps, the flow structure on the bore centreline plane is dramatically different to that on the valve centreline at the low BSR condition, so the flow cannot be considered as a simple two-dimensional barrel vortex. Linear and angular momentum will be transferred from one plane to another as the high velocity swirl tongue moves in three dimensions around the cylinder. The low dynamic BSR at 320° after TDC indicates that by this stage any large scale rotational motion has largely disappeared. However, this does not necessarily imply that velocities are low or that turbulent breakdown is complete; bulk convective motion of the kind seen in plane B-B after 260° after TDC will give rise to a low BSR value but high mean velocities.

In the high BSR case the behaviour of the PIV-based BSR is similar for both vertical planes as shown in figure (5.39). This is indicative of a more organised two-dimensional barrel vortex in which the in-cylinder gas rotates in a more organised fashion. The mean BSR at IVC is 1.7, this comparing favourably with the impulse swirl measurement of 1.8. It therefore appears that the steady flow characterisation described in [5.16] is indeed suitable for the characterisation of the initial in-cylinder BSR at IVC. The mean BSR value is first seen to rise after IVC to a maximum of approximately 3.0 at 260° after TDC and then decays slowly toward the 320° crank angle.

The behaviour of the LDV-based dynamic TVR of Hu *et al* [5.17] shows a significantly different behaviour to the PIV-based BSR values as shown in figure (5.40). The initial TVR of a little under 1.5 is under-estimated compared to the nominal steady flow rig BSR value of 1.7 in that study. The TVR then gradually decays from its value at IVC to a local minimum value of 1.2. Beyond approximately 280° the TVR increases and then decays rapidly after 320° crank angle.

A possible explanation for the discrepancy between the dynamic TVR behaviour from LDV measurements and the BSR values from PIV measurements, aside from any subtle differences between cylinder heads, is that the LDV-based TVR is based on a limited number of velocity measurements in just two orthogonal profiles. It is therefore possible that the high momentum swirl tongue may at some crank angles coincide with the measurement profiles and at other crank angles fall between the orthogonal measurement locations. The structure of the curve in figure (5.40) may therefore be due to incomplete sampling of the non-uniform angular momentum distribution in the flow. However, the trends from both measurement techniques indicate an increase in the rotation rate of the barrel vortex prior to its degeneration. This is consistent with the generally accepted description of vortex "spin-up" in engines of this nature.

It is clear that caution must be applied when attempting to characterise the complex in-cylinder flow using a limited number of point measurements. The difference in the behaviour of the BSR for different planes for the low barrel swirl case is in keeping with the different flow structures observed in the two planes in the PIV velocity maps.

5.5 Results From Fired Experiments

A limited number of PIV images were recorded for a part throttle skip-fired condition with an approximately stoichiometric air/propane mixture. The experimental details and engine operating conditions for the fired experiments were described in chapter 4. The chief aims of the fired experiments were to prove the engine design for firing operation and to investigate the possibility of making PIV measurements in the flow ahead of flame fronts. PIV images were recorded for flowfields with and without combustion at the same crank angle in order to demonstrate the effects of combustion-induced flow.

5.5.1 Typical Fired PIV Image

PIV images were recorded at a range of crank angles after the 5° before TDC ignition angle. A single PIV image recorded at 25° after TDC was selected for interrogation. This displayed a flame front which passed through the horizontal light sheet and therefore gave an indication of the flame front shape and the pre-flame flow structure.

The locations of the light sheet, flame front and piston crown in relation to the cylinder head at this crank angle are shown schematically in figure (5.41). A PIV image recorded using a laser pulse separation of 30μs is shown in figure (5.42). The silicone oil seeding is destroyed at the flame front as confirmed by Armstrong [5.18] and therefore acts as a flame front marker. The instantaneous flame front location is clearly seen as the boundary between seeded and unseeded gas. Close inspection of the seeded area adjacent to the flame front in figure (5.42) reveals that there is significant large scale motion ahead of the flame. This motion is always approximately perpendicular to the flame front surface and is indicative of expansion-induced flow as reported in previous LDV studies (see for example (5.19)).

As with the motored PIV experiments, careful orientation of the light sheet was required to minimised striations in the light sheet. The uniformity of the light sheet is seen to deteriorate significantly after passage through the flame. The additional striations can be seen to originate at the intersection of the light sheet with wrinkles in the flame surface and are therefore probably due to refraction at high incidence angles to the flame front normal. The flame front itself is irregular, as expected of turbulent combustion, showing detail down to sub-millimeter length scales. A number of apparently unconnected islands of burned gas are seen ahead of the main body of the flame. It is not clear from a single slice through the flame front whether these are truly unconnected islands or merely fingers of the wrinkled flame front protruding through the light sheet.

5.5.2 PIV Vector Maps

Figure (5.43) shows the PIV vector map corresponding to the PIV image of figure (5.42). A tracing of the flame front has been superimposed. The large scale structure which was apparent in the original PIV image is clearly reproduced in the vector map. Typical velocities adjacent to the flame front are of the order of 5 ms^{-1}.

Figure (5.44) shows the corresponding flow in half of plane H-H at the same condition but without combustion. Flow velocities were everywhere lower than in the fired flow field and for this reason a higher laser pulse separation of 50µs was employed. The velocity map in figure (5.44) is sparse and has not been interpolated. This is because the original PIV image showed a high degree of small scale eddy motion, which could not be resolved in the interrogation process due to the velocity gradient considerations discussed in chapter 2. The locations of the eddies have been added with careful reference to the original PIV image. It can be seen that the large scale flow still demonstrates the remnants of the "wing" vortex structure seen in the motored experiments before TDC, albeit with reduced bulk velocities. This indicates that under motored conditions, the large scale barrel vortex structure has not completely broken down into microturbulence even significantly after TDC. This is consistent with the known ability of pentroof combustion chambers to sustain tumbling motion throughout the compression stroke and into the early stages of the power stroke.

The contrast between the motored and fired flow fields clearly indicates that the expanding flame front significantly modifies the pre-flame flow field. Therefore, although motored flow measurements may be useful for describing the flowfield which affects ignition and early flame development, it is not clear whether such measurements can provide a reliable indication of the flow conditions which affect the majority of the combustion event.

5.6 Closure

A set of motored PIV images and measurements from three measurement planes within the engine have been presented. The images and measurements indicate the practical problems associated with acquisition of high quality PIV data in a four-valve engine of realistic geometry. Aside from the theoretical considerations of velocity gradients and measurement dynamic range, the major practical difficulties for in-cylinder PIV measurements were flare and, for horizontal planes, light sheet quality. Despite these difficulties, it has been demonstrated that valuable flow data can be acquired routinely in motored PIV experiments from planes both parallel and perpendicular to the cylinder axis.

The flow structures revealed in the motored PIV measurements are in good qualitative agreement with other studies performed in similar engine geometries. Flow velocities observed at different stages of the compression process are also in agreement with the experimental work of others. Of particular importance are the high velocities observed in the combustion chamber flow close to the spark location at the ignition crank angle. The combustion chamber velocities were higher for the high BSR case, due to the increased ability of the combustion chamber geometry to sustain an ordered tumbling motion during the late stages of compression. The major conclusions regarding the evolution of the motored in-cylinder flow may be summarised as follows;

1) The induction process is characterised by the formation of two counter-rotating vortices. The relative strengths of the two vortices determine the net angular momentum of the flow at IVC.

2) Even for the high BSR case, the flow shortly after IVC is not a solid body rotation. Instead, the flow during the early stages of compression is characterised by a high momentum "swirl tongue" of gas which circulates throughout the cylinder volume.

3) The flow evolution is highly dependent on the BSR. There is evidence that the relative velocity of the flow at the piston face and the instantaneous piston speed profoundly affects the flow evolution in the later half of the compression stroke.

4) For the high BSR case, the barrel vortex shows a tendency to "spin-up" part way through the compression stroke due to partial conservation of angular momentum.

5) The barrel vortex is preserved to a late stage in compression for the high BSR case. There is evidence of remaining large scale motion in the early stages of the power stroke in the motored flow, even for the low BSR case.

6) High velocity bulk flows across the spark electrode are formed at the ignition crank angle. Velocities are significantly higher in the high BSR case.

Dynamic PIV-based BSR values averaged over the two measurement planes are in excellent agreement with the steady flow values derived from impulse swirl meter measurements. There is some qualitative agreement in the "vortex spin-up" trend seen in the PIV and LDV dynamic BSR values from similar engines. However, quantitative comparisons indicate that caution is required in characterising the in-cylinder flow using a limited number of measurement points.

The agreement of preliminary CFD predictions with the PIV measurements for crank angles during the early stages of compression is encouraging. However, the details of the flow fields after modification by piston motion and compression in the later half of the compression stroke were less well reproduced. It is possible that improved initial and boundary conditions are required, with particular regard to the flow details in the inlet port and valve curtain.

Preliminary PIV measurements under fired conditions showed that the pre-flame flow was significantly modified by flame expansion. The ability of the optical engine to withstand part throttle combustion conditions was proven. This gives confidence for the application of PIV for combustion studies in future work.

While the results presented here represent a significant advance for in-cylinder whole-field velocimetry, there remain some serious practical and theoretical limitations in the current measurement technique. In certain measurement conditions, this required significant post processing and interpolation of the PIV, thereby reducing the measurement spatial resolution and measurement confidence. In the worst case of measurements close to TDC in vertical planes, quantitative whole-field PIV measurements were prevented. In the next chapter, the limitations of the current measurements will be discussed and potential methods for relieving these limitations will be presented.

CHAPTER 6

LIMITATIONS OF THE PRESENT TECHNIQUE AND SUGGESTIONS FOR IMPROVEMENT

6.1 Introduction

The application of double-exposed PIV recording and autocorrelation analysis has provide much useful insight into the formation and breakdown of large scale in-cylinder fluid motion in this study. It has also been demonstrated that, with careful experimental technique, the measurement process can be made sufficiently robust for the industrial application of routine in-cylinder flow mapping. This is evidenced by the investment of the industrial sponsors in a duplicate PIV engine facility, which will enable in-house characterisation of in-cylinder flow in future engine development programs. However, it should be recognised that the current measurement technique is subject to certain practical and theoretical limitations. Further progress in the study complex, three dimensional flows, the study of flows near TDC and the rigorous validation of CFD simulations will require that the practical problems and theoretical limitations of the current technique are addressed.

The major practical limitations are as follows;

1) Optical access for viewing vertical planes near TDC
2) Limitations of the optical correction for viewing vertical planes
3) Stray illumination or "flare"
4) Image recording and interrogation time.

Recent developments in optical engine design, flow seeding particles and fast correlation techniques now present the opportunity for addressing these practical limitations. In addition to the practical considerations, the following fundamental theoretical limitations of autocorrelation analysis also require consideration;

1) Directional ambiguity
2) Measurement dynamic range
3) Velocity gradient limitations to spatial resolution.

As discussed in chapter 2, these fundamental limitations may all be relieved by implementation of cross-correlation. Recent practical developments for improving the PIV measurement process for in-cylinder flow measurement will now be discussed.

6.2 Practical Limitations

6.2.1 Limitations of Optical Access

In the present optical engine, the clear aperture of the piston crown window was insufficient to illuminate or view the complete cylinder width at the cylinder head without excessive light sheet divergence or wide angle lenses. A maximum sheet width of 57mm was permitted at the piston face, compared to the 84.45mm bore diameter. Although this optical access was sufficient to prove the value of in-cylinder PIV measurements, future optical engines would benefit from larger piston windows in relation to the cylinder bore. Enlargement of the piston window would be essential if details of near-wall flows become of interest.

Optical access for viewing vertical sheets is limited in the current engine by the lack of optical access above the cylinder head face. In order to gain partial access into the combustion chamber volume, it was necessary to place the camera lens centreline approximately half way down the cylinder axis. Therefore, the view of the flow adjacent to the piston crown became limited during the first half of the induction and power strokes and during the second half of the compression and exhaust strokes. This is because the piston face at these crank angles had moved above the camera lens centreline. Optical access for viewing vertical planes toward TDC crank angles was severely limited; only a thin slice of the flow field being visible. The value of PIV images is therefore restricted at these conditions, since knowledge and control of the flow conditions near TDC are vital for the ignition and combustion processes.

The situation could be improved significantly by introduction of an optical window into the side wall of the pent roof combustion chamber. This would require some careful engineering, since the combustion chamber wall has different radii of curvature in the horizontal and vertical planes and also contains cooling channels. However, the experience of others (see for example [6.1]) suggests that the insertion of flat or cylindrical windows in the combustion chamber wall for motored and fired studies is certainly possible and can enable detailed study of the ignition, flow and combustion processes without significantly compromising clearance space geometry or mechanical integrity. The introduction of such access in the PIV engine would enable the entire flow field, from the piston face to the apex of the pent roof, to be imaged. The details of the flow within the spark gap at the time of ignition would then be open to scrutiny and correlations of pre-combustion flow structure with the combustion parameters would be possible. An additional advantage of cylinder head optical access would be that the piston face would always be in view and could therefore be used to provide a consistent origin for the measurement co-ordinates.

A second limit to useful optical access into the combustion chamber was the presence of a band of seed material at the top of the piston stroke. This was left by the upper piston ring and caused two practical difficulties. The first of these was the introduction of striations into horizontal light sheets introduced close to the cylinder head face. The second was degradation of particle images when viewing through the fouled region. A practical solution to this problem is to reduce the total seed throughput during an experiment. This could be achieved by automating the PIV recording sequence and by introducing seed only immediately prior to each image recording. The latter could be achieved either using a continuous output atomiser with a diverter valve to block seed input to the inlet plenum, or by means of an atomiser with a pulsed output. If the seed density can be controlled automatically, the total seed throughput could potentially be reduced by one or two orders of magnitude. This would significantly reduce the engine down-time required for window cleaning operations.

6.2.2 Limitations of Optical Correction

The optical correction for imaging vertical planes within the engine cylinder, which was described in chapter 3, represents a significant advance for in-cylinder PIV measurements. However, the simple single-element solution used in this work limited the useful field of view to within typically 10-15mm of the cylinder walls. Together with optical access considerations, this would prevent the detailed investigation of near-wall flows. A more thorough treatment of the optical correction problem using finite ray tracing and multiple lens corrective systems is likely to achieve correction to within several millimeters of the cylinder walls, thereby making greater use of improved piston crown light sheet access. The use of more complex corrective systems would also give the potential for control of image distortion in addition to point aberrations, thereby simplifying calibration procedures for near-wall measurements. Investigation of the possibility of using alternative window materials of reduced thickness would also improve the off-axis aberrations of particle images.

6.2.3 Stray Illumination or "Flare"

In the PIV images, flare caused significant image noise due to film fogging and prevented measurements close to the combustion chamber walls. For example, it was not possible to visualise the high velocity near-wall flows known to exist during the induction stroke. Flare was minimised in the PIV experiments by blackening all metallic surfaces of the combustion chamber and by careful cleaning of the optical windows after every one or two engine runs. The use of careful camera focusing and optical correction minimised the laser pulse energy which was required to image the seed particles. Despite this care, flare still caused significant difficulties for measurements near TDC and whenever the inlet or exhaust valves were open. For pulse energies below approximately 50 mJ, the level of scattered light in the camera image plane as measured by the seed monitor was found to vary in direct proportion to the illuminating pulse energy. At higher energies, the flare increased at a greater rate due to laser-induced surface damage of the combustion chamber surfaces.

The use of sub-micron seeding particles was the prime reason for the high pulse energies used in this work. Seed particles of this size were chosen to provide compatibility with prior LDV measurement conditions and for accurate flow-following to turbulent frequencies of the order of 10-20 kHz. However, the velocity gradient considerations discussed in chapter 2 suggest that there is little need to achieve flow following of this accuracy, since the conventional PIV correlation techniques cannot reveal the smallest temporal and spatial flow scales which the particles are able to follow. Therefore, it should be possible to increase the particle size without compromising the overall frequency response of the velocimeter. The sensitivity of the Mie scattering coefficient to the particle diameter should ensure that large increases in scattered signal strength can be achieved with relatively small losses in flow following fidelity. This will enable the illumination pulse energy to be reduced proportionally, thus reducing the effects of flare.

Optimisation of the particle size should be carried out with reference to full Mie scattering theory, since large departures from the mean trend occur for particle sizes of the order of the wavelength of the illuminating radiation. In addition, the particle flow following behaviour should be modelled to investigate the size dependency of the frequency response as well as the effects of centrifugal forces in high tumble or high swirl flows.

As an example, the use of hollow spherical particles of 3μm diameter as described in [6.2] should allow similar flow-following fidelity to the smaller oil droplets used in this study, with an order of magnitude increase in the side scattered light intensity. Liquid oil droplets of 2.6μm diameter will give similar increases in the scattered intensity, with a reduction in the 99% fidelity flow following frequency to ~1kHz [6.3]. However, caution must be applied with regard to centrifugally induced radial particle motion in high rotation rate bulk flows, such as those encountered in high swirl Diesel engines.

An alternative approach to stray light rejection, using fluorescent seed droplets has also been demonstrated and the use of rare-earth doped glass particles for enhanced fluorescence yield has been suggested [6.4]. These techniques utilise the shift in the fluorescence wavelength of light scattered from seed particles to filter out the laser light scattered from test section surfaces. In addition, the effects of stray light may be further reduced at the PIV interrogation stage by morphological filtering of the digital interrogation region [6.5]. This method uses existing knowledge of the typical particle image properties to digitally suppress extraneous image noise caused by flare.

The digital approach to noise control has its greatest potential advantage in the case of digital PIV image recording. If the mean value of the background image intensity due to flare is sufficiently small, this may be subtracted from subsequent digital PIV recordings to give a reduced noise image of the seeded flow. Further work is required to investigate these numerous possibilities for flare rejection.

6.2.4 Image Recording and Interrogation Time

The time taken to record, process and interrogate photographic PIV images in this study effectively prevented the acquisition of ensemble averaged flow data. A small number of PIV images were recorded at each measurement condition to visually assess the effects of cycle to cycle variability in the large scale flow. For the large scale flow structure after IVC and before tumble breakdown, the flow structures showed little variation from one image to the next. However, during the later stages of compression the flow varied significantly in successive images. Therefore, ensemble-averaged data is required at these conditions if meaningful comparisons of PIV data with CFD simulations and ensemble averaged LDV data are to be made. This would require many PIV images to be recorded and interrogated at each flow condition.

With the present instrumentation, fifteen to thirty PIV images could be recorded from the engine in a 5-10 minute period. It then took approximately 2 hours to photographically process the images and to prepare them for interrogation. The interrogation time for an image recorded at a crank angle of 300 degrees after TDC from plane B-B was approximately 8 hours. A further 30 minutes was then required to validate each PIV image in the post processing procedure. Additional time was required to recondition the optical engine, adjust light sheets and camera positions for the various measurement planes and other practical tasks.

The PIV data presented in this thesis represents a total period of approximately eight weeks of data acquisition, preparation and analysis. The repetitive nature of much of the work makes such an endeavour unattractive for routine flow mapping and the timescales involved make routine ensemble-averaged studies unfeasible. Therefore, improvements in image recording and interrogation speed are desirable, if not essential if PIV is to find widespread acceptance in industrial engine research and development.

The major bottleneck in the measurement process was the interrogation time. Increased digital interrogation speed can be purchased in the form of faster digital processors or customised interrogation systems. For example, Meinhart *et al* have reported a custom digital PIV processor capable of interrogation rates over 1000 times faster than the hardware used in this study, with a similar FFT resolution [6.6]. The limiting step in that system was the rate of data transfer from a large format CCD array to the parallel digital processor. Still higher interrogation rates are potentially possible using optical correlation techniques [6.7], although practical high speed systems have yet to be demonstrated with realistic PIV images. It is important when comparing optical processing with digital processing to recognise that only the latter provides a simple and flexible means for the noise control which is required for improving valid data rates in demanding measurement applications.

The photographic image recording time could be reduced significantly by automation, as discussed in the previous section. This would also provide the potential for reducing window fouling and increasing the number of accumulated photographic images between engine cleaning operations. The high spatial resolution afforded by photographic recording is required for the study of large flow areas. However, the advent of large CCD arrays integrated with fast digital correlators will also enable large velocity data sets to be collected rapidly from relatively small fields [6.8]. For example, this will allow the flow field close to the spark plug at ignition to be correlated with combustion parameters for the fundamental study of flow-induced cyclic variability and other flow/flame interactions.

6.3 Limitations of Autocorrelation Interrogation

6.3.1 Directional Ambiguity

Double-exposed PIV recording and autocorrelation-based interrogation gives each velocity vector subject to a 180° directional ambiguity. Directional ambiguity was addressed in the current work only by assuming bulk flow directions from prior knowledge of the flow structure. Such a-priori knowledge will not necessarily be available in the case of new engine designs or in the measurement of small scale, non-deterministic flow structure during periods of high turbulence. This represents a restriction on the general applicability of PIV in the evaluation of new engine designs. Unresolved directional ambiguity also prevents the calculation of important quantities such as Barrel Swirl Ratios, strain rates and circulation.

Several techniques have been developed to resolve directional ambiguity. These may be divided into those which rely on autocorrelation analysis and those which require cross-correlation analysis. Cross-correlation methods have several additional advantages over autocorrelation methods and will be described separately in section 6.3.4 of this chapter. Autocorrelation-based techniques involve the introduction of a known and constant spatial shift in the position of the second exposure particle images relative to the recording medium. This technique is known as "image shifting". The magnitudes of the two components of the image shift are chosen to be larger than the most negative displacement vector components in the flow. The interrogation region therefore always contains a signal peak in the positive quadrant of the autocorrelation plane. The fixed image shift is then subtracted from the displacement vector of the positive signal peak to give the unambiguous, signed velocity vector. With this technique, the magnitude of the velocity dynamic range is halved in order to provide directional information.

Image shifting with photographic recording systems has been achieved in steady and periodic flows using a number of opto-mechanical and electro-optic methods. Electronic image shifting has also been demonstrated with CCD imaging systems [e.g. 6.9], but is presently limited to relatively low speed applications. The most conceptually simple shifting technique is rotating or oscillating mirror method first described by Adrian [6.10]. This uses the motion of a mirror placed at 45° to the camera optical axis to introduce the required image shift. The practical difficulties of accurately phase-locking the mirror motion to that of a high speed engine and synchronising the mirror position with the measurement crank angle makes this technique unsuitable for application to engine studies. The use of drum cameras for imaging shifting has been demonstrated, in which the film rotation provides the necessary image translation relative to the film [6.5]. This method reduces the synchronisation problems of rotating mirror methods when used with a high repetition rate laser. However, the use of drum cameras is less convenient than techniques using conventional photographic cameras in terms of experimental complexity and film handling.

Electro-optic image shifting techniques which overcome the synchronisation problems of moving mirror systems have been described by Landreth and Adrian [6.11] and Lourenco [6.12]. These rely on the use of double pulsed illumination in which the polarisation plane of the light is rotated through 90° between the two exposures. This is readily achieved with high pulse energy beams using commercial Pockels cells, which are capable of polarisation switching in as little as a few nanoseconds. However, the Mie scattering coefficient for side scattered light is known to be sensitive to particle size and the polarisation plane of incident light. Based on polarisation ratio predictions and measurements by Hodges *et al* [6.13], it appears fortuitously that the side-scattered intensity is approximately independent of the incident polarisation for spherical liquid droplets in the size range 0.5-5.0 μm. The polarisation sensitive techniques therefore appear suitable for engine applications.

6.3.2 Dynamic Range

As discussed in chapter 2, the measurement dynamic range using autocorrelation analysis is already limited typically to less than 10 in realistic PIV experiments. This is due to the presence of a broad self-correlation peak in the autocorrelation plane, which dictates the minimum displacement vector which can be measured. It should be noted that the further reduction in the dynamic range caused by the image-shifting methods of ambiguity resolution will be unacceptable for most in-cylinder flow measurement applications. The only practical means of expanding the measurement dynamic range is to eliminate the self-correlation peak by the application of cross-correlation analysis. This in turn requires the first and second particle image fields to be uniquely identified by some means. Various methods for achieving this will be described in section 6.3.4.

6.3.3 Velocity Gradients

The limitations of velocity gradients on the correlation process were discussed in chapter 2. The important limitation afflicting autocorrelation is the inverse relationship between the measurement dynamic range and the maximum tolerable velocity gradient within each interrogation region. In practical in-cylinder flows it is velocity gradient considerations which limit the effective spatial resolution of the measurements and hence the flow length scales which may be investigated.

In the measurements presented in this study, the smallest full scale flow reversal which could be resolved without significant data dropout at the high velocity end of the dynamic range was approximately 16.8mm. At crank angles close to TDC, the reduced clearance height produces full scale flow reversals of approximately half this diameter, with many smaller scale eddies appearing after TDC. Therefore, it appears that the autocorrelation technique is not appropriate when investigation of small scale structures is important. In many cases in the engine experiments, significant interpolation with detailed reference to the original PIV image was required to replace invalid data caused by velocity gradient dropout. This degree of manual intervention introduced an undesirable subjective element into the interrogation process. Further to this, the need for significant post-processing and interpolation negates the theoretical advantages of the correlation techniques over alternative particle tracking methods. Fortunately, cross-correlation interrogation provides a means of reducing the severe velocity gradient limitation of autocorrelation, while simultaneously improving signal to noise and solving the problem of directional ambiguity.

Cross-correlation of the initial and final particle images fields eliminates the central self-correlation peak. This allows the interrogation region size and pulse separation to be reduced without compromising the dynamic range. This reduces the variation in particle pair separations within each region and therefore reduces velocity gradient degradation of the signal peak. Lawson gives a theoretical dynamic range increase over autocorrelation of a factor of 18 for a cross-correlation experiment having the same interrogation region size and signal to noise ratio [6.14]. This increased dynamic range may be traded directly for improved velocity gradient tolerance, and hence spatial resolution, by reduction of the laser pulse separation. Therefore, the potential exists for simultaneously improving measurement dynamic range and velocity gradient tolerance if cross-correlation can be implemented in practice. This would permit full scale flow reversals at the integral length scale to be resolved in the PIV vector maps, raising the possibility of fundamental study of the details of flow/flame interactions.

Further improvements to the cross-correlation velocity gradient tolerance are possible using more sophisticated, if time-consuming, correlation techniques. Correlation methods with a higher degree of distortion invariance are receiving increased interest for whole field velocimetry as the limitations of conventional PIV become increasingly accepted. Huang *et al* [6.15] and Jambunathen *et al* [6.16] described novel methods for reducing velocity gradient data loss in cross correlation experiments. Their techniques rely on the digital distortion of one of the particle image fields based on an estimate of the velocity gradient in the region of data dropout. The distortion parameters are adjusted iteratively until the correlation coefficient of the initial particle image field with the distorted field converges to a pre-set threshold level. The mean velocity and estimates of the small scale velocity gradient can then be made from the location of the correlation peak and the distortion parameters used in the final iteration. Techniques such as this are computationally intensive, but may be essential for fully automated interrogation of highly turbulent flows which display high spatial velocity gradients.

6.3.4 Methods for Implementing Cross-Correlation

The benefits of cross-correlation over autocorrelation interrogation are numerous. In addition to directional ambiguity resolution, increased signal-to-noise ratio and improved dynamic range, further improvements in tolerance to out of plane motion and variations in seed density are offered. The possibility of reducing the laser pulse separation automatically restricts out of plane motion for a given laser sheet thickness, thereby improving data yield in regions of three dimensional flow. Cross-correlation also relieves the restriction of ensuring that more than two particle pairs are present in each interrogation region, and the number of spurious correlation peaks for a given particle image density is also reduced. Therefore, a wider range of seeding densities can be tolerated, so that close control of seed density is simplified during an experiment. This may prove important for fired flow studies in which the seed density ahead of and behind a flame front are affected by compression and expansion respectively. The improved tolerance to seed density variations may also permit the use of pulsed atomisers, thus reducing seed throughput and significantly reducing engine down-time. Cross-correlation therefore offers many important potential advantages over autocorrelation analysis.

A basic requirement for the implementation of cross-correlation is that the first and second particle image fields can be identified uniquely in the PIV recording. This may be achieved by one of three general methods; image shifting, image labelling or image separation. Recent developments in these areas will now be discussed briefly with regard to potential application to in-cylinder flow measurements.

6.3.4.1 Image shifting

In simple velocity fields where the changing flow direction may be tracked from one interrogation region to its neighbour using continuity criteria, cross correlation can be implemented on a double-exposed, image shifted recording [6.17]. The image shift may be introduced by any of the techniques given in section 6.3.1. The magnitude of the image shift must be sufficiently large to translate the second particle field such that the interrogation regions corresponding to the first and second exposures do not overlap. In other words, the shift should be at least the size of the initial interrogation region. The first and second areas may then be cross-correlated to give the unambiguous displacement vector. However, the approximate location of the second particle field must be estimated from neighbouring velocity measurements to avoid having to correlate very large regions which may contain many unpaired particles. In the case of flows giving a high degree of data dropout, or where there are many flow reversals, it may not be possible to predict the approximate location of the second particle image field. In such cases, the first and second particle image fields in a double exposure must be completely separated or uniquely labelled at the recording stage prior to cross-correlation.

6.3.4.2 Image separation

The first and second particle image fields can be completely separated at the recording stage by recording the PIV images with a high speed cine or drum camera. Successive exposures are then located on separate areas of the photographic film and may then be cross-correlated to give the unambiguous vector field. This technique has been demonstrated in velocity and flame speed measurements in a rapid compression combustion bomb [6.18].

Alternative image separation techniques can be envisaged which utilise colour or polarisation properties of scattered light to physically separate the two PIV images for recording on separate areas of photographic emulsion or electronic imaging arrays. However, with these methods, precise spatial registration of the two frames is required to avoid large errors in the velocity measurements. With electronic recording media the frame-to-frame registration of the first and second images is less of a problem. Using standard resolution video-rate CCD technology, frame intervals down to 20ms are possible. This has enabled, for example, low speed flows to be studied by cross-correlating successive frames in a video sequence [6.19]. However, much smaller frame intervals of the order of 5-50μs are required for typical engine flows. It is likely that custom-designed, large area frame-transfer CCD arrays with the necessary frame interval can be produced and will become commercially available in the near future.

6.3.4.3 Image labelling

Particle image labelling involves changing the appearance of the first and second particle images in a double-exposed recording so that they may be distinguished uniquely at the interrogation stage and subsequently cross-correlated. With these techniques, the problem of frame-to-frame registration is eliminated since both exposures are recorded on the same film, but care must be taken to minimise cross-talk between the two exposures and to ensure that the labelled images encounter identical optical paths through the imaging system. Certain image labelling techniques also offer the significant advantage of improved flow visualisation when compared to image-separated or image-shifted recordings. This could prove very useful for rapid qualitative evaluation of the in-cylinder flow prior to obtaining detailed quantitative data from the interrogation process.

Image labelling by polarisation [6.20], colour [6.21] and dual reference beam holographic recording [6.22] have been demonstrated to give potential for cross-correlation, although only the two colour method has been applied in engines to-date [6.23].

Reeves *et al* [6.20] demonstrated a method for labelling the first and second particle images in a double-exposed recording by means of a polarisation sensitive mask placed in the pupil plane of a conventional camera lens. This allowed the individual particle images to be ruled with a number of horizontal or vertical fringes according to the polarisation of the illuminating light and the details of the mask design. The images could then be separated by digital spatial filtering, or by optical filtering techniques described in earlier work [6.24]. However, aberrations introduced by the polarising element in the camera lens and the introduction of thick flat or curved optical windows in the imaging path restricted the diffraction limited field of view to a small region close to the optical axis. This rendered the technique unviable for engine studies, although it is possible that future optimisation of the system design could overcome this limitation.

With two-colour image labelling, chromatic aberrations may cause significant relative distortion of the two images. Any distortion will have to be calibrated and compensated for in the resulting vector field. Distortions due to the imaging lens can be minimised by illumination with similar wavelengths of laser light, although this may cause significant cross-talk between the two recorded images. The use of highly corrected achromatic lenses is essential in this technique, which has so far only been applied in test sections with flat walls. Further work is required to investigate the chromatic aberrations of typical optical engine cylinders and corrective optical elements. The application of two-colour labelling may therefore demand a more sophisticated solution to the optical correction problem.

Image labelling using holographic recording has the potential advantage that considerations of polarisation ratios and chromatic aberrations can be neglected. The use of image-plane holography with dual reference beams in orthogonal planes has been demonstrated as a proof of principle with large simulated particles [6.22]. Further work is required to investigate the practicality of applying this technique to realistic measurement situations using microscopic seed particles within typical engine flows.

6.4 Potential for Three-Dimensional Measurements

Previous discussion within this Thesis has related to the measurement of the two in-plane velocity components within planar measurement areas. However, future measurement needs may demand three component measurements within planar regions or even full 3-D volume measurements of three velocity components. The ability to measure three velocity components would allow a fuller interpretation of the flowfield from a single PIV recording. This could be invaluable in cases where optical access considerations prevent the measurement of a velocity component of interest using planar techniques. The provision of optical access is particularly difficult in compression-ignition engines due to their often complex piston bowl shapes and high compression ratio operation. In flat-top piston engines, measurement of full three-component velocity fields through the piston crown would potentially eliminate the requirement for imaging through cylindrical windows and therefore eliminate optical correction requirements. Although techniques for three-dimensional PIV measurements are typically not as mature as the simpler 2-D techniques, the prospects for such measurements will be discussed briefly.

6.4.1 Planar Measurements of Three Velocity Components

Two possible methods for estimating the out-of-plane velocity component from planar measurements are stereoscopic PIV and colour depth coding of the light sheet. The basic stereoscopic recording technique using two separate cameras is described by Adrian in [6.25] and an example of a stereoscopic PIV application using a single camera with a modified lens is given in reference [6.26]. In the basic stereoscopic technique, the planar measurement region is recorded from two different angles and the particle image displacements in corresponding regions of the separate recordings are used to calculate the three velocity components. Using this method, the perspective errors discussed in chapter 2 may be eliminated. However, the maximum permitted angle between the two views is limited by depth of field and aberration considerations and this typically gives a significantly reduced measurement accuracy for the out-of-plane velocity component. Even for small angles between the camera lens optical axis and the light sheet normal, significant aberrations will be introduced using flat engine windows and the use of simple optical correction for cylindrical windows may be entirely precluded. The need to accurately register the two separate frames with respect to each other is a further practical difficulty afflicting stereoscopic methods and the use of two separate camera lenses requires that the magnification and field distortion of both are identical.

A method of layering three light sheets of different colour in streak photography measurements was described by Kuwahara *et al* [6.27]. Analysis of the colour changes within individual streak tracks allowed the out-of-plane velocity component of each particle to be estimated. However, the colour recognition was only sufficient to give the sign of the out-of-plane component and a coarse estimate of its magnitude and it is unlikely that such a technique is viable for accurate determination of all three velocity components.

6.4.2 Three-Component Measurements within Extended Volumes

Stereoscopic methods using high depth of field imaging have been used in PTV studies of the full 3-D flow fields within water analogue engine cylinders, such as in reference [6.28]. The use of a large depth of field means that this technique offers relatively poor spatial resolution and that careful and lengthy calibration of the 3D object co-ordinates with respect to the planar image co-ordinates is necessary. Further to this, the use of small camera apertures requires that large seed particles are used, so that the technique may not be applied readily to gas flows.

Holographic imaging techniques offer the potential for large aperture, and hence high resolution, recording of three-dimensional particle distributions. As an approximation to full volume 3-D measurements, an apparatus was described by Hinsch *et al* which allowed the simultaneous holographic recording of several parallel planes at different locations within the flow field [6.29]. The three velocity components within each measurement plane could be estimated by selectively reconstructing each planar region and using conventional stereoscopic methods for evaluation of the three velocity components. However, this approach had the disadvantage of experimental complexity and it is unlikely that the necessary multitude of light sheets could be achieved within an engine cylinder without prohibitive levels of flare.

The approach of Barnhart *et al* [6.30] was to record holographically a full 3-D volume of a double-exposed particle image field. The flow volume was imaged stereoscopically, with dual reference beams to selectively reconstruct the first and second real images of each small interrogation volume. Phase conjugate image reconstruction allowed aberrations in the large aperture recording optics to be minimised, this technique also providing the possibility for aberration correction through cylindrical or other window geometries. The imaging and reconstruction arrangements allowed the first and second particle image fields to be cross-correlated for each of the two stereo channels, thus permitting the third velocity component to be estimated. The accuracy of the out-of-plane component was reported to be of similar magnitude to that of the in-plane components with this method. However, to achieve suitable interrogation times for the 400,000 individual interrogation volumes in the flow, a sophisticated parallel digital processor was required.

An alternative approach, described by Coupland and Halliwell [6.31], is to use conventional holographic recording of a flow volume followed by a novel all-optical autocorrelation or cross-correlation interrogation process. This approach has the potential for extremely rapid interrogation and preliminary investigation shows that the correlation technique is invariant to phase aberrations of low spatial frequency. The technique may therefore prove useful for measurements through cylindrical and other test sections, although further work is required to confirm the suitability of the technique in realistic measurement conditions.

6.5 Closure

The major limitations in the current work have been described and methods for necessary improvements to the experimental techniques have been explained with reference to recent advances in PIV technology. Further progress in in-cylinder PIV require that the optical access for viewing vertical planes near TDC is improved and that a more sensible compromise between particle scattering and flow following is made. The basis of this compromise should be to match the velocity gradient response of the particles to that of the interrogation process, instead of attempting to achieve accurate flow-following to the maximum turbulent frequency content of the flow. This approach will minimise flare for a given set of interrogation parameters. Detailed velocity measurements near the cylinder walls will require improved optical correction using refractive or holographic techniques, or increased piston-crown optical access.

Cross-correlation is essential for improvement of the velocity gradient sensitivity of the correlation process. The numerous advantages of cross correlation are well known. However, there is little consensus as to the best method for achieving in practice the necessary image separation or labelling and further work is required in this area.

The prospects for future three-dimensional velocity measurements in engines has been discussed briefly. Much further work is required in this area to investigate the various options for full and partial 3-D measurements in realistic engine experiments.

CHAPTER 7

CONCLUSIONS AND SUGGESTIONS FOR FUTURE WORK

7.1 Conclusions

Particle Image Velocimetry has been applied to the study of in-cylinder fluid motion within a four-valve, production geometry optical SI engine displaying barrel swirl. In contrast to previous work, velocity measurements of high spatial resolution have been made in both horizontal and vertical planes within the engine's optical cylinder.

A review of the important in-cylinder flow processes in engines of this type has been given to provide the practical context for the requirement for whole field in-cylinder velocity measurements. The important experimental parameters involved in the optimisation of PIV experiments using autocorrelation interrogation have also been discussed with reference to previous studies. The major theoretical limitations for autocorrelation analysis are the restricted maximum velocity dynamic range, limited signal-to-noise ratio, out-of-plane particle motion and poor velocity gradient tolerance. Given these restrictions, there is little margin for error in the optimisation of an autocorrelation PIV experiment and significant data dropout can be expected in applications to turbulent, reversing and three-dimensional in-cylinder flows. In practice, flare from stray illumination is an additional source of significant data loss. The successful application of autocorrelation PIV therefore demands close control of all of the optimisation parameters.

A significant advance in this work has been the development of a simple method for achieving optical correction of astigmatism when recording particle images through the thick wall of the optical engine cylinder. The technique uses an inexpensive meniscus cylindrical lens to achieve coincidence of the meridional and sagittal virtual foci within the engine cylinder. This allowed near diffraction-limited particle images to be formed for regions close to the optical axis, the off-axis performance being sufficient to permit velocity measurements to within 10-15mm of the cylinder walls.

A complete PIV engine facility has been described, which features some valuable techniques for ensuring rapid and reliable acquisition of PIV images from the engine. This included methods for precise laser synchronisation to the engine crank position and the use of datum plates for alignment of laser light sheets within the engine cylinder. On-line monitoring of seed density using a photodetector in the camera's image plane was used to adjust the seeding to a level appropriate to the compression factor at the measurement crank angle. Precise camera focusing was achieved using a CCD microscope and this was found essential for optimising the corrective optic and camera lenses to achieve the best particle image characteristics over the whole field of view.

A set of motored PIV images and measurements from three measurement planes within the engine have been presented. The flow structures revealed in the motored PIV measurements were in good qualitative and quantitative agreement with other studies performed in similar engine geometries. Motored flow measurements were performed for two inlet configurations producing a low and high Barrel Swirl Ratio (BSR). The major conclusions regarding the evolution of the motored in-cylinder flow may be summarised as follows;

1) The induction process was characterised by the formation of counter-rotating vortices. The relative strength of the vortices was determined by the inlet configuration and dictated the net angular momentum of the flow at IVC.

2) During the early stages of compression, the flow was characterised by a high momentum "swirl tongue" of gas which circulated throughout the cylinder volume. The flow was more two-dimensional and was closer to a simple solid body rotation for the high BSR configuration.

3) The evolution of the flow structure close to the piston face was dependent on the relative values of the gas velocities and the instantaneous piston speed.

4) For the high BSR case, the barrel vortex displayed a tendency to "spin-up" part way through the compression stroke due to partial conservation of angular momentum.

5) The barrel vortex was preserved to a late stage in compression for the high BSR case. There was also evidence of remaining large scale motion in the early stages of the power stroke in the case of motored flow with the firing inlet configuration.

6) High velocity bulk flows in the vicinity of the spark electrode were formed at the ignition crank angle. Velocities were significantly higher for the high BSR configuration.

Dynamic PIV-based BSR values averaged over the two measurement planes were in close agreement with the steady flow values derived from impulse swirl meter measurements. However, quantitative comparisons with LDV-based Tumble Vortex Ratios agreed less closely. This indicates that caution may be required in attempting to characterise the in-cylinder flow using a limited number of point measurements.

The agreement of preliminary CFD predictions with the PIV measurements for crank angles during the early stages of compression was encouraging. However, the details of the flow fields after modification by piston motion and compression in the later half of the compression stroke were less well reproduced. It is possible that improved initial and boundary conditions for the CFD models are required, with particular regard to the flow details in the inlet port and valve curtain.

Preliminary PIV experiments under fired conditions have proved the suitability of the engine design and the PIV technique for part-throttle fired studies using propane. This gives confidence for the application of PIV to routine combustion studies in future work. The pre-flame flow field was significantly modified by flame expansion. The flow ahead of the flame front displayed little small scale structure and typical velocities were two to three times those in the motored case at the same crank angle.

Motored PIV measurements can certainly provide valuable data for CFD validation and for characterising the flow conditions affecting flame initiation and early growth of the flame kernel. However, while the flow conditions in the early stages of combustion are known to be crucial with regard to cyclic variability, only a small fraction of the fuel mass is burnt during this period. Therefore, the routine application of PIV under fired conditions will be essential if the combustion-modified flow field, which affects the majority of the combustion process, is to be studied.

7.2 Suggestions for Future Work

The experimental developments and flow measurements presented in this work represent a significant advance for the practical application of in-cylinder whole-field velocimetry.

During the course of this work, a variety of different experimental problems had to be overcome in order to proceed with the program of flow measurements requested by the industrial sponsor. There is significant scope for future work in improving further the experimental technique and in new applications of PIV to the study of in-cylinder flow processes.

The problem of window fouling by seed material was a significant problem and could be addressed by investigating possibilities for pulsed atomisation and by improving the rate of image acquisition through automation of the measurement process. Problems of flare could be reduced using larger seed particles, whose size should be chosen according to the frequency response of the velocimeter as opposed to the maximum turbulent frequency in the flow. The optimisation of the seed properties would require detailed modelling of particle scattering and flow-following characteristics.

Further progress in the study of flows in vertical planes near TDC require improvements to the optical access for viewing into the combustion chamber. The problem of achieving a consistent datum within the measurement plane should also be addressed.

Detailed velocity measurements near the cylinder walls will require improved optical correction using refractive or holographic techniques, or increased piston-crown optical access. The off-axis performance of the refractive optical correction used in this study would benefit from a systematic finite ray tracing design optimisation, which would typically require a multiple optical element solution. The use of cylindrical field flatteners and alternative window materials and thicknesses should be investigated in this process.

Cross-correlation is essential for improvement of the velocity gradient sensitivity of the interrogation process. The numerous advantages of cross correlation over autocorrelation analysis are now well known. Given the quality of data which has been achieved with careful application of conventional autocorrelation PIV, the application of cross-correlation will significantly ease experimental optimisation and improve measurement confidence. However, there is at present little consensus as to the best method for achieving in practice the necessary image separation or labelling and further work is required in this important area. Consideration should also be given to alternative correlation techniques which offer improved tolerance to velocity gradients and the potential for direct estimation of small scale gradients.

The potential for three-dimensional velocity measurements in engines should be investigated with regard to stereoscopic and holographic techniques. Much further work is required in this area to investigate the various options for full and partial 3-D measurements in realistic engine experiments. It is possible that all-optical correlation of holographic PIV recordings may provide an alternative means for achieving aberration-invariant correlation without recourse to refractive optical correction or phase conjugate imaging.

The ability to study quantitatively the details of complex in-cylinder flows presents a variety of opportunities for future studies. For studies of cyclic variability, statistically significant data sets will be required and the rates of data acquisition and interrogation will have to be increased appropriately. The advent of increasingly large electronic imaging arrays with built-in image shifting or image separation facilities, together with fast digital correlators will provide an efficient means for rapid data collection required in such studies. However, the present area-bandwidth product of electronic devices when compared to photographic emulsion, limits their application to the study of relatively small areas of flow.

The proven ability to measure velocities ahead of a propagating flame front will enable the fundamental study of the interactions between flow and flame in SI engines. Of particular interest is the effect of the bulk and small scale flow structure at the spark location on the initiation of combustion. Studies of this nature will require the simultaneous application of a number of in-cylinder optical and classical flow and combustion diagnostics and this will present interesting challenges for experimental design. Further PIV applications of interest to general IC engine research are the study in-cylinder flows in two-stroke and compression-ignition engines, in which the details of bulk motion are equally crucial to engine operation.

REFERENCES

CHAPTER 1

1.1 Heywood, J.B., "Fluid Motion Within the Cylinder of Internal Combustion Engines-The 1986 Freeman Scholar Lecture", Journal of Fluids Engineering, March 1987 vol 109 pp3-35.

1.2 Arcoumanis, C., "Fluid mechanics of internal combustion engines-a review", Proc Inst. Mech. Engrs. vol 201 No C1, 1987.

1.3 Arcoumanis, C., Hu, Z., Vafidis, C., Whitelaw, J.H., "Tumbling Motion: A Mechanism for Turbulence Enhancement in Spark-Ignition Engines", SAE paper #900060, 1990.

1.4 Endres, H., Schulte, H., Krebs, R., "Combustion System Development Trends for Multi-Valve Gasoline Engines", SAE paper # 900652, 1990.

1.5 Mikulik, L.A., Quissek, F., Fraidl, G.K., "Development of Low Emission High Performance Four Valve Engines" SAE paper # 900227, 1990.

1.6 "Combustion Effects of Asymmetric Valve Strategies", Automotive Engineering, pp49-53, Dec 1993.

1.7 "Mazda's Lean Burn Catalyst", Automotive Engineering, pp49-51, Dec 1994.

1.8 Benjamin, S.F., "The development of the GTL 'barrel swirl' combustion system with application to four-valve spark ignition engines", IMechE C54/88, 1988.

1.9 Omori, S., Iwachido, K., Motomochi, M., Hirako, O., "Effect of Intake Port Flow Pattern on the In-Cylinder Tumbling Air Flow in Multi-Valve SI Engines", SAE paper # 910477, 1991.

1.10 Inoue, T., Igushi, S., Yamada, Y., Furuno, S., "In-Cylinder Gas Motion, Mixture Formation and Combustion of 4 Valve Lean Burn Engine" 9th Int Vienna Motor Symposium, 1998.

1.11 Kiyota, Y., Akashino, K, Ando, H., "Concept of Lean Combustion by Barrel-Stratification", SAE paper # 920678, 1992.

1.12 Baritaud, T.A., "Optical and Numerical Diagnostics for SI Engine Combustion Studies", COMODIA 94 Int. Symp., Yokohama, Japan, July 1994.

1.13 Kuwahara, K., Watanabe, T., Takemura, J., Omori, S., Kume, T., Ando, H., "Optimisation of In-Cylinder Flow and Mixing for a Centre-Spark Four-Valve Engine Employing the Concept of Barrel-Stratification", SAE paper # 940986, Detroit, 1994.

1.14 Bradley, D., Sheppard, C.G.W., "Limitations to turbulence enhanced burning rates in lean burn engines", IMechE C46/88, 1988.

1.15 Parsi, M., Daneshyar, H., "Measurements of the Three-Dimensional Turbulent flow in the Cylinder of an I.C.Engine", in 'Instrumentation for Combustion and Flow in Engines', Durao, D.F.G et al (eds), pp 377-390,1989.

1.16 Kyriakides, S.C., Glover, A.R., "A study of the correlation between in-cylinder air motion and combustion in gasoline engines", IMechE C55/88, 1988.

1.17 Arcoumanis, C., "Application of Laser Anemometry and Raleigh Scattering to Engine Flows", in 'Instrumentation for Combustion and Flow in Engines', D.G.Durao et al (eds), pp 235-253, 1989.

1.18 Shack, D.H., Reynolds, W.C., "Application of Particle Tracking Velocimetry to the Cyclic Variability of the Pre-Combustion Flow Field in a Motored Axisymmetric Engine", SAE Trans., vol 100(3), paper # 910475, 1991.

1.19 Ronnback, M., Le, W.X., Linna, J-R., "Study of Induction Tumble by Particle Tracking Velocimetry in a 4-Valve Engine", SAE paper # 912376, 1991.

1.20 Reuss, D.L., Adrian, R.J., Landreth, C.C., French, D.T., Fansler, T.D., "Instantaneous Planar Measurements of Velocity and Large-Scale Vorticity and Strain Rate in an Engine Using Particle Image Velocimetry", SAE paper # 890616, 1989.

1.21 Nino, E., Gadjeczko, B.F., Felton, P.G., "Two-Color Particle Image Velocimetry in an Engine With Combustion", SAE paper # 930872, 1993.

1.22 Reeves, M., Garner, C.P., Dent, J.C., Halliwell, N.A.H., "Particle Image Velocimetry Measurements of Barrel Swirl in a Production Geometry Optical IC Engine", SAE paper # 940281, 1994.

1.23 Adrian, R.J., "Particle Imaging Techniques For Experimental Fluid Mechanics", Annual Review of Fluid Mechanics, 23, pp261-304, 1991.

1.24 Zhang, L., Ueda, T., Takatsuki, T., Yokota, K., "A Study of the Cycle-to Cycle Variation of In-Cylinder Flow on a Motored Engine", COMODIA 94 Int. Symp., Yokohama, Japan, July 1994.

1.25 Weller, H.G., Uslu, S., Gosman, A.D., Maly, R.R., Herweg, R., Heel, B., "Prediction of Combustion in Homogeneous-Charge Spark-Ignition Engines", Int. Symposium COMODIA 94, Yokohama, Japan, pp163-169, 1994.

1.26 Khalighi, B., Huebler, M.S., "A Transient Water Analog of a Dual-Intake-Valve Engine for Intake Flow Visualisation and Full-Field Velocity Measurements", SAE paper # 880519, 1988.

1.27 Kent, J.C., Mikulec, A., Rimai, L., Adamczyk, A.A., Mueller, S.R., Stein, R.A., Warren, C.C., "Observations on the Effects of Intake-Generated Swirl and Tumble on Combustion Duration", SAE paper # 892096, 1989.

1.28 Clerk, D., "Cylinder Actions in Gas and Gasoline Engines", SAE Journal vol 8, p 523, 1921

1.29 Lee D.W., "A Study of Air Flow in an Engine Cylinder", NACA report no 653, 1939.

1.30 Alcock, J.F., "Air Swirl in Oil Engines", Proc. Instn. Mech. Engrs, 24, p645, 1930.

1.31 Chapman, J., Garrett, M.W., Warburton, A., "A New Standard for Barrel Swirl Movement", IMechE c427/18/156

1.32 Johnston, S.C., Robinson, C.W., Rorke, W.S., Smith, J.R., Witze, P.O., "Application of Laser Diagnostics to an Injected Engine", SAE paper # 790092, 1979.

1.33 Maly, R., "Ignition Model for Spark Discharges and the Early Phase of Flame Front Growth", Proc. 18th Int. Symp. on Comb., pp 1747-1754, The Combustion Institute, 1981.

1.34 Gatowski, J.A., Heywood, J.B., Deleplace, C., "Flame Photographs in a Spark-Ignition Engine", Combust. Flame, vol 56, pp71-81, 1984.

1.35 Namazian, M., Hansen, S.P., Lyford-Pike, E.J., Sanchez-Barsse, J., Heywood, J.B., Rife, J., "Schlieren Visualisation of the Flow and Density Fields in the Cylinder of a Spark-Ignition Engine", SAE Trans, vol 89, paper # 800044, 1980.

1.36 Namazian, M., Heywood, J.B., "Flow in the Piston-Cylinder-Ring Crevices of a Spark Ignition Engine: Effect on Hydrocarbon Emissions, Efficiency and Power", SAE Trans., vol 91, paper # 820088,1982.

1.37 Huber, E.W., Stock, D., Pischinger, F., "Investigation of Mixture Formation and Combustion in a Diesel Engine with the Aid of the Schlieren Method", CIMAC 9th Int. Congress on Combustion Engines, Sweden, 1971.

1.38 Fujikawa, T., Ozasa,T., Kosuka, K., "Development of Transparent Cylinder Engines for Schlieren Observation", SAE paper # 881632, 1988.

1.39 Semenov, E.S., "Device for Measuring the Turbulence in Piston Engines", Instruments and Experimental Techniques, Vol 1, No 1, 1958.

1.40 Melling, A., Whitelaw, J.H., "Design of Laser Doppler Anemometers for Reciprocating Engines", Report No., CHT/76/6, Imperial College of Science and Technology, London, Nov 1976.

1.41 Witze, P.O., "A Critical Comparison of Hot-Wire Anemometry and Laser Doppler Velocimetry for I.C. Engine Applications", SAE paper # 800132, 1980.

1.42 Bicen, A.F., Vafidis, C., Whitelaw, J.H., "Steady and Unsteady Airflow Through the Intake Valve of a Reciprocating Engine", Trans. ASME, J.Fluids Eng., vol 107, p 413, 1985.

1.43 Tindal, M.J., Cheung, R.S., Yianneskis, M., "Velocity Characteristics of Steady Flows through Engine Inlet Ports and Cylinders", SAE paper # 880383, 1988.

1.44 Williams, T.J., Tindal, M.J., "Cylinder Gas Flow and Combustion in Compression Ignition Engines", IMechE conf on Combustion in Engines, Cranfield Inst. Tech., C84/75, 1975.

1.45 Arcoumanis, C., Hu, Z., Whitelaw, J.H., "Steady Flow Characterisation of Tumble-Generating Four-Valve Cylinder Heads", Proc. Instn. Mech. Engrs, Journal of Automobile Engineering, Vol 207, pp203-210, 1993.

1.46 Hu, Z., Vafidis, C., Whitelaw, J.H., Chapman, J., Head, R., "Correlation Between In-Cylinder Flow, Performance and Emissions Characteristics of a Rover Pentroof Four-Valve Engine", IMechE, c488/026, p 157, 1992.

1.47 Wigley, Patterson and Renshaw, "Swirl Velocity Measurements in a Firing Production Diesel Engine", Fluid Mechanics of Combustion Systems (ed T. Morel, R.P. Lohman, J.M. Rackley), ASME 1981.

1.48 Witze, P.O., Martin, J.K., Borgnakke, C., "Measurements and Predictions of the Precombustion Fluid Motion and Combustion Rates in a Spark Ignition Engine", SAE paper # 831697, 1983.

1.49 Witze, P.O, "Velocity Measurements in the End-Gas Region during Homogeneous-Charge Combustion in a Spark Ignition Engine", th Int Symp on App. of Laser Tech to Fluid Mech., Lisbon, 1990.

1.50 Margary, R., Nino, E., Vafidis, C., "LDA Measurements of the Flow Field and Flame Visualisation Inside an Internal Combustion Engine", Paper 905053, Proc 18th FISITA Congress, Turin, Italy, May1990, pp383-394.

1.51 Tabaczyinski, R.J., "Turbulence Measurements and Modelling in Reciprocating Engines-an Overview", IMechE C51/83.

1.52 Liou, T-M., Hall, M., Santavicca, D.A., Bracco, F.V., "Laser Doppler Velocimetry Measurements in Valved and Ported Engines" SAE paper # 840375, 1984.

1.53 Enotiades, A.C., Vafidis, C., Whitelaw, J.H., "Interpretation of Cyclic Flow Variations in Motored Internal Combustion Engines", Experiments in Fluids, 10, 77-86, 1990.

1.54 Hall, M.J., Bracco, F.V., Santavicca, D.A., "Cycle-Resolved Velocity and Turbulence Measurements in an IC Engine With Combustion", SAE paper # 860320, 1986.

1.55 Glover, A.R., Hundleby, G.E., Hadded, O., "The Development of Scanning LDA for the Measurement of Turbulence in Engines", SAE paper # 880378, 1988.

1.56 Bates, S.C., "A Transparent Engine For Flow and Combustion Visualisation Studies", SAE paper # 880520, 1988.

1.57 Trigui, N., Affes, H., Kent, J.C., "Use of Experimentally Measured In-Cylinder Flow Field Data at IVC as Initial Conditions to CFD Simulations of Compression Stroke in I.C. Engines-A Feasibility Study", SAE paper # 940280, 1994.

1.58 Khalighi, B., "Intake-Generated Swirl and Tumble Motions in a 4-Valve Engine with Various Intake Configurations- Flow Visualisation and Particle Tracking Velocimetry", SAE paper # 900059, 1990.

1.59 Haghgooie ,M., Kent, J.C., Tabaczynski, R.J., "Verification of LDA and Seed Generator Performance", Experiments in Fluids, 4, pp27-32, 1986.

1.60 Reuss, D.L., Bardsley, M., Felton, P.G., Landreth, C.C., Adrian, R.J., "Velocity, Vorticity, and Strain-Rate Ahead of a Flame Measured in an Engine Using Particle Image Velocimetry", SAE paper # 900053, 1990.

1.61 Armstrong, N.W.H., "Planar Flowfield Measurements in Premixed Turbulent Combustion", PhD Thesis, Cambridge University, Aug 1992.

1.62 Stolz, W., Kohler, J., Lawrenz, W., Meier, F., Bloss, W.H., Maly, R.R., Herweg, R., Zahn, M., "Cycle Resolved Flow Field Measurements using a PIV Movie Technique in a SI engine", SAE Int. Fuels and Lubricants Meeting and Exposition, San Fransisco, paper # 922354, Oct 1992.

1.63 Lecordier, B., Mouquillard, M., Trinite, M., "Simultaneous 2D Measurements of Flame Front Propagation by High Speed Tomography and Velocity Field by Cross-Correlation", Proc. of 8th Int. Symp. on App. of Las. Tech. to Fluid Mech., Lisbon, Portugal, July 1994.

1.64 Bone, W.A., Townend, D.T.A., "Flame and Combustion in Gases", 1927, Longmans, London, 1927.

1.65 Keck, J.C., "Turbulent Flame Structure and Speed in Spark-Ignition Engines", Proc. 19th Int Symp on Combustion, The Combustion Institute, pp 1451-1466, 1982.

1.66 Bouchard, C.L., Taylor, C.F., Taylor, E.S., "Variables Affecting Flame Speed", SAE J., vol 41, No 5. Nov 1937.

1.67 Semenov, E.S., "Studies of Turbulent Gas Flow in Piston Engines", Otdelenie Tekhnicheskikh Nauk, No. 8., NASA Technical Translation F97,1958.

1.68 Tabaczynski, R.J., "Turbulence and Turbulent Combustion in Spark-Ignition Engines", Prog. Energy Combust. Sci., Vol 2 pp 143-165, 1976.

1.69 Lancaster, D.R., Krieger, R.B., Sorenson, S.C., Hull, W.L., "Effects of Turbulence on Spark-Ignition Engine Combustion", SAE paper # 760160, 1976.

1.70 Witze, P.O., "Mesaurements of the Spatial Distribution and Engine Speed Dependence of Turbulent Air Motion in an I.C. Engine", SAE paper # 770220, 1977.

1.71 Mattavi, J.N., "Effects of Combustion Chamber Design on Combustion in Spark Ignition Engines", SAE paper # 821578, 1982.

1.72 Hayder, M.E., Varma, A.K., Bracco, F.V., "A Limit to TDC Turbulence Intensity in Internal Combustion Engines", AIAA Journal of Propulsion and Power, vol 1 part 4, pp300-308, 1985.

1.73 Gosman, A.D., Tsui, Y.Y., Vafidis, C., "Flow in a Model Engine with a Shrouded Valve- A Combined Experimental and Computational Study", SAE paper # 850498, 1985.

1.74 Vafidis,C., Vorropoulos, G., Whitelaw, J.H., "Effects of Intake Port and Combustion Chamber on In-Cylinder Turbulence in a Motored Reciprocating Engine", Fluid Flow and Heat Transfer in Reciprocating Machinery, eds T Morel et al , ASME FED vol 62, 1987.

1.75 Benjamin, S.F., "A Phenomenological Model for 'Barrel' Swirl in Reciprocating Engines", Proc. Inst. Mech. Engrs., Journal of Automobile Engineering, vol 206, pp 63-71, 1991.

1.76 Hadded, O., Denbratt, I., "Turbulence Characteristics of Tumbling Air Motion in Four-Valve S.I. Engines and their Correlation with Combustion Parameters", SAE paper # 9104780, 1991.

1.77 Chapman, J., Draper, A., Fairhead, G.S., Wallace, S., "Optimisation of Combustion Chamber Design", IMechE, C382/030, 1989.

1.78 Ando, H., Sanbayashi, D., Kuwahara, K., Iwachido, K., "Characteristics of Turbulence Generated by Tumble and its Effects on Combustion", COMODIA 90 Int. Symp., p443, Japan, 1990 .

1.79 Furuno, S., Iguchi, S., Oishi, K., Inoue, T., "The Effects of 'Inclination Angle of Swirl Axis' on Turbulence Characteristics in a 4-VAlve Lean-Burn Engine with SCV", SAE paper # 902139, 1990.

1.80 Robinson, S., Blunsdon, C.A., Dent, J.C., Garner, C.P., "Charge coupled device camera/computer analysis of flame propagation in a spark ignition engine, and some comparisons with a computational fluid dynamic model", IMechE C430/066, 1991.

1.81 Hu, Z., "Turbulence Enhancement in Spark-Ignition Engines", PhD Thesis, Imperial College of Science, Technology and Medicine, London, Feb1992.

1.82 Kuwahara, K., Kawai, T., Ando, H., "Influence of Flow Field Structure after the Distortion of Tumble on Lean-Burn Flame Structure", COMODIA 94 Int. Symp., Yokohama, Japan, 1994.

1.83 Bianco, Y., Cheng, W.K., Heywood, J.B., "The Effects of Initial Flame Kernel Conditions on Flame Development in SI Engine", SAE paper # 912402, 1991.

1.84 Torres, A., Henriot, S., "3D Modelling of Combustion in Lean Burn Four-Valve Engines: Influence of Intake Configuration", COMODIA 94 Int. Symp., Yokohama, Japan, 1994.

1.85 Henriot, S., Le Coz, J-F., Pinchon, P., "Three Dimensional Modelling of Flow and Turbulence in a Four-Valve Spark Ignition Engine - Comparison with LDV Measurements", SAE paper # 890843, 1989.

1.86 Haworth, D.C., El Tahry, S.H., Huebler, M.S., Chang, S., "Multidimensional Port- and-Cylinder Flow Calculations for Two- and Four-Valve-Per-Cylinder Engines: Influence of Intake Configuration on Flow Structure", SAE paper # 9000257, 1990.

1.87 Le Coz, J-F., Henriot, S., Pinchon, P., "An Experimental and Computational Analysis of the Flow Field in a Four-Valve Spark Ignition Engine-Focus on Cycle-Resolved Turbulence", SAE paper # 900056, 1956.

1.88 Tatschl, R., Wieser, K., Reitbauer, R., "Multidimensional Simulation of Flow Evolution, Mixture Preparation and Combustion in a 4-Valve SI Engine", Proc of Int Symposium COMODIA 94, Yokohama, Japan, 1994.

CHAPTER 2

2.1 Burch, J.M., Tokarski, J.M.J, "Production of Multiple Beam Fringes from Photographic Scatterers", Optica Acta 15(2) pp101-111, 1968.

2.2 Barker, D.B., Fourney, M.E., "Displacement Measurements in the Interior of 3-D Bodies Using Scattered Light Speckle Interferometry", The Engineering Uses of Coherent Optics: Proc. of Conf. Held at the University of Strathclyde, April 1975, ed. E.R. Robertson, Cambridge University Press, pp 249-262, 1976.

2.3 Dudderar, T.D., Simpkins, P.G., "Laser Speckle Photography in a Fluid Medium", Nature, 270, pp45-47, 1977.

2.4 Grousson, R., Mallick, S., "Study of Flow Pattern in a Fluid by Scattered Laser Light" Applied Optics 16 (9) pp 2334-2336, 1977.

2.5 Barker, D.B., Fourney, M.E., "Measuring Fluid Velocities with Speckle Patterns", Experimental Mechanics 16 (6), pp209-214, 1977.

2.6 Meynart, R., "Instantaneous Velocity Field Measurements in Unsteady Gas Flow by Speckle Velocimetry", Applied Optics, 22 (4), pp 535-540, 1983.

2.7 Pickering, C.J.D., Halliwell, N.A.H.,"Speckle Photography in Fluid Flows: Signal Recovery with Two-Step Processing, Applied Optics 23(8), pp1128-1129, 1984.

2.8 Adrian, R.J., "Scattering Particle Characteristics and Their Effect on Pulsed Laser Measurements of Fluid Flow: Speckle Velocimetry vs. Particle Image Velocimetry", Applied Optics, 23, pp1690-1691, 1984.

2.9 Huntley, J.M., "Speckle Photography Fringe Analysis: Assessment of Current Algorithms", Applied Optics, 28(20), 1989.

2.10 Mao, Z.Q., Halliwell, N.A.H, Coupland, J.M., "Particle Image Velocimetry: High-Speed Transparency Scanning and Correlation-Peak Location in Optical Processing Systems", Applied Optics 32(26) pp5089-5091, 1993.

2.11 Farrell, P.V., "Optical Evaluation Methods in Particle Image Velocimetry", Optics and Lasers in Engineering, 17, pp 187-207, 1992.

2.12 Meinhart, C.D., Prasad, A.K., Adrian, R.J., "Parallel Digital Processor System for Particle Image Velocimetry", 6th Int Conf on Applications of LAser Technology to Fluid Mechanics, Lisbon, Portugal, 1992.

2.13 Adrian, R.J., "Particle-Imaging Techniques for Experimental Fluid Mechanics", Annual Review of Fluid Mechanics, 23, pp 261-304, 1991.

2.14 Hinsch, K.D., "Particle Image Velocimetry", in 'Speckle Metrology', ed., Rajpal S. Sirohi, Marcel Dekker, Inc., pp 235-324,1993.

2.15 Lourenco, L.M., "Particle Image Velocimetry: Photographic and Video Techniques", Von Karman Institute Lecture Series-Laser Velocimetry, Rhode Saint Genese, Belgium, June 1991.

2.16 Willert, C.E., Gharib, M., "Digital Particle Image Velocimetry", Experiments in Fluids, 10, pp181-193, 1991.

2.17 Westerweel, J., Nieuwstadt, F.T.M., "Measurement of Dynamics of Coherent Flow Structures using Particle Image Velocimetry" Proc. 5th Int. Symp. on Applications of Laser Anemometry to Fluid Mechanics, Lisbon, Portugal, 1990.

2.18 Lourenco, L.M., Gogineni, S.P., LaSalle, R.T., "On-Line Particle-Image Velocimeter: an Integrated Approach", Applied Optics, 33(13), pp 2465-2470,1994.

2.19 Lawson, N.J., "The Application of Particle Image Velocimetry to High Speed Flows", PhD Thesis, Loughborough University of Technology, March 1995.

2.20 Adrian, R.J., "Statistical Properties of Particle Image Velocimetry Measurements in Turbulent Flow" in *'Laser Anemometry in Fluid Mechanics'* Vol III, Ladoan Institute Superior Tecnico, Lisbon, Portugal, pp115-129, 1988.

2.21 Keane, R.D., Adrian, R.J., "Optimisation of Particle Image Velocimeters. Part 1: Double Pulsed Systems", Meas. Sci. Tech., 1, pp 1202-1215, 1990.

2.22 Prasad, A.K., "Effect of Resolution on the Speed and Accuracy of Particle Image Velocimetry Interrogation", Experiments in Fluids, 13, pp 105-116, 1992.

2.23 Adrian, R.J., "Image Shifting to Resolve Directional Ambiguity in Double-Pulsed Velocimetry", Applied Optics, vol 25, No 21, pp 3855-3856, 1986.

2.24 Keane, R.D., Adrian, R.J., "Theory of Cross-Correlation Analysis of PIV Images", Applied Scientific Research, 49, Kluwer Academic Publishers, pp 191-215, 1992.

2.25 Goss, L.P., Post, M.E., Trump, D.D., Sarka, B., "Two-Color Particle Velocimetry", Proc. ICALEO vol 68, pp 101-111, 1989.

2.26 Reeves, M., Lawson, N.J., Halliwell, N.A., Coupland, J.M., "Particle Image Velocimetry: Image Labelling by Encoding of the Point Spread Function by Application of a Polarisation-Sensitive Pupil-Mask", Applied Optics, 34, No 1,1995.

2.27 Sanbayashi, D., Ando, H., Kumagai, H., "Feasibility of using Several Powder Materials as the Seeding Particle or LDV Measurement", JSAE Review, vol 12, No 2, April 1991.

2.28 Kuwahara, K., Ando, H., "TDC Flow Field Structure of Two-Intake-Valve Engines with Pentroof Combustion Chamber", JSME International Journal, Series B, vol 36, No 4, 1993.

2.29 Haghooie, M., Kent, J.C., Tabaczynski, R.J., "Verification of LDA and Seed Generator Performance", Experiments in Fluids, 4, pp 27-32,1986.

2.30 Durst, F., Melling, A., Whitelaw, J.H., "Principles and Practice of Laser Doppler Anemometry", Academic Press, 1981.

2.31 Nino, E., Gajdeczko, B.F., Felton, P.G., "Two-Color Particle Image Velocimetry in an Engine With Combustion", SAE paper # 930872, 1993.

2.32 Tabaczynski, R.J., "Turbulence and Turbulent Combustion in Spark-Ignition Engines", Progress in Energy and Combustion Science, vol 2, pp143-165, 1976.

2.33 "Kodak Technical Pan Film", Kodak Technical Literature, Kodak Publication No. p-255(H), 1993.

2.34 Ikeda, Y., Nishigaki, M., Ippommatsu, M., Hosokawa, S., Nakajima, T., "Optimum Seeding Particles for Successful LDV Measurements", Proc. 6th Int. Conf. on App. of Las. Tech. to Fluid Mech., Lisbon, Portugal, 1990.

2.35 Coupland, J.C., Pickering, C.J.D, "Particle Image Velocimetry: Estimate of Measurement Confidence at Low Seeding Densities", Optics and Lasers in Engineering, vol 9, pp201-210, 1988.

2.36 Armstrong, N.W.H., "Planar Flowfield Measurements in Premixed Turbulent Combustion", PhD Thesis, Cambridge University, August 1992.

2.37 Lecordier, B., Mouquillard, M., Trinite, M., "Simultaneous 2D Measurement of Flame Front Propagation by High Speed Tomography and Velocity Field by Cross Correlation", Proc. 8th Int. Symp. on App. of Laser Tech. to Fluid Mech., Lisbon, Portugal, July 1994.

2.38 Witze, P.O., Baritaud, T.A., "Particle Seeding for Mie Scattering Mesaurements in Combusting Flows", Proc. 3rd Int. Symp. on App. of Laser Tech. to Fluid Mech., Lisbon, Portugal, 1986.

2.39 Ruess, D.L., Bardsley, M., Felton, P.G., Landreth, C.C., Adrian, R.J., "Velocity, Vorticity and Strain-Rate Ahead of a Flame Measured in an Engine Using Particle Image Velocimetry", SAE paper # 900053, 1990.

2.40 Corcione, F.E., Valentino, G., "Analysis of In-Cylinder Turbulent Air Motion Dependence on Engine Speed", SAE paper # 940284, 1994.

2.41 Pickering, C.D., Halliwell, N.A., "Particle Image Velocimetry: Photographic Film Noise", Applied Optics, 23(7), pp2961-2969, 1984.

2.42 Stolz, W., Kohler, J., Lawrenz, W., Meier, F., Bloss, W.H., Maly, R.R., Herweg, R., Zahn, M., "Cycle Resolved Flow Field Measurements Using a PIV Movie Technique in a SI Engine", SAE paper # 922354, 1992.

2.43 Huang, H.T., Fiedler, H.E., Wang, J.J., "Limitation and Improvement of PIV. Part I: Limitation of conventional techniques due to deformation of particle image patterns", Experiments in Fluids, 15, pp 168-174, 1993.

2.44 Huang, H.T., Fiedler, H.E., Wang, J.J., "Limitation and Improvement of PIV. Part II: Particle image distortion, a novel technique", Experiments in Fluids, 15, pp 263-273, 1993.

2.45 Jambunathan, K., Ju, X.Y., Dobbins, B.N., Ashforth-Frost, S., "An improved cross correlation technique for particle image velocimetry", Meas. Sci. Technol. 6, pp507-514, 1995.

CHAPTER 3

3.1 Clerk, D., "Cylinder actions in Gas and Gasoline Engines", SAE Journal vol 8, p 523, 1921.

3.2 Bates, S.C., "A Transparent Engine for Flow and Combustion Visualisation Studies", SAE paper # 880520, 1988.

3.3 Omori, S., Iwachido, K., Motomochi, M., Hirako, O., "Effect of Intake Port Flow Pattern on the In-Cylinder Tumbling Air Flow in Multi-Valve SI Engines", SAE paper # 910477, 1991.

3.4 Zhang, L., Ueda, T., Takatsuki, T., Yokota, K., "A Study of the Cycle-to Cycle Variation of In-Cylinder Flow on a Motored Engine", COMODIA 94 Int. Symp., Yokohama, Japan, pp 541-546, July 1994.

3.5 Brown, D.C., "Close-Range Camera Calibration", Photogrammetric Engineering, vol 37, pp 855-866, 1971.

3.6 Bicen, A.F., "Refraction Correction for LDA Measurements in Flows with Curved Optical Boundaries", Imperial College Report, Department of Mechanical Engineering Fluids Section, Report no. FS/81/17, June 1981.

3.7 Boadway, J.D., Karahan, E., "Correction of Laser Doppler Anemometer Readings for Refraction at Cylindrical Interfaces", DISA information, no 26, 1981.

3.8 Vikram, C.S., "Particle Field Holography", Cambridge Studies in Modern Optics, 11, Cambridge University Press, pp 159-166, ISBN 0-521-41127-0, 1992.

3.9 Fujikawa, T., Ozasa, T., Kosuka, K., "Development of Transparent Cylinder Engines for Schlieren Observation", SAE paper # 881632, 1988.

3.10 Khalighi, B., "Intake-Generated Swirl and Tumble Motions in a 4-Valve Engine with Various Intake Configurations-Flow Visualisation and Particle Tracking Velocimetry", SAE paper # 900059, 1990.

3.11 Periera, J.C.F., "Refractive Index Matching for LDV Measurements Near Walls and in Complex Geometries" in *'Instrumentation for Combustion and Flow in Engines'*, eds Durao et al, Kluwer Academic Publishers, pp 267-284, 1989.

3.12 Weller, H.G., Uslu, S., Gosman, A.D., Maly, R.R., Herweg, R., Heel, B., "Prediction of Combustion in Homogeneous-Charge Spark-Ignition Engines" COMODIA 94 Int. Symp., Yokohama, Japan, 1994.

3.13 Kuwahara, K., Kawai, T., Ando, H., "Influence of Flow Field Structure after the Distortion of Tumble on Lean-Burn Flame Structure", COMODIA 94 Int. Symp., Yokohama, Japan, 1994.

3.14 Barnhart, D.H., Adrian, R.J., Papen, G.C., "Phase-Conjugate Holographic System for High-Resolution Particle-Image Velocimetry", Appl. Opt. vol 33, no 30, pp 7159-7170, Oct 1994.

3.15 Coupland, J.M., Halliwell, N.A.H., "Particle Image Velocimetry: Three Dimensional Fluid Velocity Measurements using Holographic Recording and Optical Correlation", Appl. Opt. no 31, pp 1005-1007, 1992.

3.16 Hecht, E., "Optics", second edition, Addison-Wesley Publishing Co., 1987.

CHAPTER 4

4.1 Chapman, J., Garrett, M.W., Warburton, A., "A New Standard for Barrel Swirl Movement", IMechE C427/18/156.

4.2 Arcoumanis, C., Hu, Z., Whitelaw, J.H., "Steady flow characterisation of tumble-generating four-valve cylinder heads" Proc. Inst. Mech. Engrs., Journal of Automobile Engineering, vol 207, pp 203-210, 1993.

4.3 Hu, Z., Vafidis, C., Whitelaw, J.H., Chapman, J., Head, R., "Correlation between in-cylinder flow, performance and emissions characteristics of a Rover pentroof four-valve engine", IMechE C448/026, pp 157-164, 1992.

4.4 Reuss, D.L., Adrian, R.J., Landreth, C.C., French, D.T., Fansler, T.D., "Instantaneous Planar Measurements of Velocity and Large-Scale Vorticity and Strain-Rate in an Engine Using Particle-Image Velocimetry", SAE paper # 890616, 1989.

4.5 Kompenhans, J., Hocker, R., "Application of Particle Image Velocimetry to High Speed Flows", von Karman Institute for Fluid Dynamics, Lecture Series 1988-06, Particle Image Displacement Velocimety, Brussels, pp67-83, March 1988.

4.6 Armstrong, N.W.H., "Planar Flowfield Measurements in Premixed Turbulent Combustion", PhD Thesis, Cambridge University, August 1992.

4.7 Lawson, N.J., "The Application of Particle Image Velocimetry to High Speed Flows", PhD Thesis, Loughborough University of Technology, March 1995.

4.8 Keane, R.D., Adrian, R.J., "Optimisation of particle image velocimeters. Part 1: Double pulsed systems", Meas. Sci. Technol. (1), pp 1202-1215, 1990.

4.9 AEA Technology, "VISIFLOW System User Manual", AEA Technology, Harwell, Oxfordshire, 1987-1995.

CHAPTER 5

5.1 Reuss, D.L., Adrian, R.J., Landreth, C.C., French, D.T., Fansler, T.D., "Instantaneous Planar Measurements of Velocity and Large-Scale Vorticity and Strain Rate in an Engine Using Particle Image Velocimetry", SAE paper # 890616, 1989.

5.2 Hu, Z., "Turbulence Enhancement in Spark-Ignition Engines", PhD Thesis, Imperial College of Science, Technology and Medicine, London, Feb1992.

5.3 Pischinger, S., Heywood, J.B., "How Heat Losses to the Spark Plug Electrodes Affect Flame Kernel Development in an SI Engine", SAE paper # 900021, 1990.

5.4 Maly, R., "Ignition Model for Spark Discharges and the Early Phase of Flame Front Growth", Proc. 18th Int. Symp. on Comb., pp 1747-1754, The Combustion Institute, 1981.

5.5 Kiyota, Y., Akashino, K, Ando, H., "Concept of Lean Combustion by Barrel-Stratification", SAE paper # 920678, 1992.

5.6 Baritaud, T.A., "Optical and Numerical Diagnostics for SI Engine Combustion Studies", COMODIA 94 Int. Symp., Yokohama, Japan, July 1994.

5.7 Kuwahara, K., Watanabe, T., Takemura, J., Omori, S., Kume, T., Ando, H., "Optimisation of In-Cylinder Flow and Mixing for a Centre-Spark Four-Valve Engine Employing the Concept of Barrel-Stratification", SAE paper # 940986, 1994.

5.8 Omori, S., Iwachido, K., Motomochi, M., Hirako, O., "Effect of Intake Port Flow Pattern on the In-Cylinder Tumbling Air Flow in Multi-Valve SI Engines", SAE paper # 910477, 1991.

5.9 Ronnback, M., Le, W.X., Linna, J-R., "Study of Induction Tumble by Particle Tracking Velocimetry in a 4-Valve Engine", SAE paper # 912376, 1991.

5.10 Khalighi, B., Huebler, M.S., "A Transient Water Analog of a Dual-Intake-Valve Engine for Intake Flow Visualisation and Full-Field Velocity Measurements", SAE paper # 880519, 1988.

5.11 Kent, J.C., Trigui, N., Choi, W.C., Guezenner, Y.G., "Detailed Measurements of In-Cylinder Fluid Dynamics Using Water Analog Simulation and 3-D Particle Tracking Velocimetry", IMechE C485/009, Proc. of Int. Conference on Optical Methods and Data Processing in Heat and Fluid Flow', pp69-74, April 1994.

5.12 Das, S., Dent, J.C., "Simulation of The Mean Flow in The Cylinder of a Motored 4-valved Spark Ignition Engine", SAE Fuels and Lubricants Meeting, paper # 952384 (also SP-1123), Toronto, October 1995.

5.13 Jones, P.M., Junday, J.S., "Full Cycle Computational Fluid Dynamics Calculations in a Motored Four Valve Pent Roof Combustion Chamber and Comparison with Experiment", SAE paper # 950286, 1995.

5.14 Le Coz, J-F., Henriot, S., Pinchon, P., "An Experimental and Computational Analysis of the Flow Field in a Four-Valve Spark Ignition Engine-Focus on Cycle-Resolved Turbulence", SAE paper # 900056, 1990.

5.15 Tatschl, R., Wieser, K., Reitbauer, R., "Multidimensional Simulation of Flow Evolution, Mixture Preparation and Combustion in a 4-Valve SI Engine", COMODIA 94 Int. Symp., Yokohama, Japan, July 1994.

5.16 Chapman, J., Garrett, M.W., Warburton, A., "A New Standard for Barrel Swirl Movement", IMechE c427/18/156
5.17 Hu, Z., Vafidis, C., Whitelaw, J.H., Chapman, J., Head, R., "Correlation Between In-Cylinder Flow, Performance and Emissions Characteristics of a Rover Pentroof 4-Valve Engine", IMechE, c488/026, p 157, 1992.

5.18 Armstrong, N.W.H., "Planar Flowfield Measurements in Premixed Turbulent Combustion", PhD Thesis, Cambridge University, Aug 1992.

5.19 Martin, J.K., Witze, P.O., Borgnakke, C., "Combustion Effects on the Preflame Flow Field in a Research Engine" SAE paper # 850122, 1985.

CHAPTER 6

6.1 Kuwahara, K., Ando, H., "TDC Flow Field Structure of Two-Intake-Valve Engines with Pentroof Combustion Chamber", JSME International Journal, Series B, vol 36, No 4, 1993.

6.2 Ikeda, Y., Nishigaki, M., Ippommatsu, M., Hosokawa, S., Nakajama, T., "Optimum Seeding Particles for Successful LDV Measurements", Proc. of 6th Int. Symp. on App. of Las. Tech. to Fluid Mech., Lisbon, Portugal, 1990.

6.3 Durst, F., Melling, A., Whitelaw, J.H., "Principles and Practice of Laser Doppler Anemometry", Academic Press, 1981.

6.4 Kohler, J., Gerblich, K., Meinhardt, P., Ziegler, G.F.W., "2-D Flow Velocity Measurements Under the Condition of High Straylight Intensity using Particle Tracking Anemometry", Intern. Symp. on Engineering Turbulence Modelling and Measurements, Dubrovnik, Croatia, 1990.

6.5 Stolz, W., Kohler, J., Lawrenz, W., Meier, F., Bloss, W.H., Maly, R.R., Herweg, R., Zahn, M., "Cycle Resolved Flow Field Measurements using a PIV Movie Technique in a SI Engine", SAE Int . Fuels and Lubricants Meeting and Exposition, San Francisco, paper # 922354, Oct. 1992.

6.6 Meinhart, C.D., Prasad, A.K., Adrian, R.J., "Parallel Digital Processor System for Particle Image Velocimetry", 6th Int. Conf. on App. of Las. Tech. to Fluid Mech., Lisbon, Portugal, 1992.

6.7 Mao, Z.Q., Halliwell, N.A.H, Coupland, J.M., "Particle Image Velocimetry: High-Speed Transparency Scanning and Correlation-Peak Location in Optical Processing Systems", Applied Optics 32(26) pp5089-5091, 1993.

6.8 Lourenco, L.M., Gogineni, S.P., LaSalle, R.T., "On-Line Particle-Image Velocimeter: an Integrated Approach", Applied Optics, 33(13), pp 2465-2470,1994.

6.9 Wormell, D.C., Sopchak, J.L., "A Particle Image Velocimetry System using a High Resolution CCD Camera", IMechE C485/014, Conf. on Optical methods and Data Processing in Heat and Fluid Flow, City University, London, U.K., April 1994.

6.10 Adrian, R.J., "Image Shifting Technique to Resolve Directional Ambiguity in Double-Pulsed Velocimetry", Applied Optics, 25, (21), pp 3855-3856, 1986.

6.11 Landreth, C.C., Adrian, R.J., "Electrooptical image shifting for particle image velocimetry", Applied Optics, 27, (20), pp 4216-4220, 1988.

6.12 Lourenco, L.M., "Particle Image Velocimetry: Photographic and Video Techniques", Von Karman Institute Lecture Series-Laser Velocimetry, Rhode Saint Genese, Belgium, June 1991.

6.13 Hodges, J.T., Baritaud, T.A., Heinze, T.A., "Planar Liquid and Gas Fuel and Droplet Size Visualization in a DI Diesel Engine", SAE paper # 910726, 1991.

6.14 Lawson, N.J., "The Application of Particle Image Velocimetry to High Speed Flows", PhD Thesis, Loughborough University of Technology, March 1995.

6.15 Huang, H.T., Fiedler, H.E., Wang, J.J., "Limitation and Improvement of PIV. Part II: Particle image distortion, a novel technique", Experiments in Fluids, 15, pp 263-273, 1993.

6.16 Jambunathan, K., Ju, X.Y., Dobbins, B.N., Ashforth-Frost, S., "An improved cross correlation technique for particle image velocimetry", Meas. Sci. Technol. 6, pp507-514, 1995.

6.17 Keane, R.D., Adrian, R.J., "Theory of Cross-Correlation Analysis of PIV Images", Applied Scientific Research, 49, Kluwer Academic Publishers, pp 191-215, 1992.

6.18 Lecordier, B., Mouquillard, M., Trinite, M., "Simultaneous 2D Measurement of Flame Front Propagation by High Speed Tomography and Velocity Field by Cross Correlation", Proc. 8th Int. Symp. on App. of Laser Tech. to Fluid Mech., Lisbon, Portugal, July 1994.

6.19 Willert, C.E., Gharib, M., "Digital Particle Image Velocimetry", Experiments in Fluids, 10, pp181-193, 1991.

6.20 Reeves, M., Lawson, N.J., Halliwell, N.A., Coupland, J.M., "Particle Image Velocimetry: Image Labelling by Encoding of the Point Spread Function by Application of a Polarisation-Sensitive Pupil-Mask", Applied Optics, 34, No 1,1995.

6.21 Goss, L.P., Post, M.E., Trump, D.D., Sarka, B., "Two-Color Particle Velocimetry", Proc. ICALEO vol 68, pp 101-111, 1989.

6.22 Coupland, J.M., Pickering, C.D. and Halliwell, N.A., "Particle Image Velocimetry: Theory of Directional Ambiguity Removal using Holographic Image Separation", Applied Optics, Vol 26 No. 9, 1987.

6.23 Nino, E., Gajdeczko, B.F., Felton, P.G., "Two-Color Particle Image Velocimetry in an Engine With Combustion", SAE paper # 930872, 1993.

6.24 Lawson, N.J., Halliwell, N.A., Coupland, J.M., "Particle Image Velocimetry: Image Labelling by use of Adaptive Optics to Modify the Point Spread Function", Applied Optics, 33, pp 4241-4247, 1994.

6.25 Adrian, R.J., "Particle-Imaging Techniques for Experimental Fluid Mechanics", Annual Review of Fluid Mechanics, 23, pp 261-304, 1991.

6.26 Arroyo, M.P., Greated, C.A., "Stereoscopic particle image velocimetry", Meas. Sci. Technol., vol 2, pp1181-1186, 1991.

6.27 Kuwahara, K., Kawai, T., Ando, H., "Influence of Flow Field Structure after the Distortion of Tumble on Lean-Burn Flame Structure", COMODIA 94 Int. Symp., Yokohama, Japan, July 1994.

6.28 Kent, J.C., Mikulec, A., Rimai, L., Adamczyk, A.A., Mueller, S.R., Stein, R.A., Warren, C.C., "Observations on the Effects of Intake-Generated Swirl and Tumble on Combustion Duration", SAE paper # 892096, 1989.

6.29 Hinsch, K., Hinrichs, H., Kuhfahl, G., Meinlschnidt, P., "Holographic Recording of 3-D Flow Configurations for Particle Image Velocimetry (PIV)", Proc. ICALEO, pp121-130, 1990.

6.30 Barnhart, D.H., Adrian, R.J., Papen, G.C., "Phase-Conjugate Holographic System for High-Resolution Particle-Image Velocimetry", Appl. Opt. vol 33, no 30, pp 7159-7170, Oct 1994.

6.31 Coupland, J.M., Halliwell, N.A.H., "Particle Image Velocimetry: Three Dimensional Fluid Velocity Measurements using Holographic Recording and Optical Correlation", Appl. Opt. no 31, pp 1005-1007, 1992.

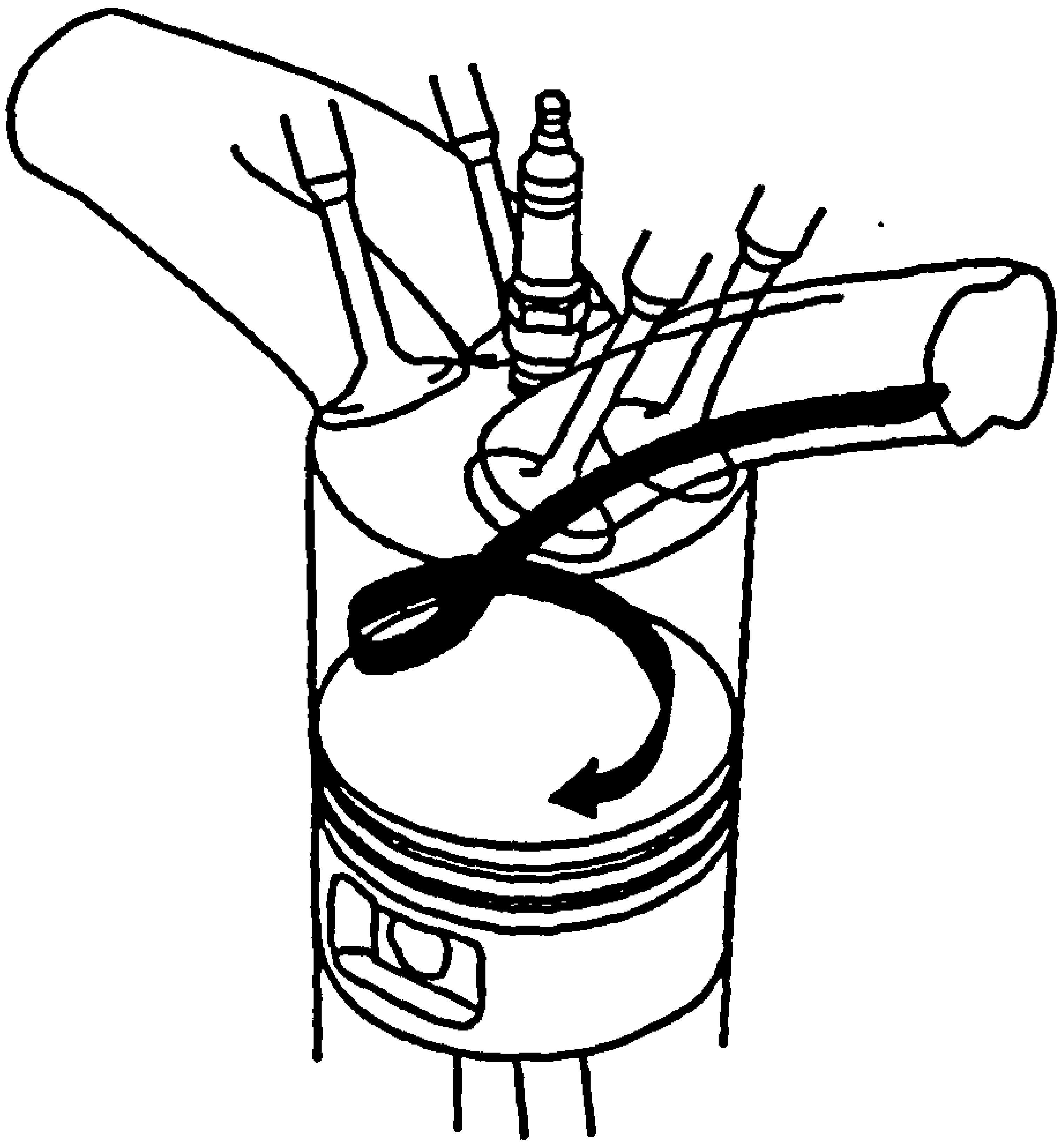

Fig 1.1 Axial Swirl (after ref [1.6])

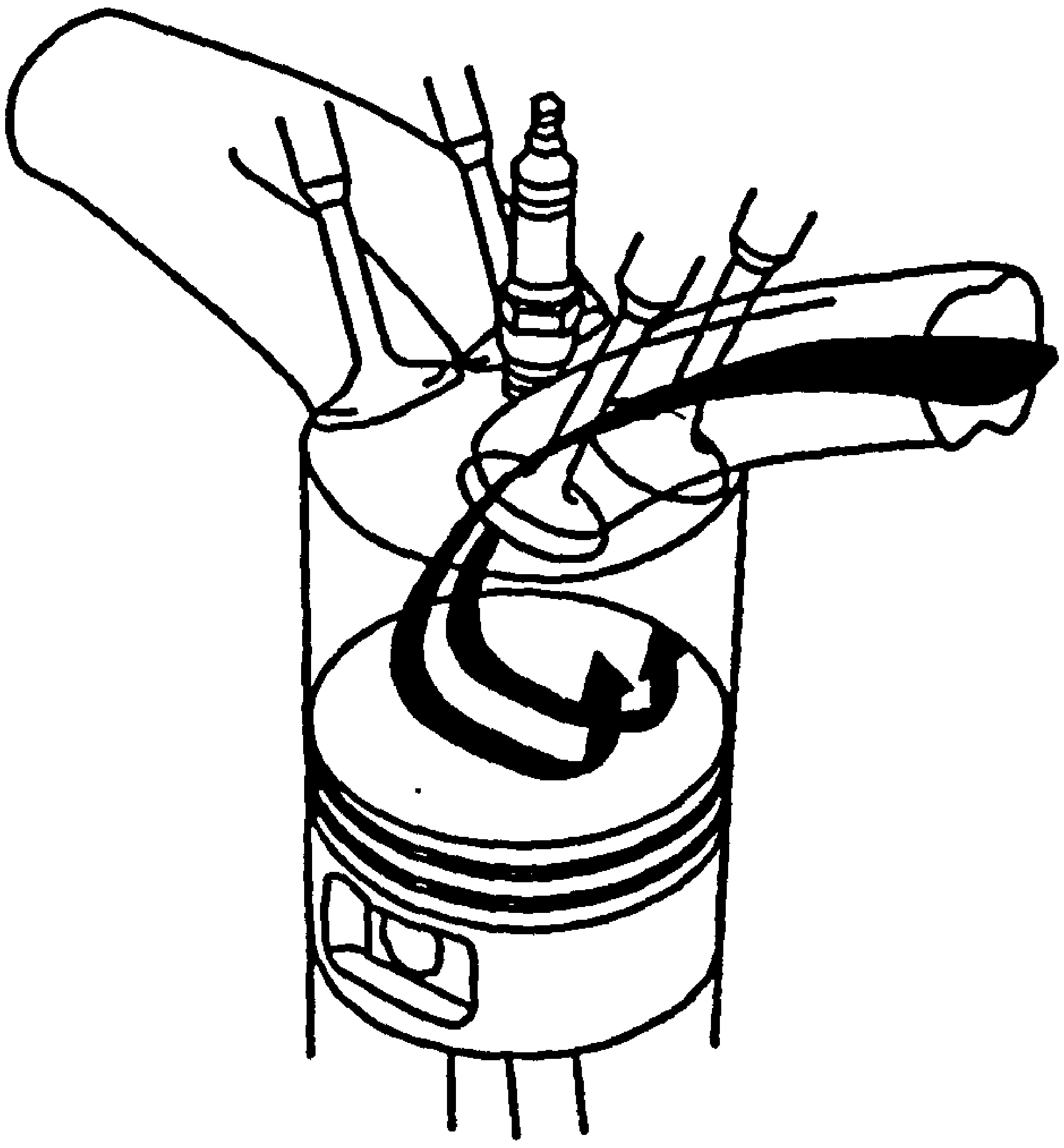

Fig 1.2 "Tumble" or "Barrel Swirl" (after ref [1.6])

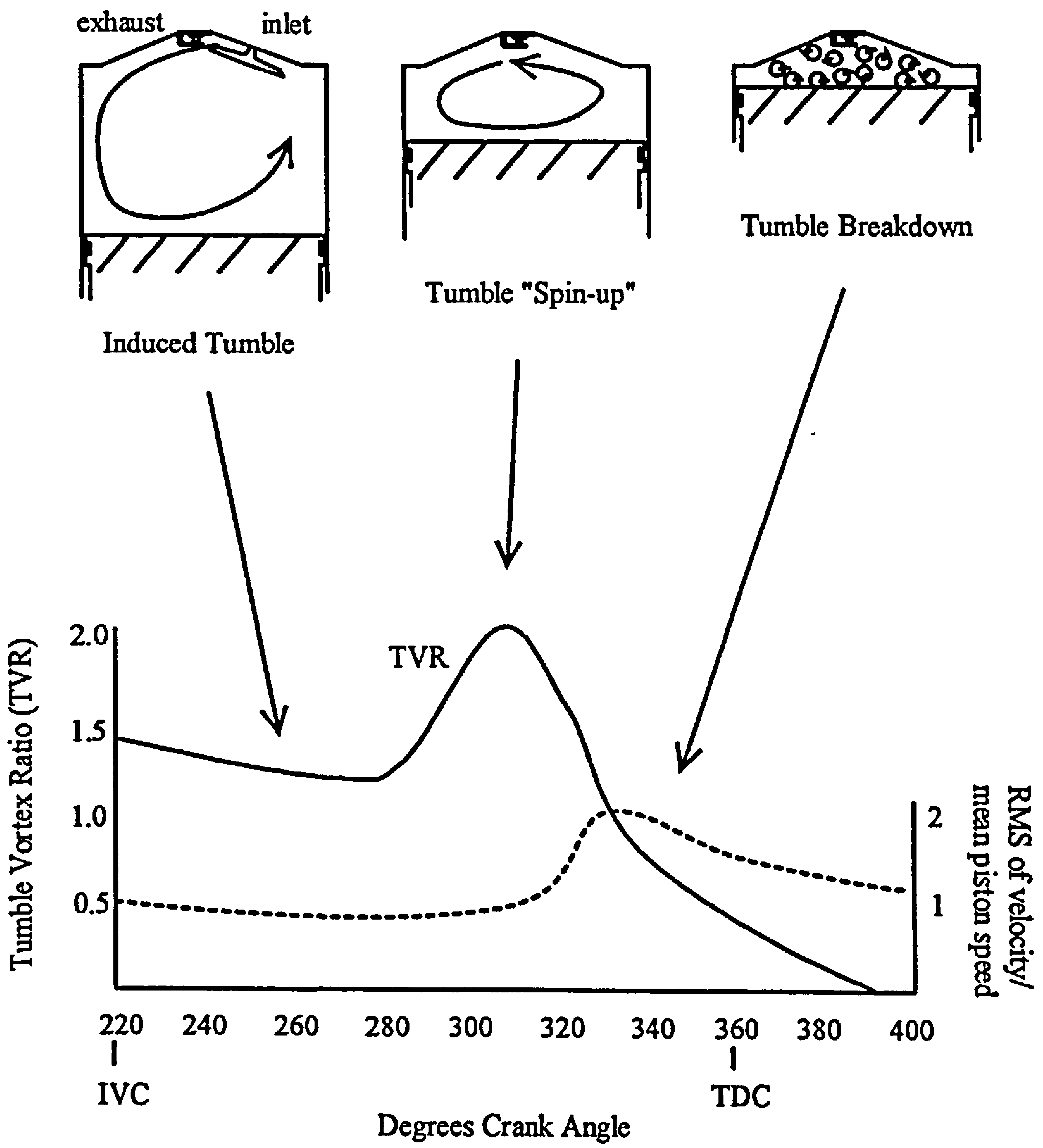

Fig 1.3 Schematic showing the process of tumble formation, spin-up and breakdown to produce enhanced TDC turbulence. Figures adapted from references [1.75] and [1.81].

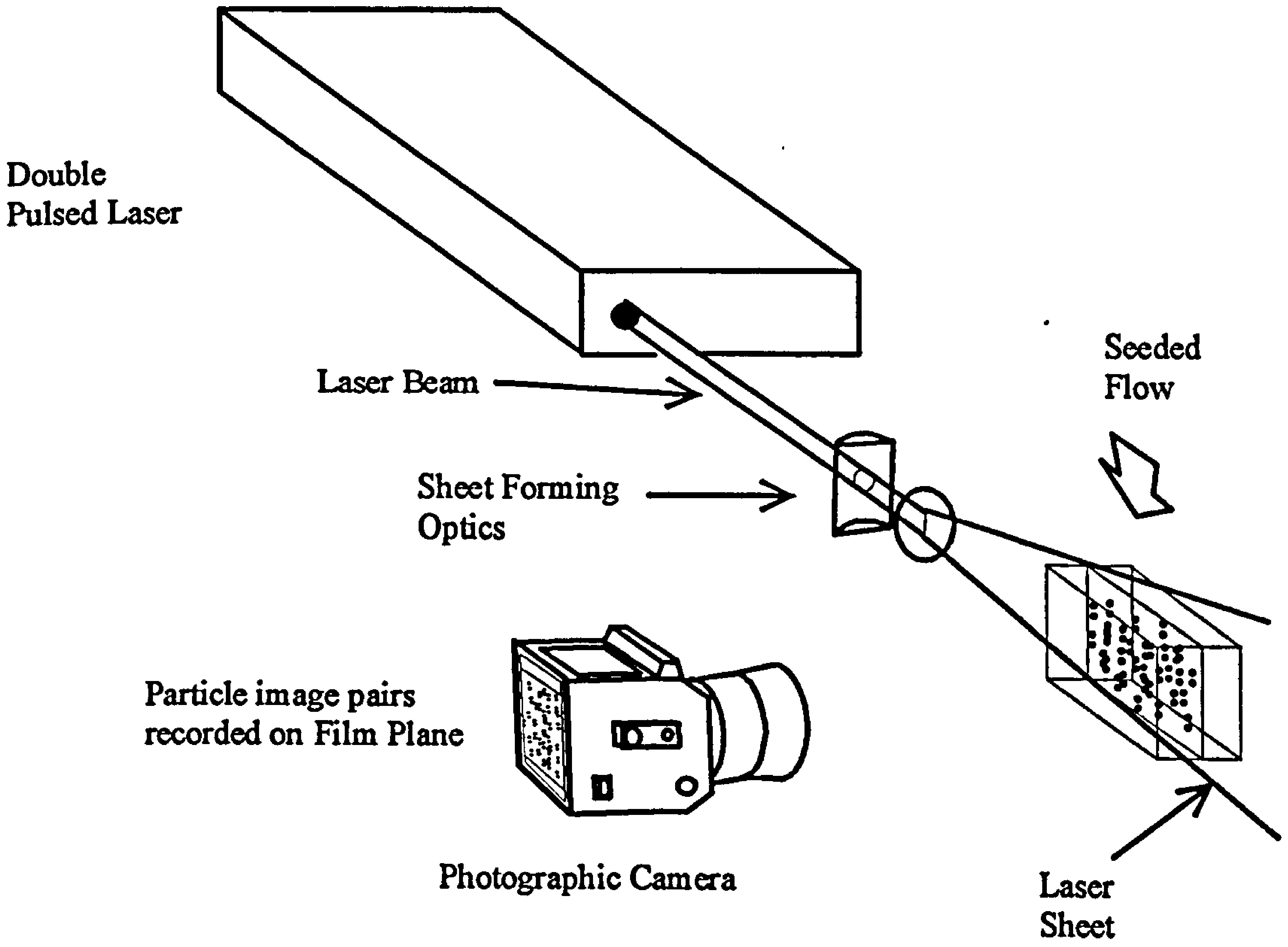

Figure 2.1 Typical photographic recording arrangement for PIV

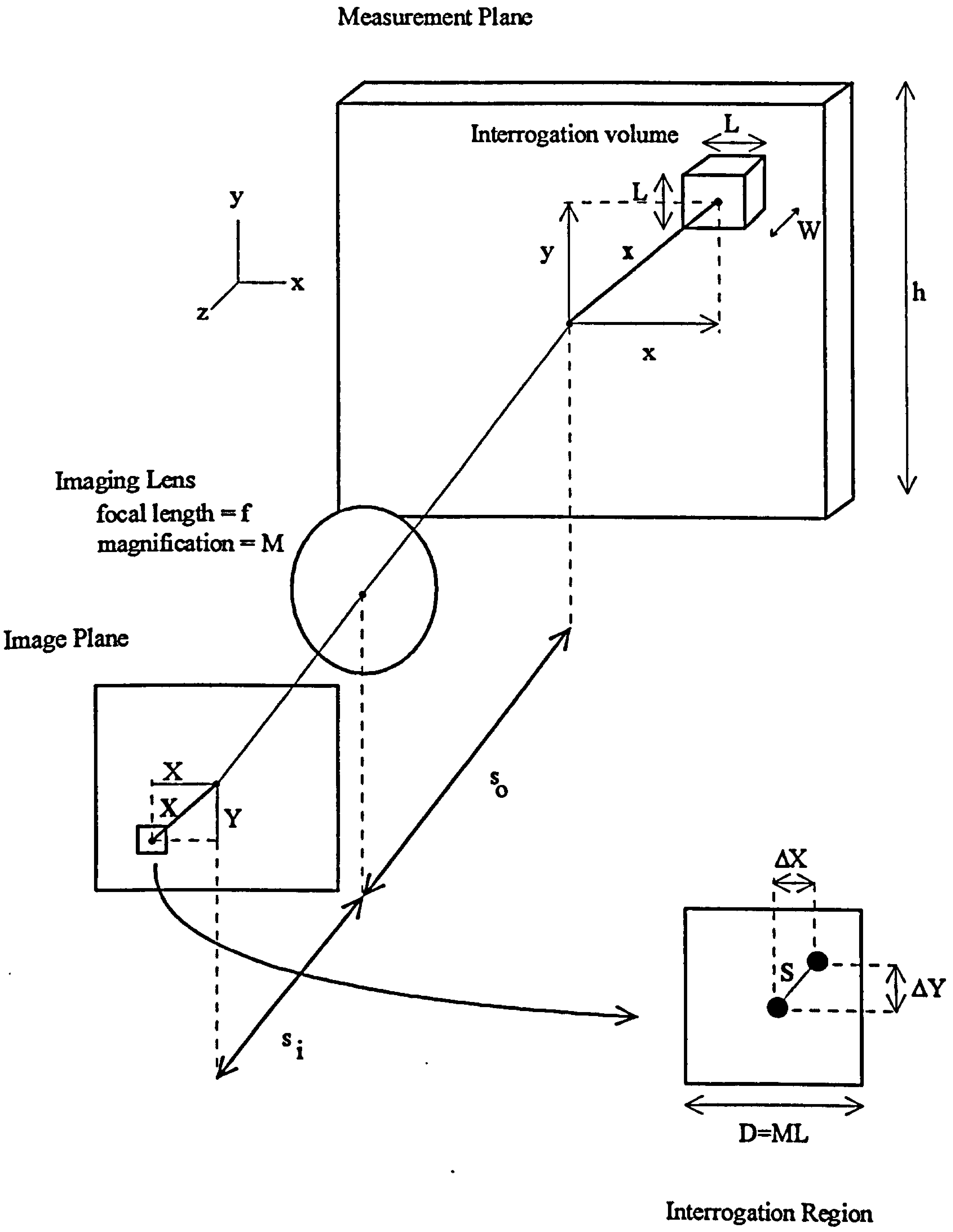

Figure 2.2 Imaging geometry for a typical PIV recording

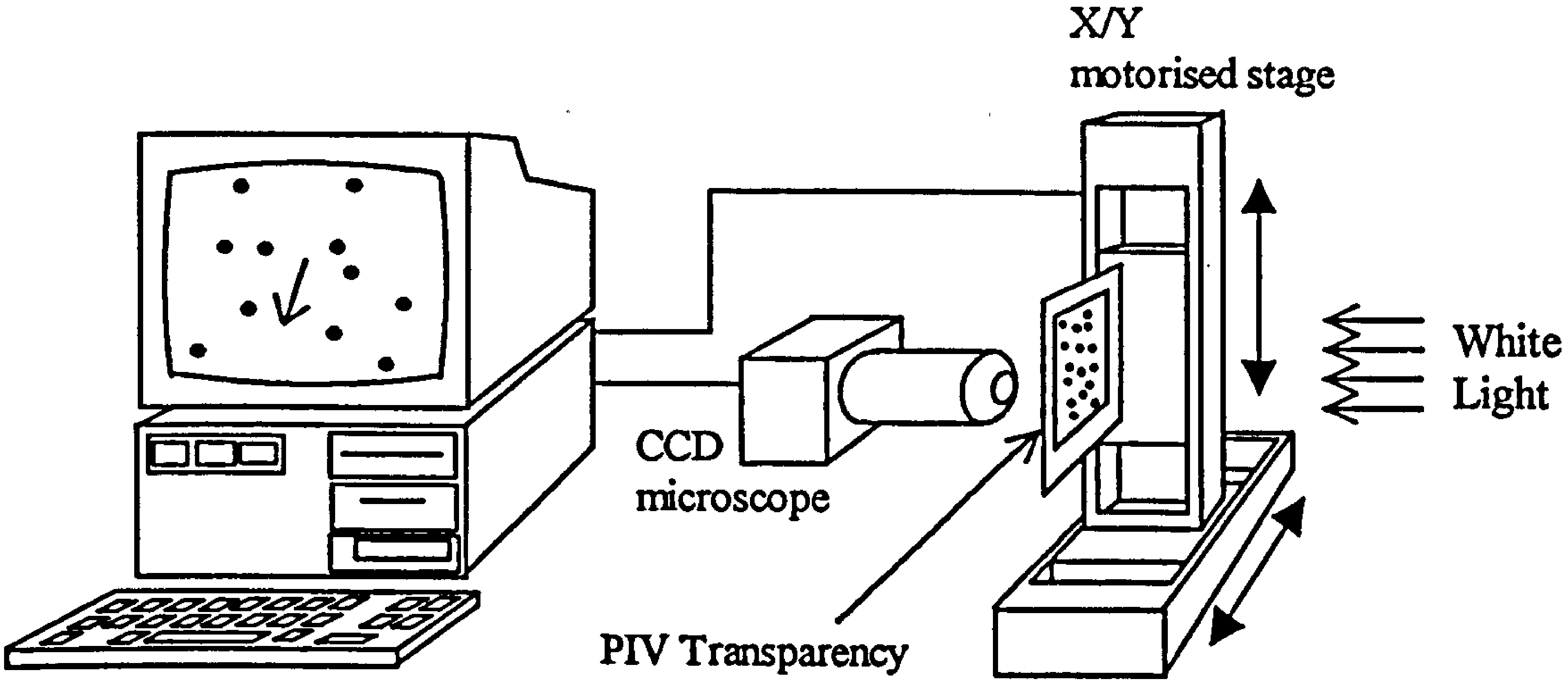

Figure 2.3 Typical digital interrogation arrangement

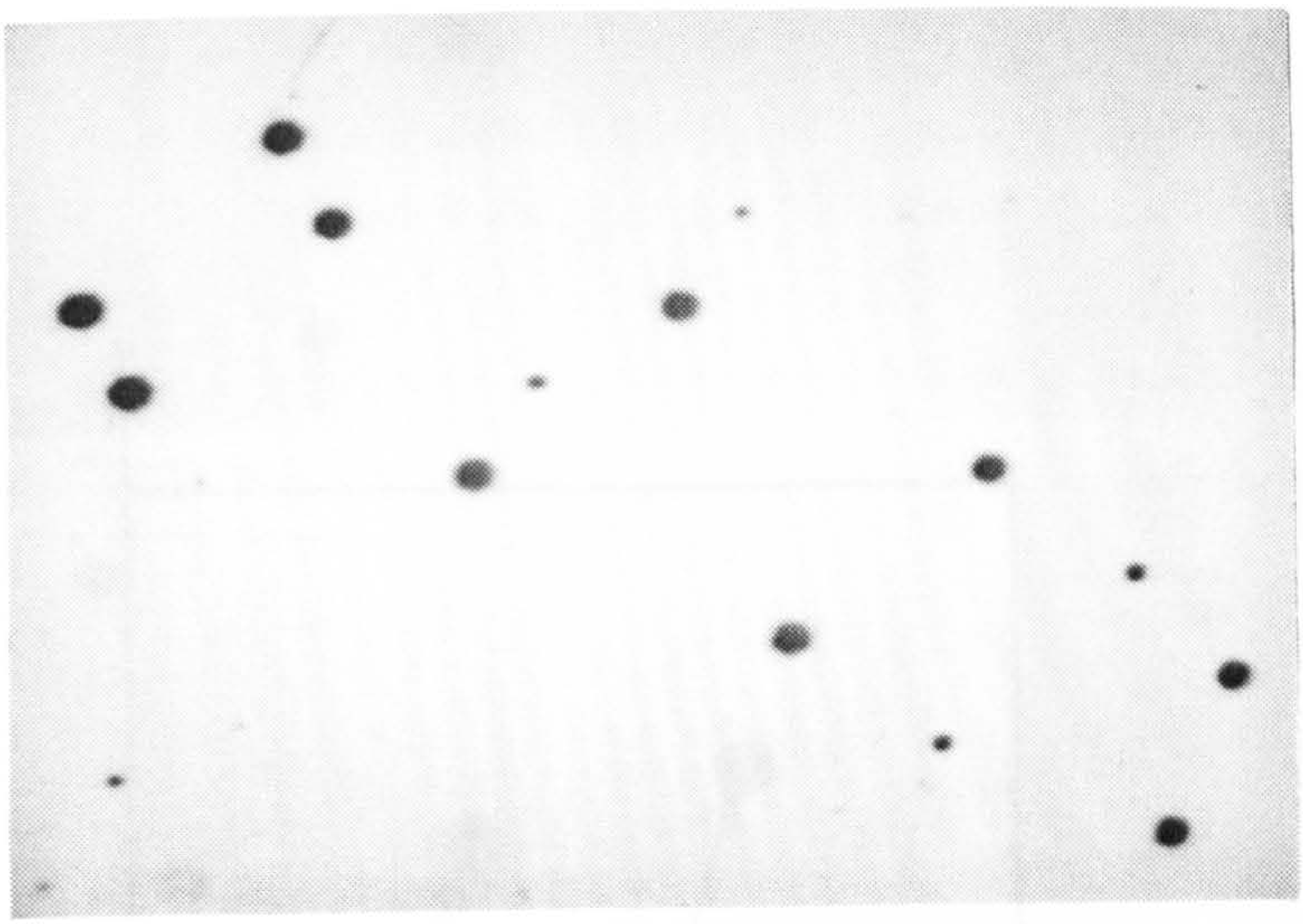

Figure 2.4 Ideal double exposed interrogation region in an experimentally simulated uniform flow.

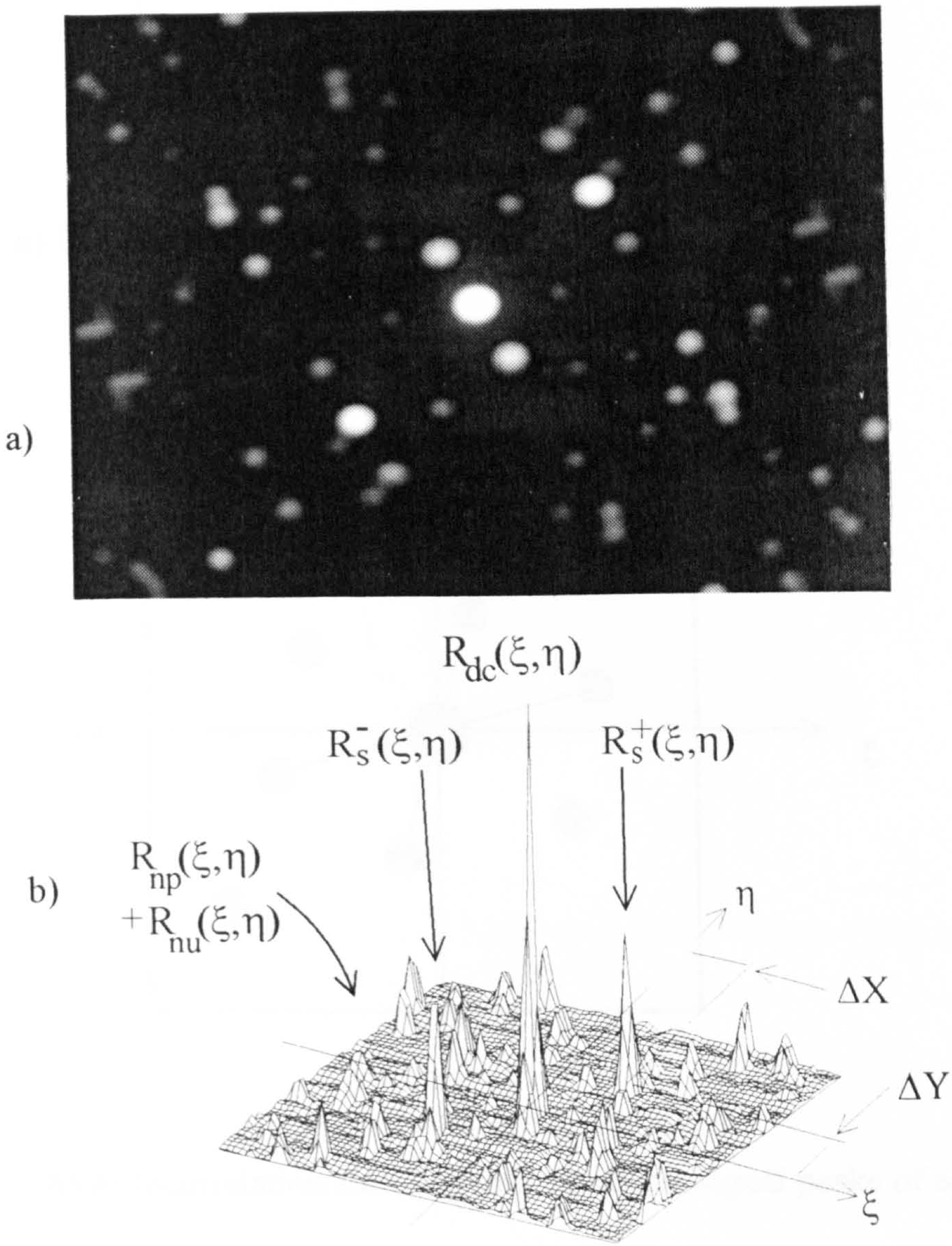

Figure 2.5 Autocorrelation of figure 2.4 showing central self- correlation peak, signal peaks and noise structure
a) as an intensity map b) as a 3D plot.

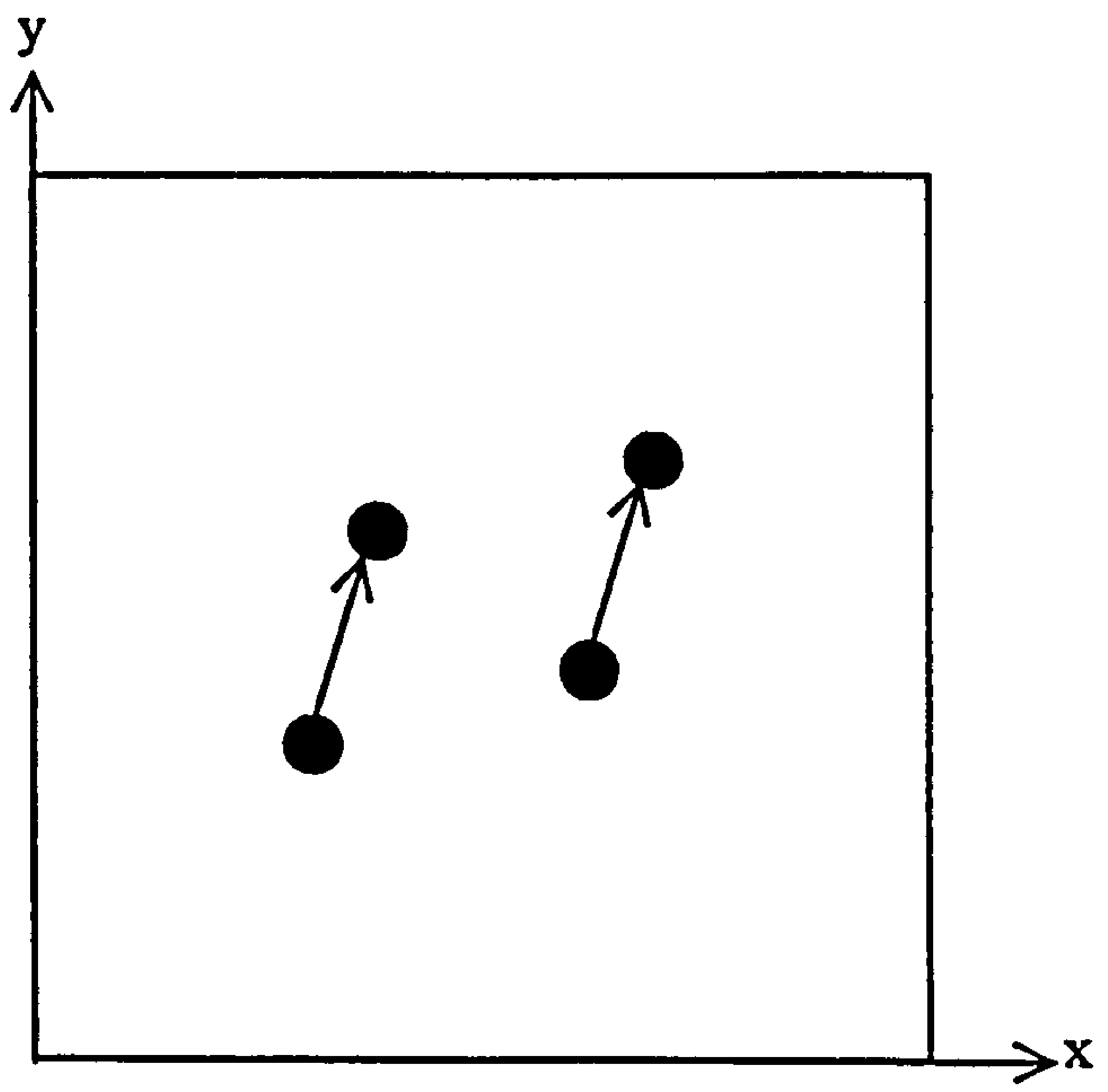

a) Particle images showing true displacement vector

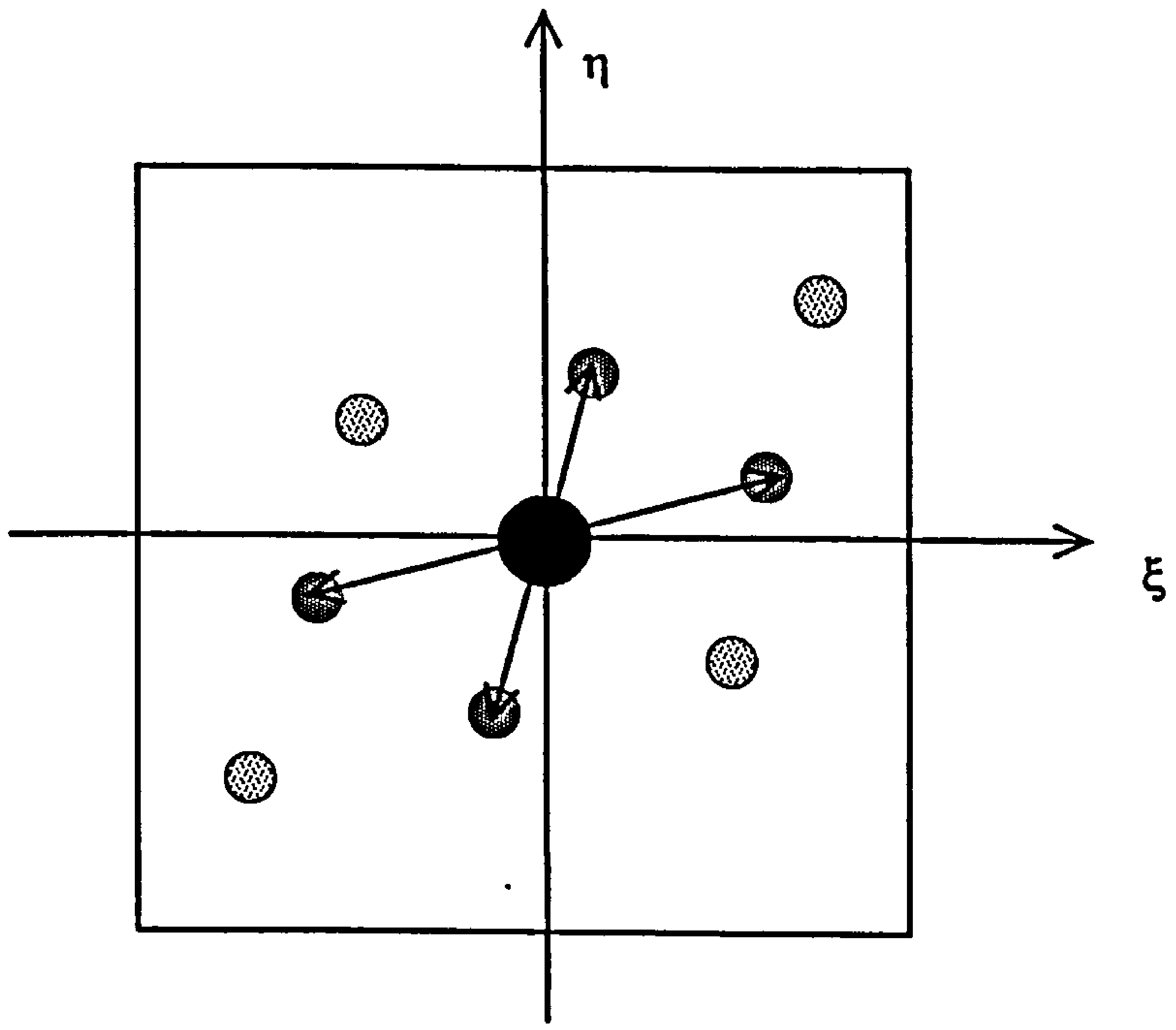

b) Autocorrelation showing four candidate signal peaks of equal magnitude

Figure 2.6 Four-fold directional ambiguity with two particle pairs per interrogation region

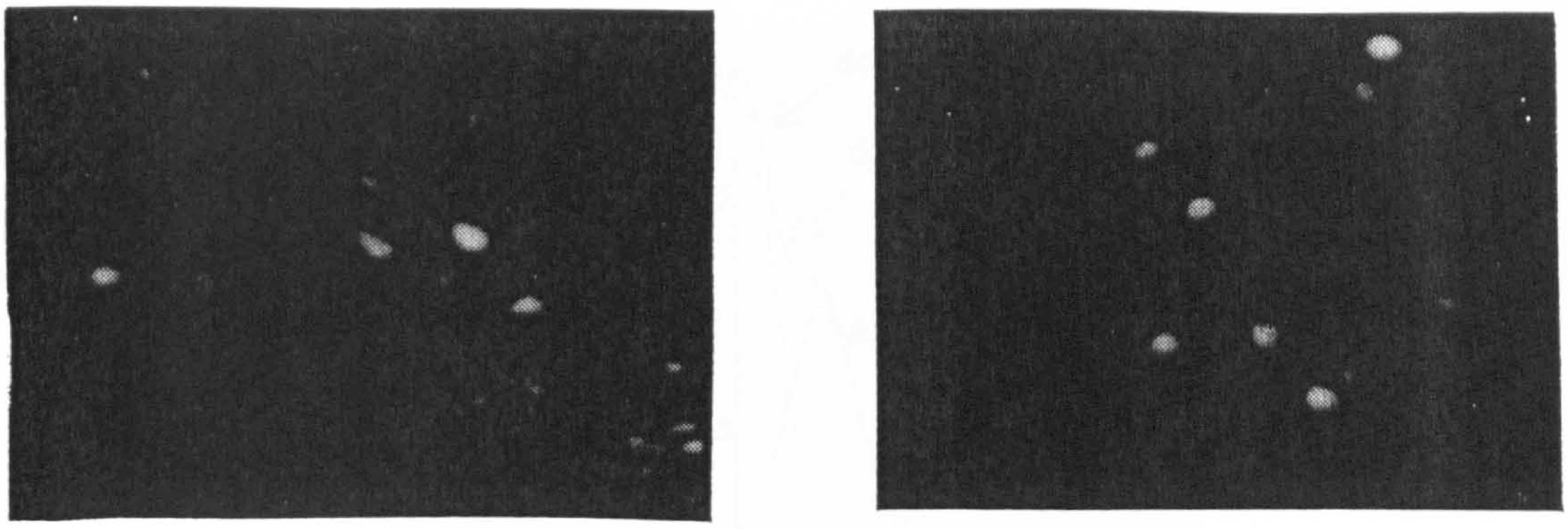

a) first exposure particle images   b) second exposure particle images

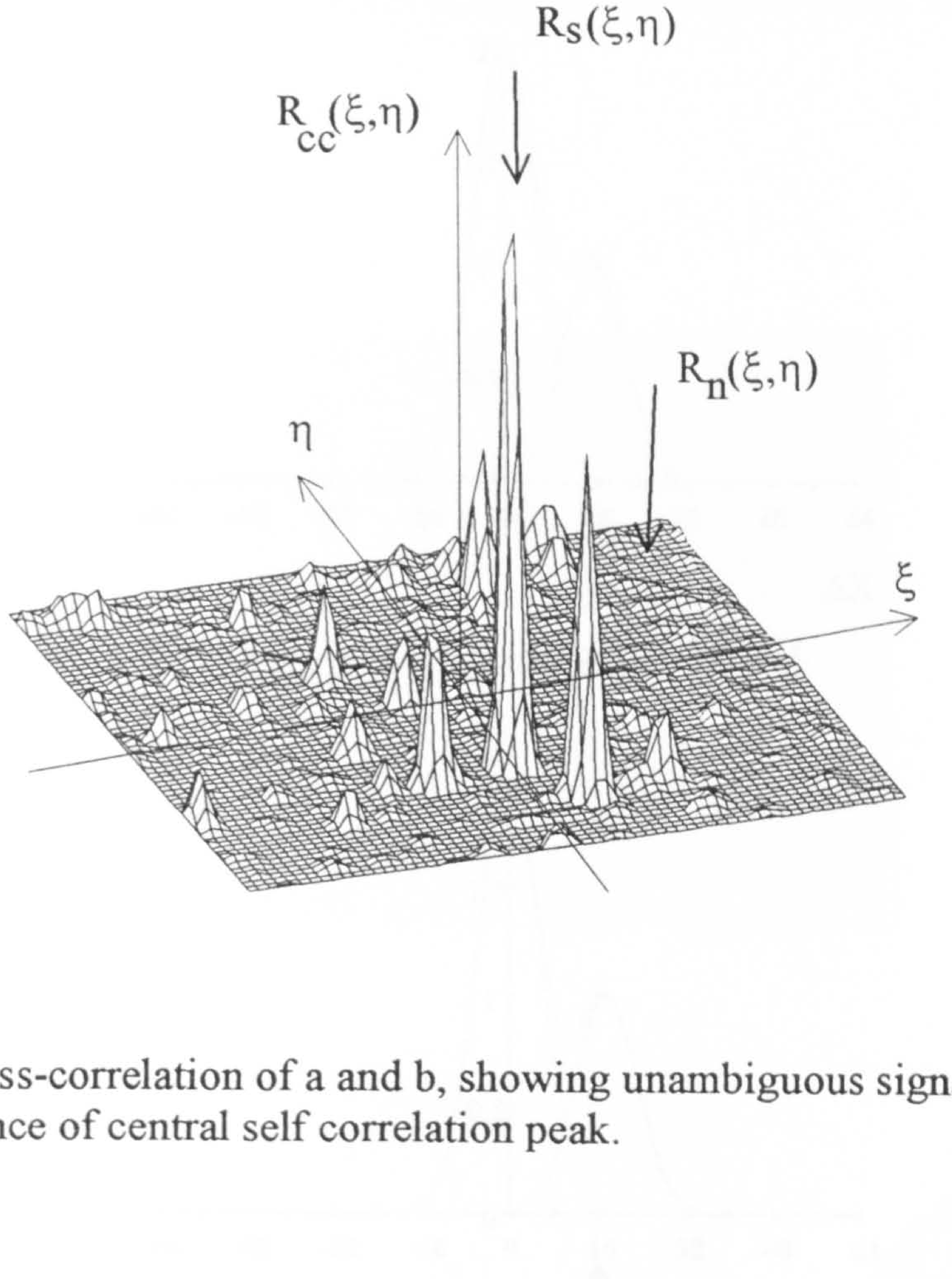

c) Cross-correlation of a and b, showing unambiguous signal peak and absence of central self correlation peak.

Figure 2.7 Separated initial and final particle image fields and their cross-correlation.

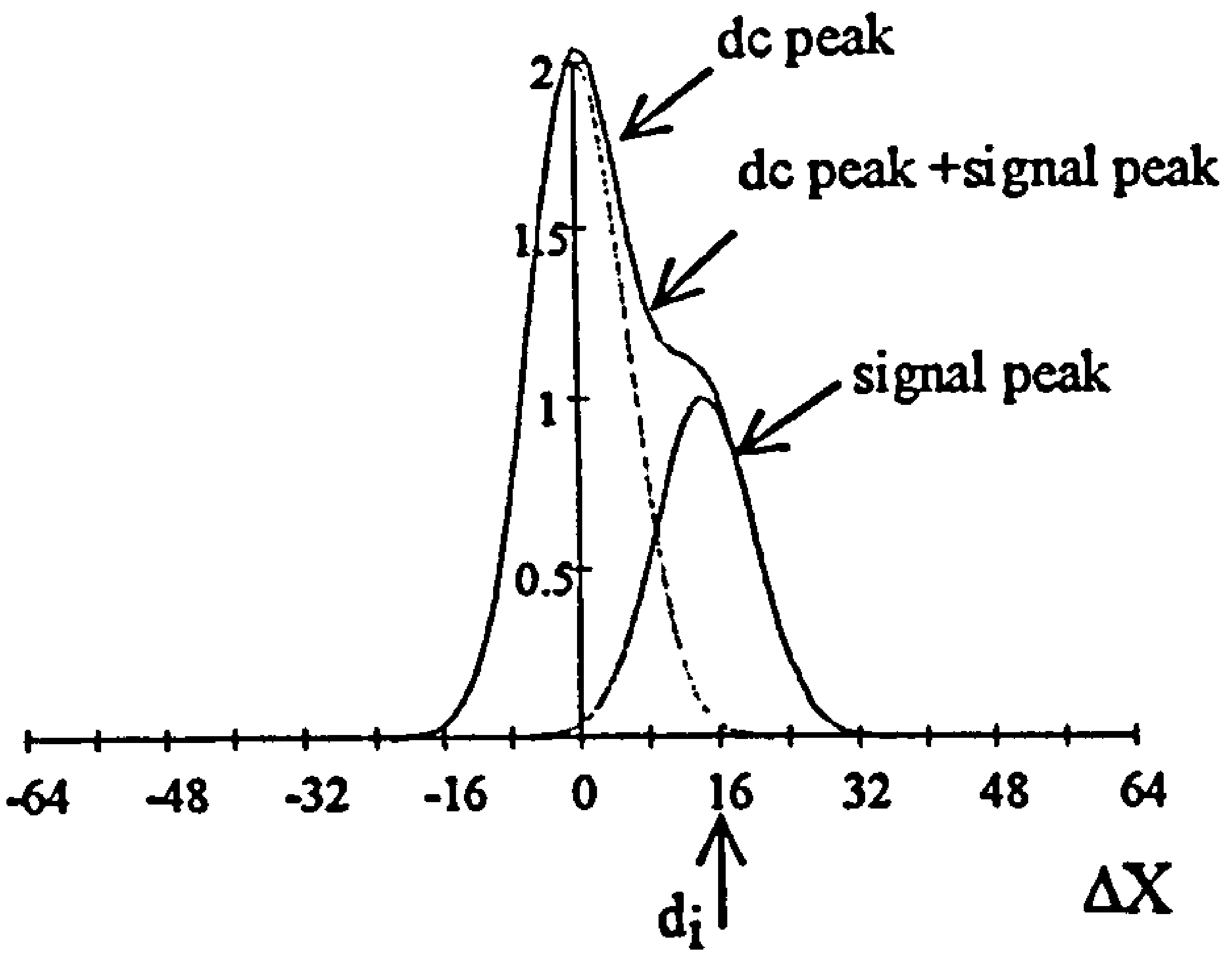

a) Signal peak unresolved: $\Delta X = 0.9d_i$

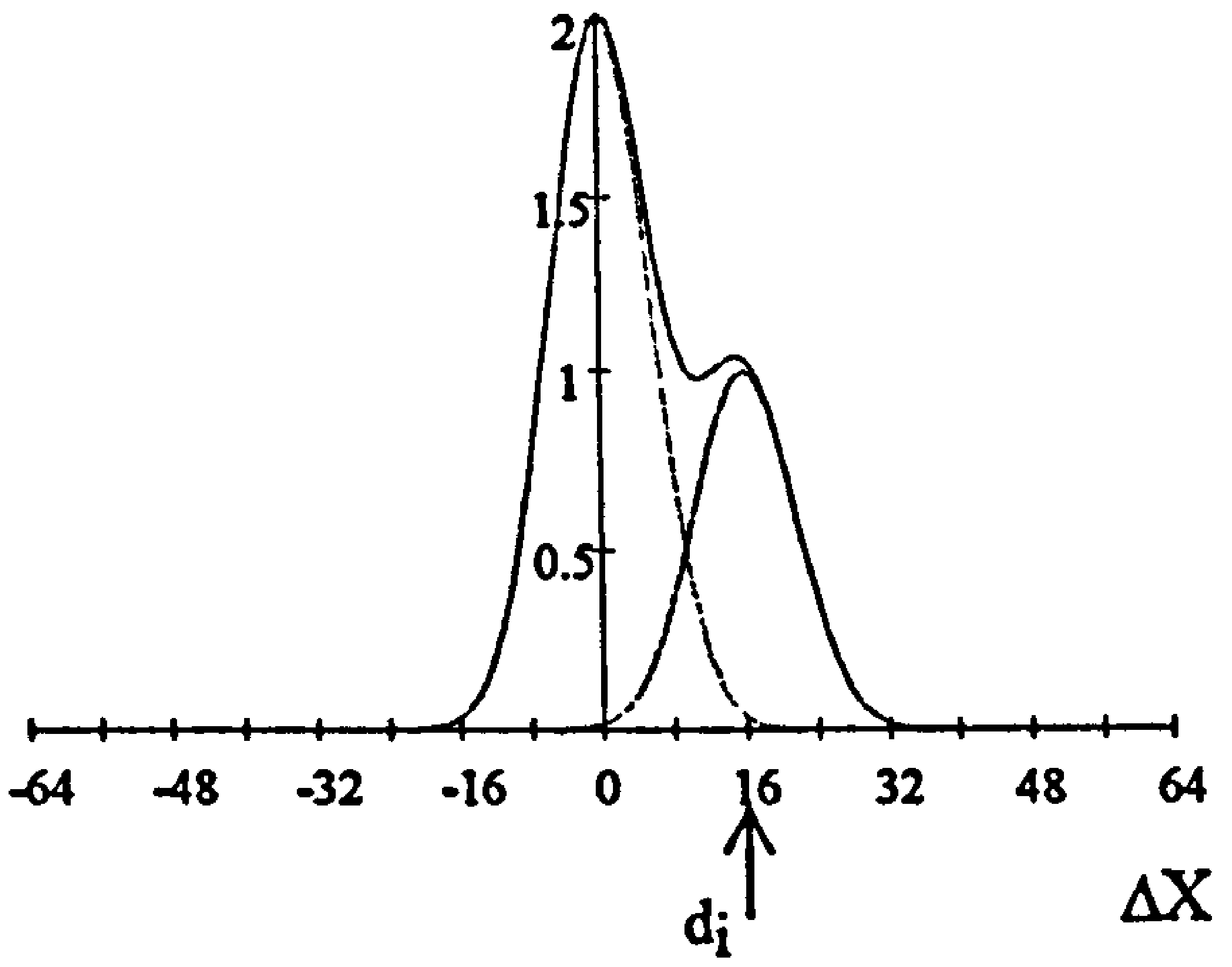

b) Signal peak just resolved: $\Delta X = d_i$

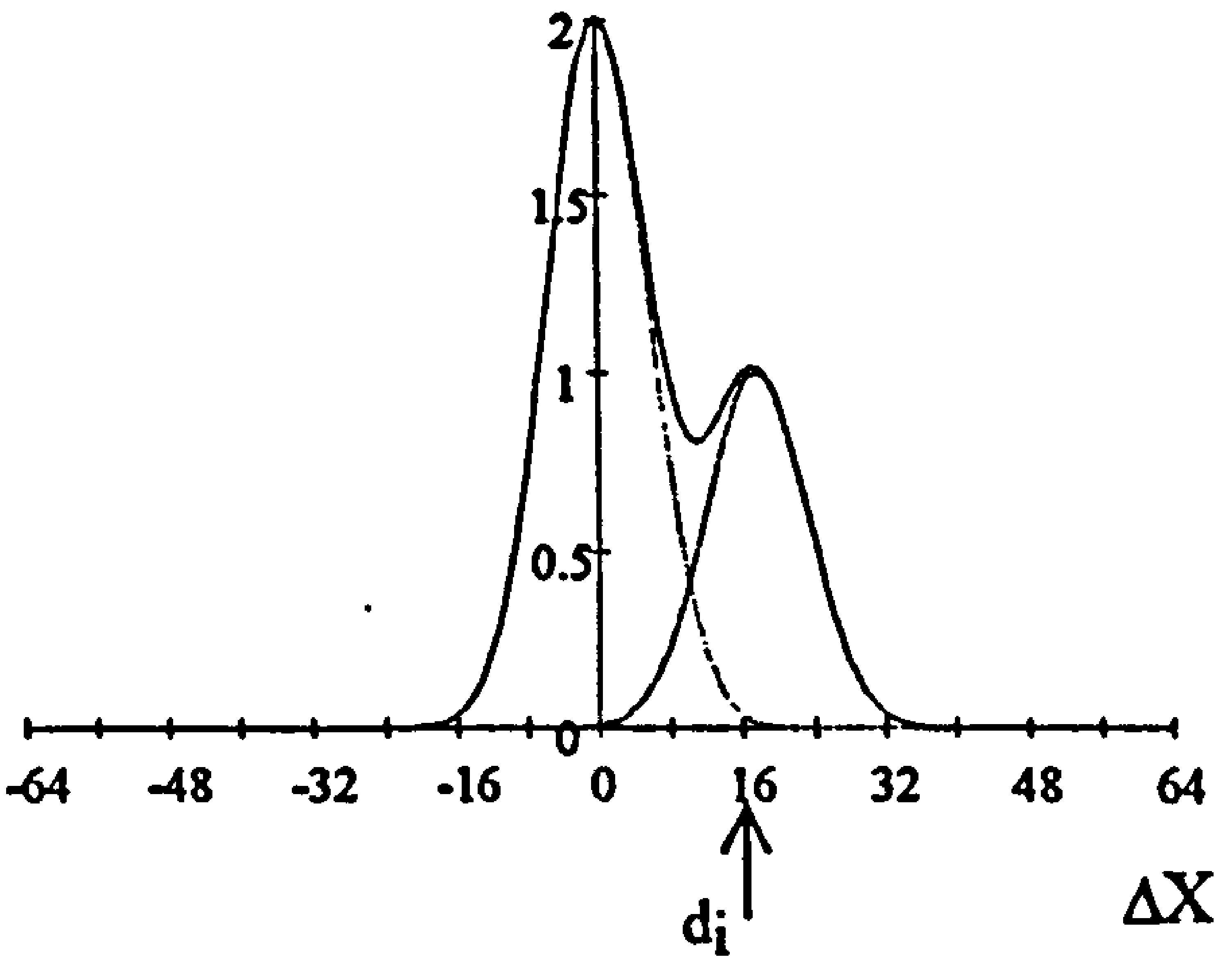

c) Signal peak well resolved: $\Delta X = 1.1d_i$

Figure 2.8 Resolution criteria for minimum detectable displacement in an autocorrelation. d_i= 16 pixels.

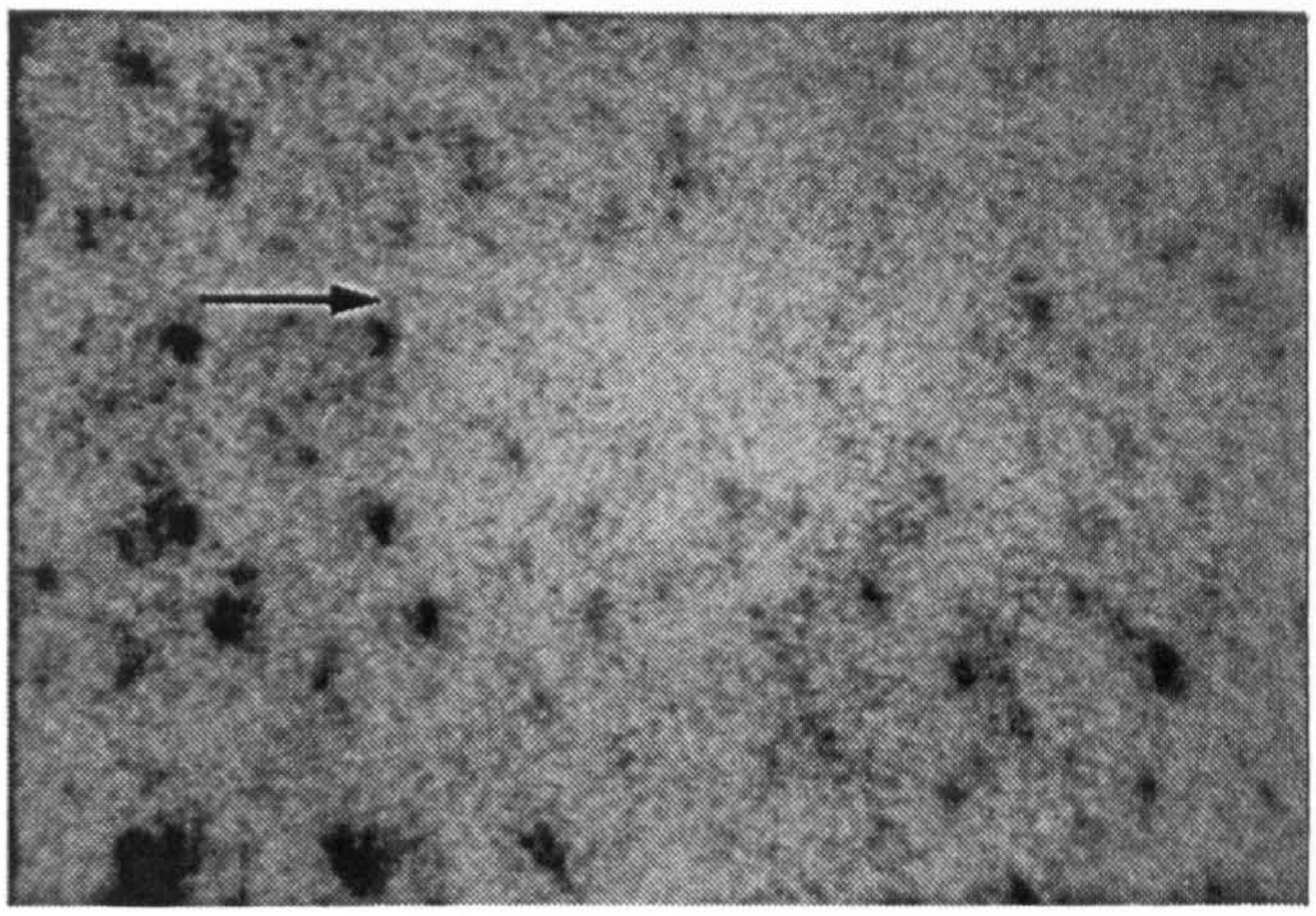

a) Particle images with horizontal displacement vector indicated

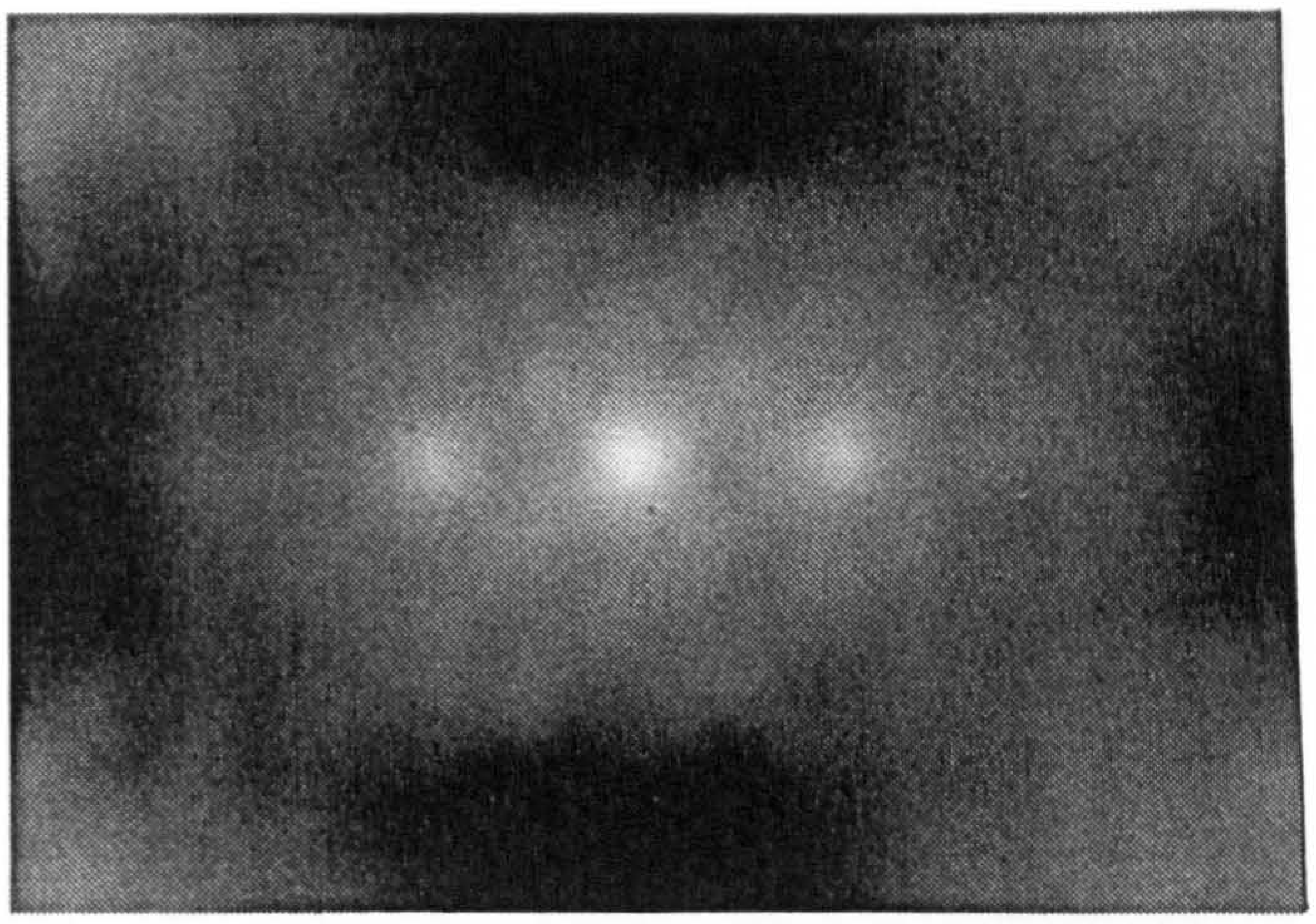

b) Autocorrelation of the above

Figure 2.9 Typical particle double-images recorded within engine flow through a flat window and their autocorrelation.

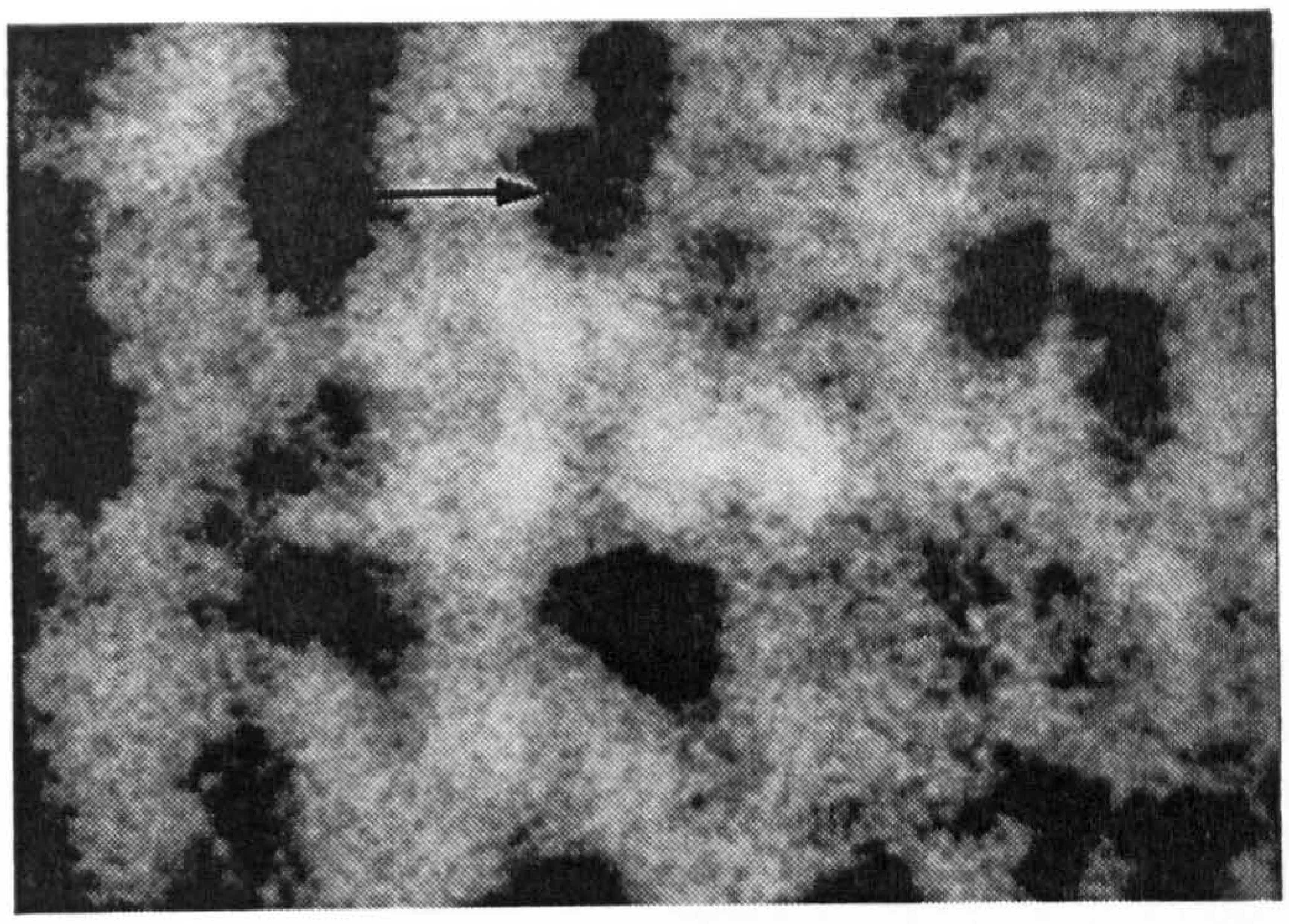

a) Particle images with horizontal displacement vector indicated. Aberrated particle image diameters approximately 100 μm.

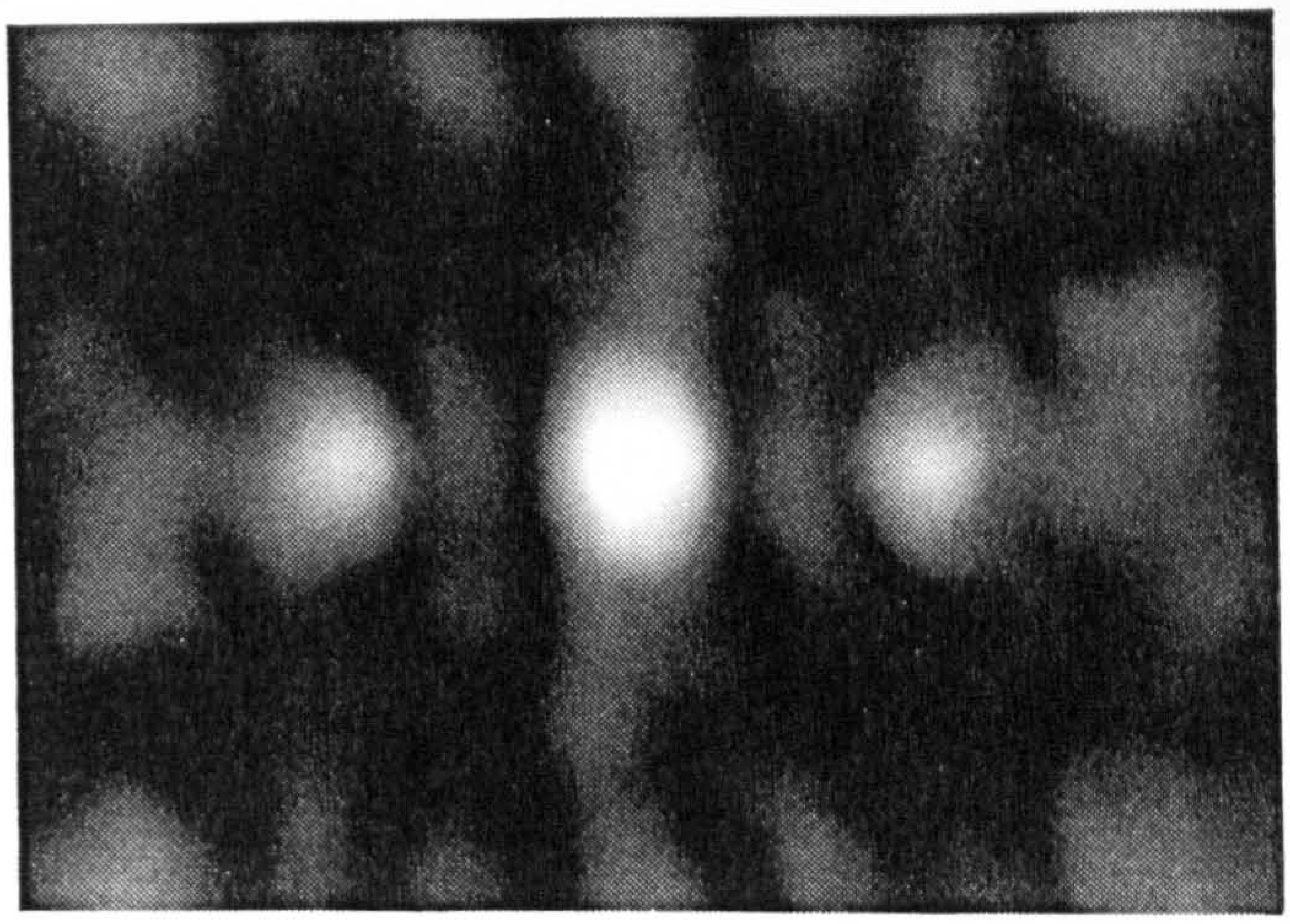

b) Autocorrelation of the above, showing enlarged, distorted peaks and limited measurement dynamic range.

Figure 2.10 Particle double-images recorded through a glass cylinder and their autocorrelation.

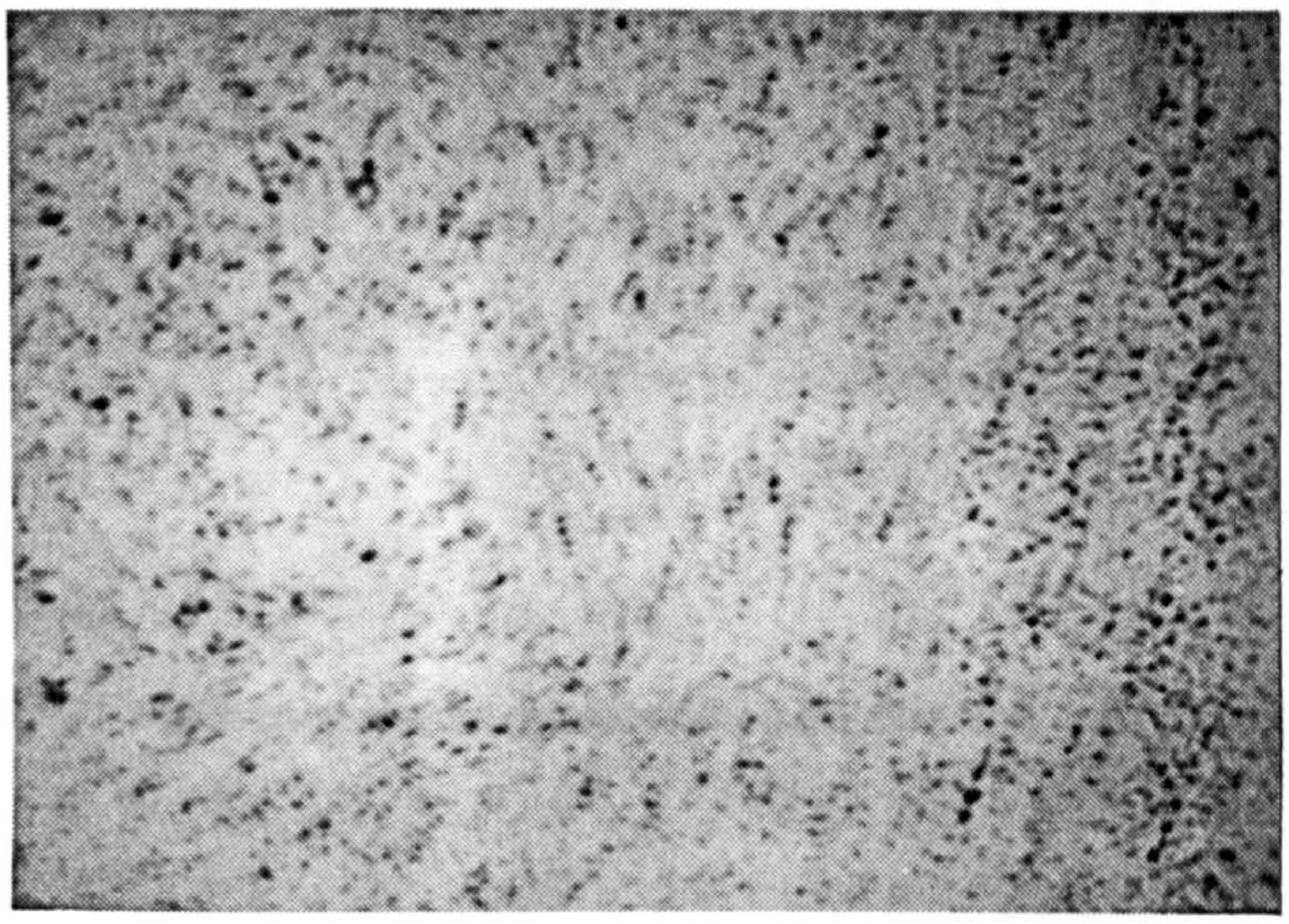

scale

1.0 mm

Figure 2.11 Detail from typical PIV image at mid-compression showing high spatial velocity gradients and small scale flow structure.

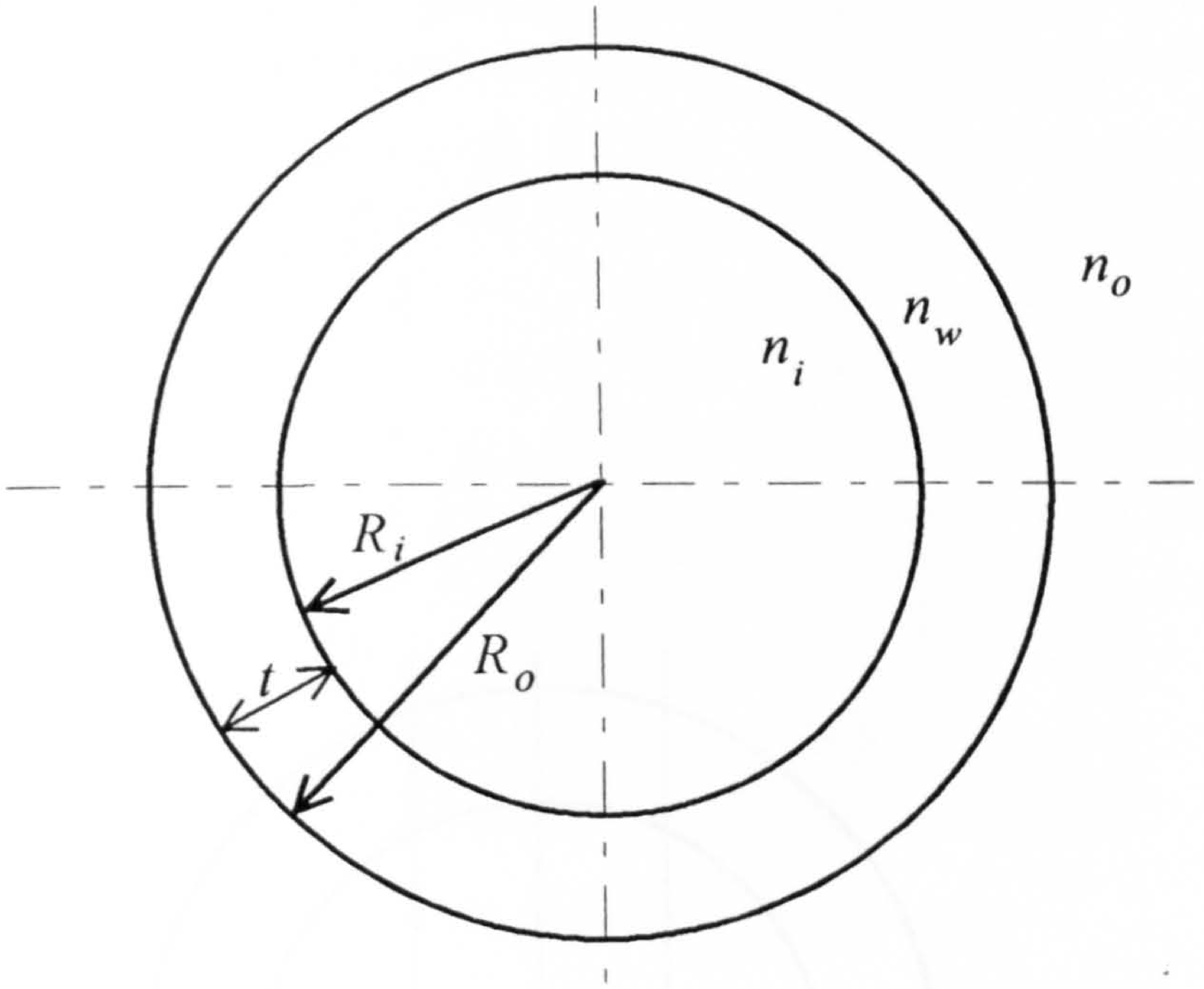

Figure 3.1 Geometry and properties of a general optical cylinder

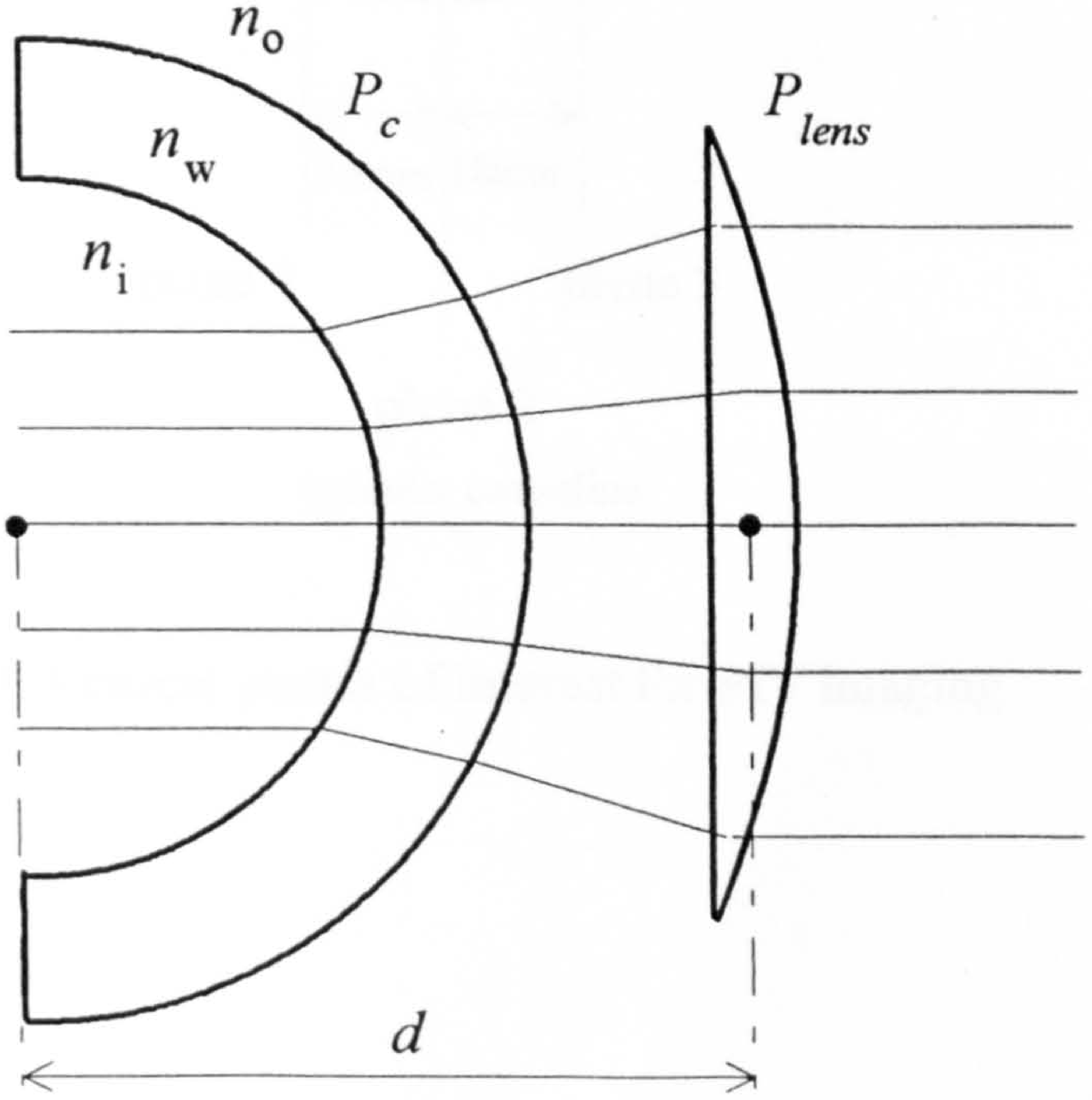

Figure 3.2 Arrangement for retaining in-cylinder collimation using a cylindrical lens

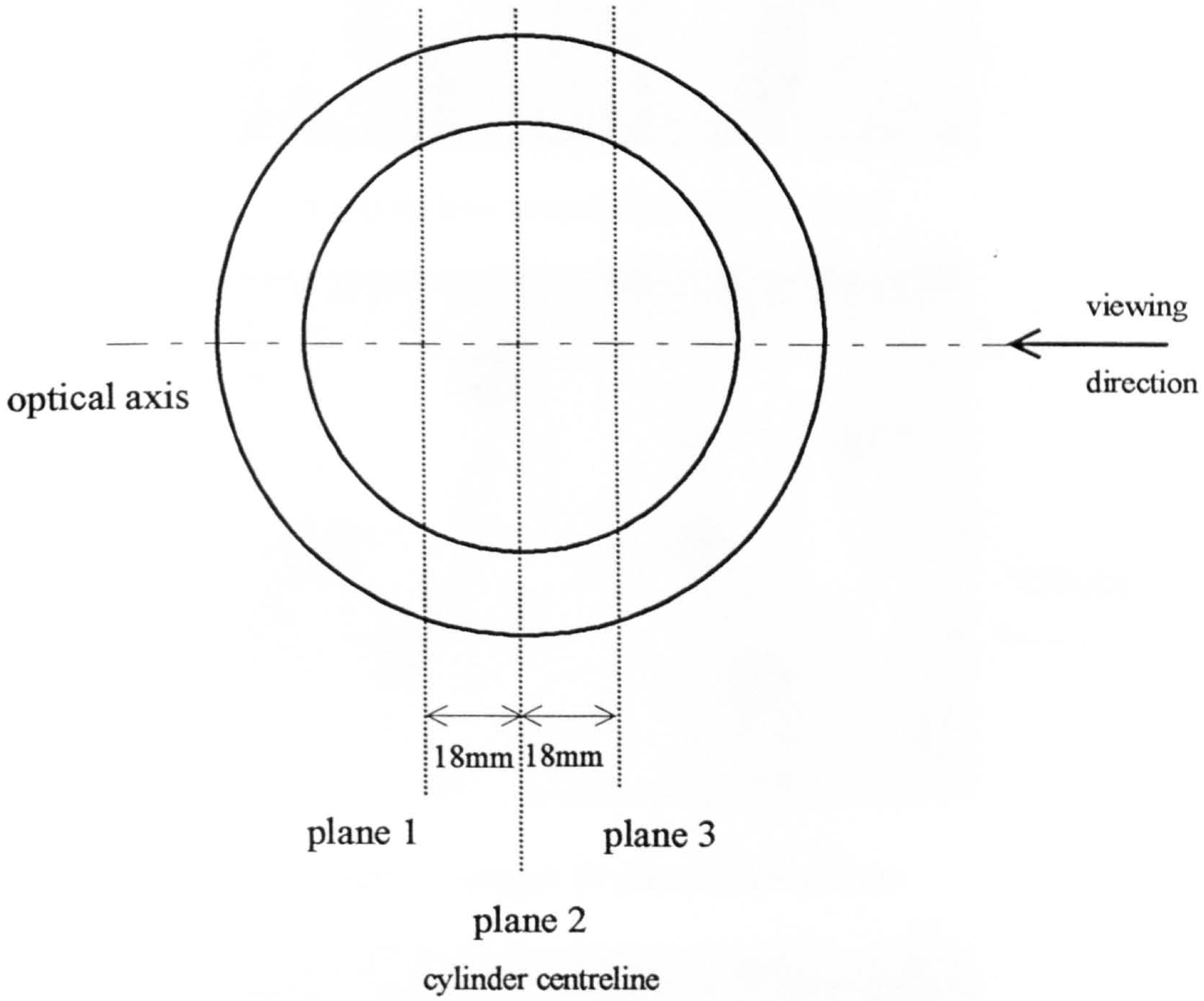

Figure 3.3 Vertical planes of interest for PIV imaging

Figure 3.4 Example astigmatic particle images from plane 2 without optical correction at three focal positions along the optical axis

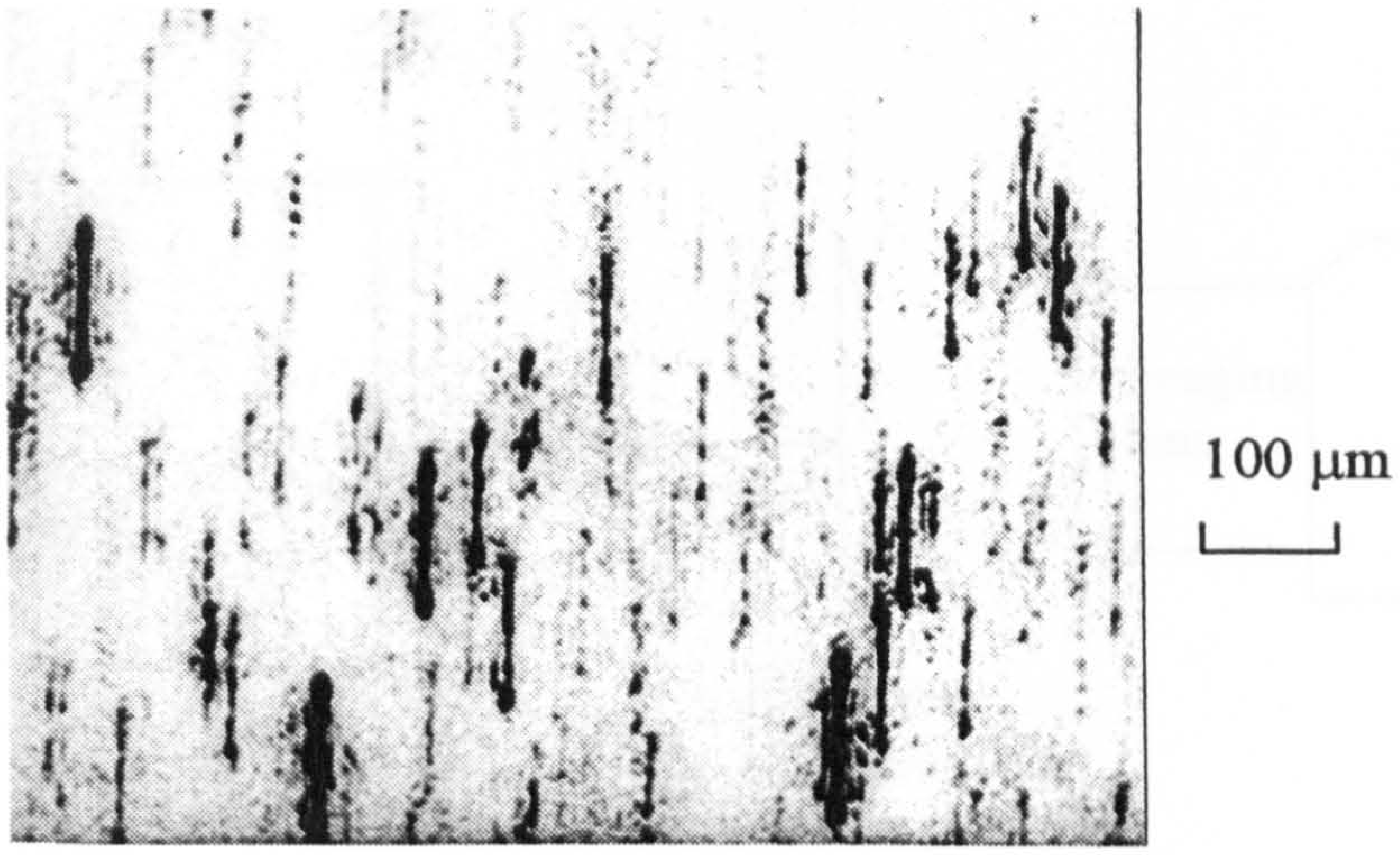

a) Vertical line focus from sagittal rays

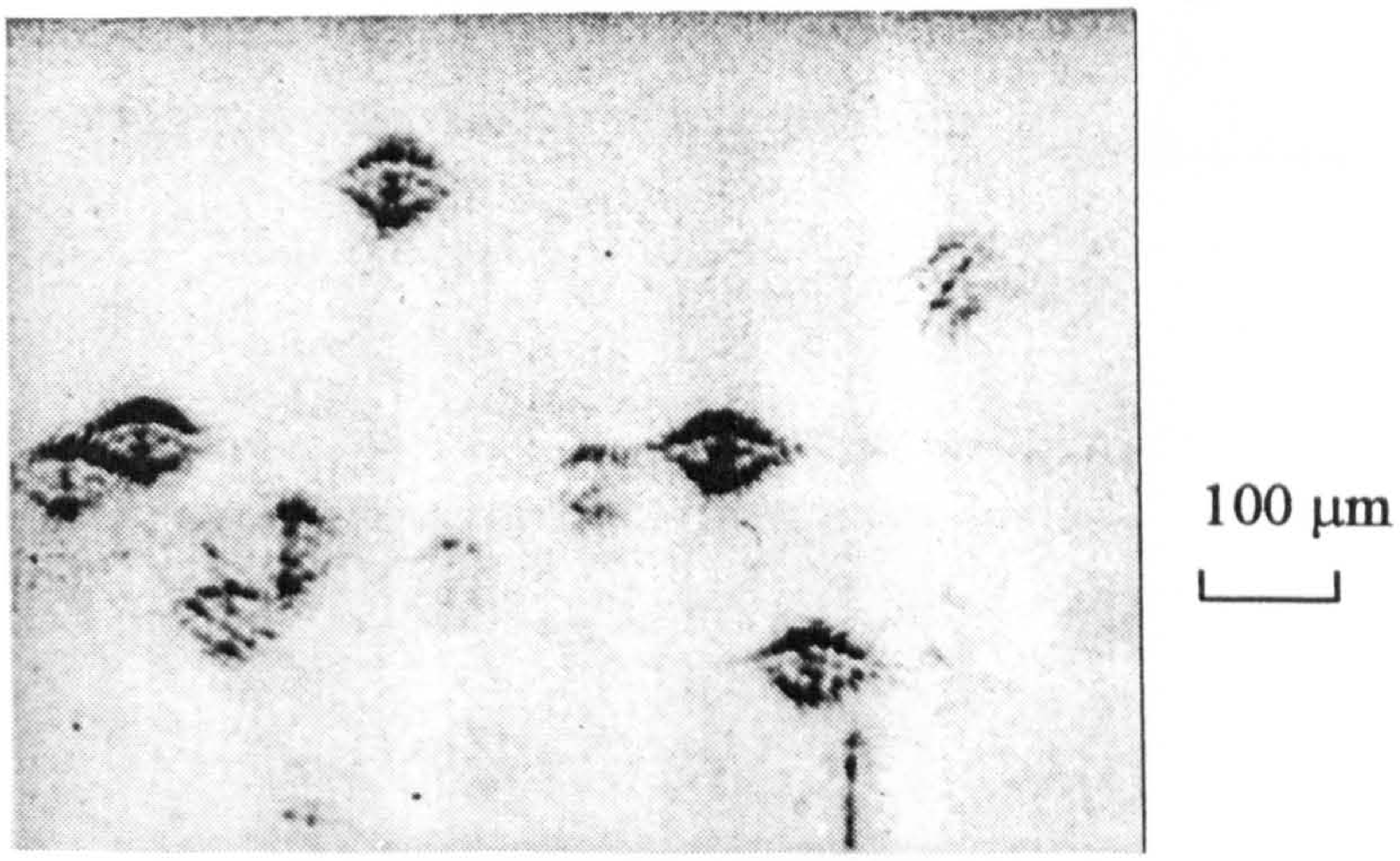

b) Particle images in plane of best focus

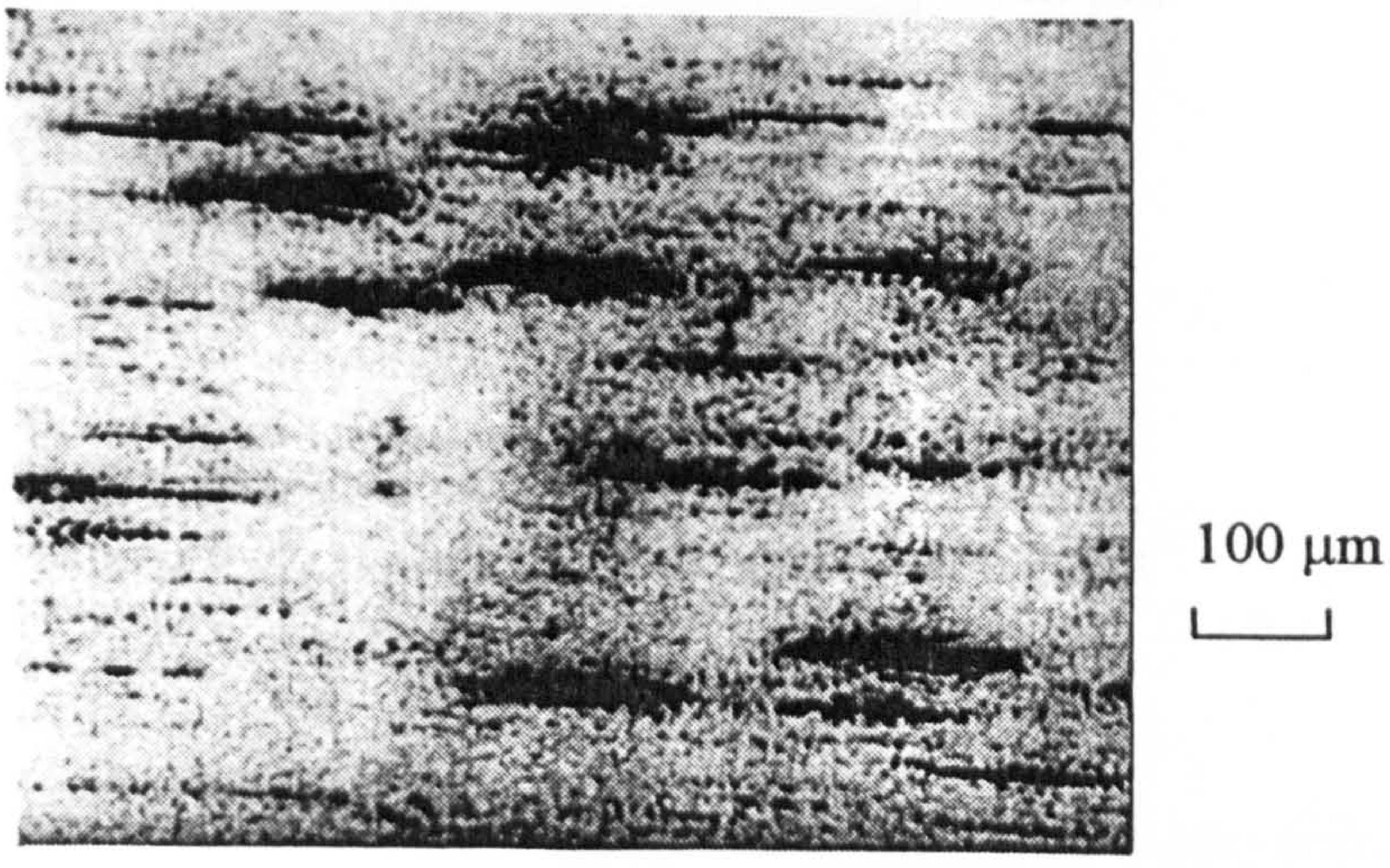

c) Horizontal line focus from meridional rays

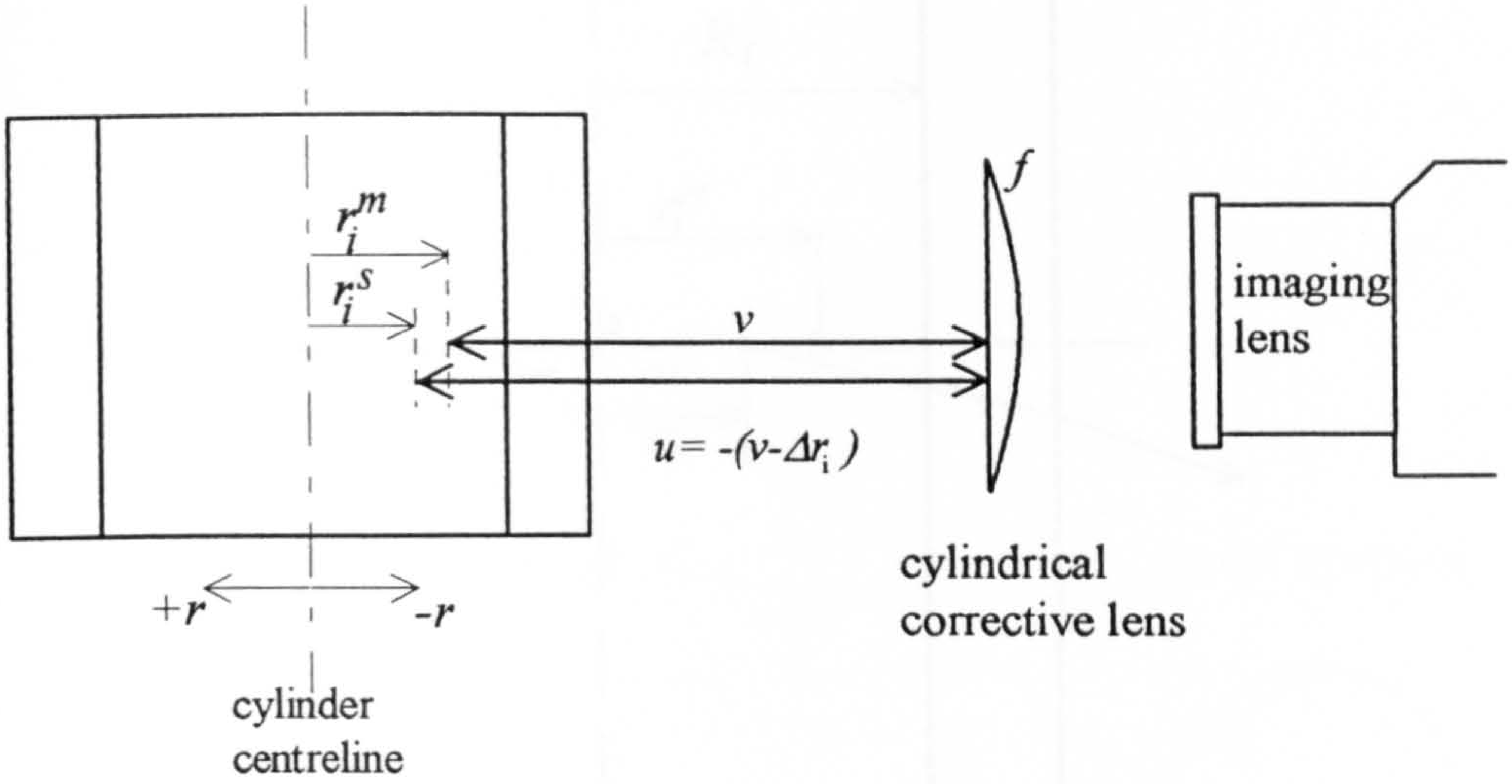

Figure 3.5 Geometry for correction of astigmatism

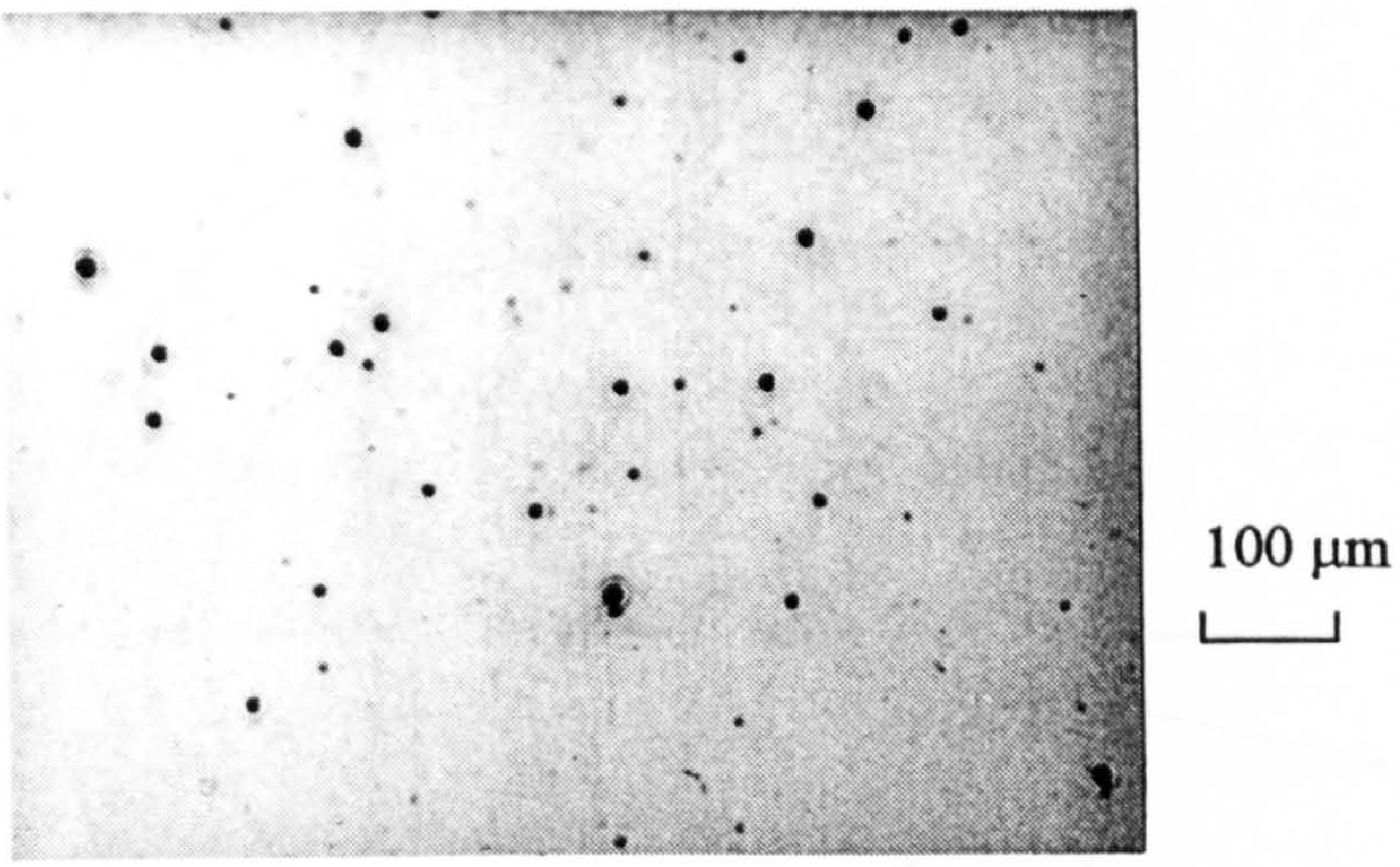

Figure 3.6 Corrected on-axis particle images from plane 2, achieved with a 4m focal length cylindrical lens

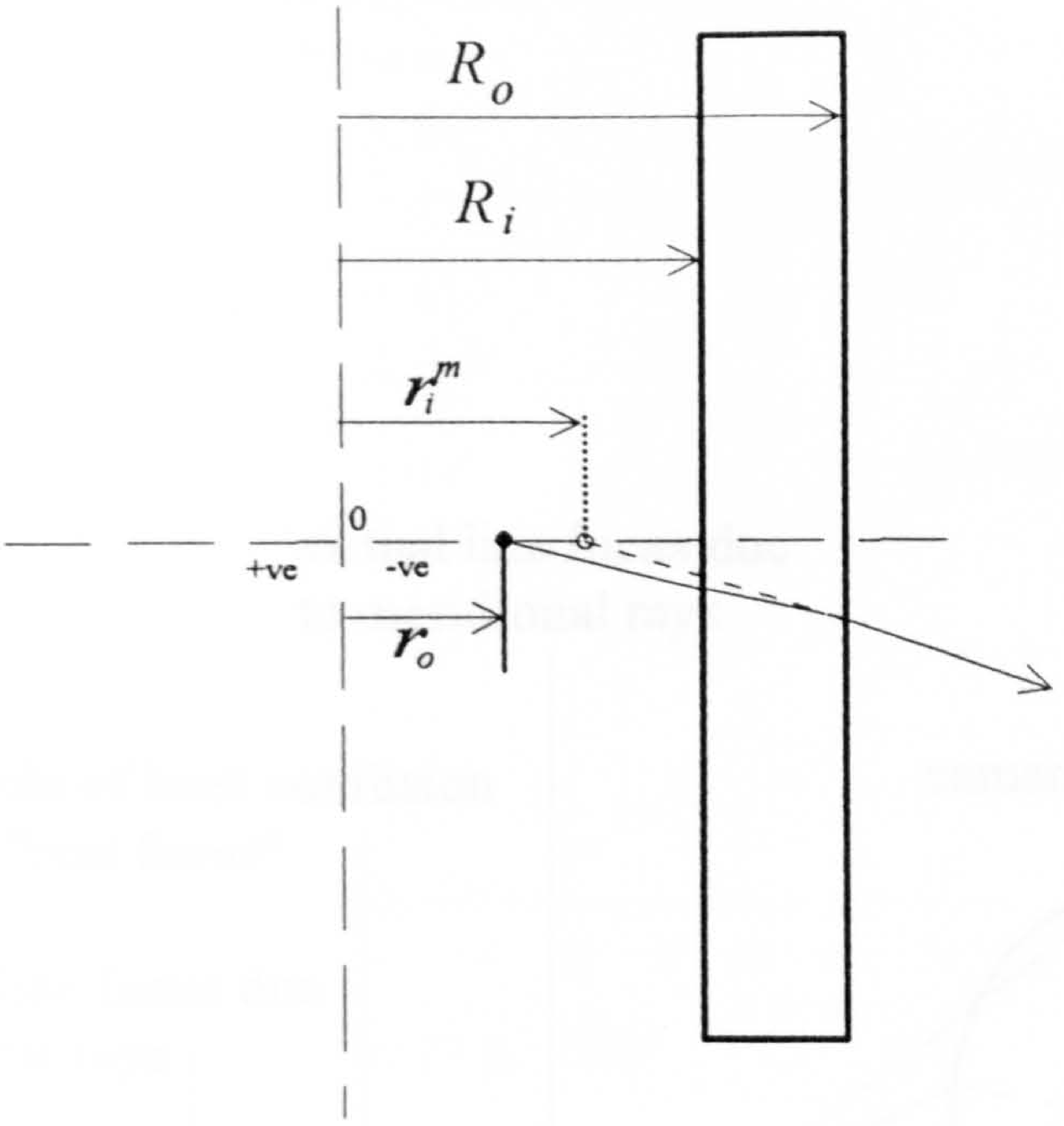

Figure 3.7 Formation of virtual image for meridional rays for an object at r_o

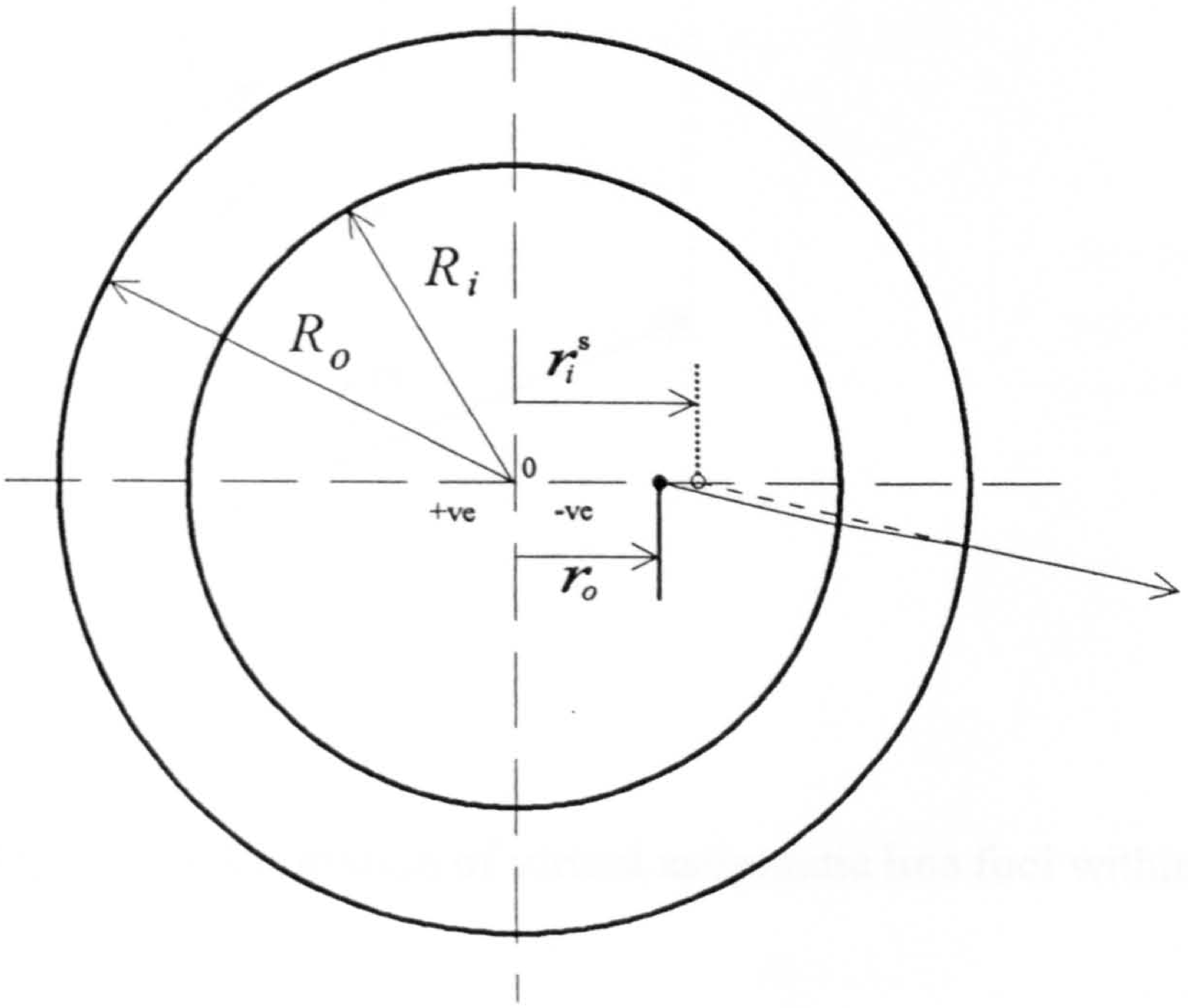

Figure 3.8 Formation of virtual image for sagittal rays for an object at r_o

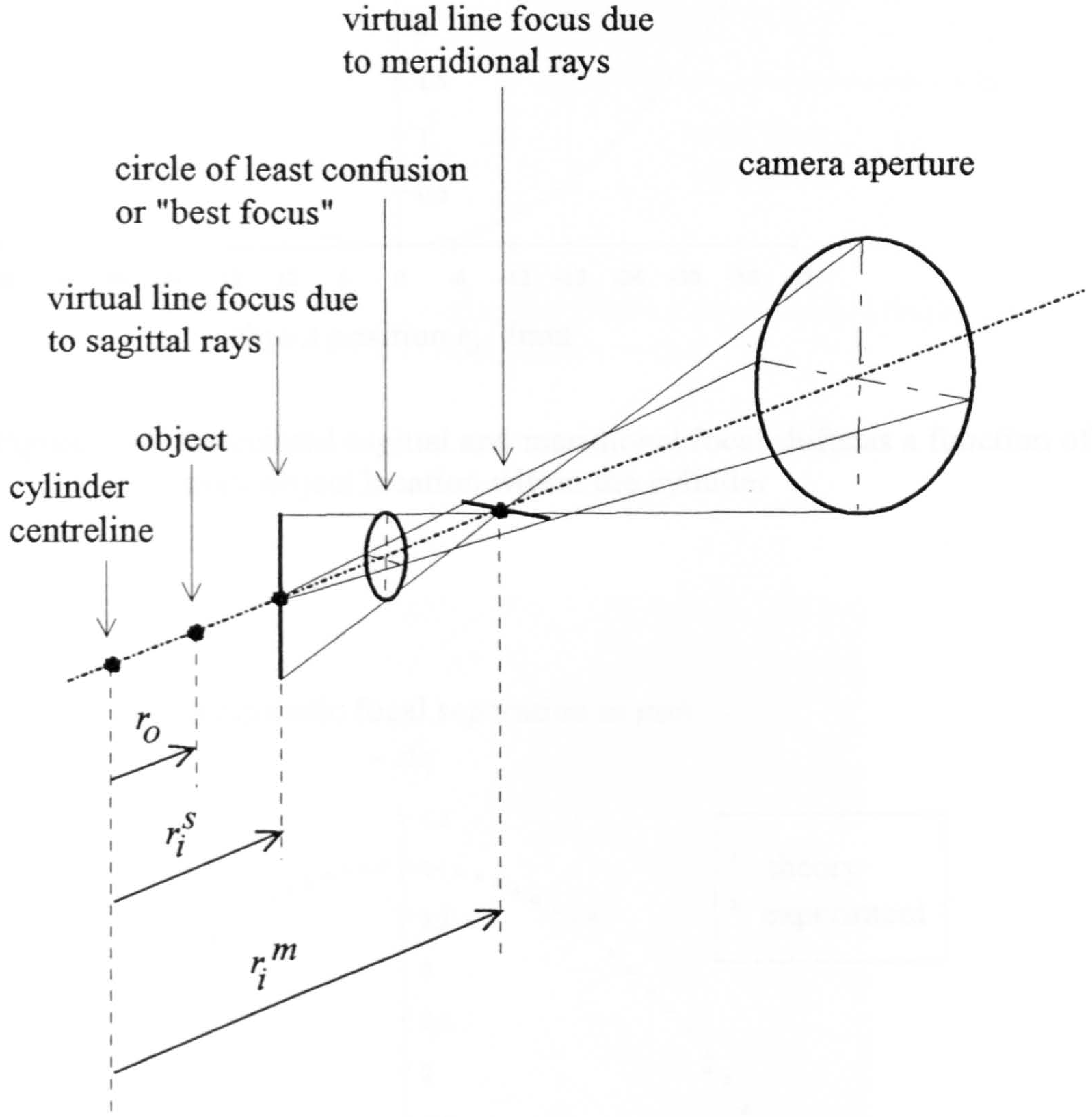

Figure 3.9 Formation of virtual astigmatic line foci within the cylinder.

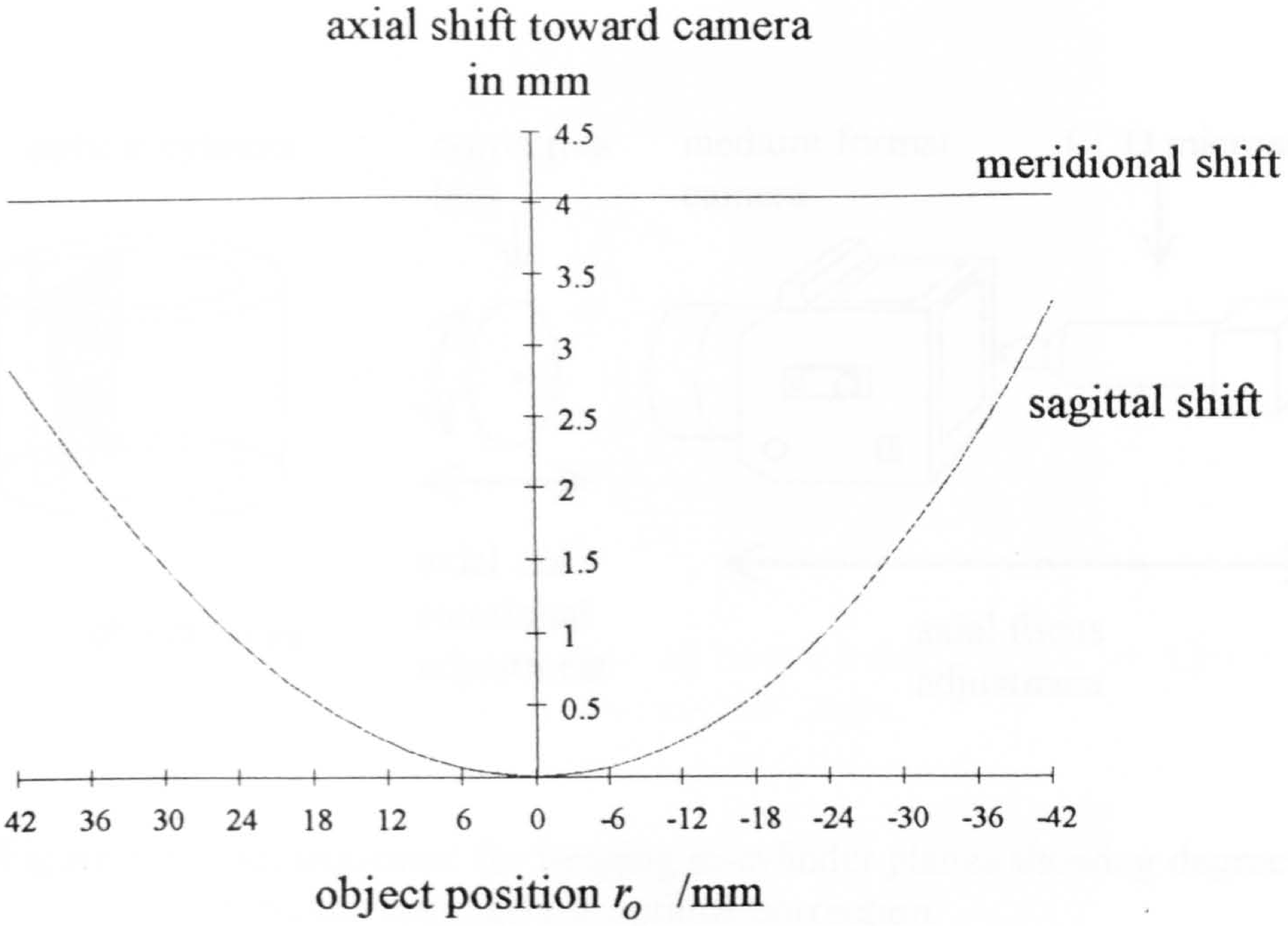

Figure 3.10 Calculated sagittal and meridional focal shifts as a function of axial object location within the cylinder

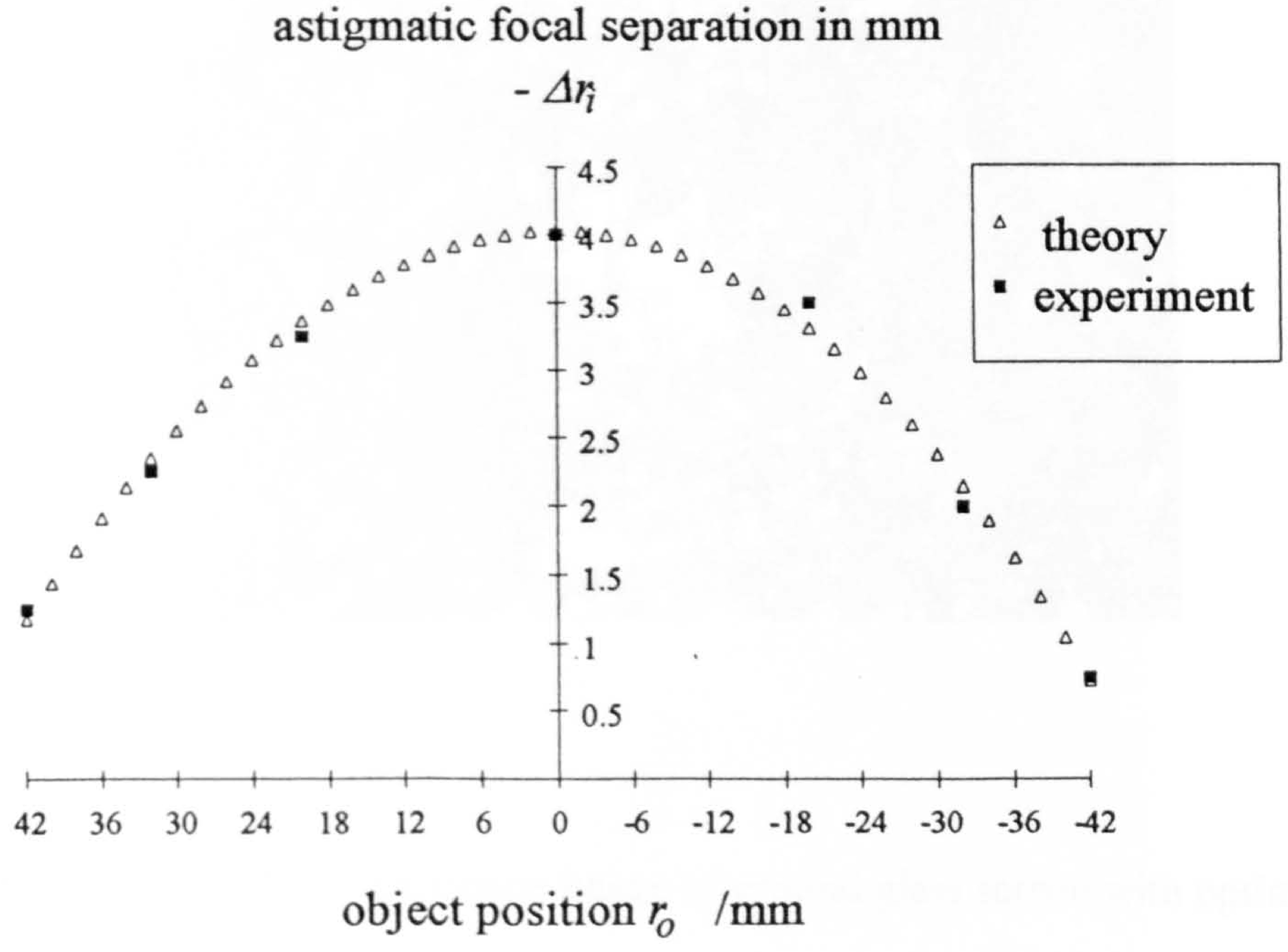

Figure 3.11 Calculated and experimental axial focal separations as a function of axial object position within the cylinder

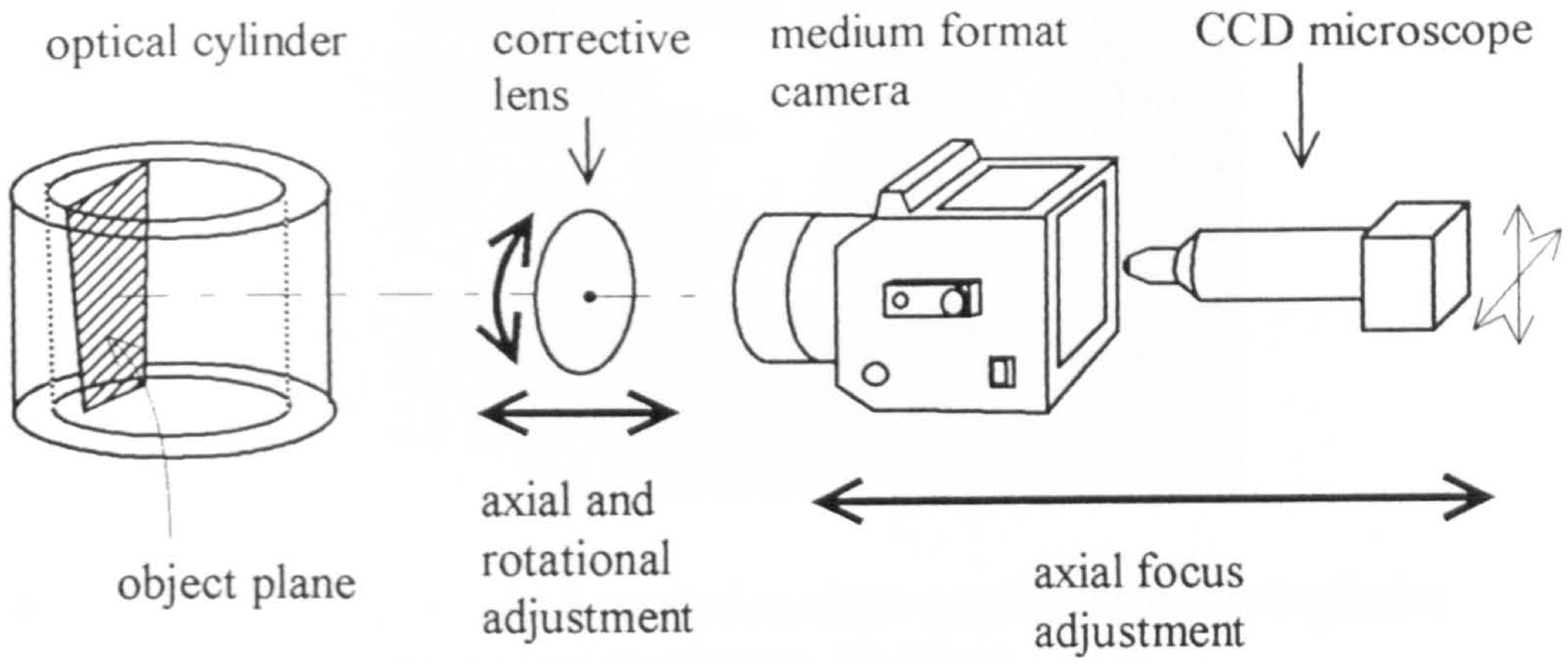

Figure 3.12 Arrangement for imaging in-cylinder planes showing degrees of freedom required for optimal correction.

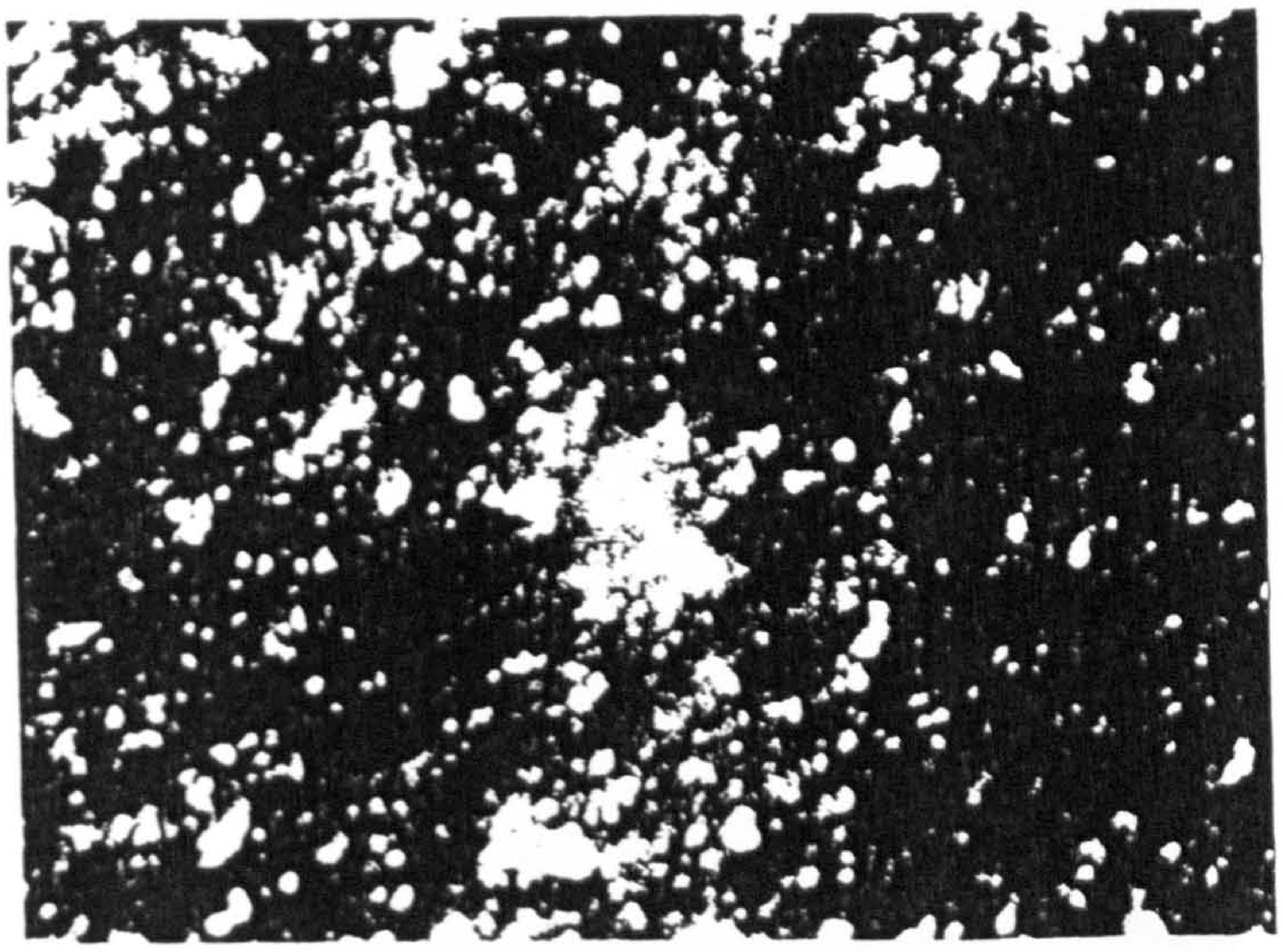

Figure 3.13 CCD microscope image of ground glass screen with optimal correction

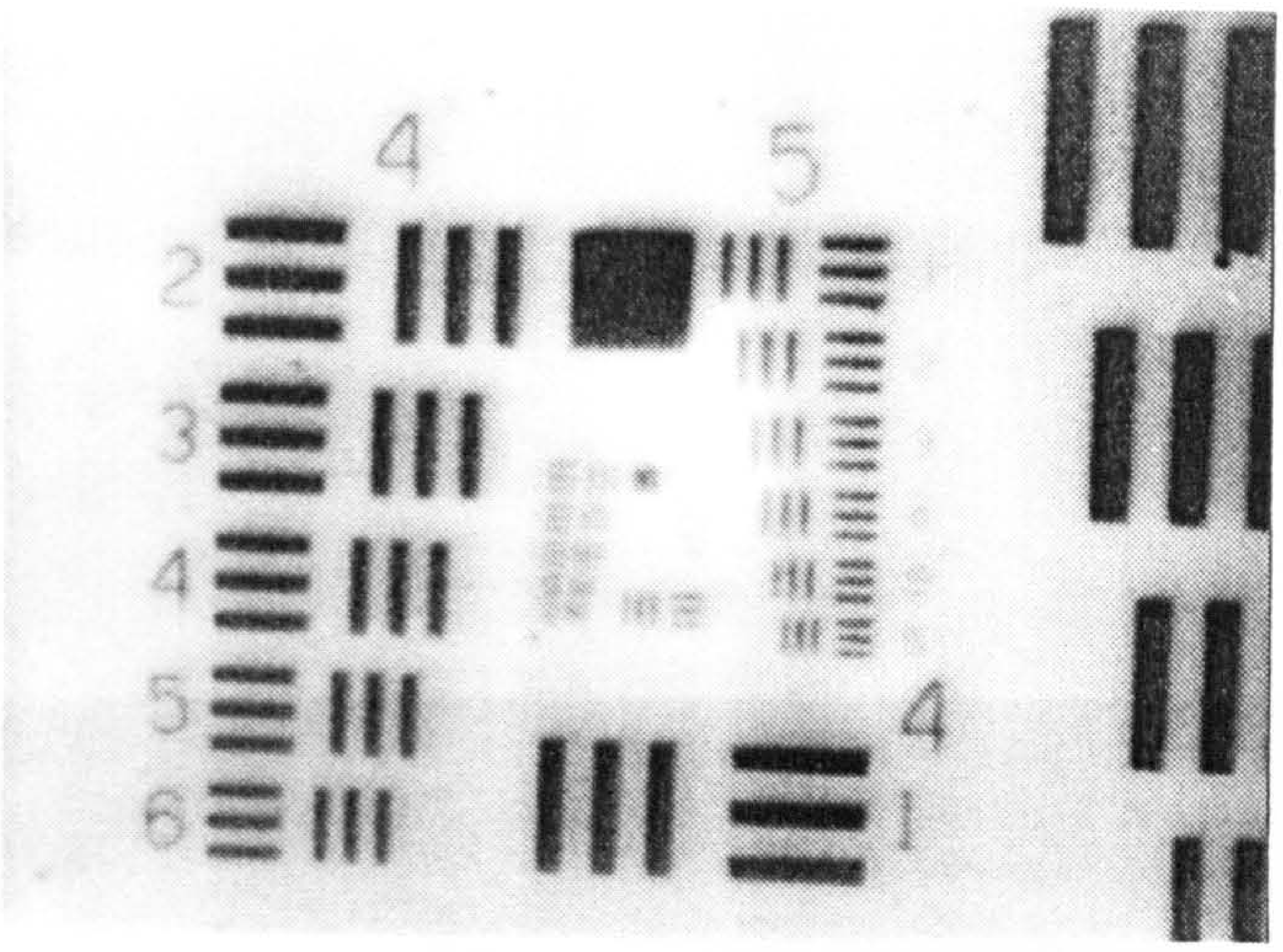

Figure 3.14 Image of USAF resolution chart outside the optical cylinder.
Full camera lens resolution: 10-20μm.

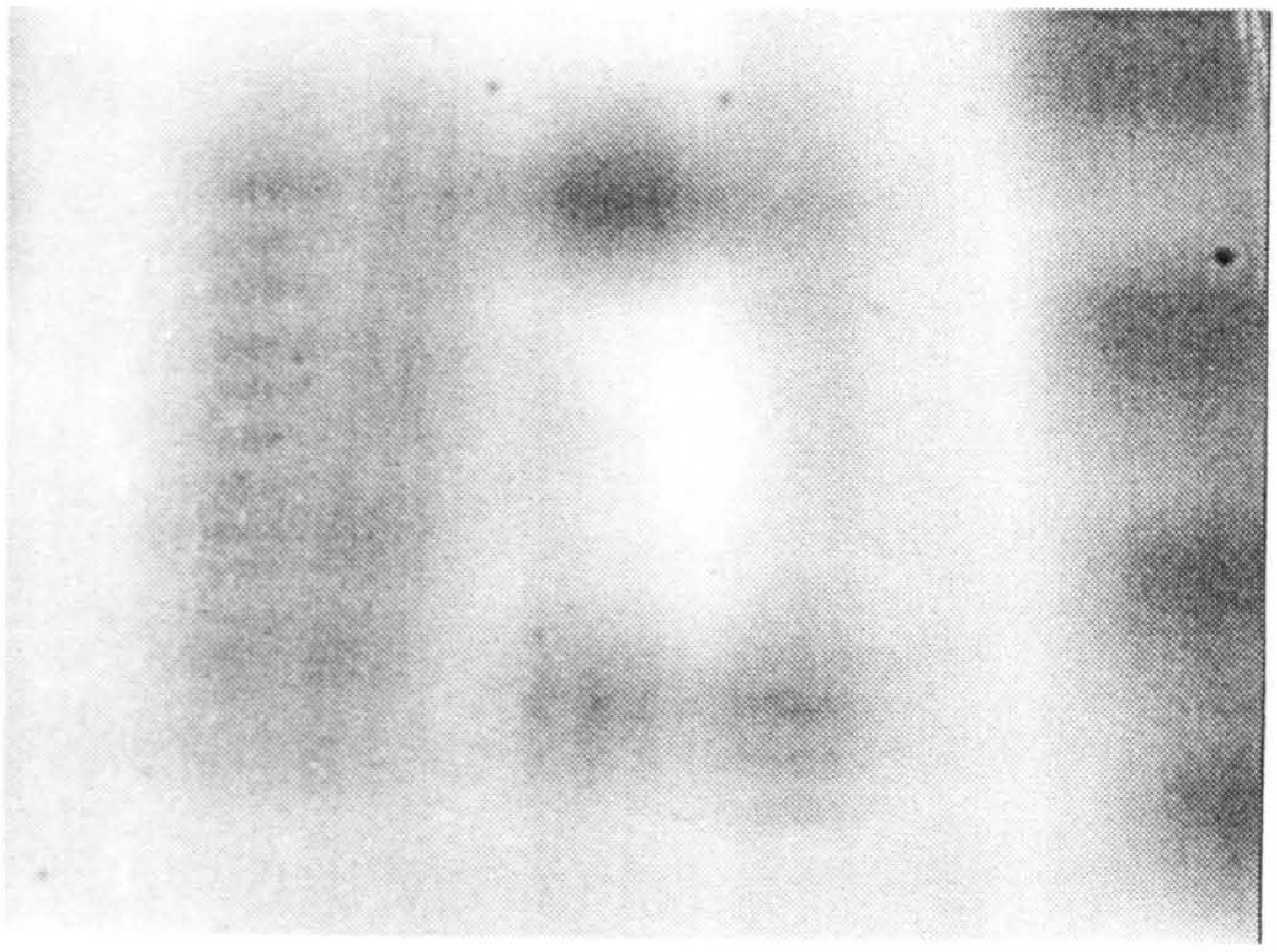

Figure 3.15 Image of USAF resolution chart in plane 2 within cylinder.
Best focus with no correction: resolution ~ 100 μm.

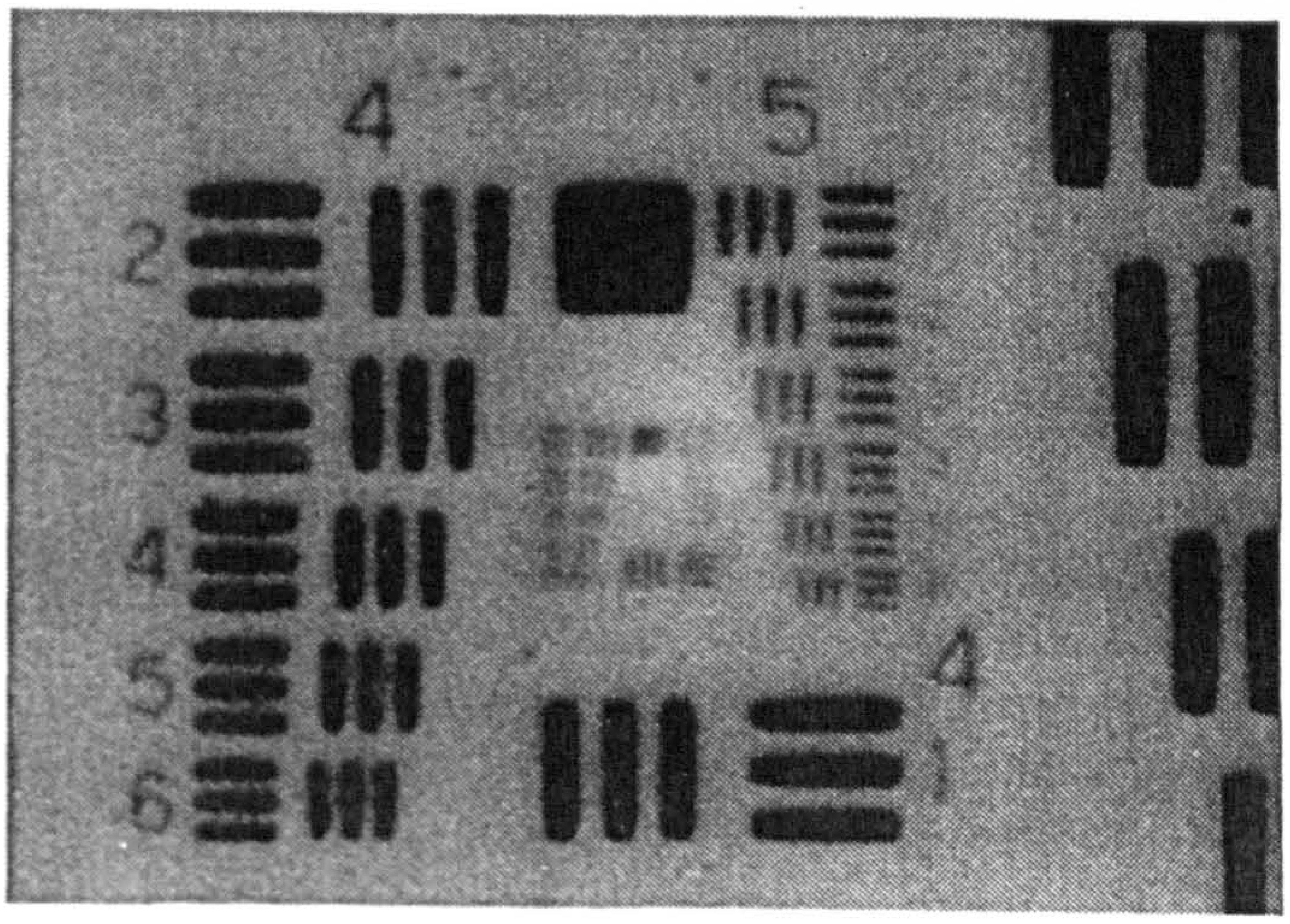

Figure 3.16 Image of USAF resolution chart in plane 2 with correction.
Resolution recovered: 10-20μm.

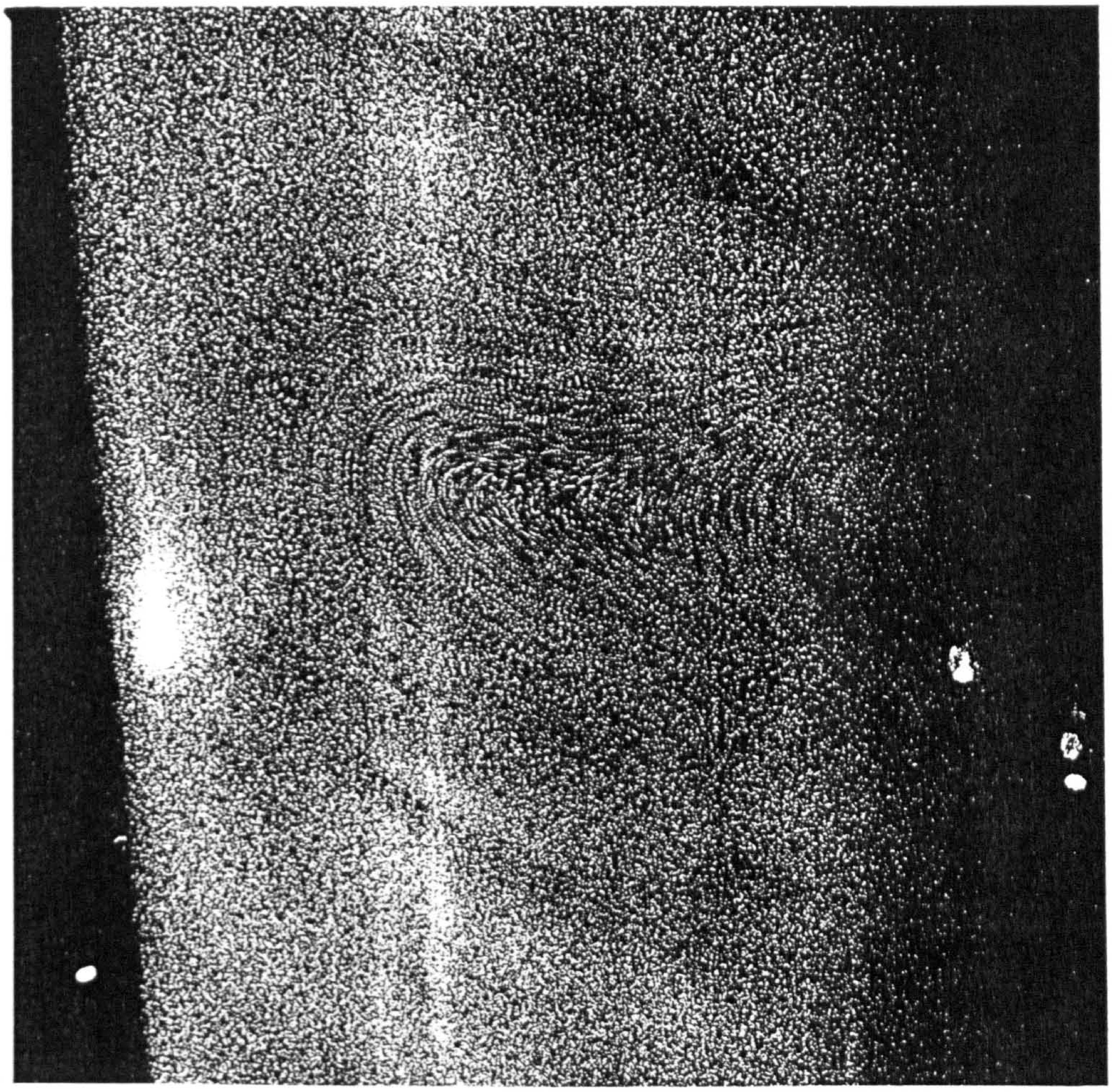

Figure 3.17 Multiple exposed images of sub-micron sized olive oil droplets convecting within the cylinder in plane 1, with optical correction. The illuminated area is approximately 4cm by 6cm.

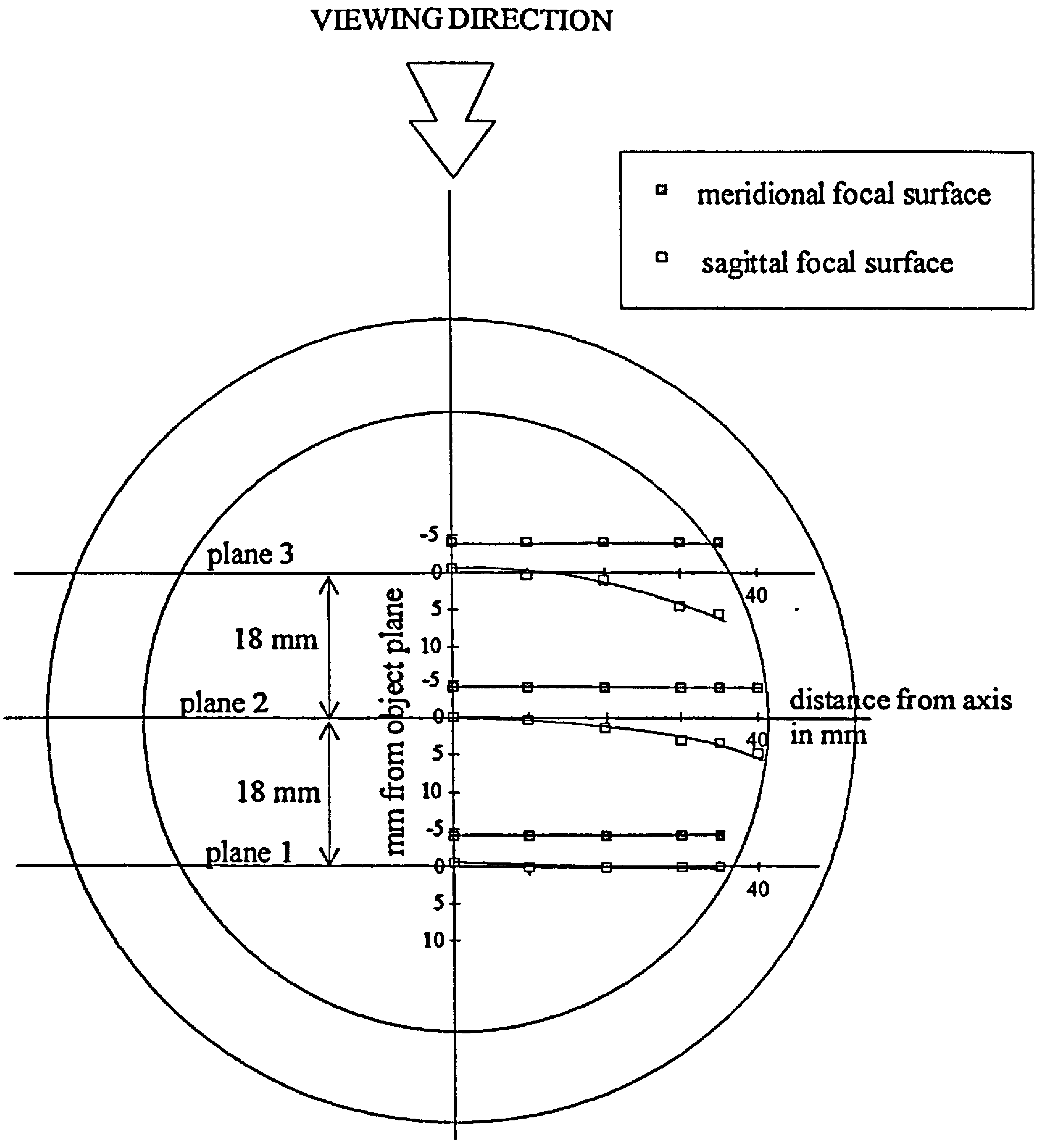

Figure 3.18 Shape of sagittal and meridional focal surfaces within engine cylinder (prior to correction).

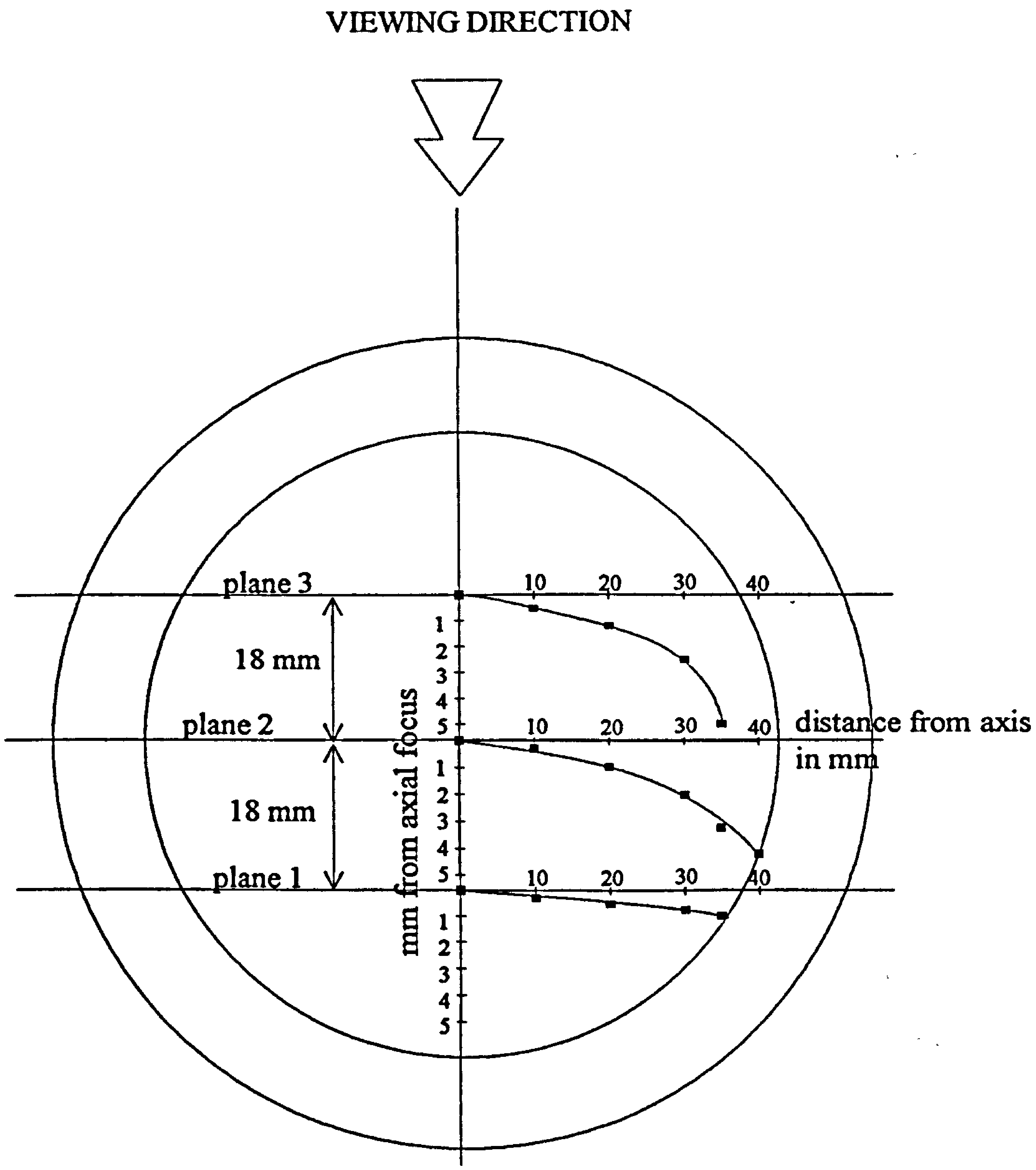

Figure 3.19 Shape of surfaces of best focus in three measurement planes with optical correction using an f=4m cylindrical lens.

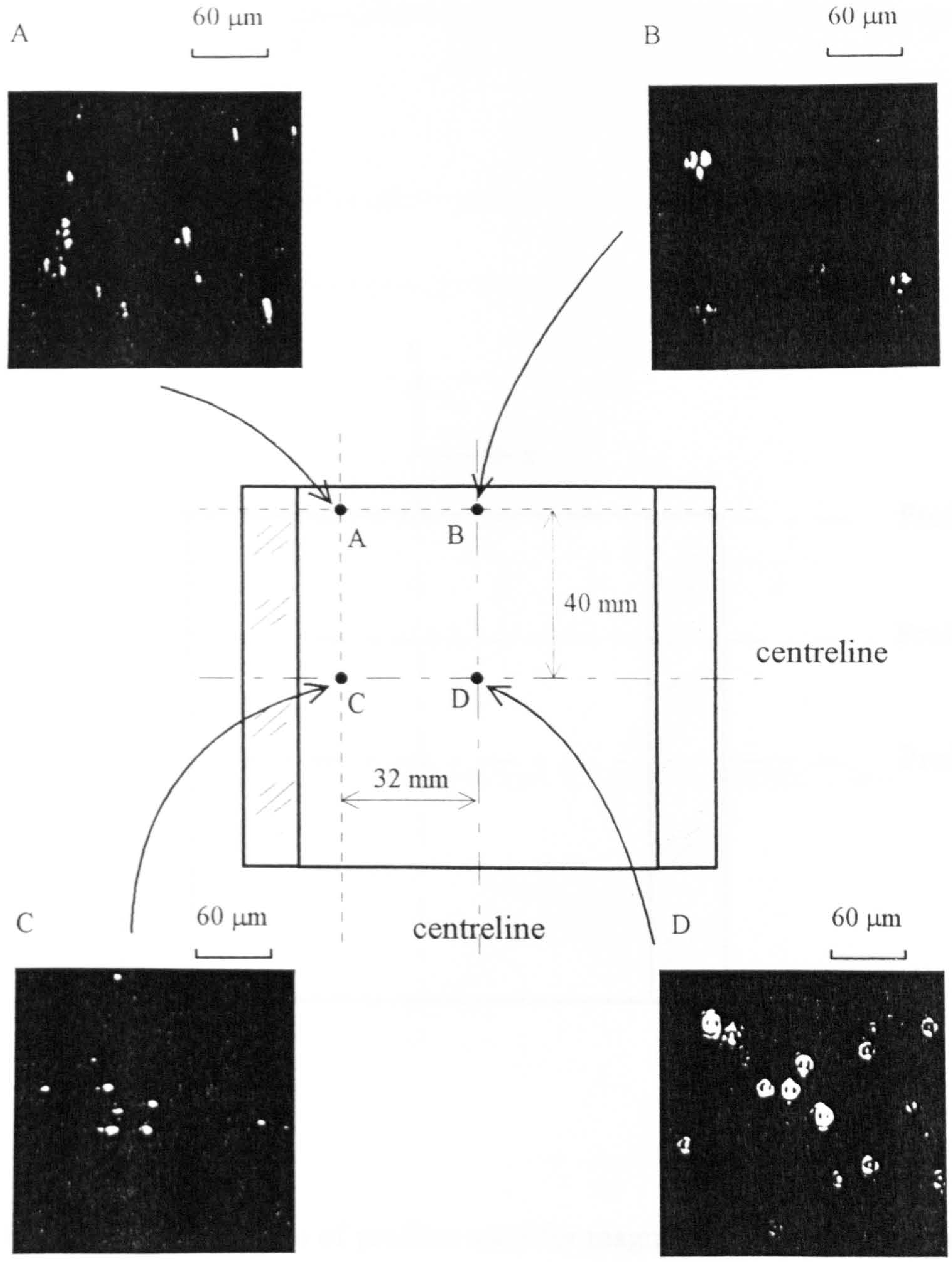

Figure 3.20 Appearance of corrected particle images in the worst case plane 2 using the f=4m corrective lens and a 1.0mm defocus at point D.

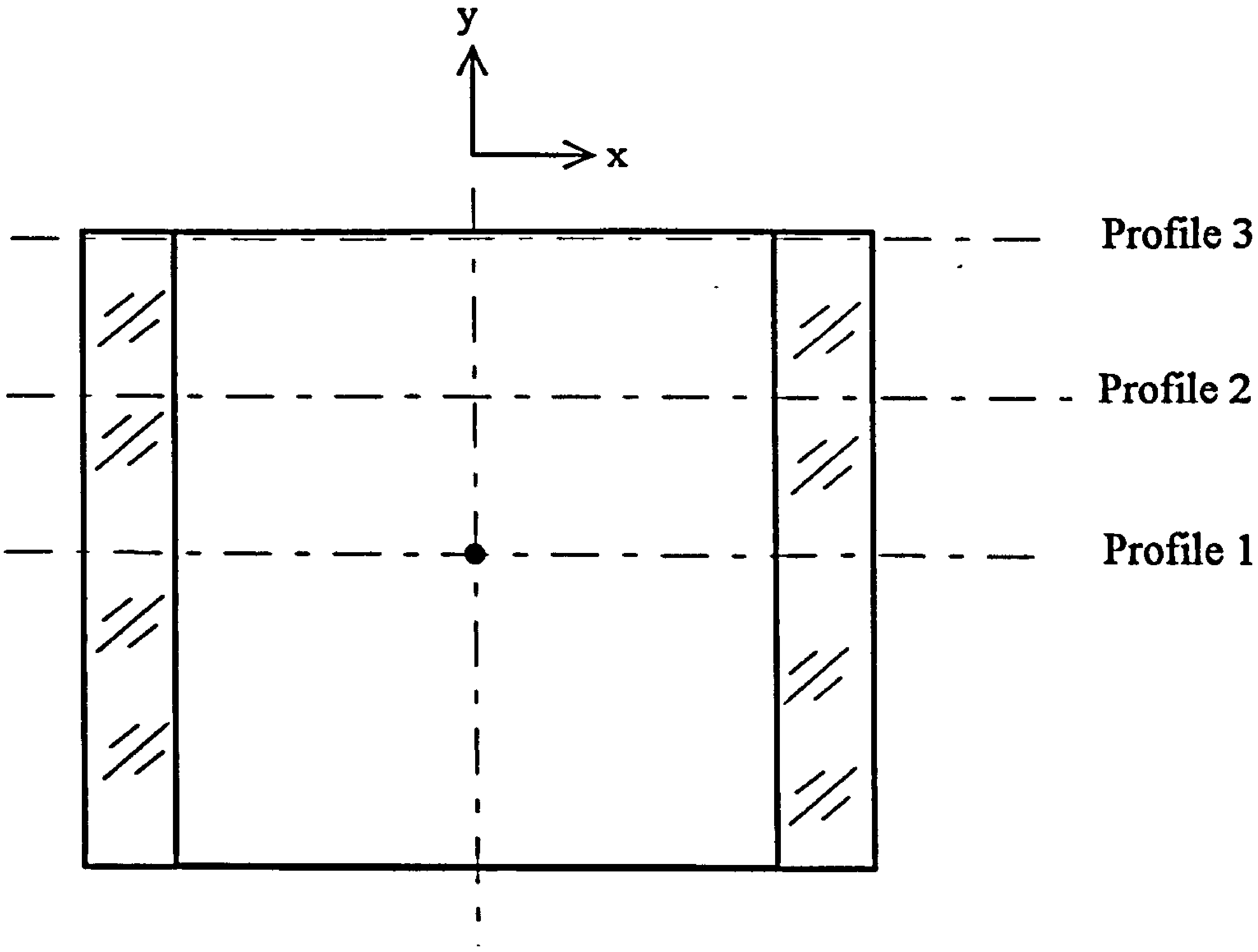

Figure 3.21 Locations of profiles used for magnification measurements

Figure 3.22 X and Y magnification changes with position within image for plane 2.

a) Y magnification against X position in film plane

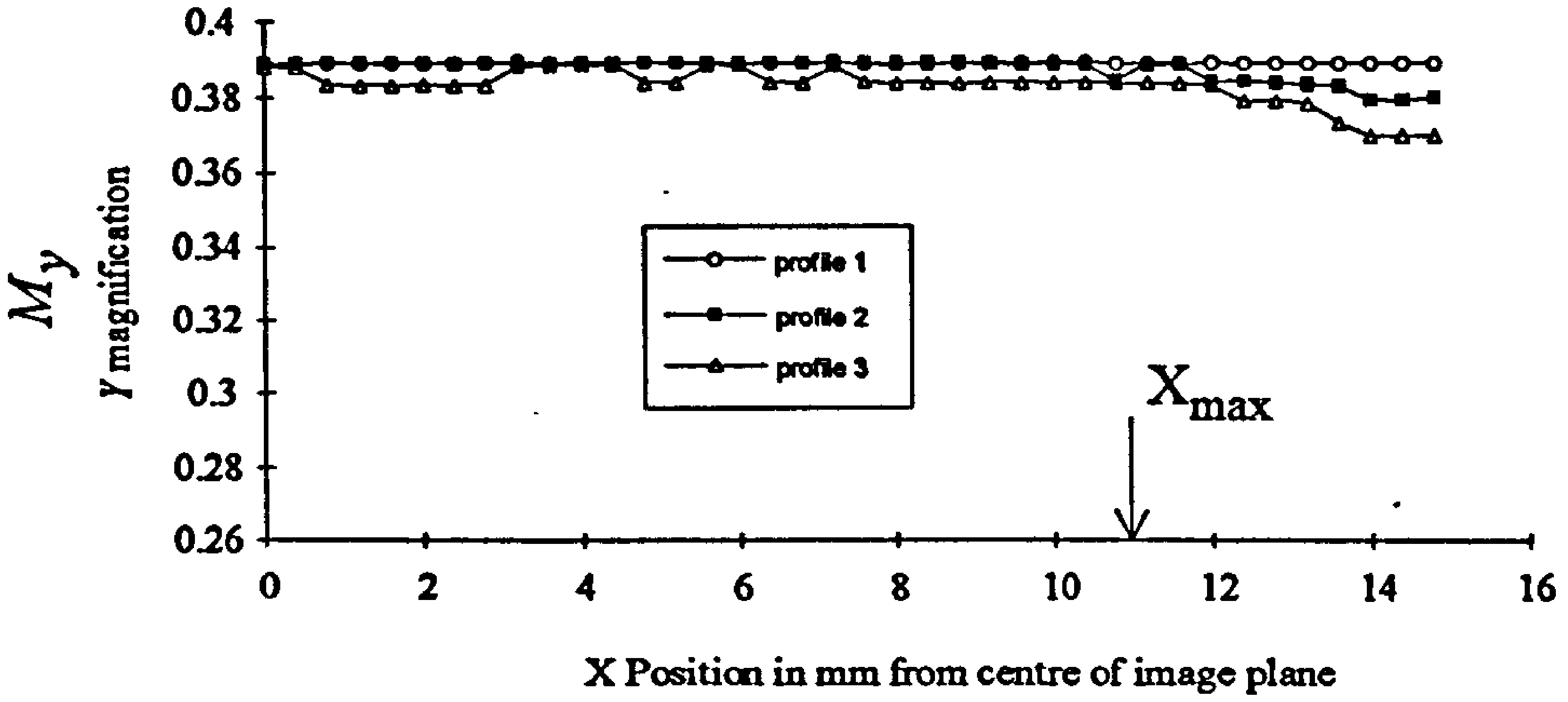

b) X magnification against X position in film plane

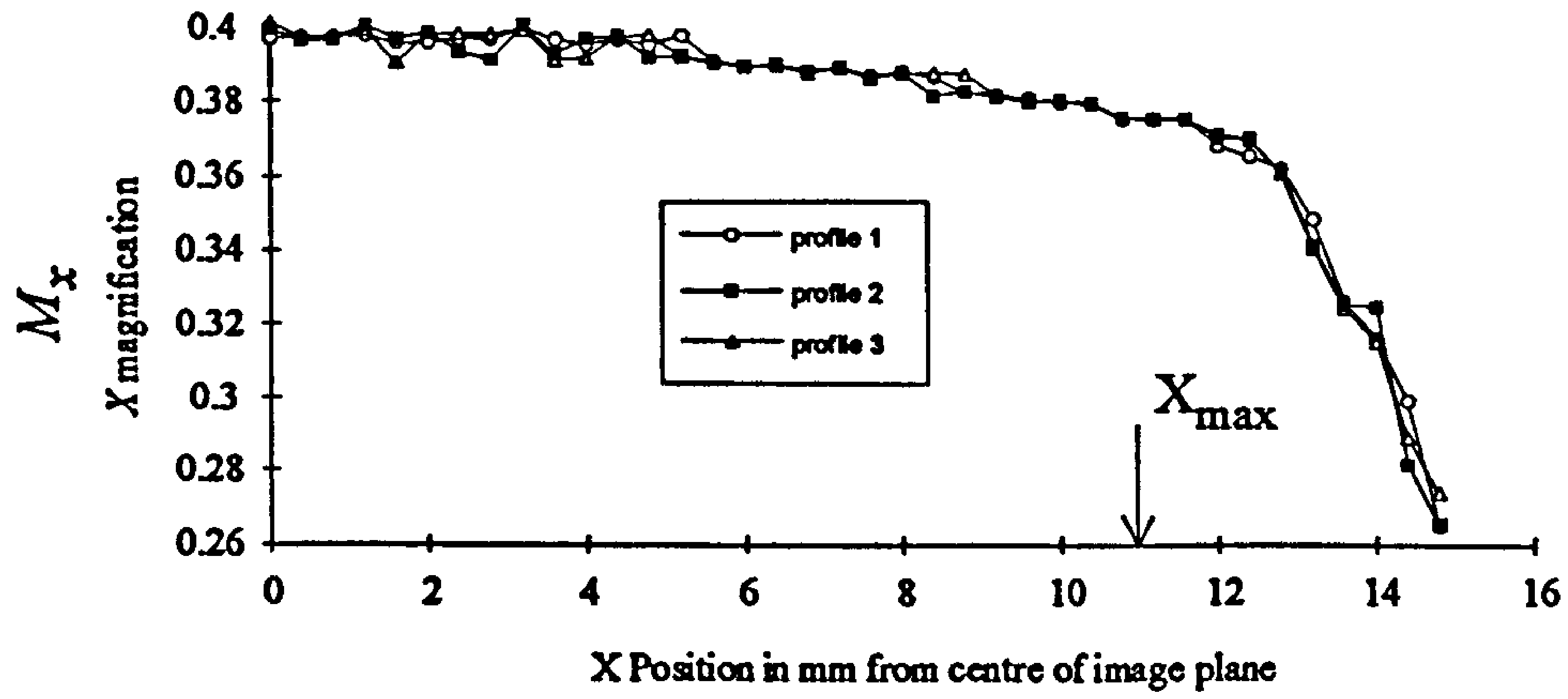

Figure 3.23 X and Y magnification changes with position within image for plane 1.

a) Y magnification against X position in film plane

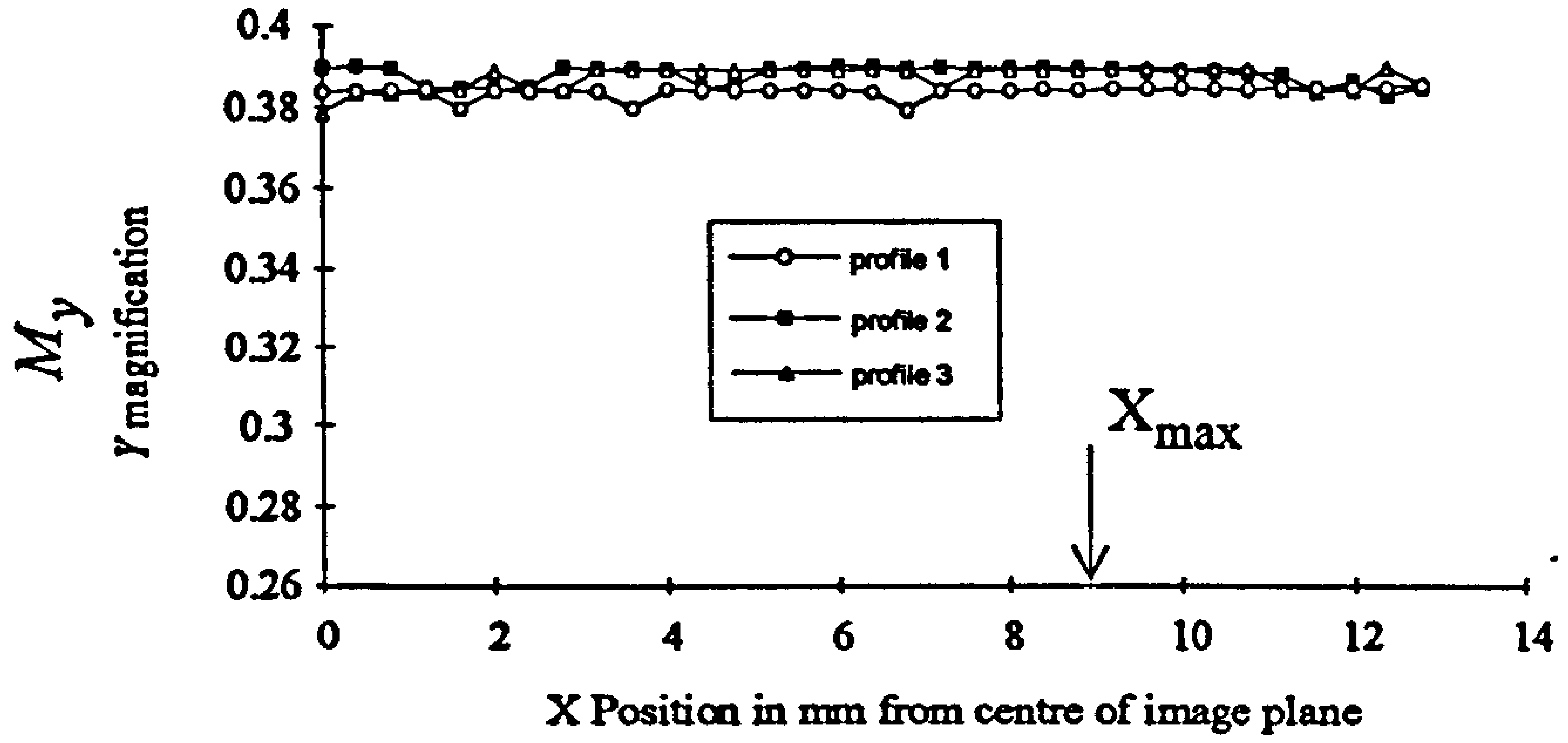

b) X magnification against X position in film plane

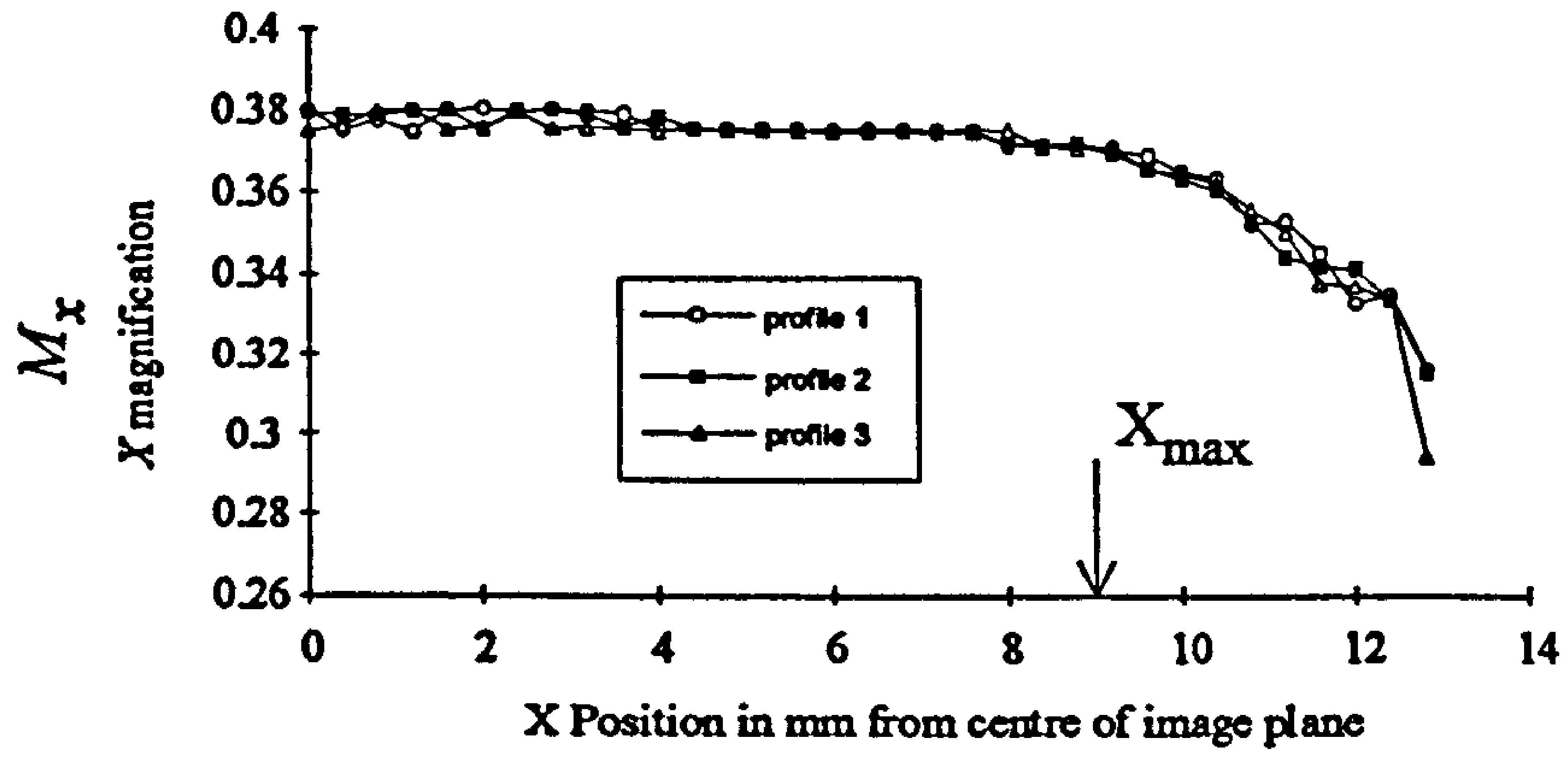

Figure 3.24 Position errors in flow due to magnification changes.
Fixed translation stage increment = 0.4mm.

a) bore centreline (plane 2) position error

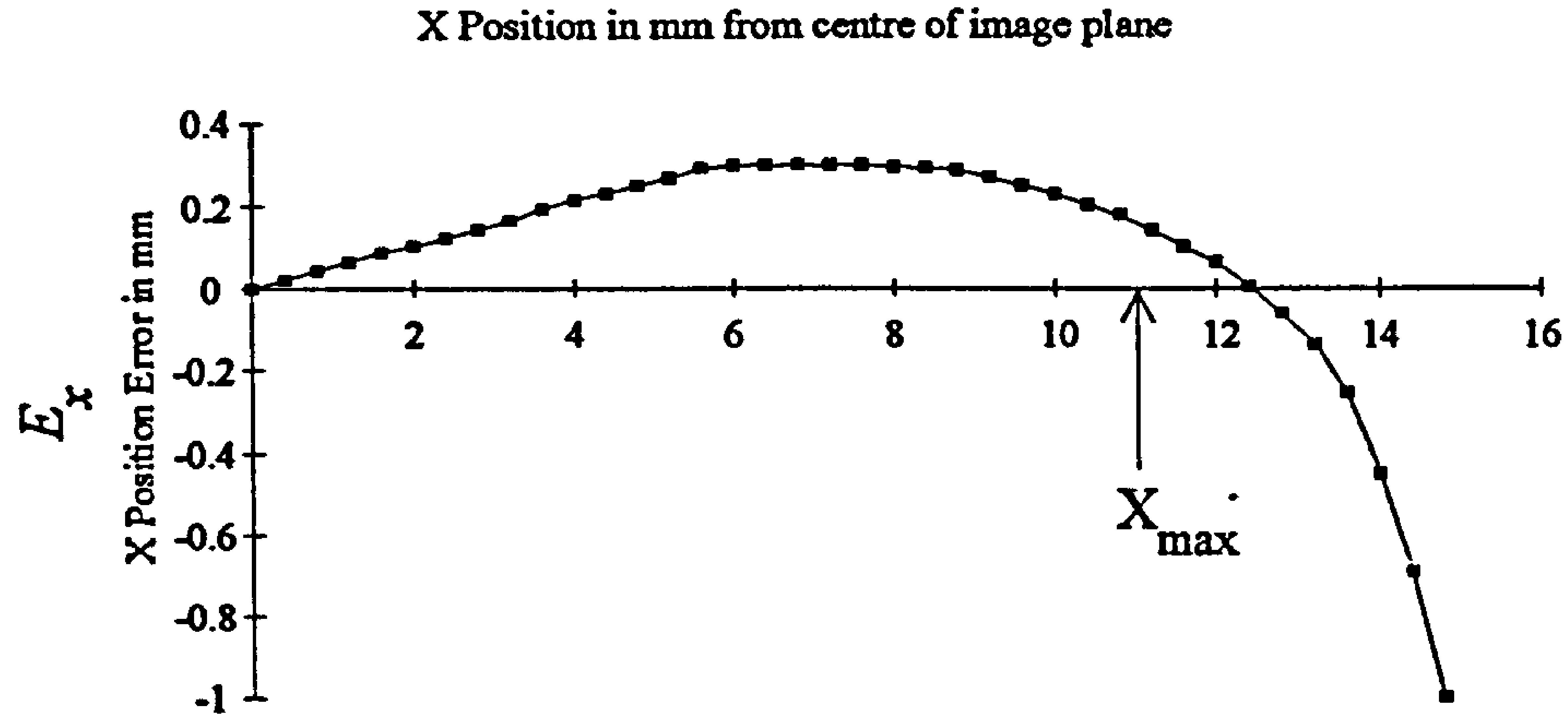

b) valve centreline (plane 1) position error

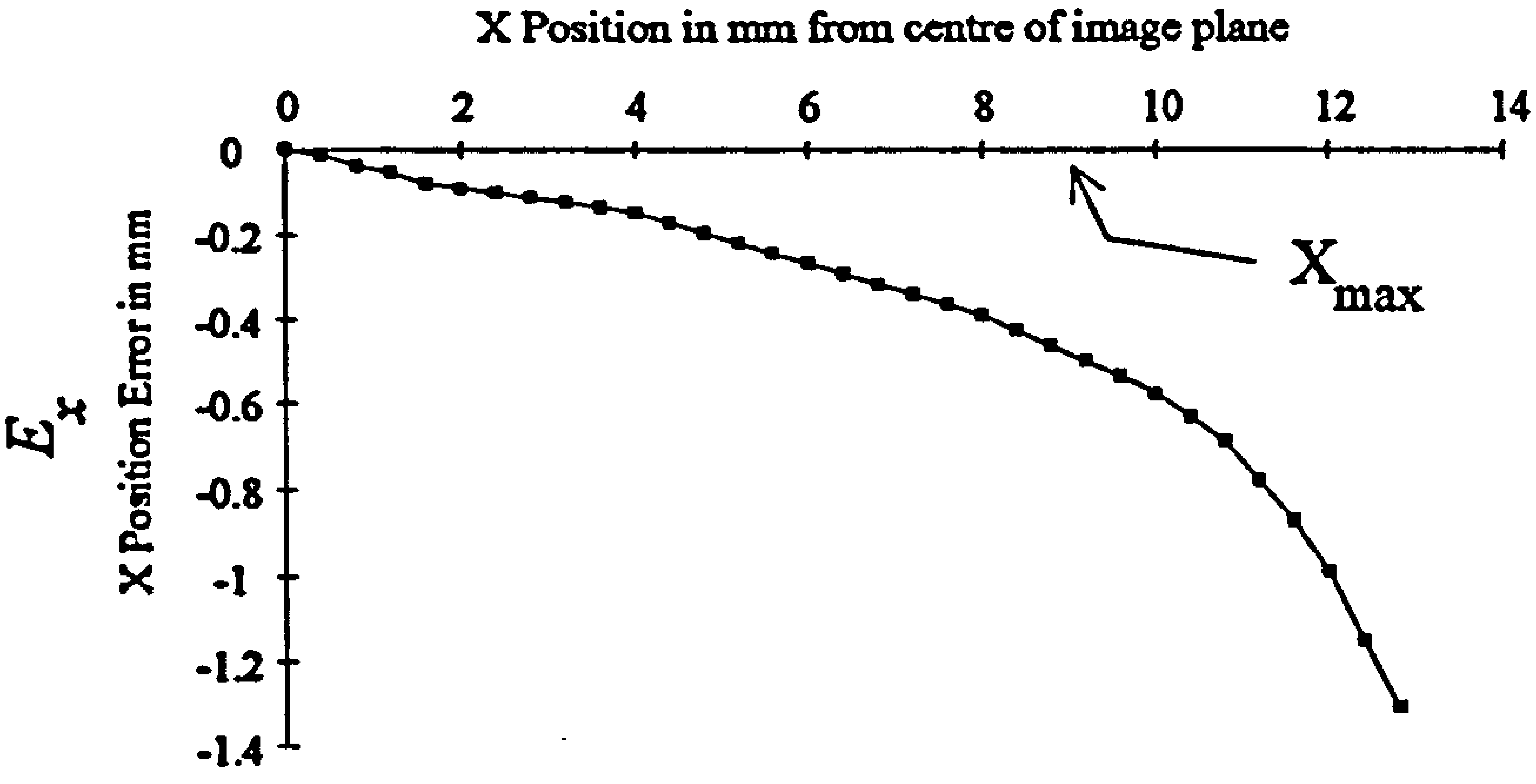

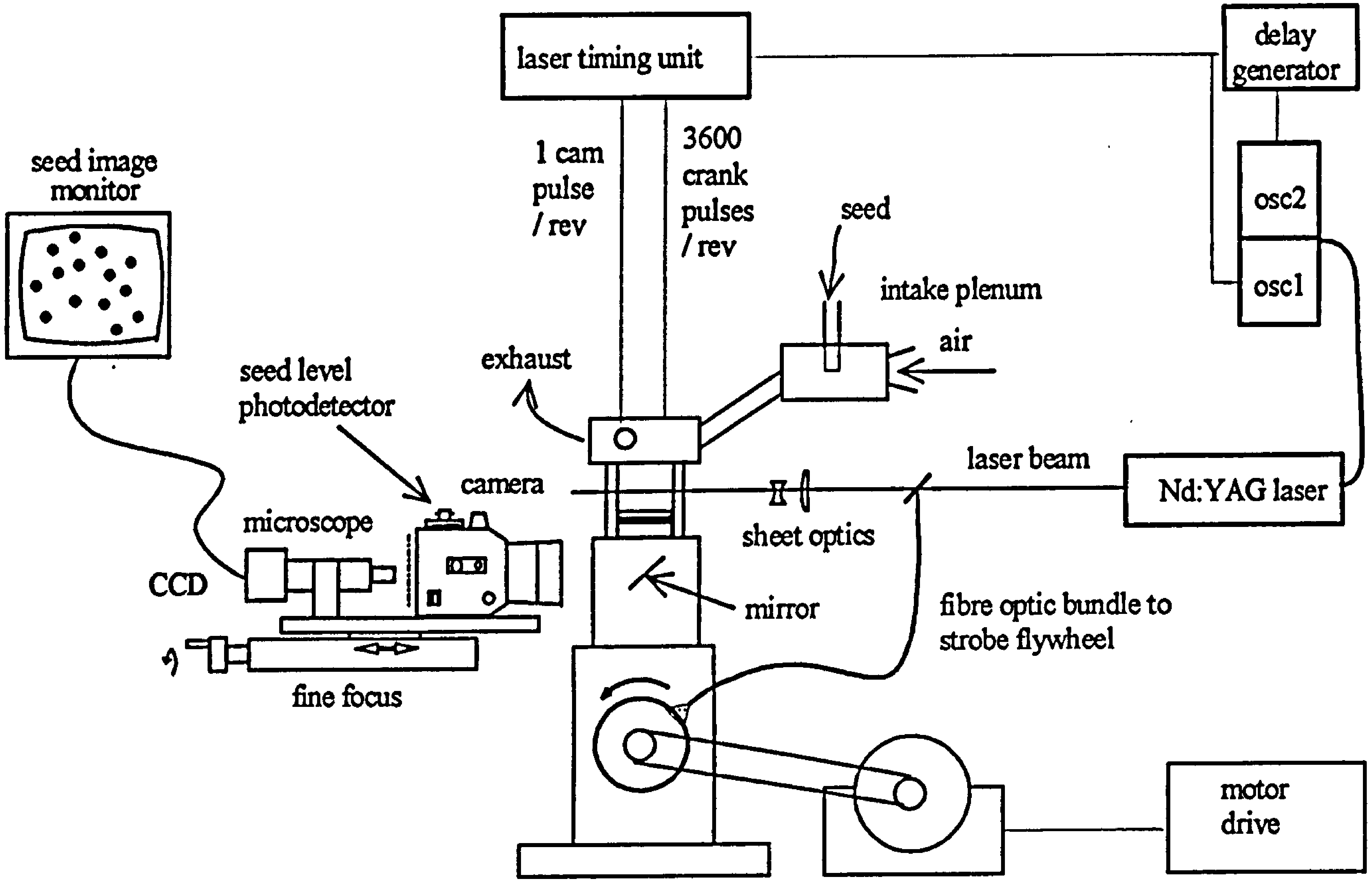

Figure 4.1 PIV engine facility showing arrangement for recording horizontal planes

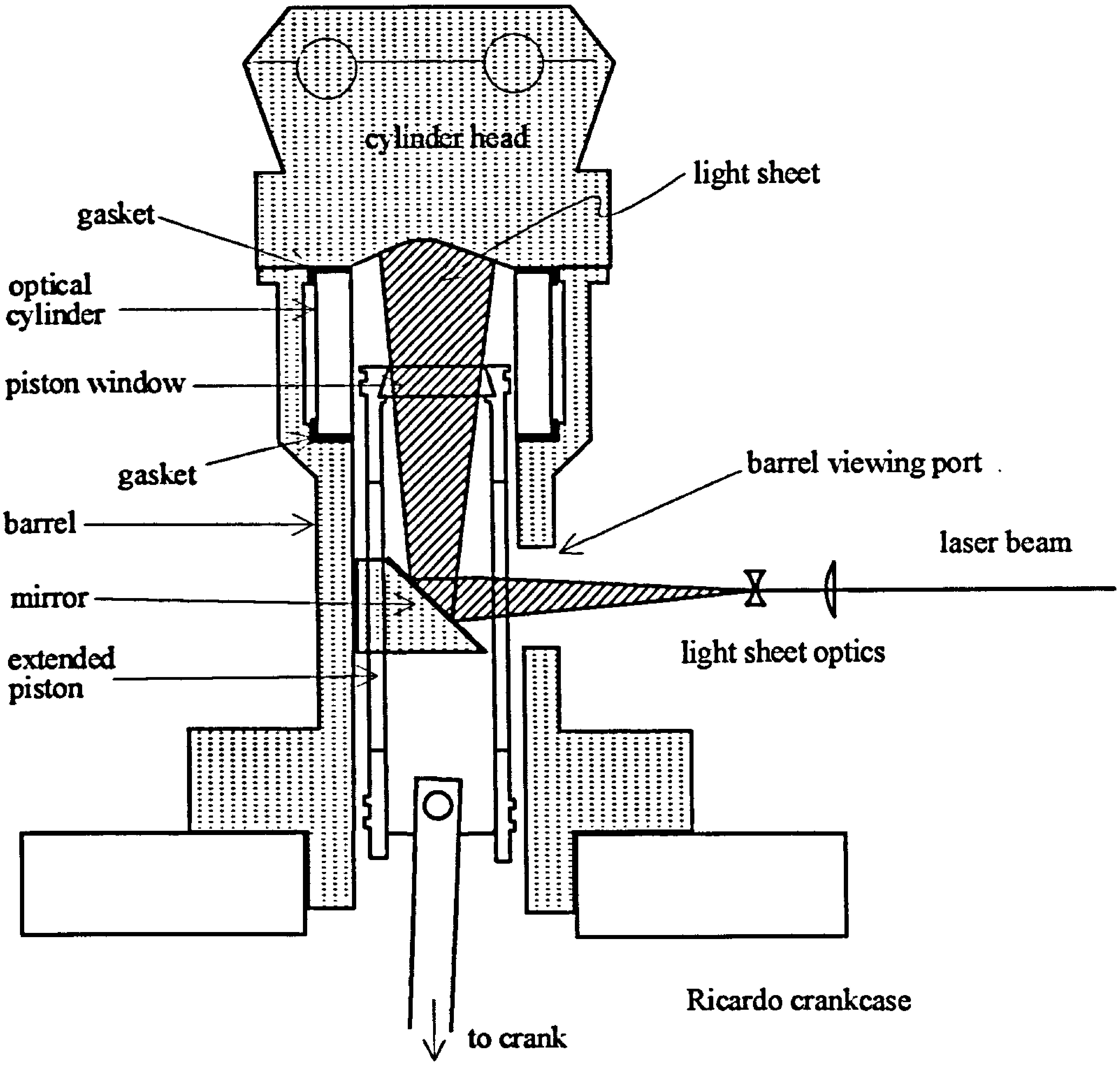

Figure 4.2 Schematic of single cylinder engine showing optical arrangement for illuminating vertical planes

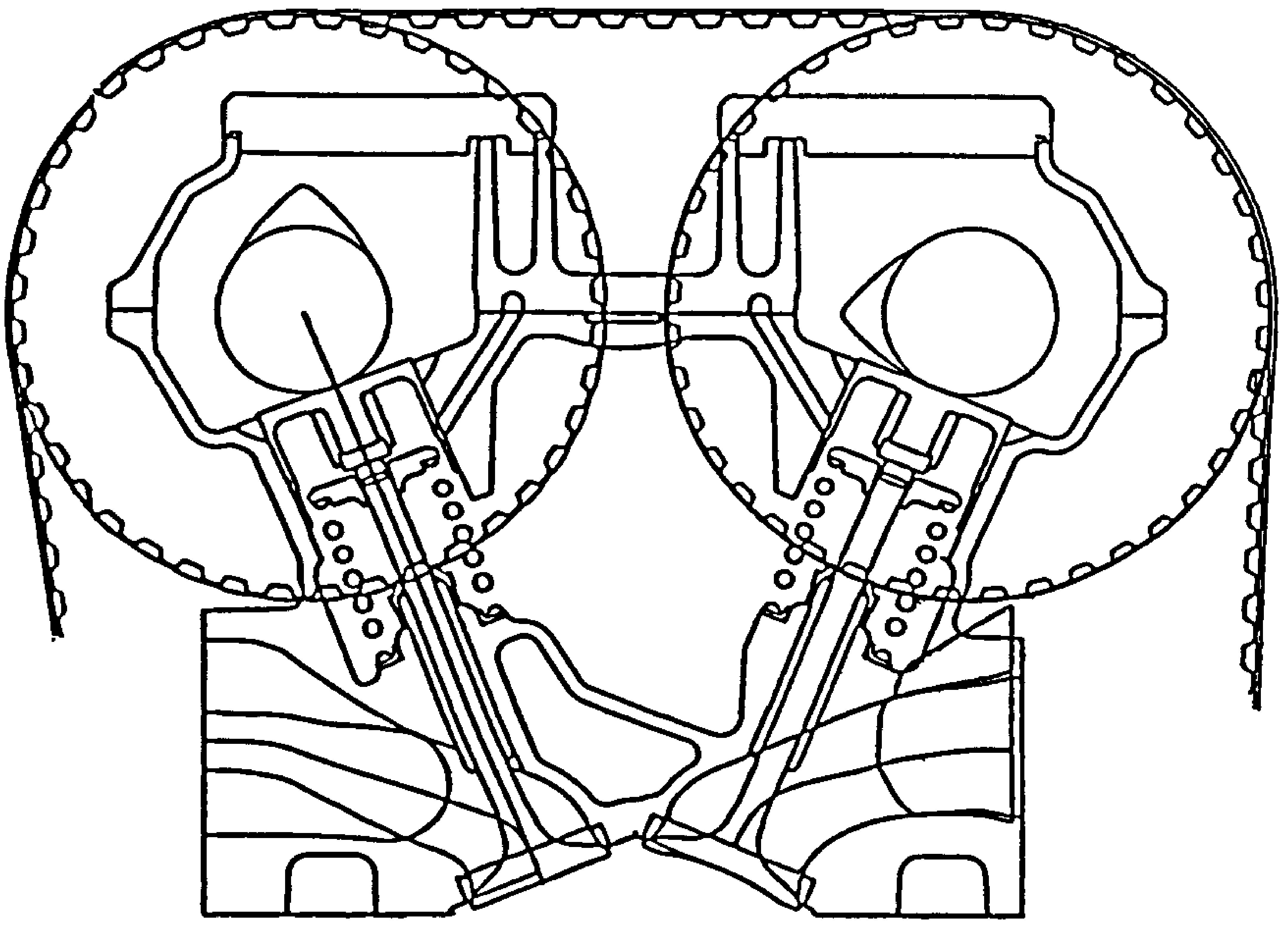

Figure 4.3 a) Section through an inlet and exhaust valve: inlet to right

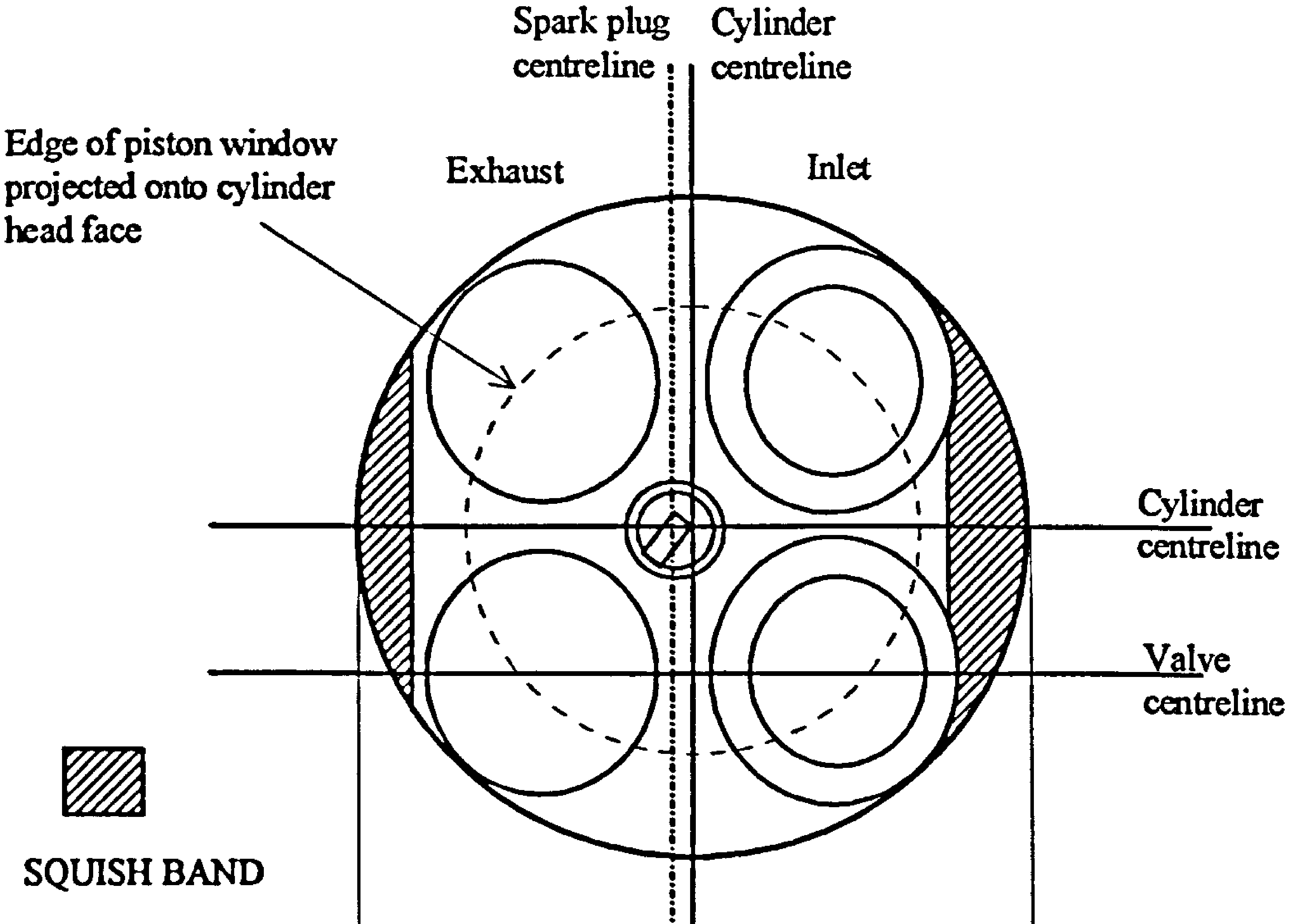

Figure 4.3b) View looking up into combustion chamber

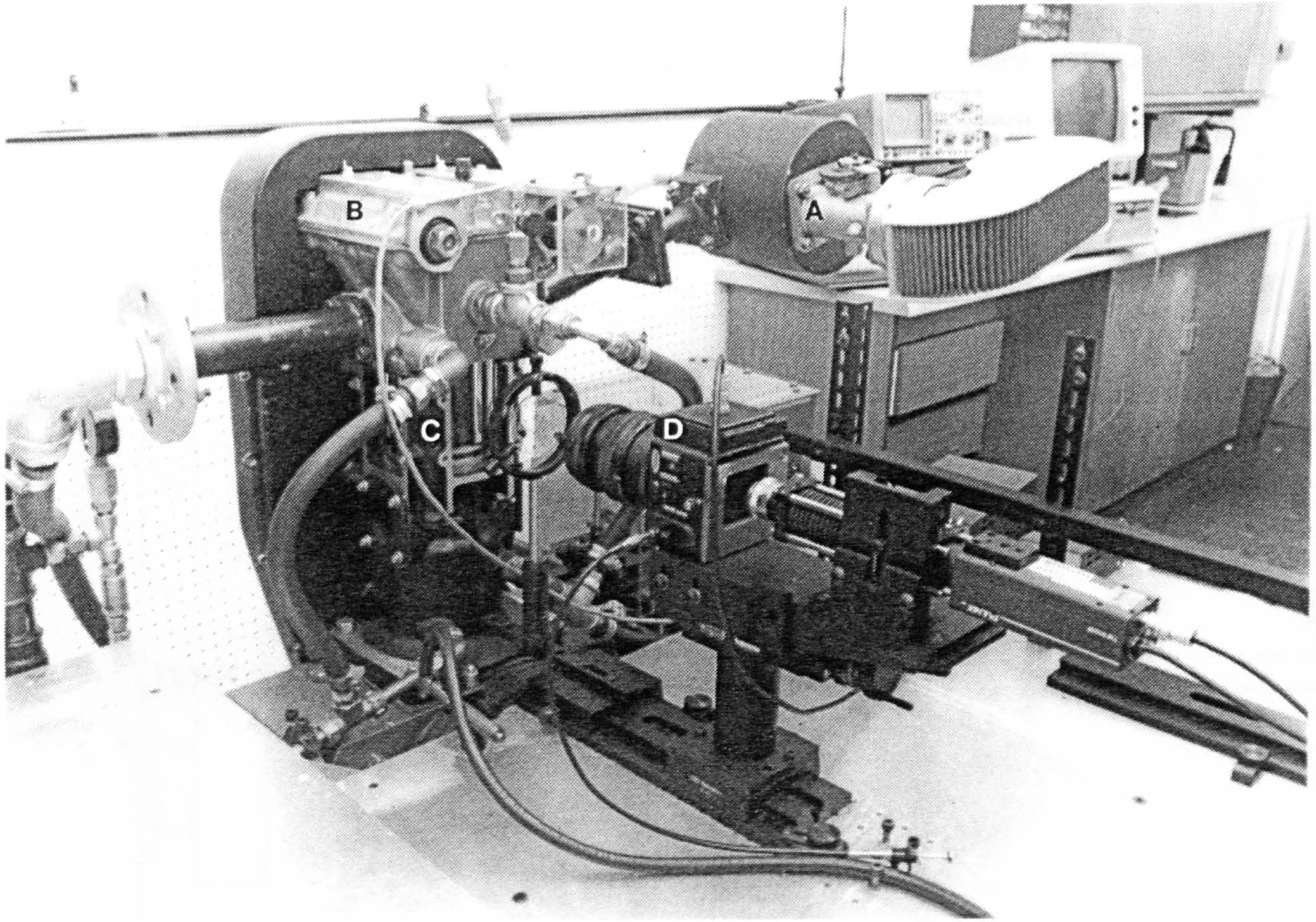

Figure 4.4 View of the assembled optical engine with optical arrangement for recording vertical planes. a) intake plenum and filter b) cylinder head c) barrel with optical cylinder d) camera

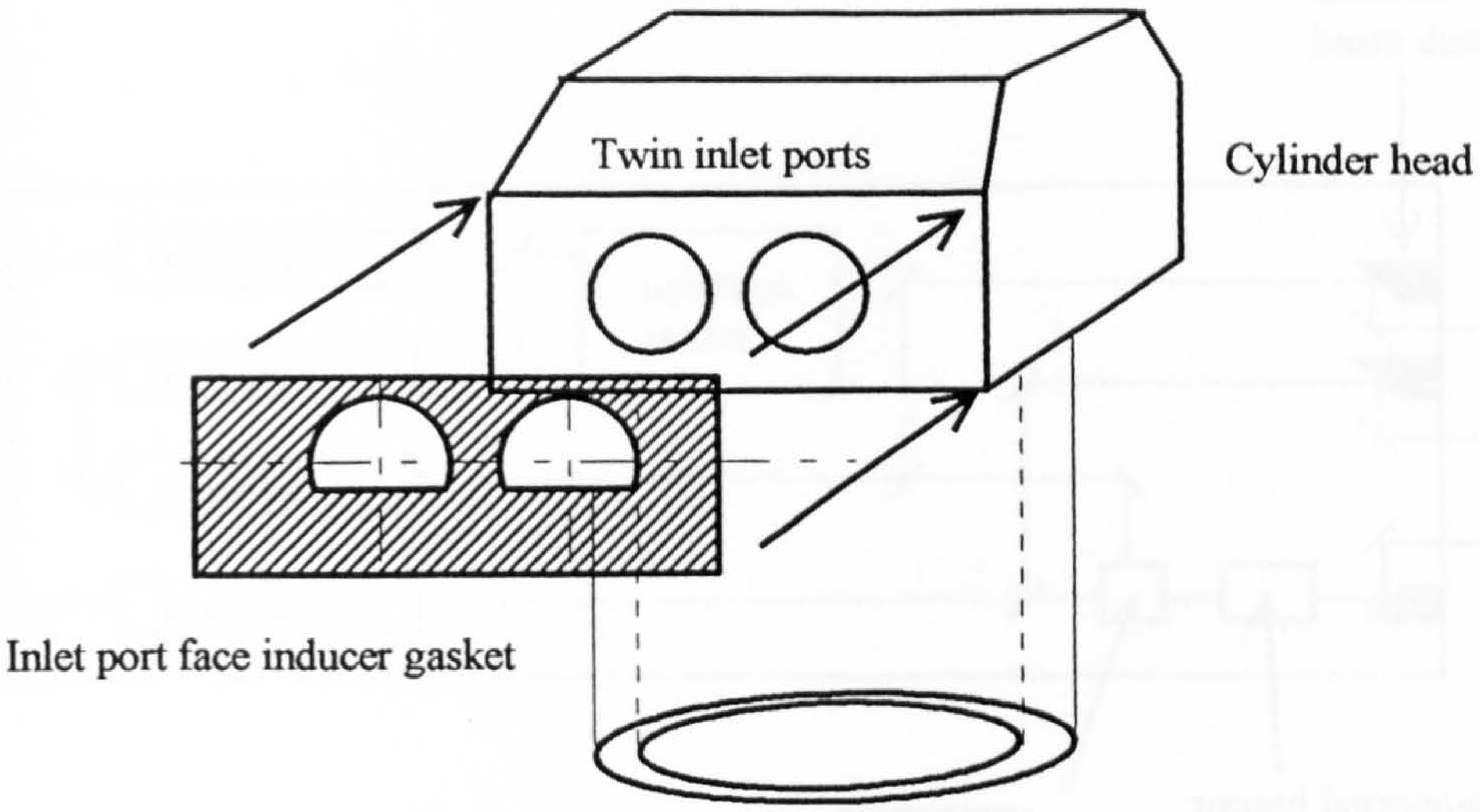

Figure 4.5 Use of inlet port face gasket to induce enhanced barrel swirl ratio

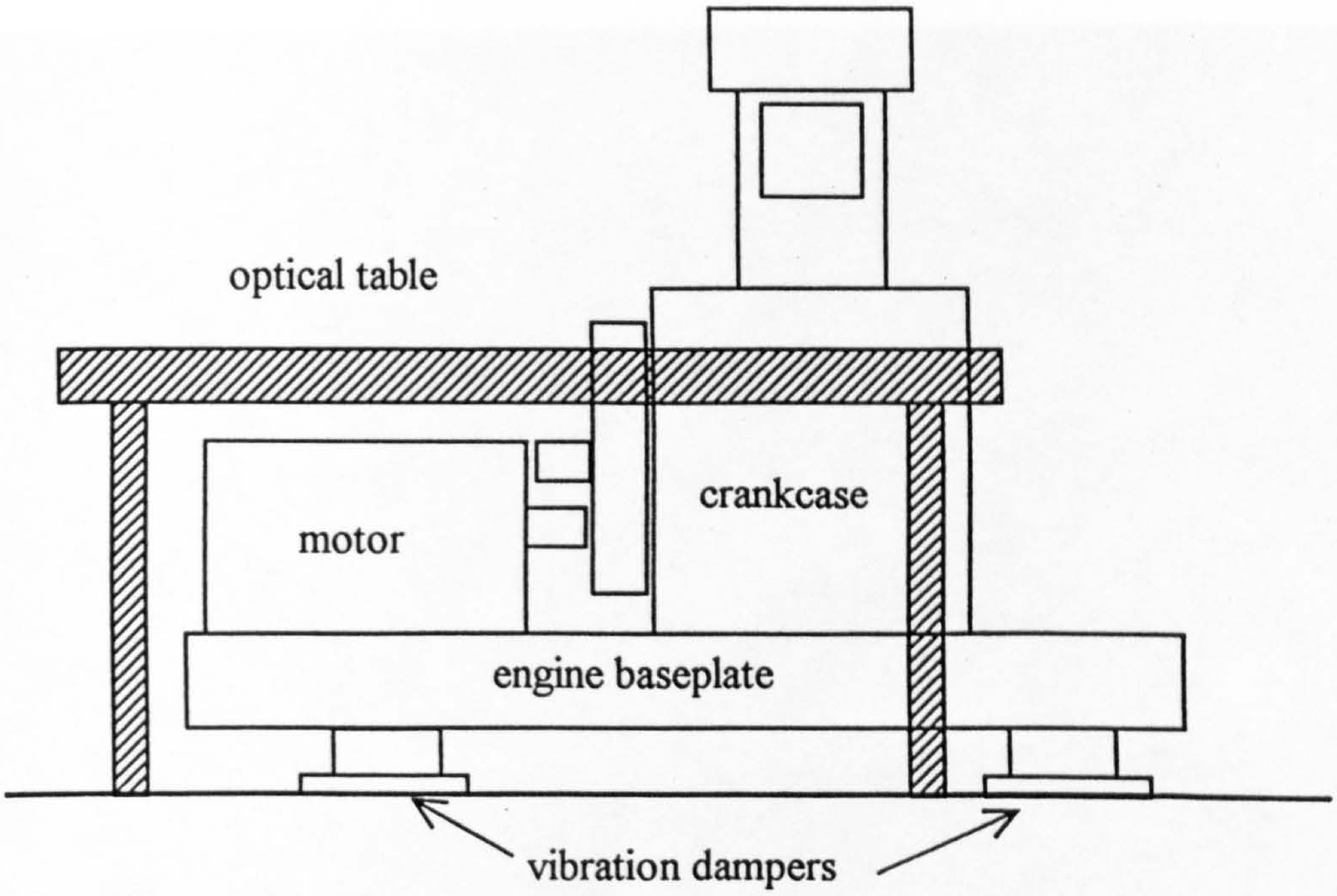

Figure 4.6 Vibration isolation of optical table and engine

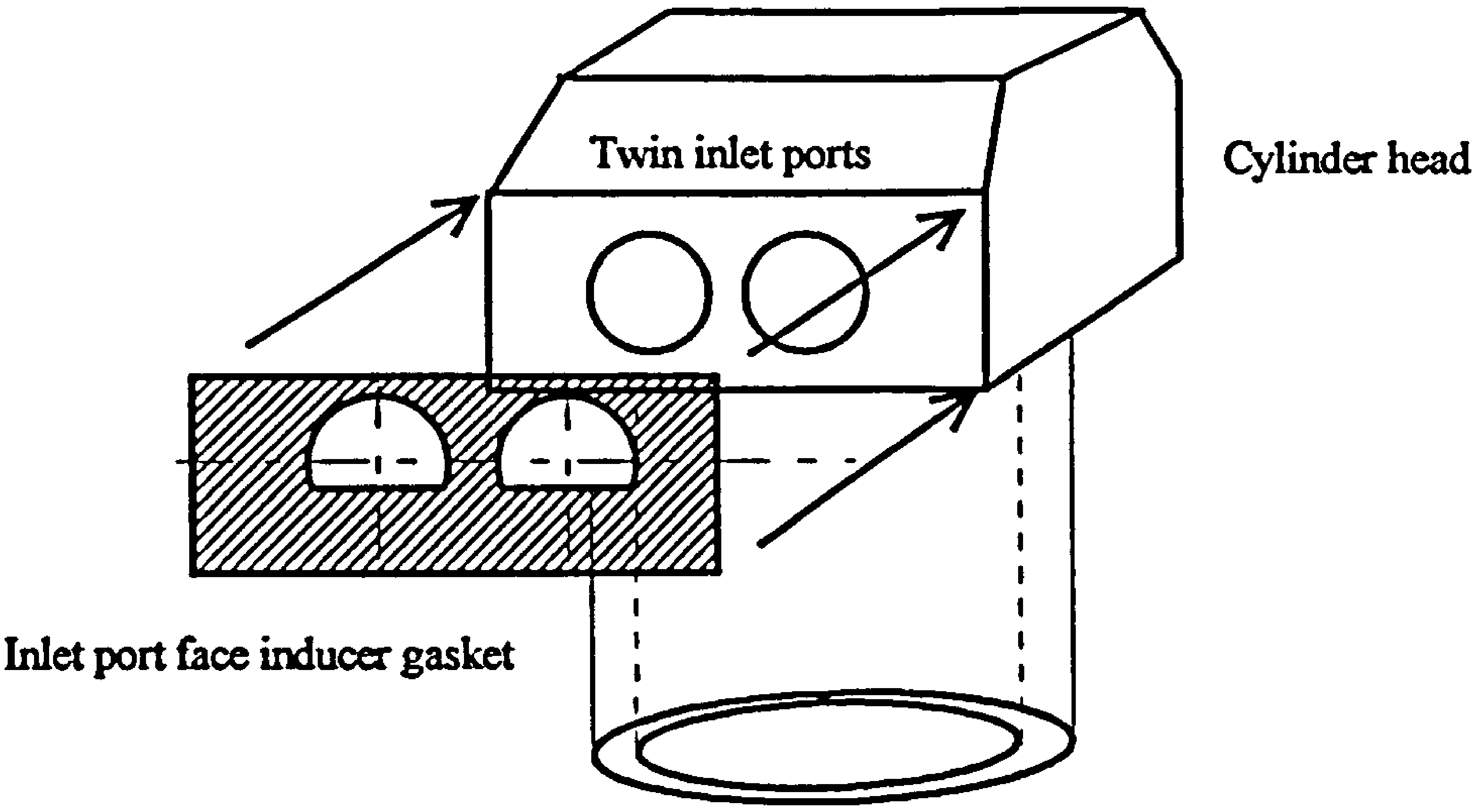

Figure 4.5 Use of inlet port face gasket to induce enhanced barrel swirl ratio

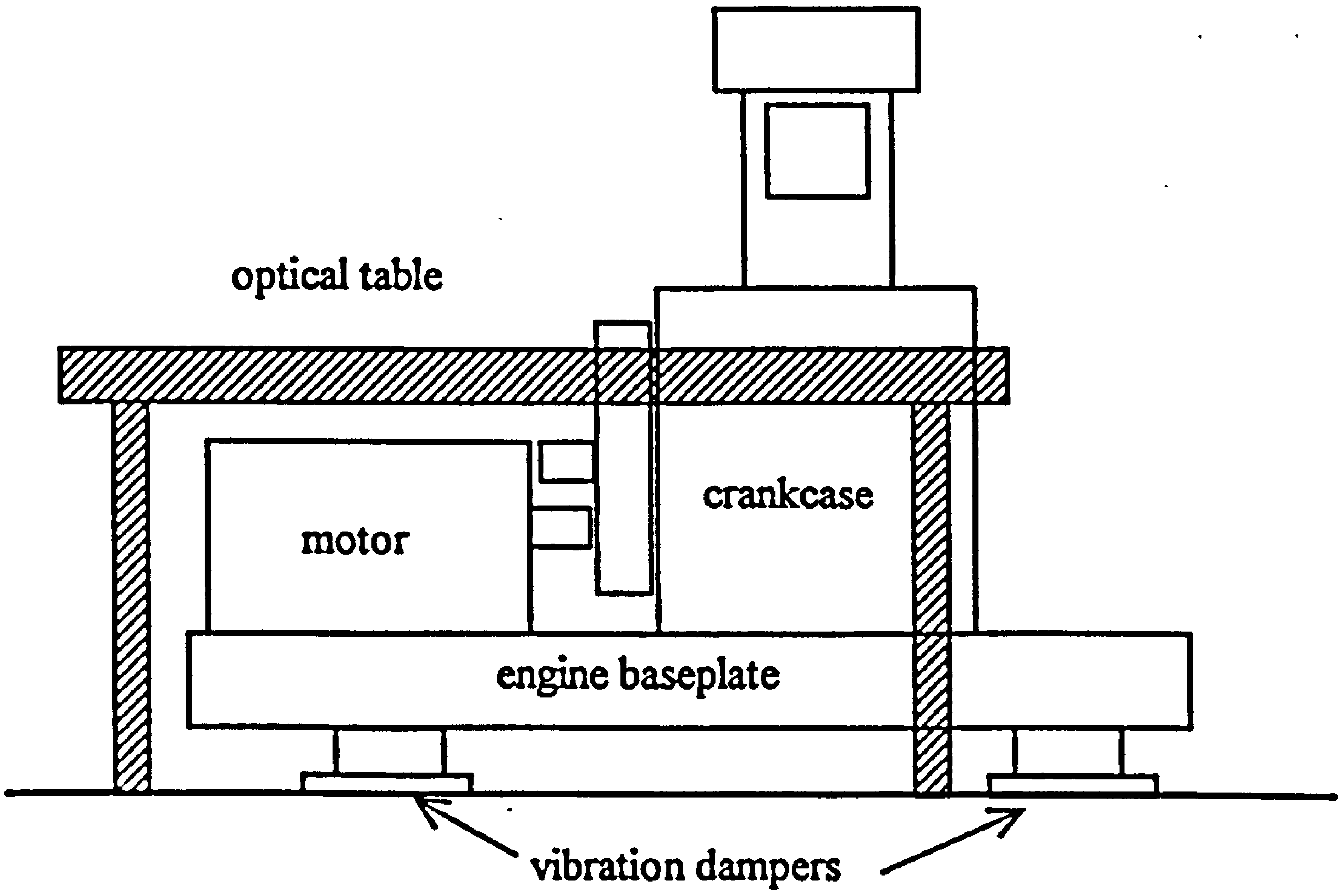

Figure 4.6 Vibration isolation of optical table and engine

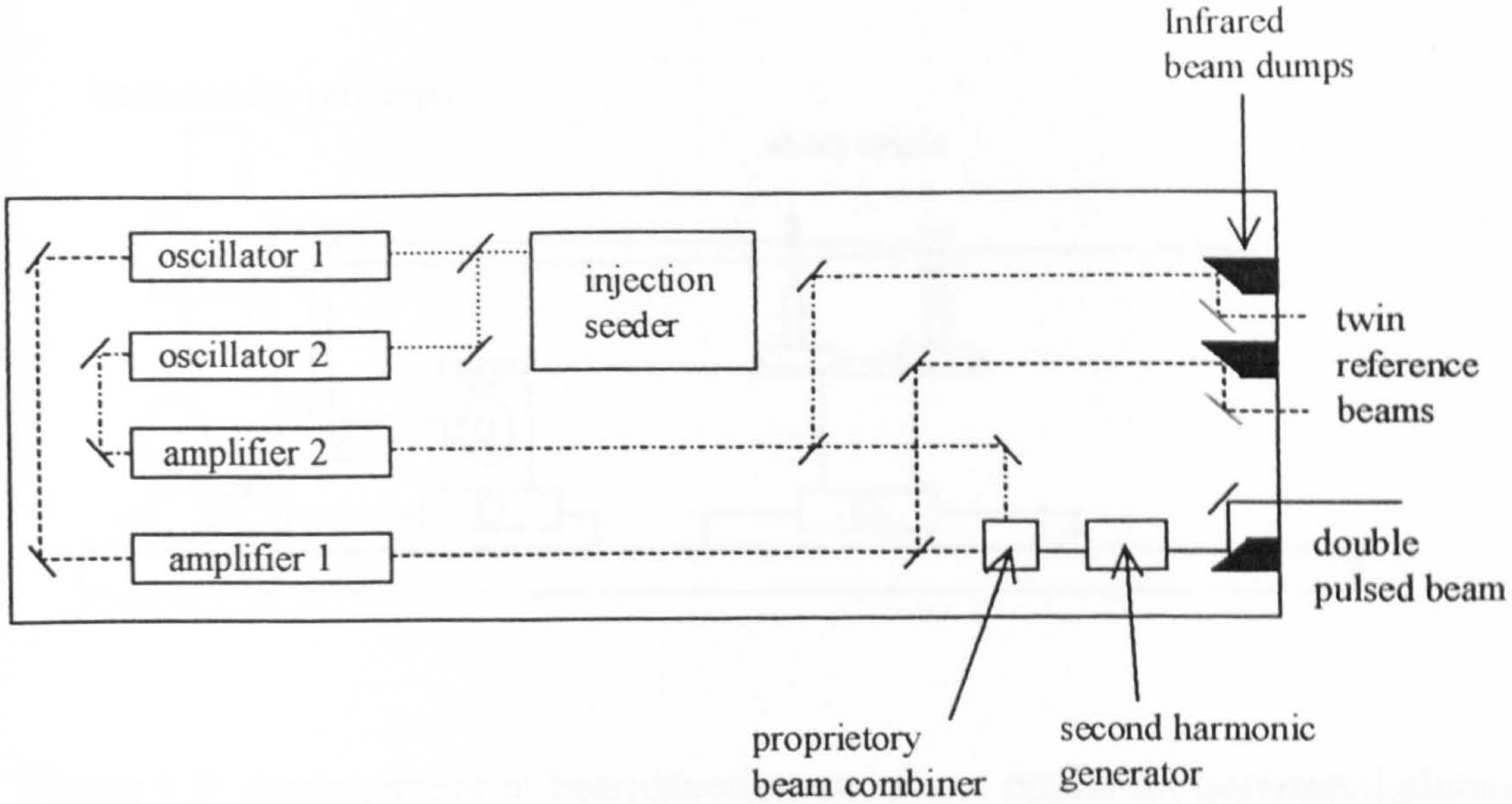

Figure 4.7 Optical layout of pulsed Nd:YAG PIV laser

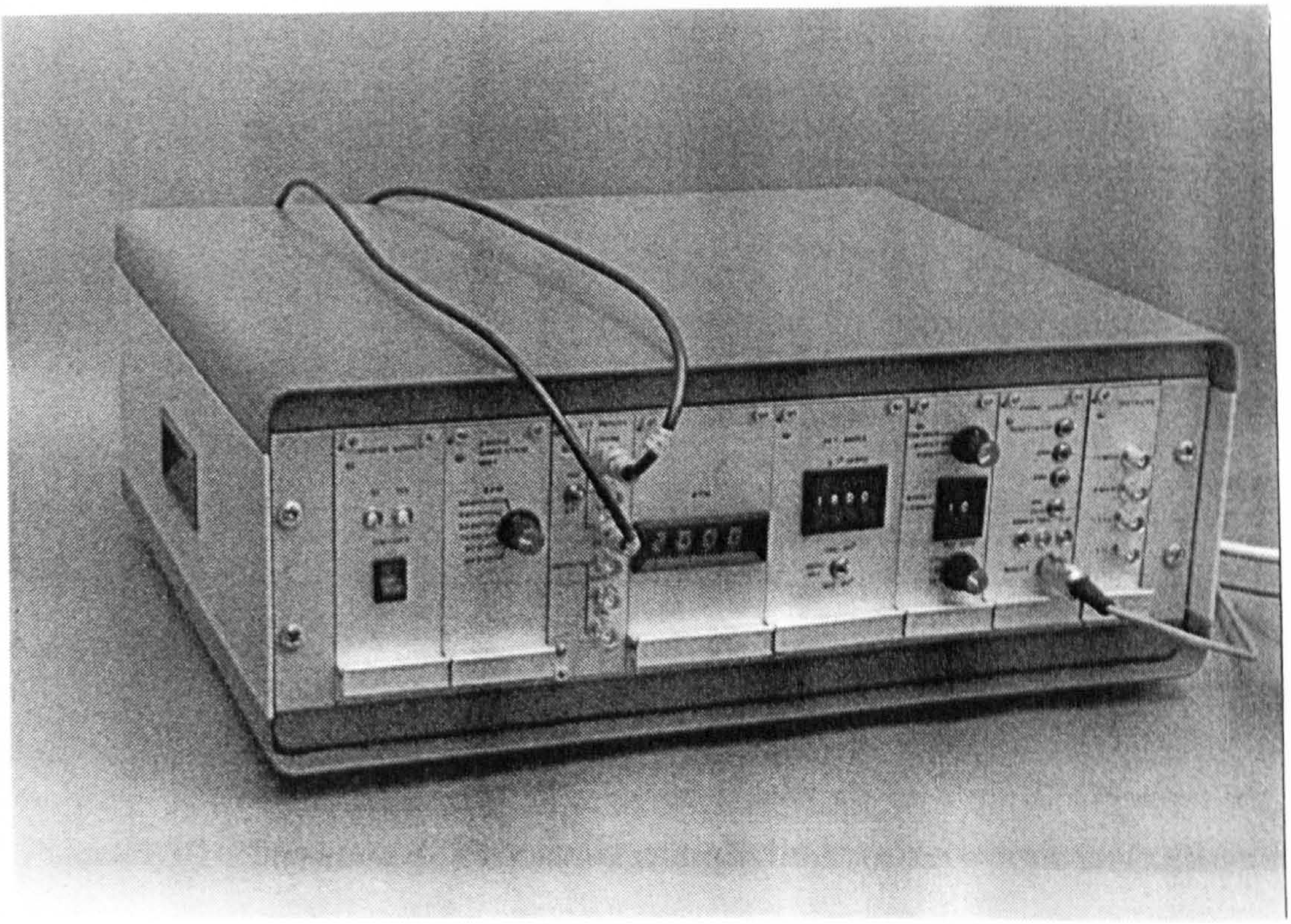

Figure 4.8 Laser / engine electronic timing unit

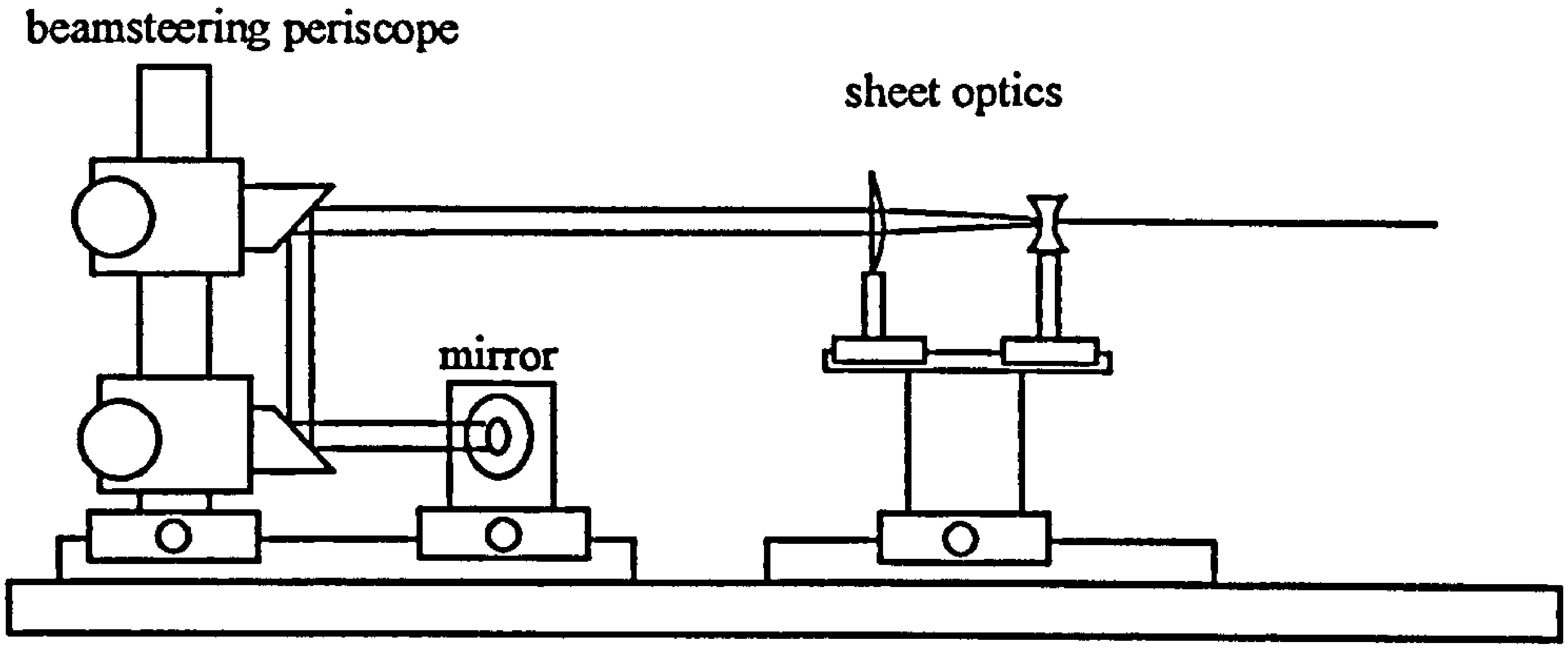

Figure 4.9 Arrangement of beamsteering and sheet optics for horizontal planes

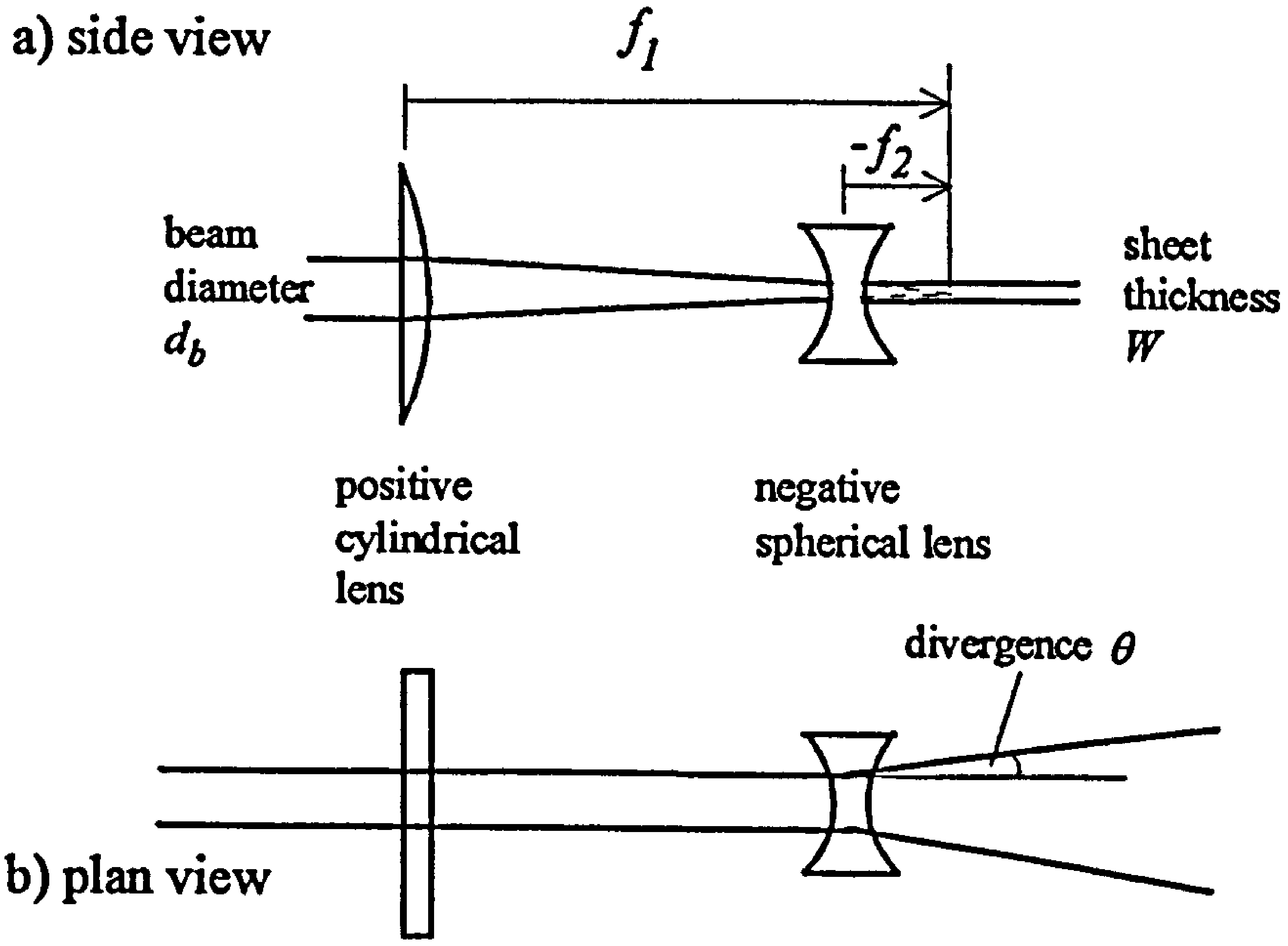

Figure 4.10 Formation of light sheet using cylindrical telescope arrangement

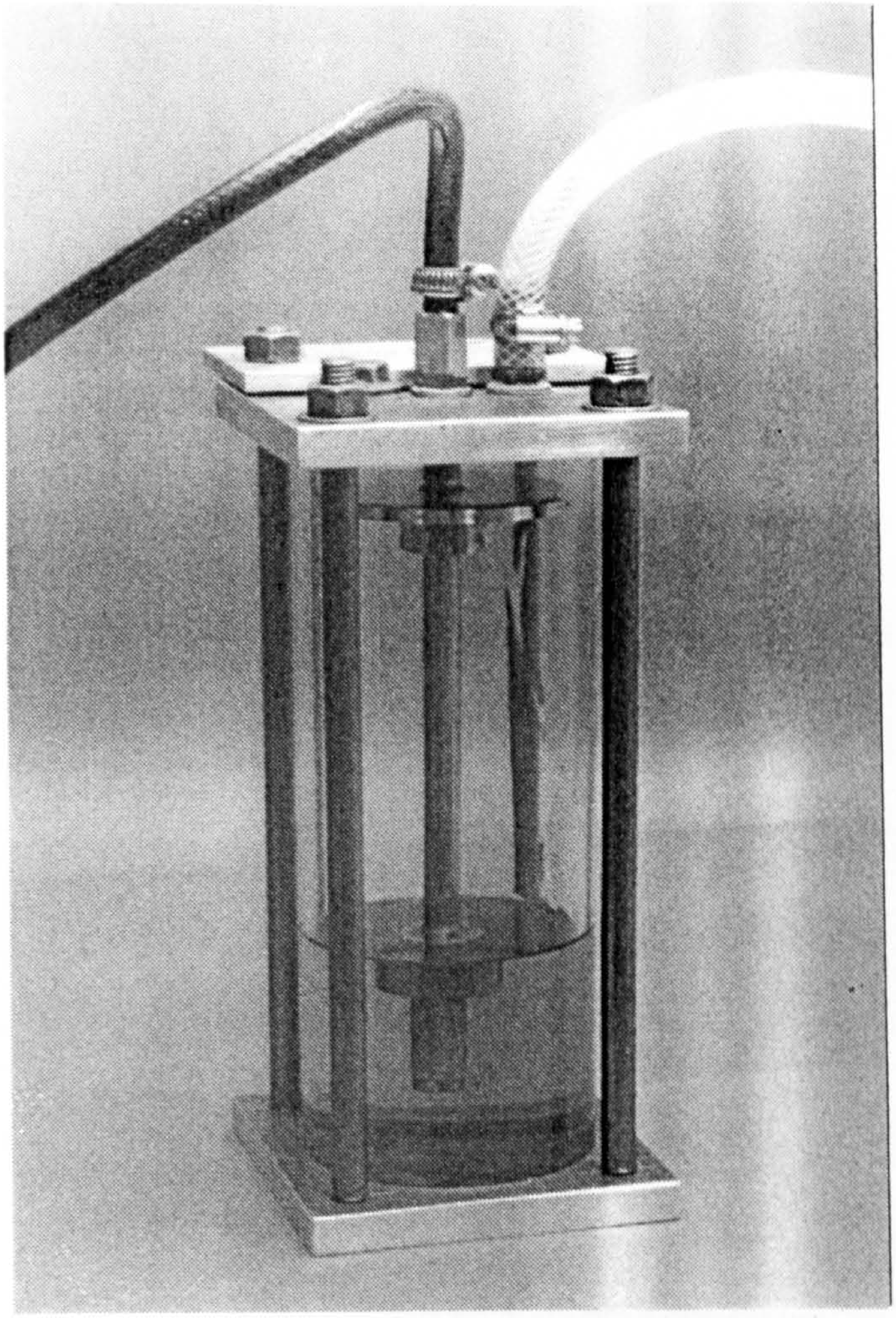

Figure 4.11 Laskin atomiser filled with silicone fluid.
Air supply through dark tube.

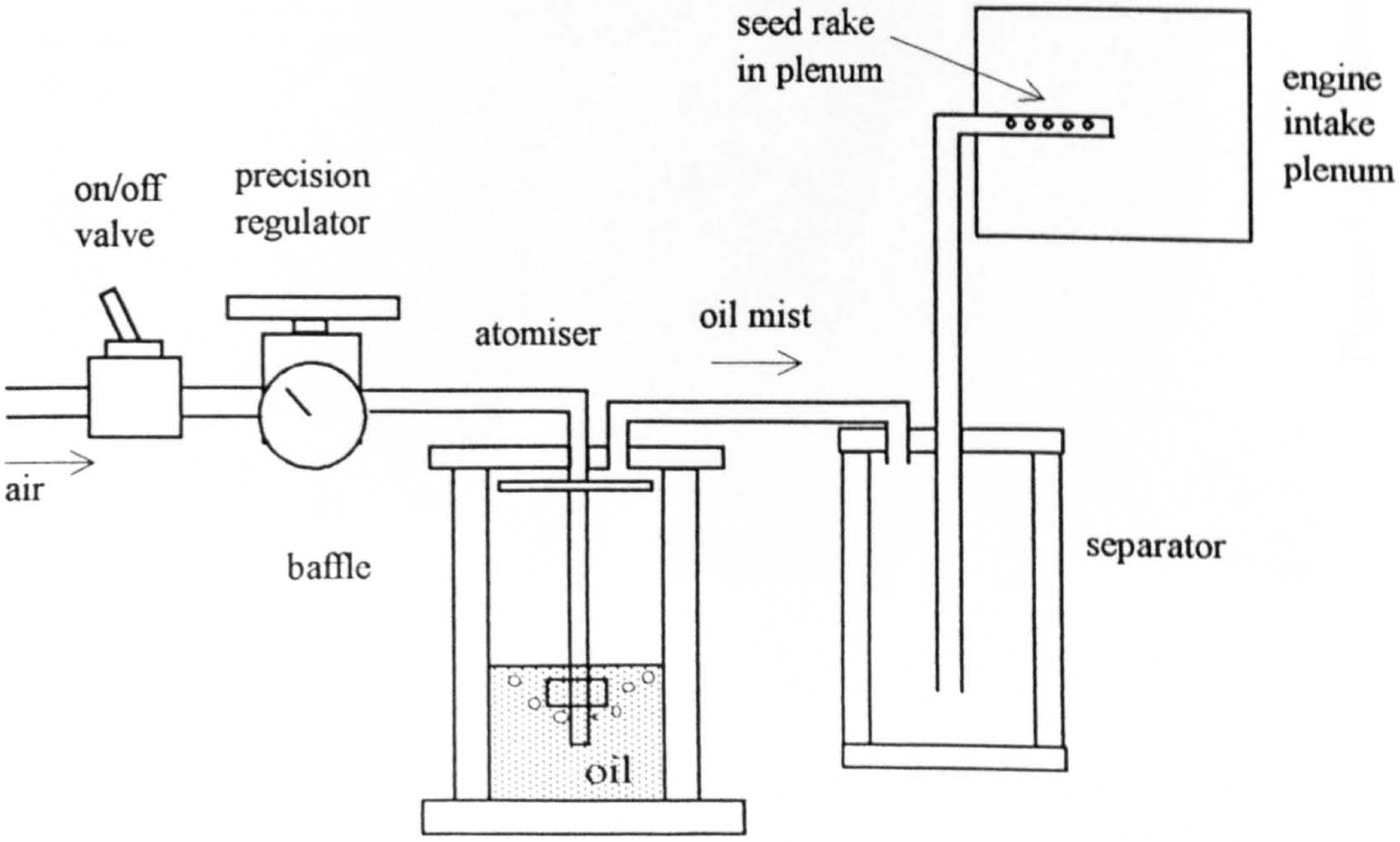

Figure 4.12 Seed generation and distribution system

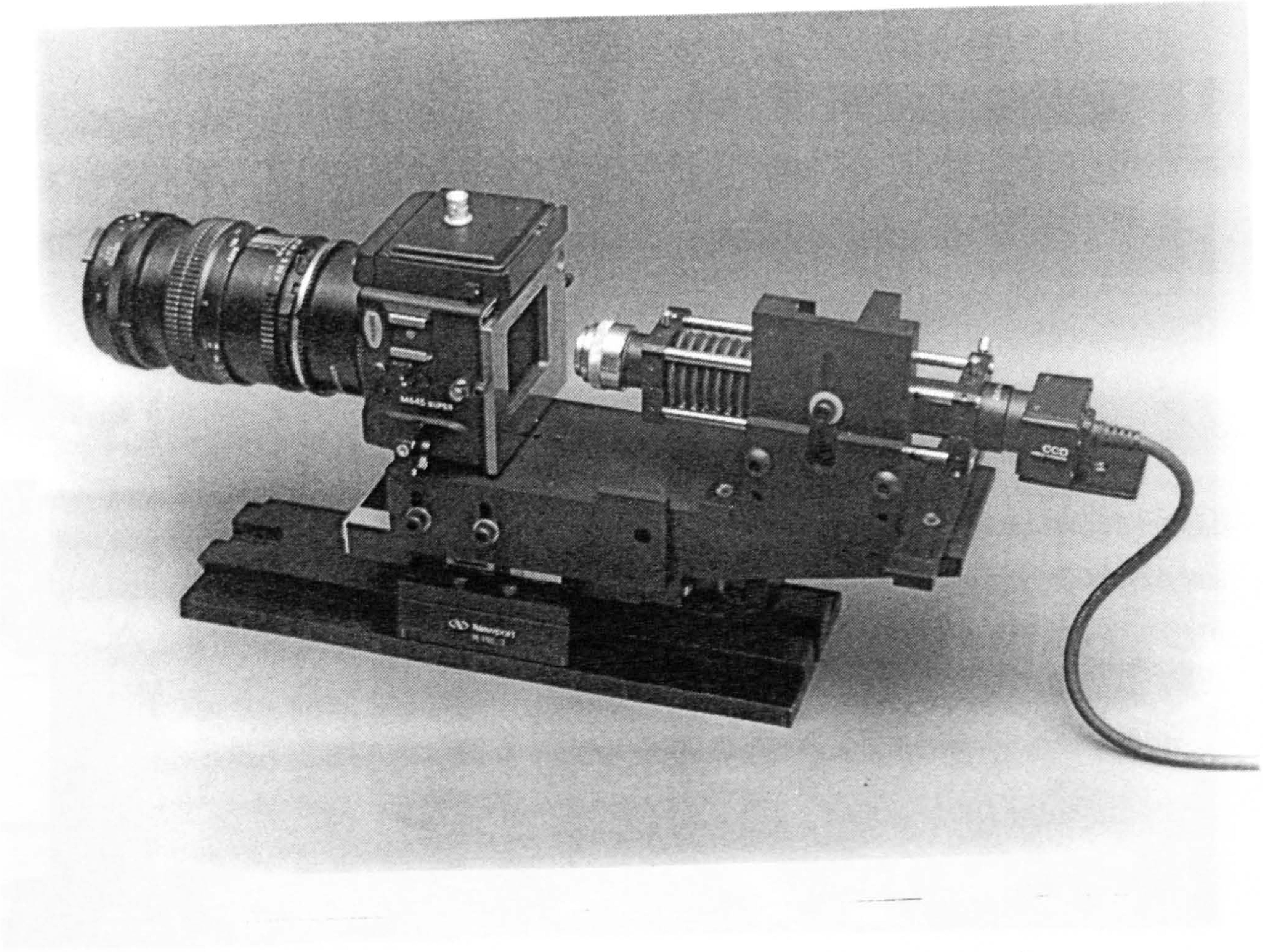

Figure 4.13 Medium format camera with CCD microscope attachment.

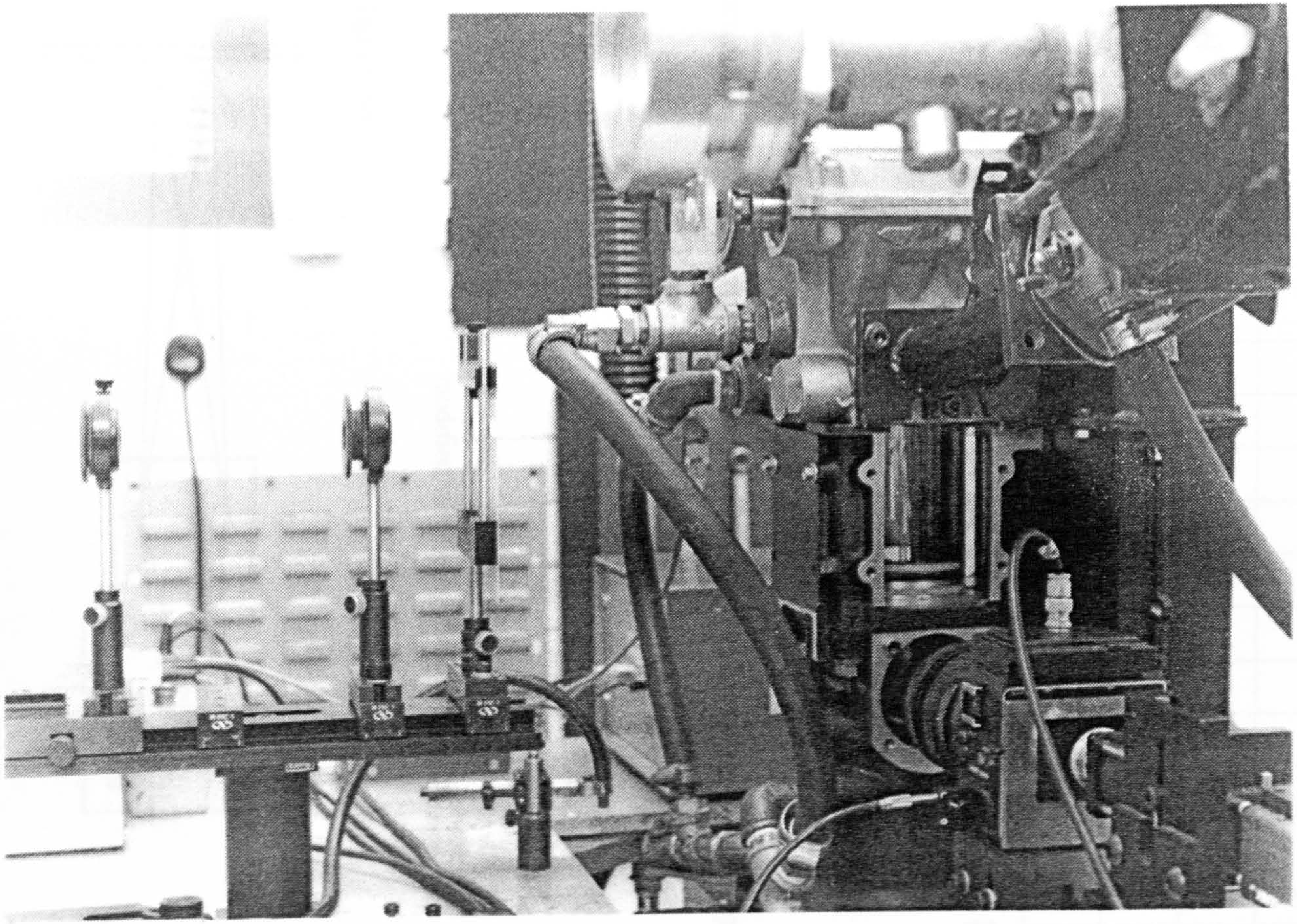

Figure 4.15 Optical arrangement for illuminating and recording horizontal plane.

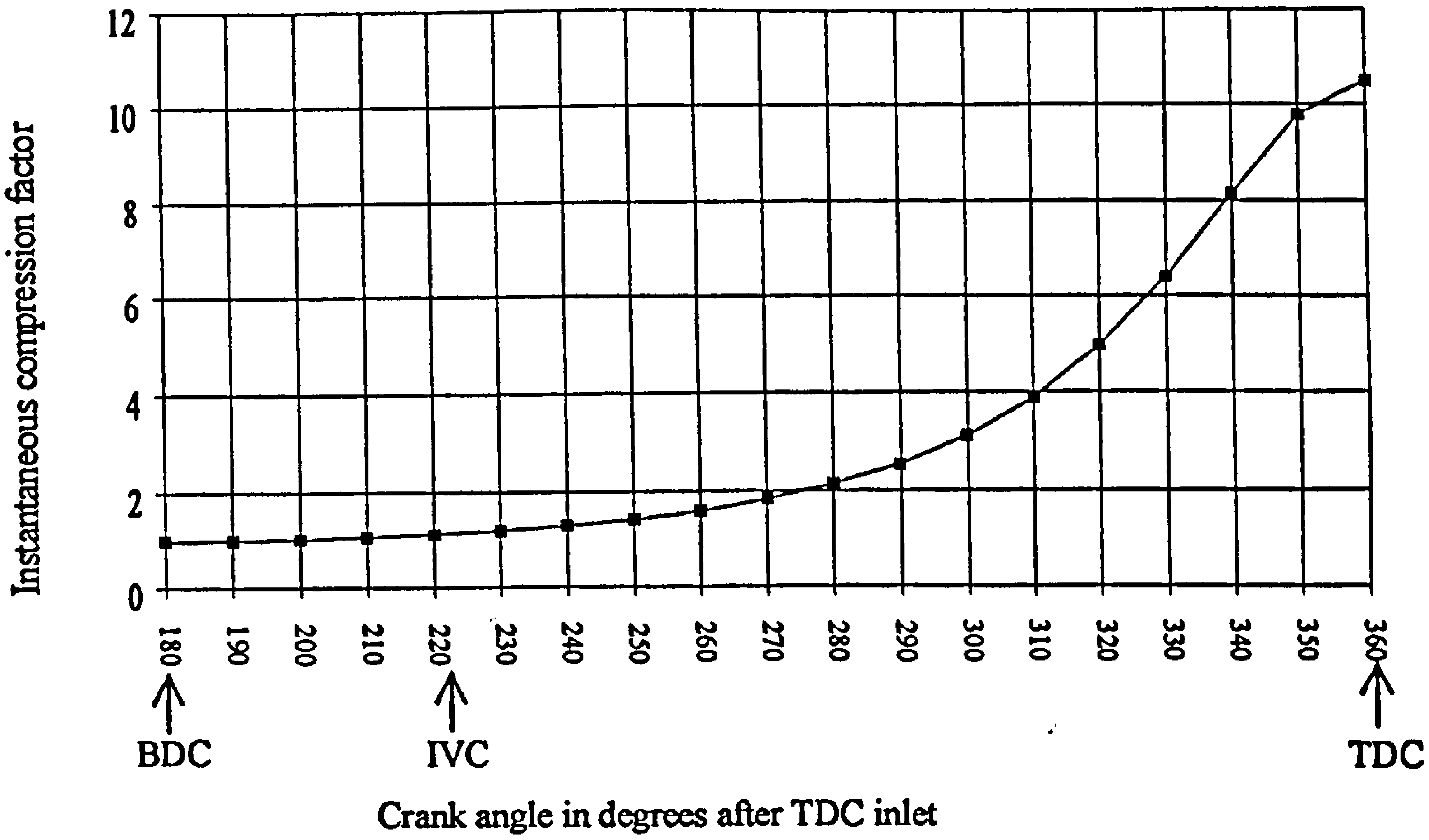

Figure 4.16 Instantaneous seed compression factor against crank angle

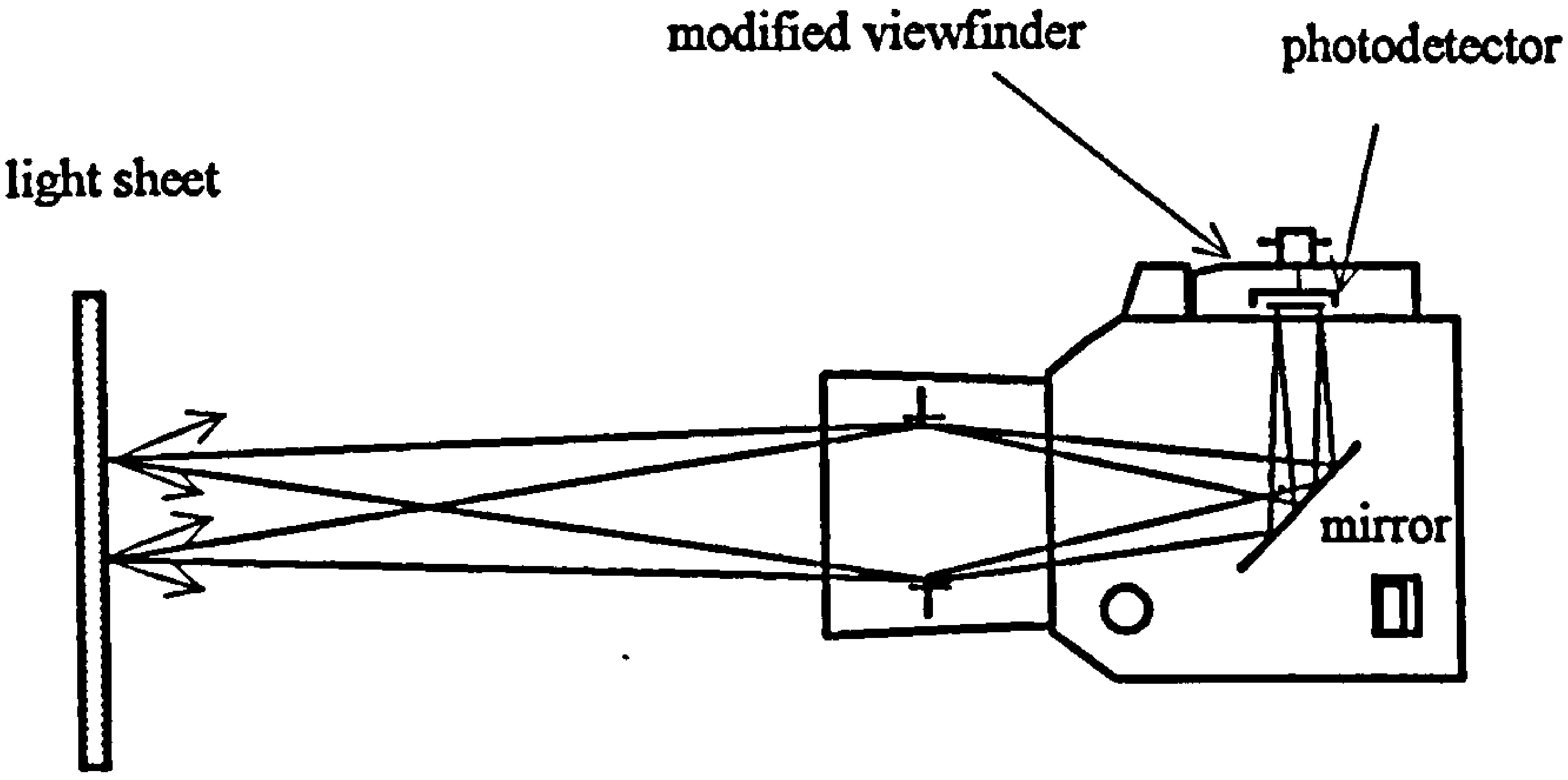

Figure 4.17 Seed monitor photovoltaic cell mounted in camera viewfinder showing scattered light collected by detector

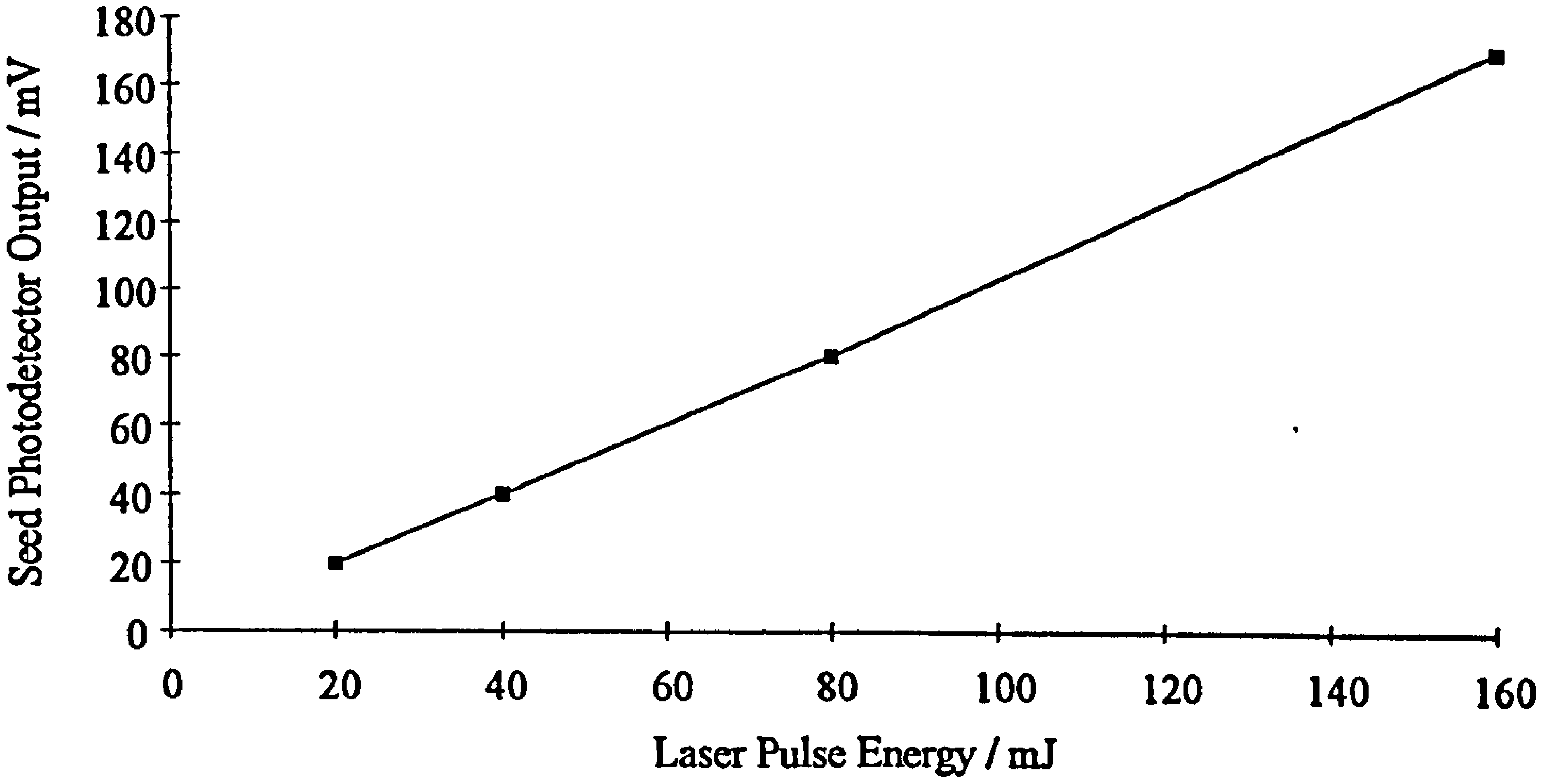

Figure 4.18 Linearity of seed monitor photodetector output at a constant seed level

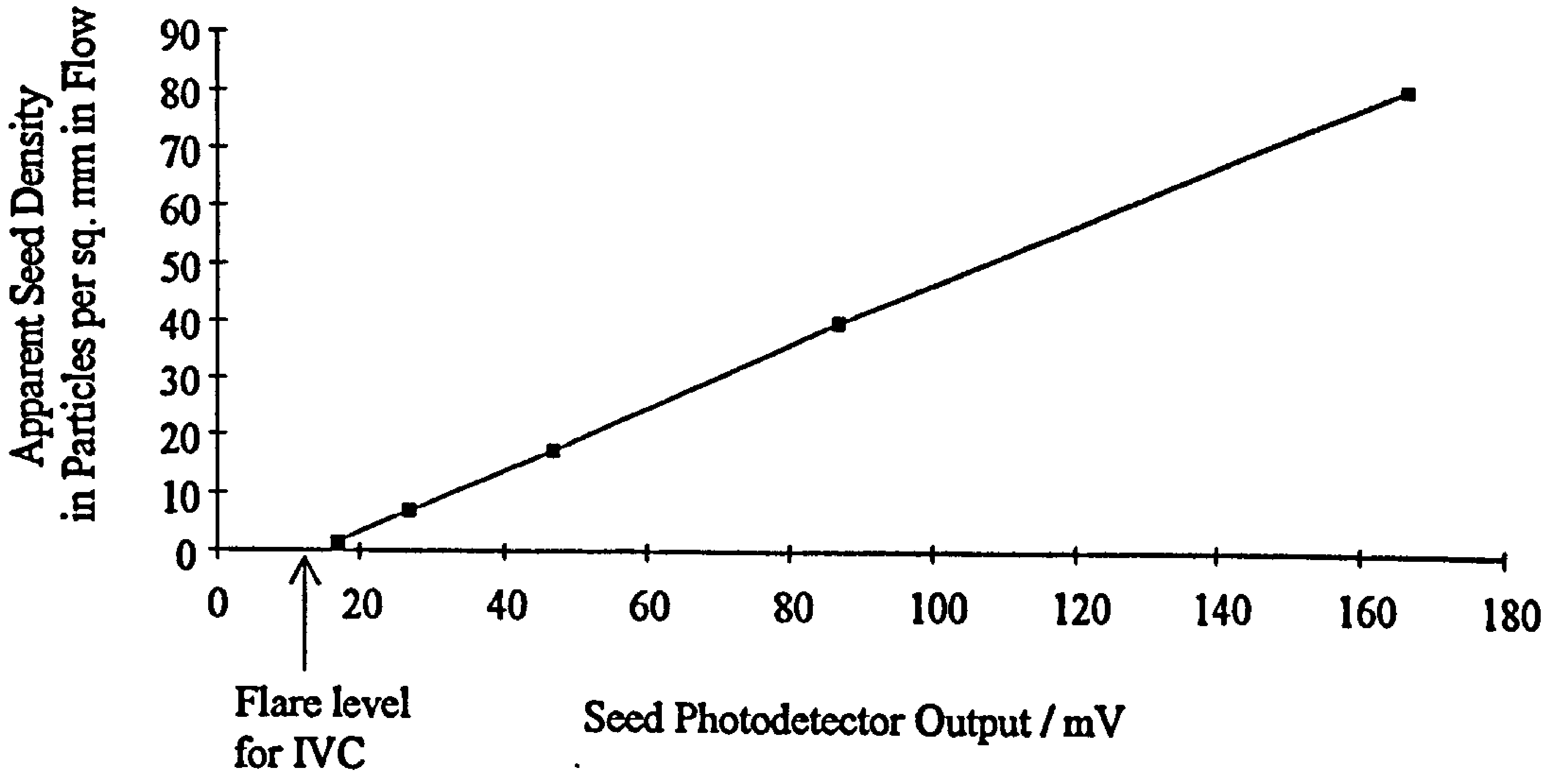

Figure 4.19 Calibration of seed level monitor for standard light sheet and camera configuration.

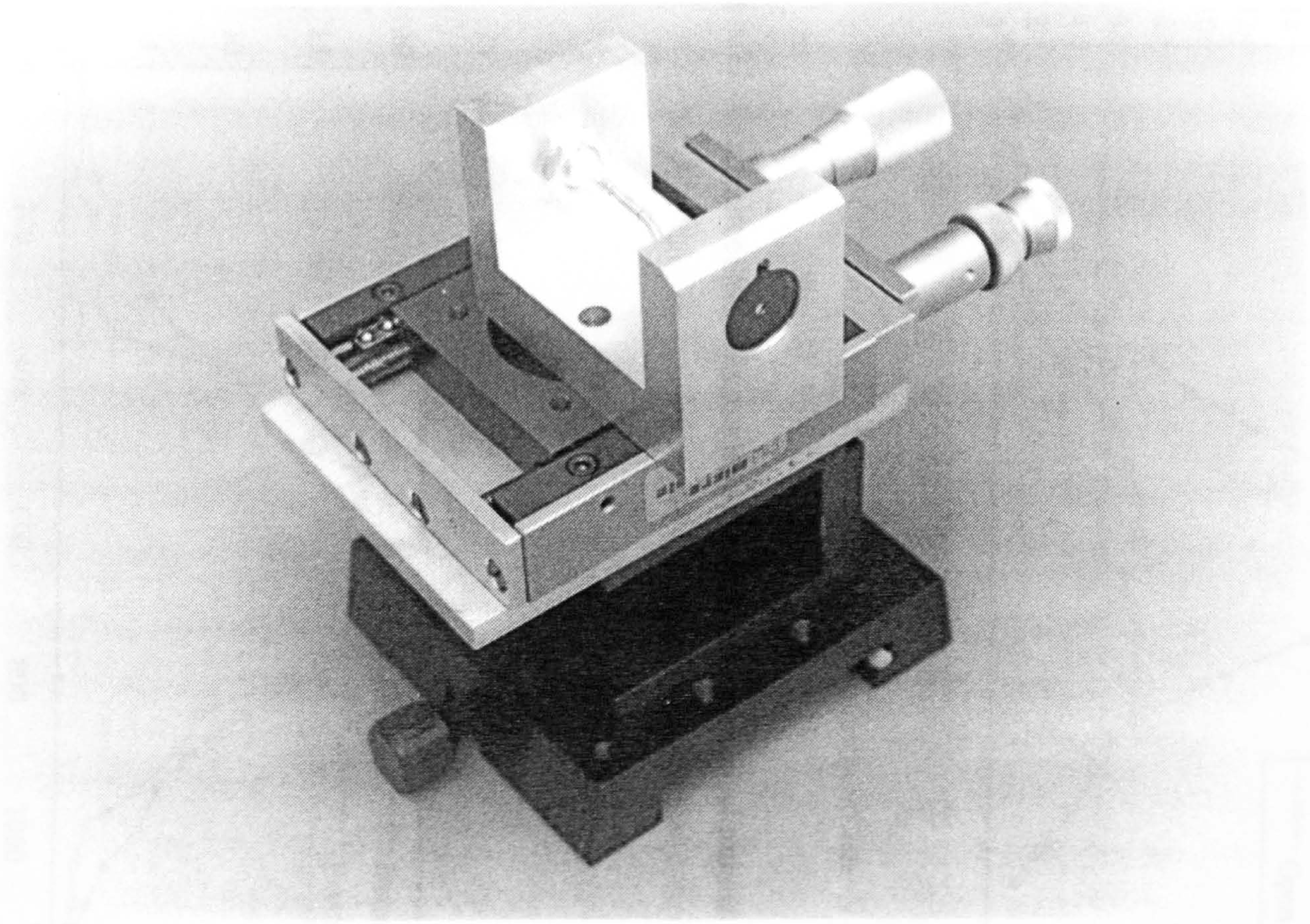

Figure 4.20 Micrometer-mounted pinhole and photodiode assembly
for the measurement of laser sheet intensity profiles

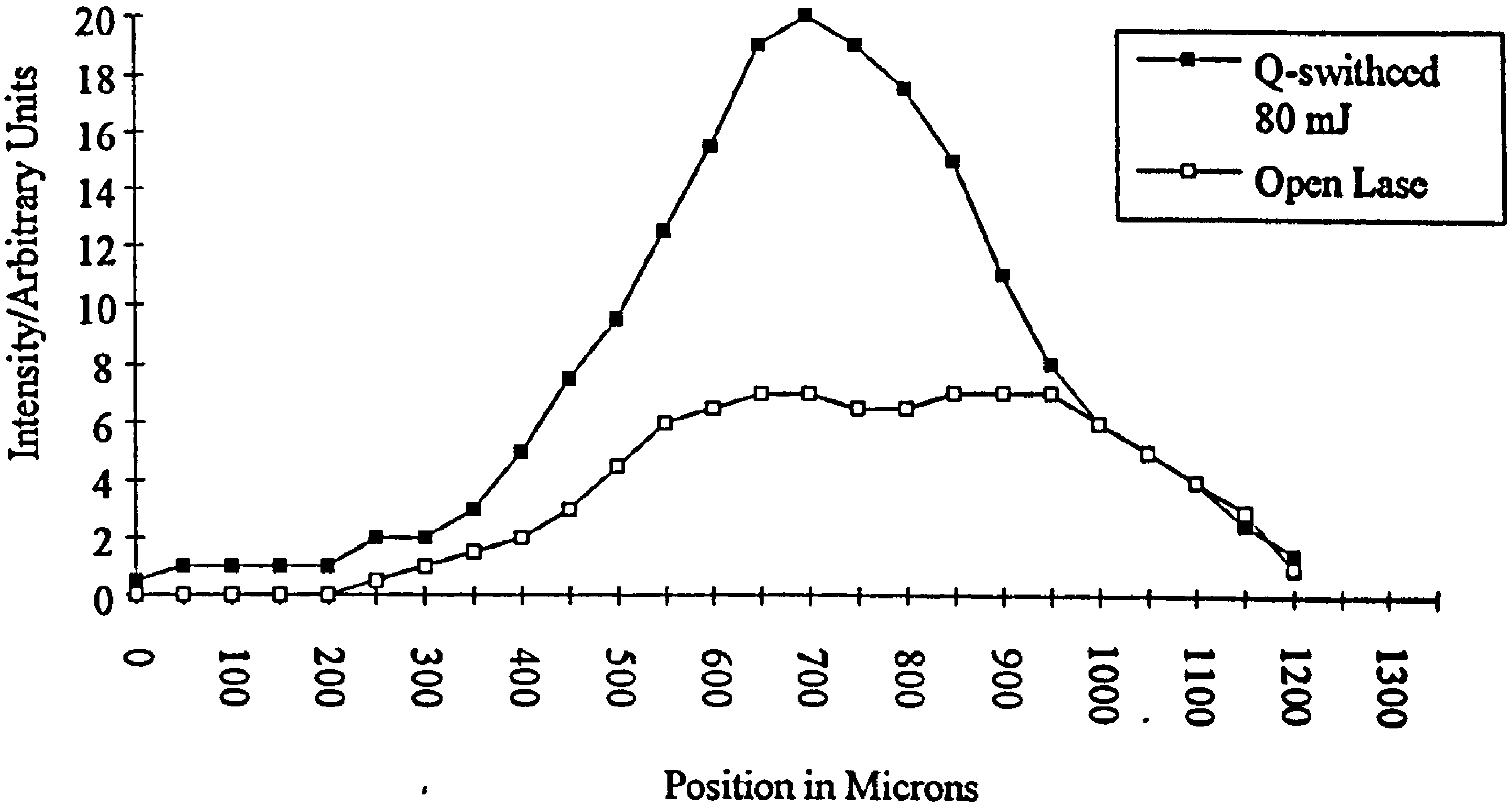

Figure 4.21 Laser sheet profiles for open lase and Q-switched pulses

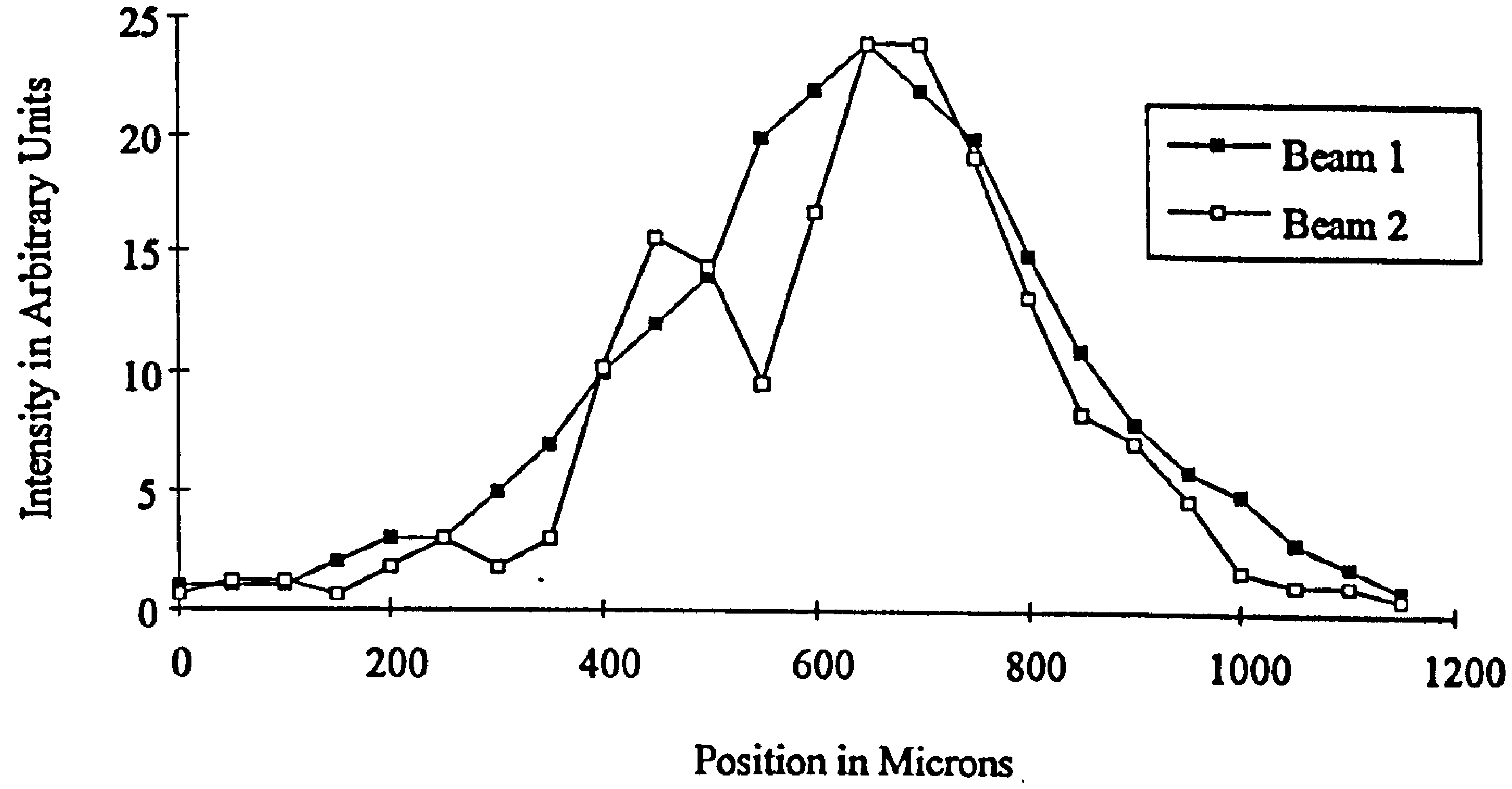

Figure 4.22 Profiles at the focus of the two individual light sheets

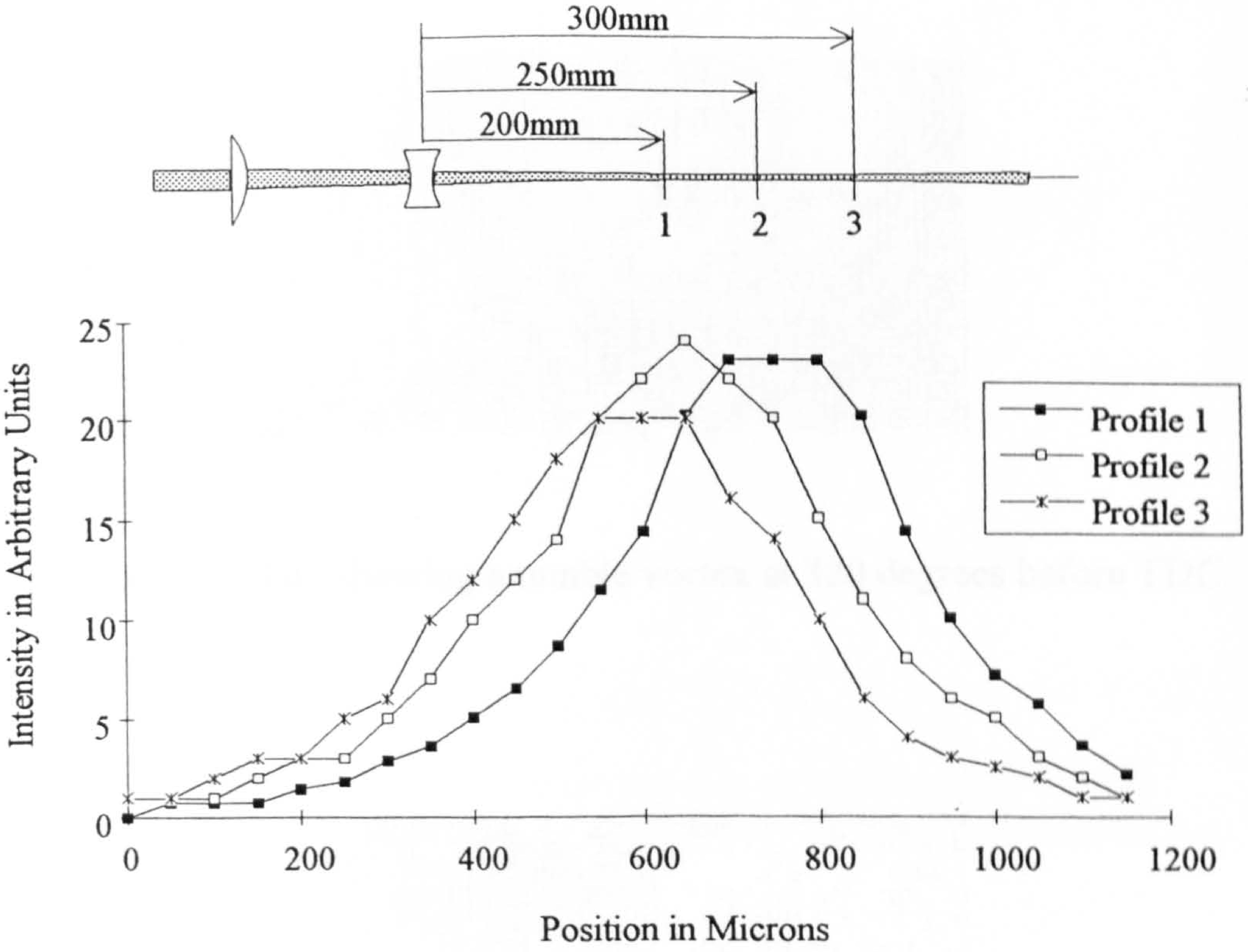

Figure 4.23 Laser sheet profiles at three locations along the optical axis

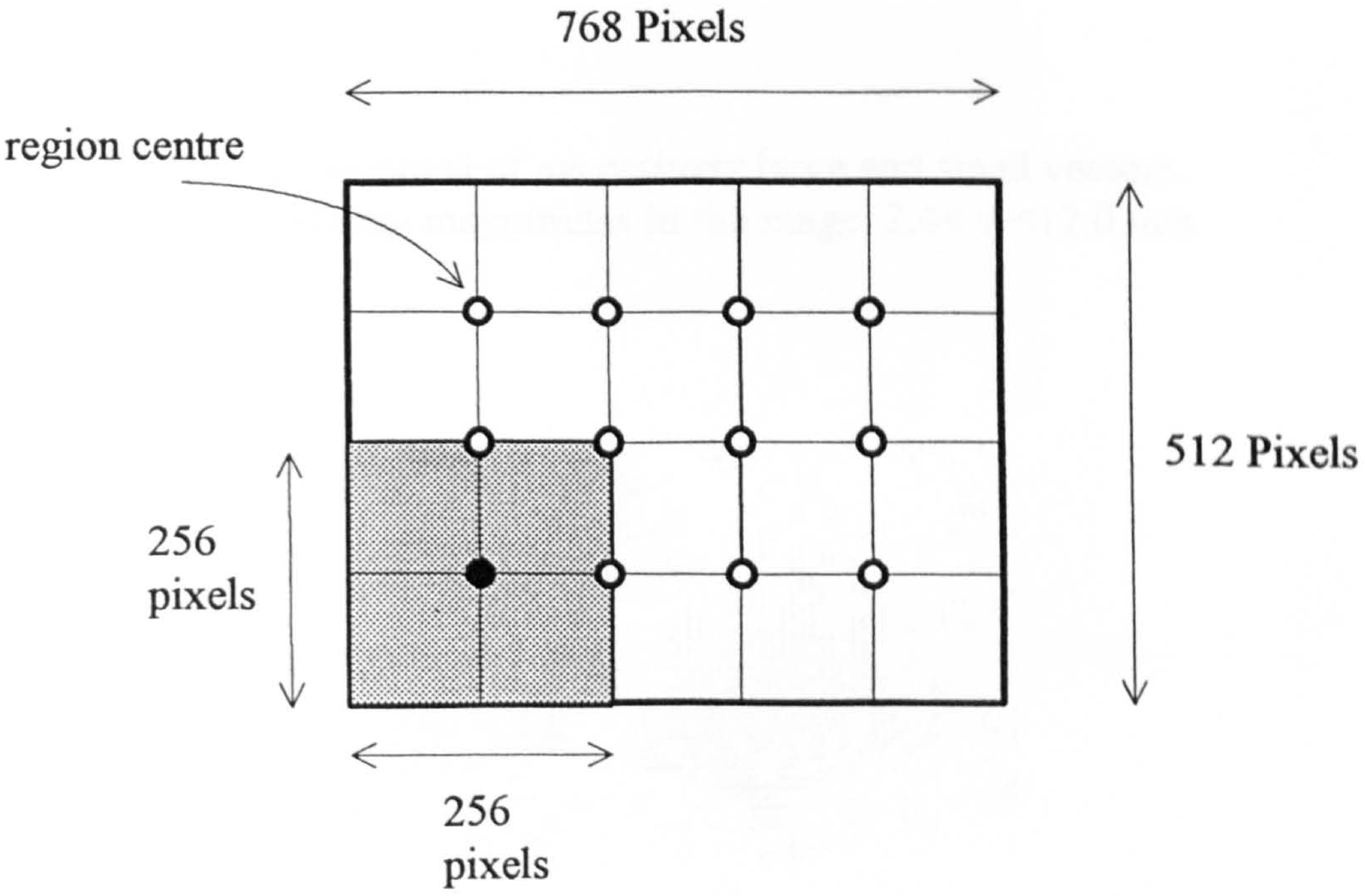

Figure 4.24 Subdivision of digitised frame into a grid of 4x3 overlapping interrogation regions. First region shown shaded.

Figure 4.25 Example of PIV Post-Processing Procedure

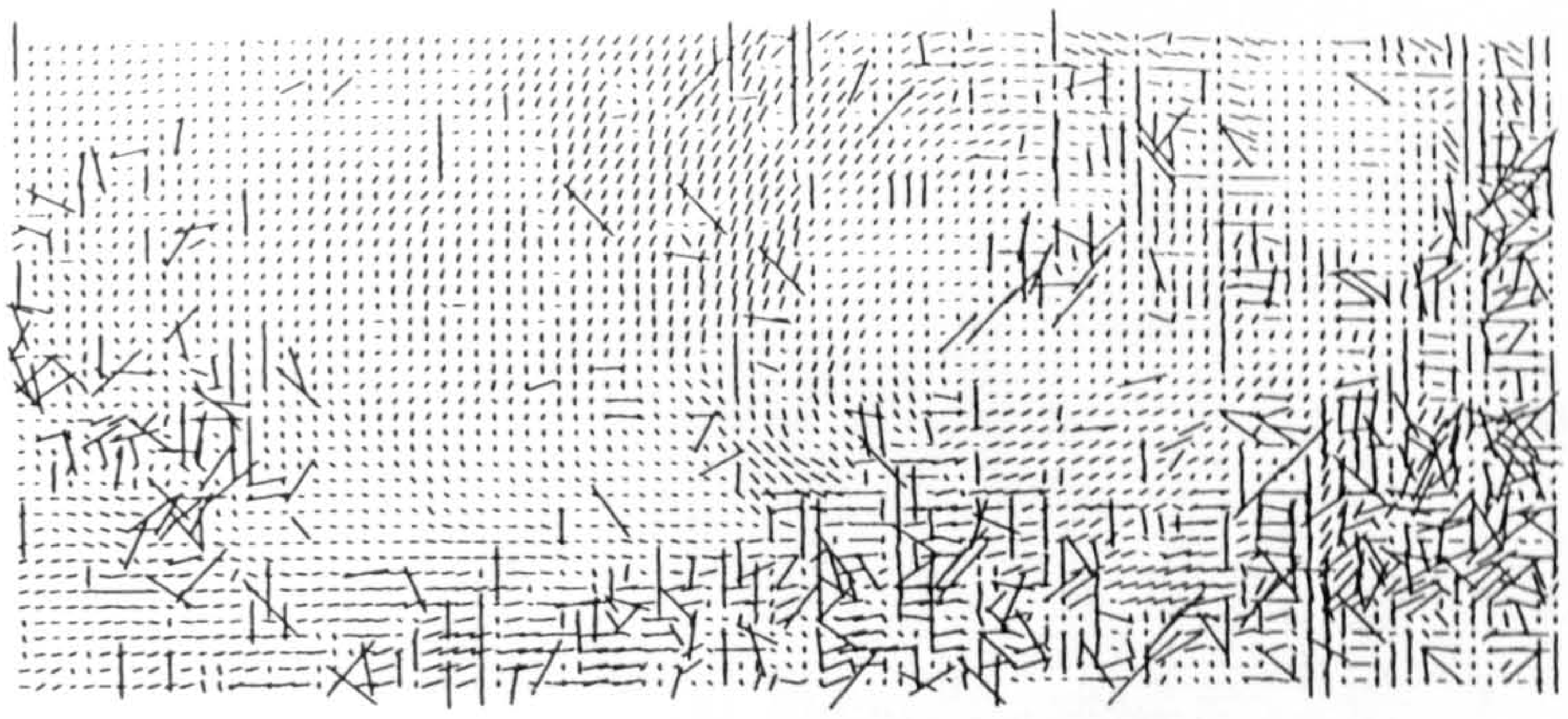

a) Raw PIV data showing a tumble vortex at 320 degrees before TDC.

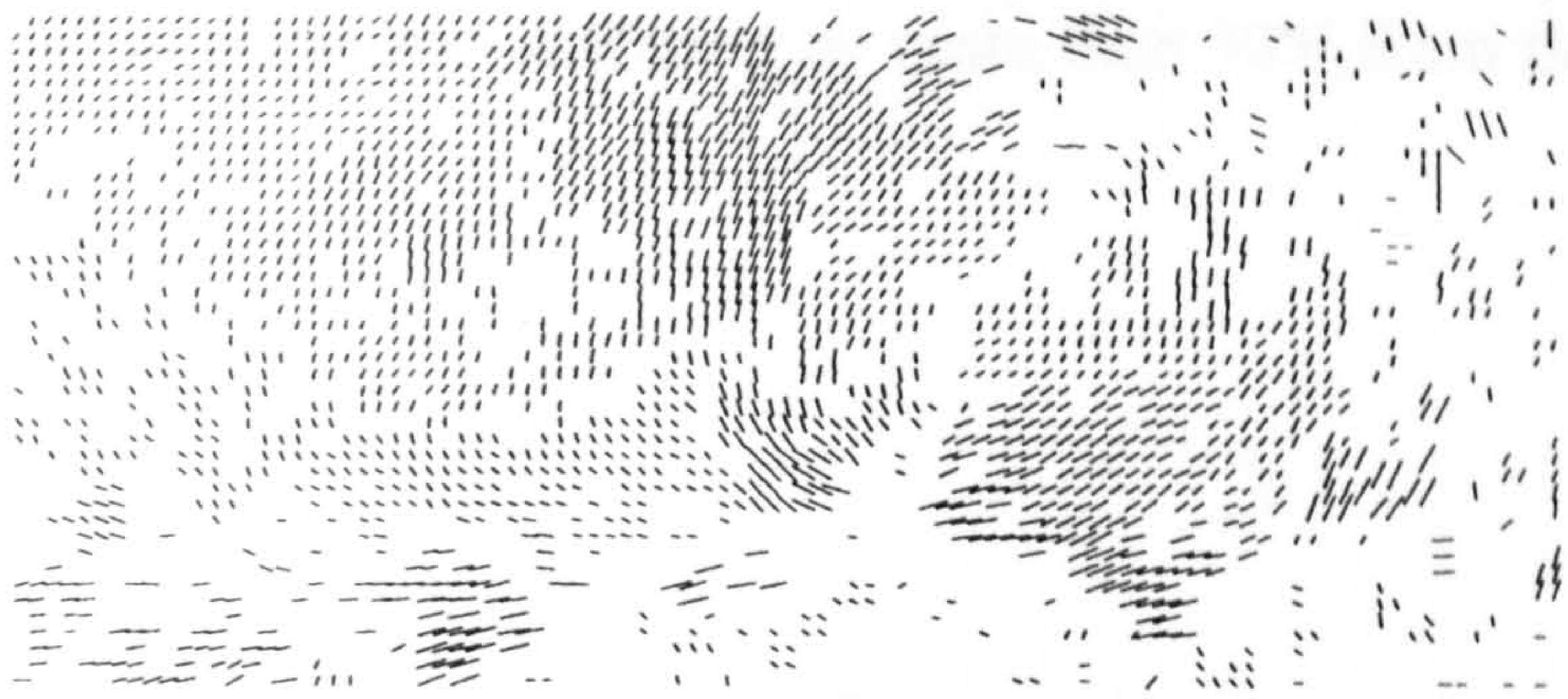

b) PIV data after removal of excessively large and small vectors. Remaining velocity magnitudes in the range 2.4< v <12.0 m/s.

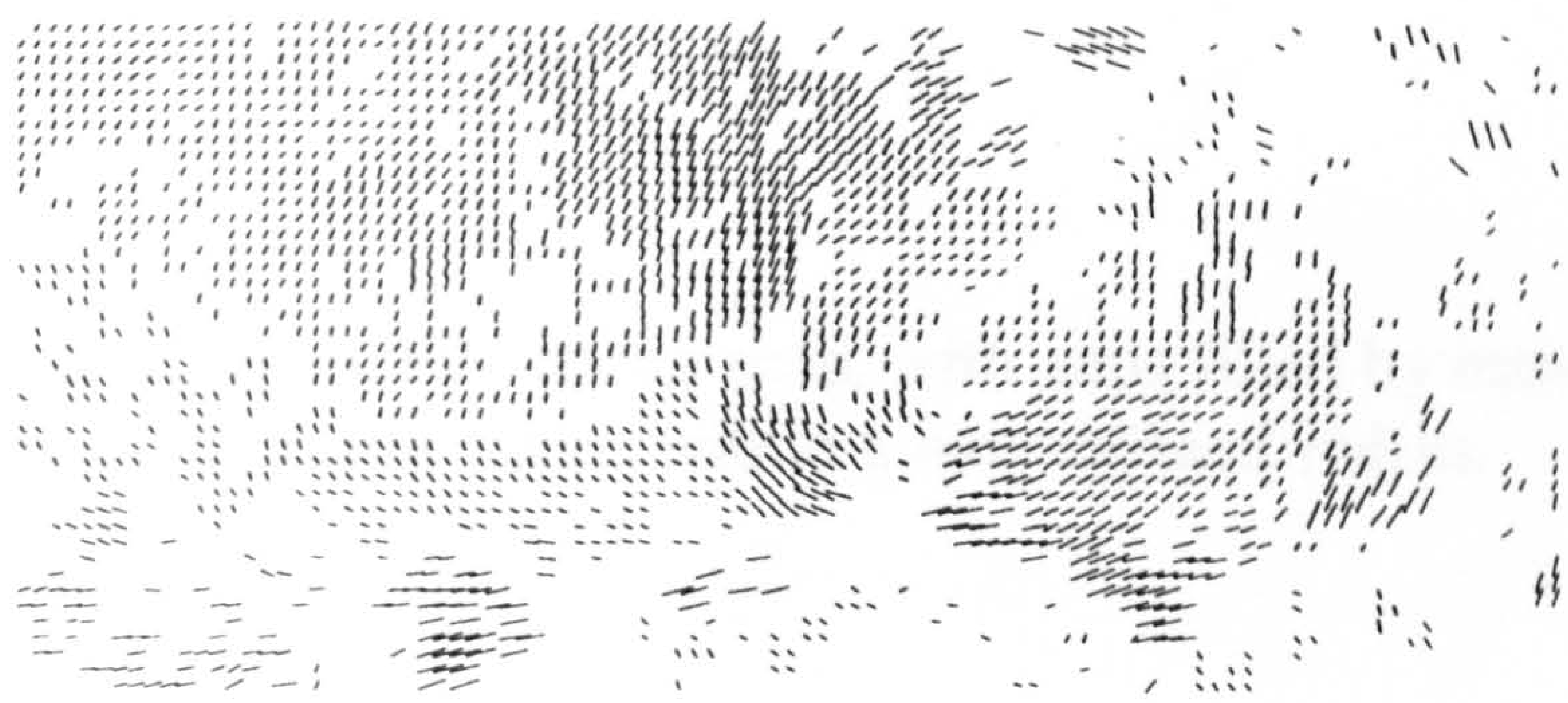

c) PIV data after removal of all vectors lying within 3° of the horizontal or vertical.

Figure 4.25 continued

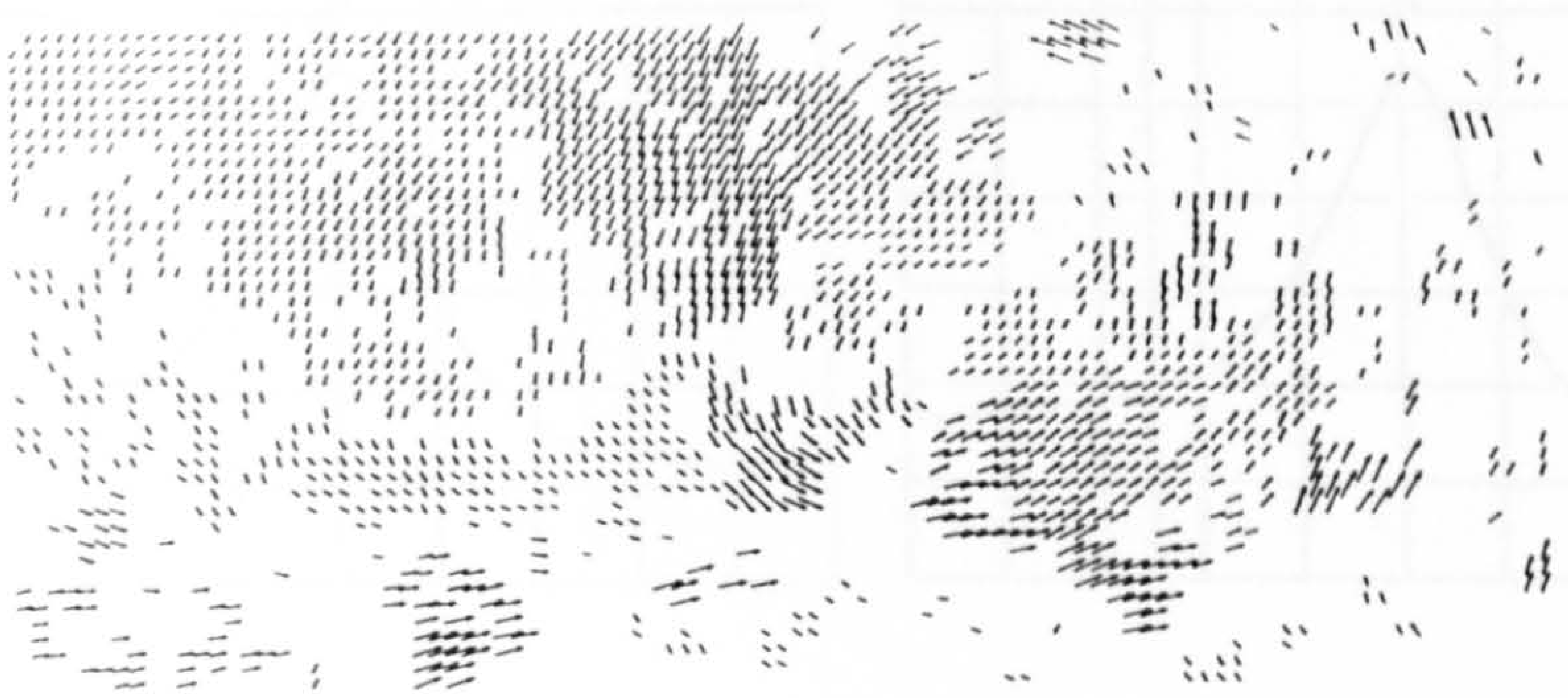

d) PIV data with manually added unambiguous directions, followed by removal of all vectors differing by more than 30% from their neighbours

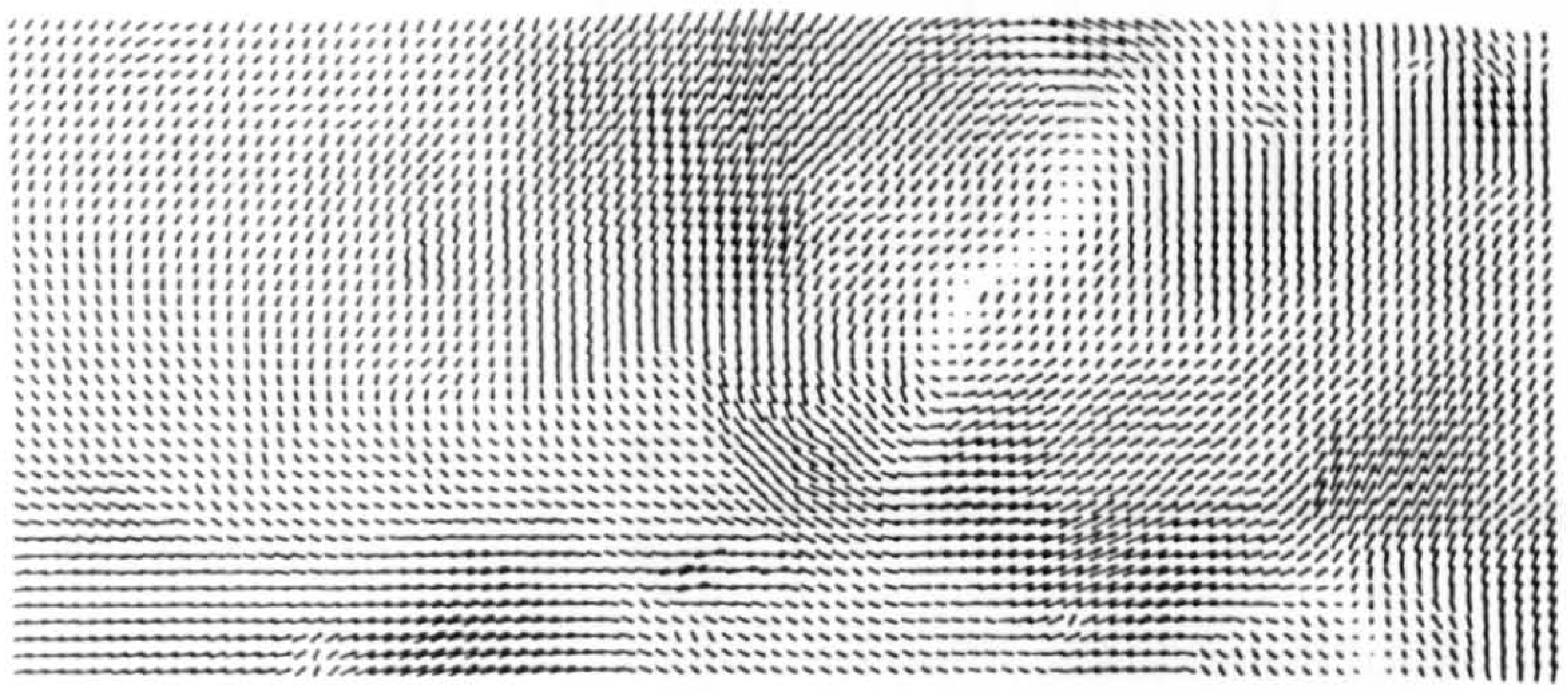

e) Final continuous PIV vector map, with gaps filled by interpolation from neighbouring values within a user-defined radius.

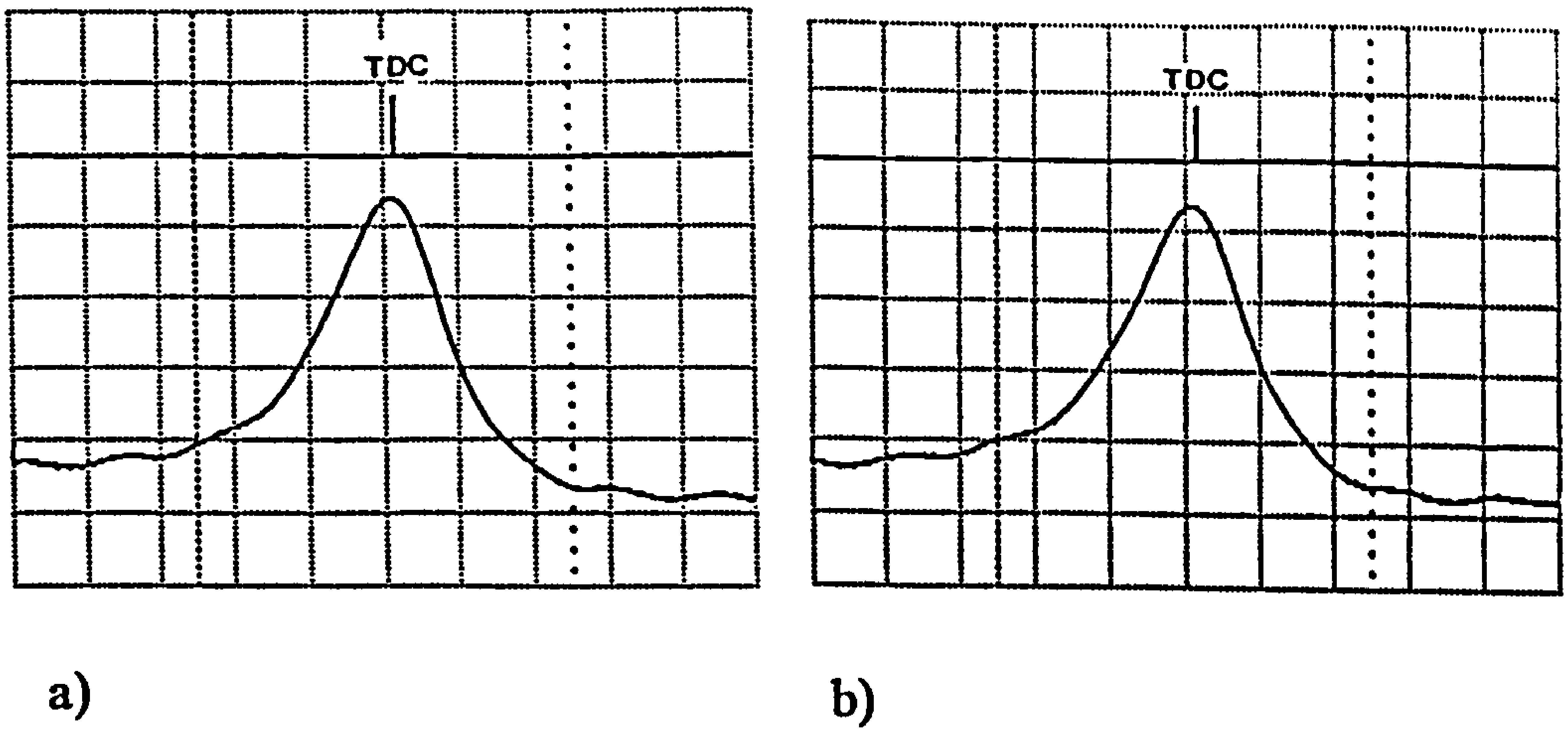

Figure 4.26 Pressure traces for engine motored at 1000RPM, Wide Open Throttle
a) standard 1.2 BSR inlet b) 1.8 BSR inlet using port face gasket
Vertical scale: 400kPa / division..

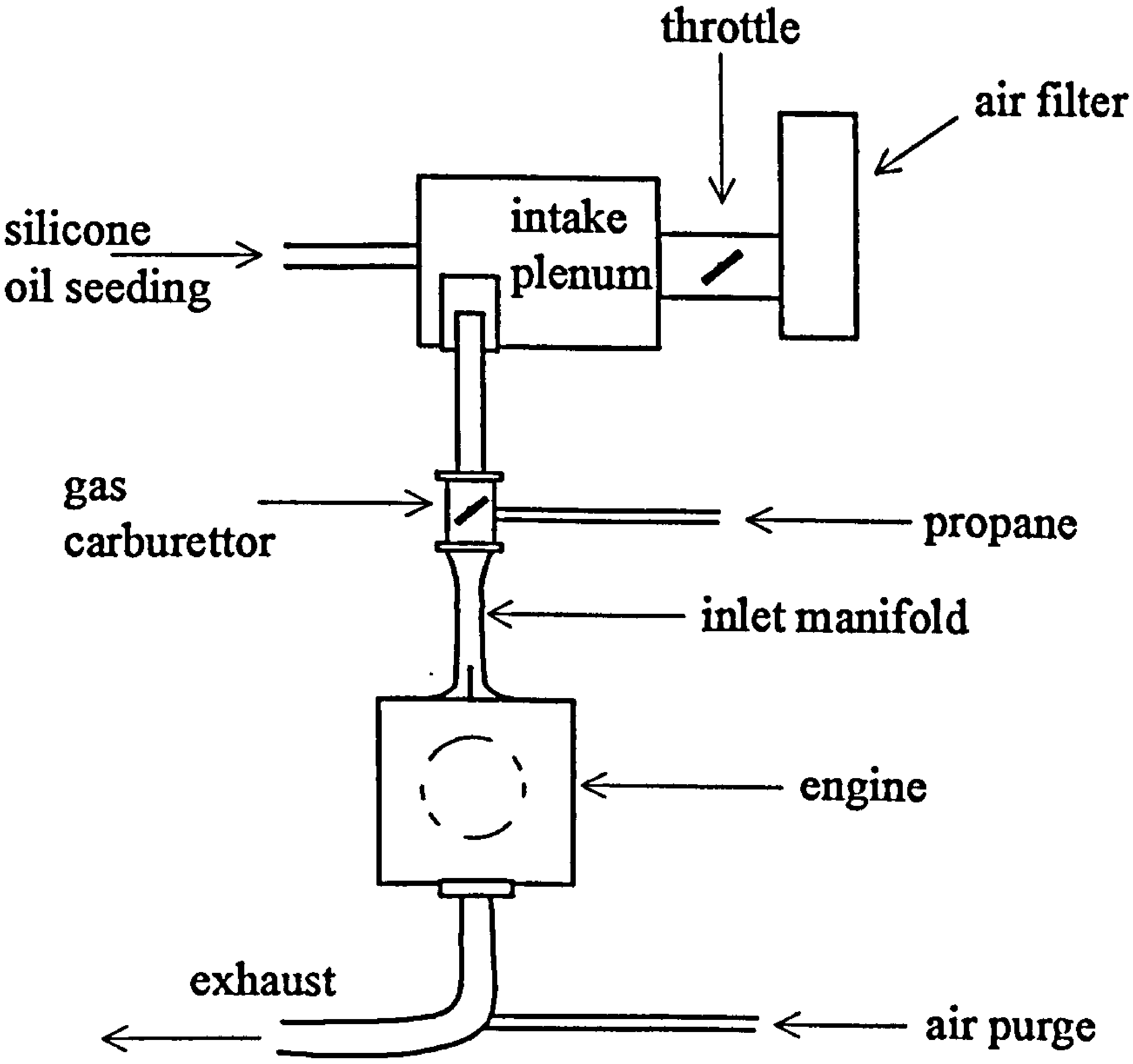

Figure 4.27 Schematic of optical engine inlet and exhaust arrangement for fired experiments

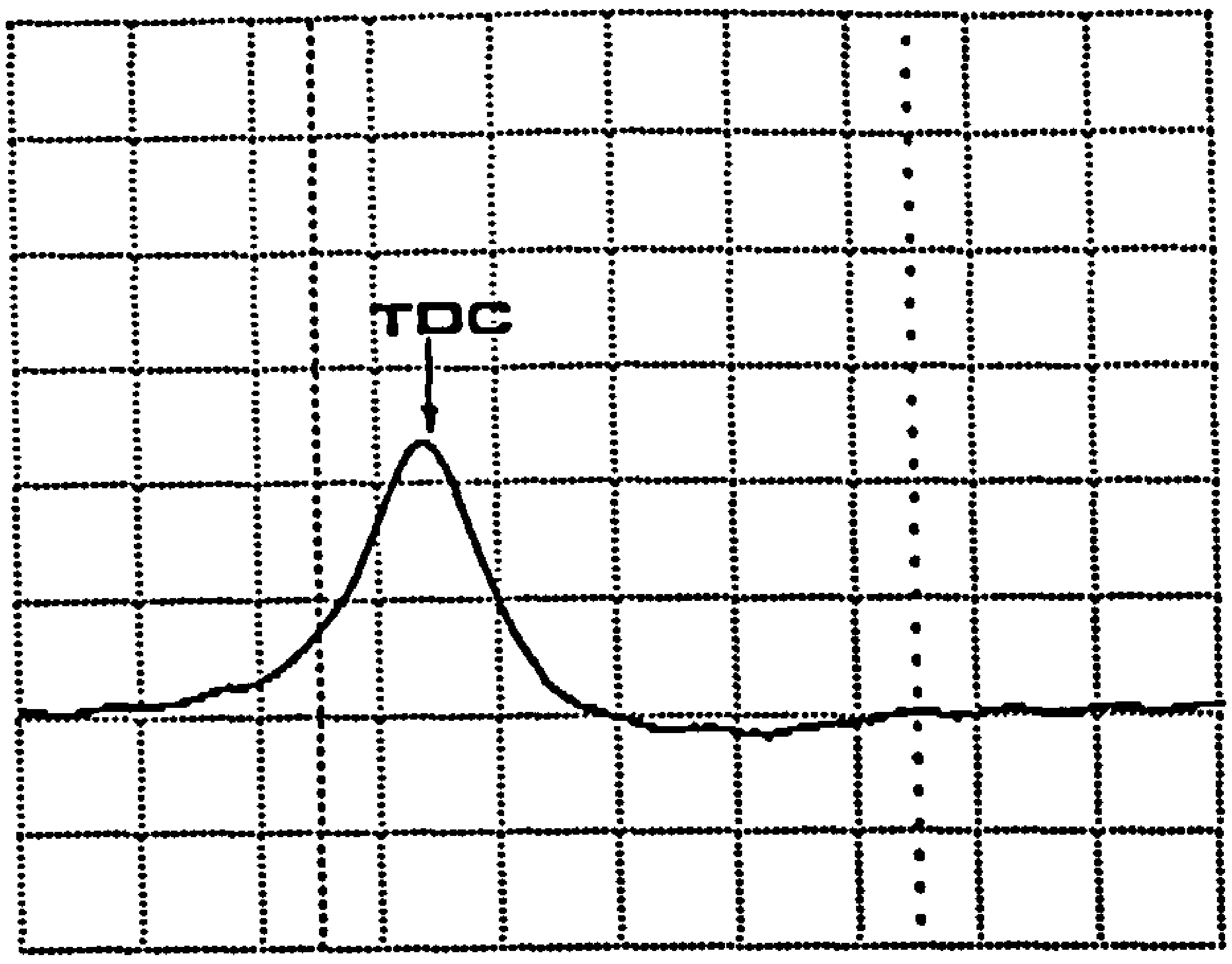

a) Motored pressure trace with propane/air mixture

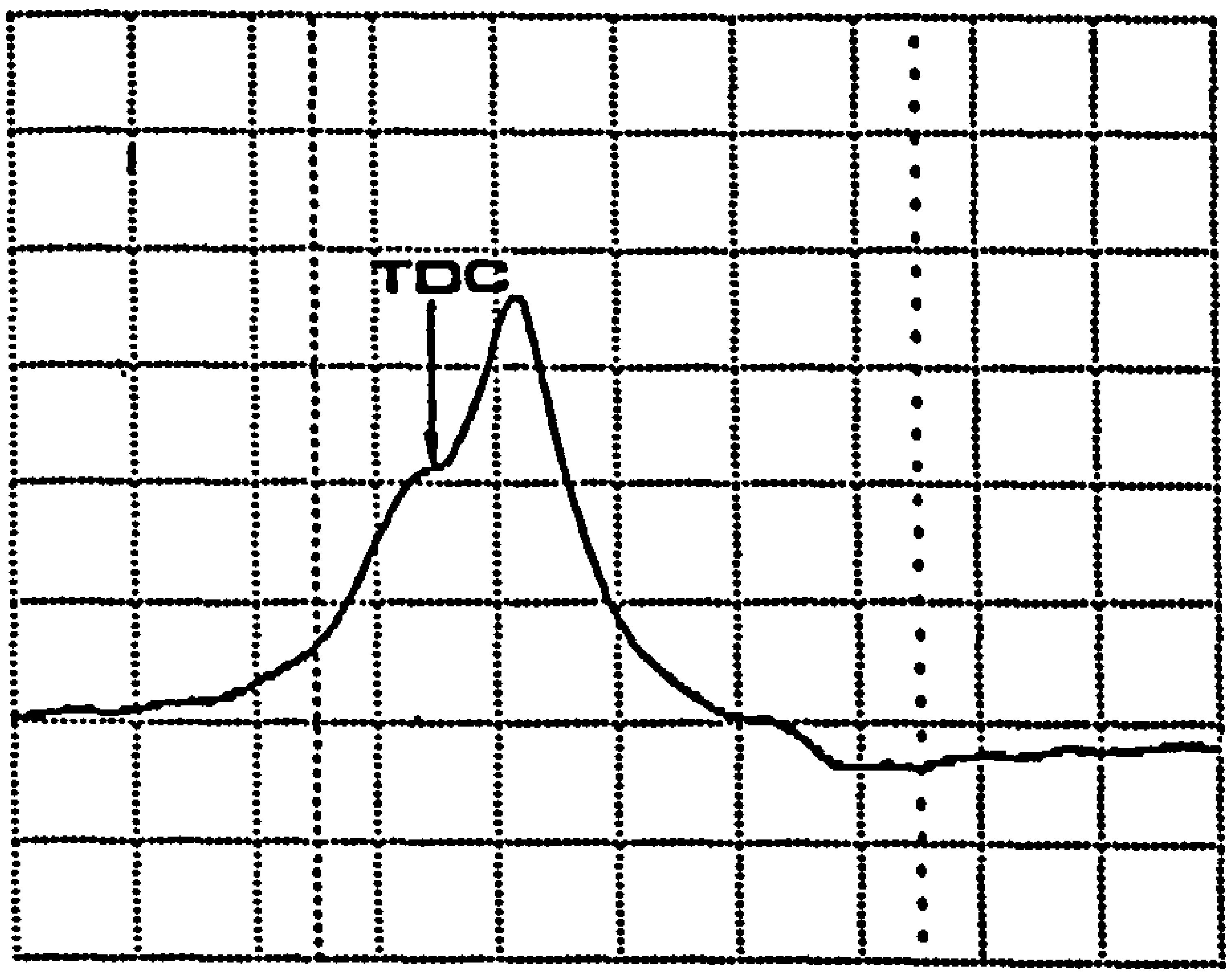

b) Typical fired pressure trace with single-shot ignition

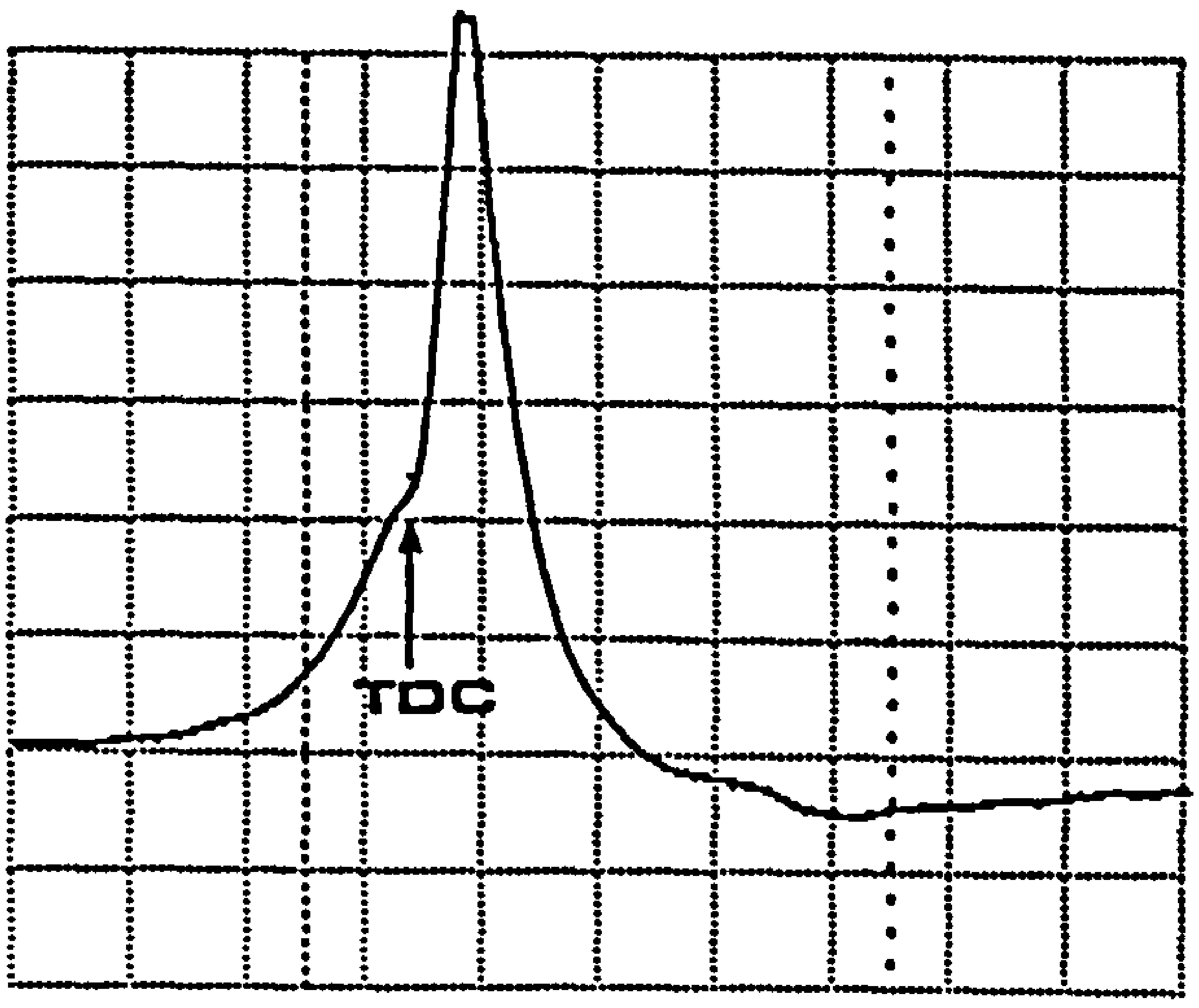

c) Abnormal pressure trace showing maximum cylinder pressure condition

Figure 4.28 Motored and fired pressure traces from the optical engine with the firing inlet configuration. Vertical scale 400kPa/div.

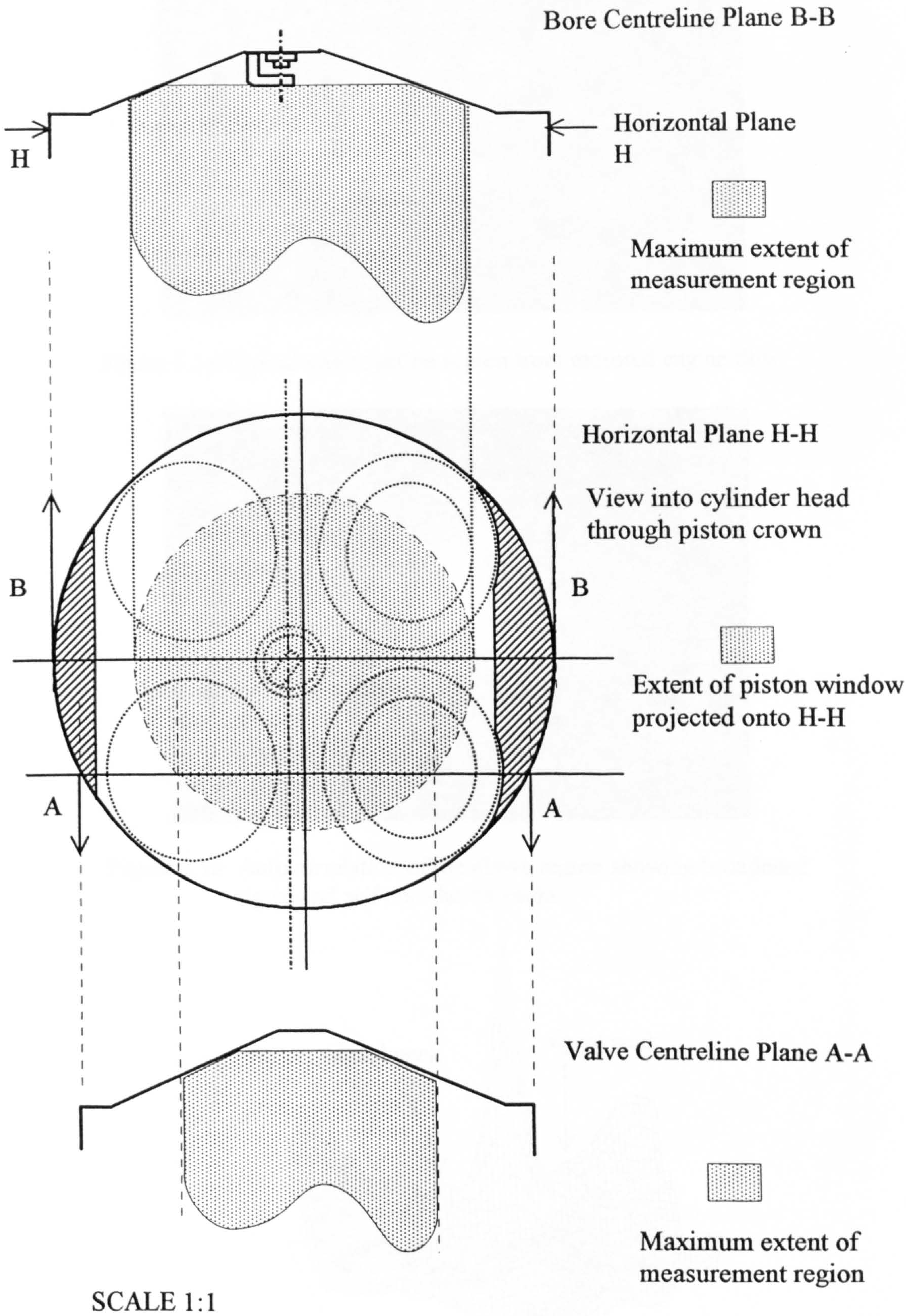

Figure 4.29 Location of measurement planes within engine cylinder

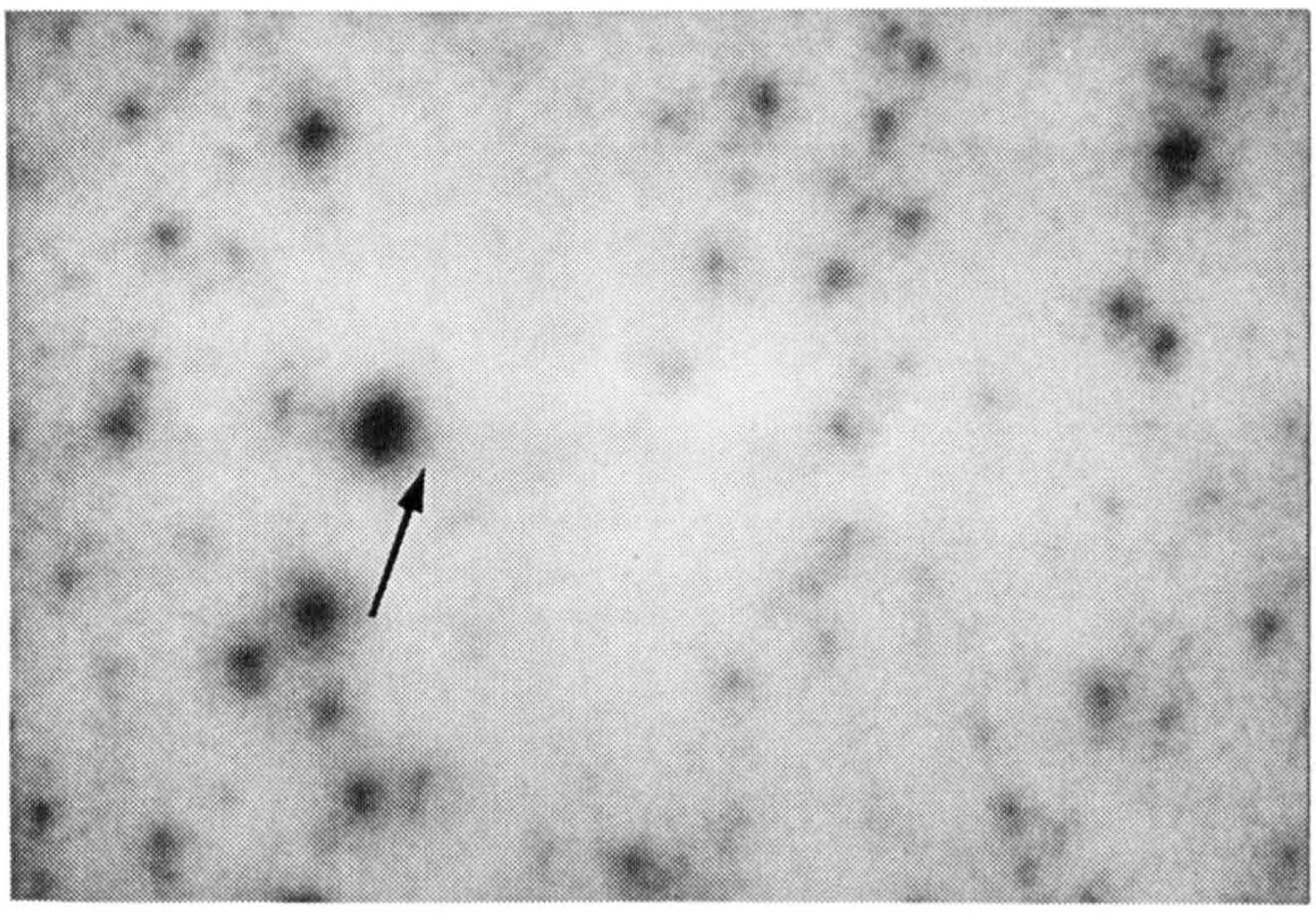

Figure 5.1a Typical interrogation region from motored engine flow.

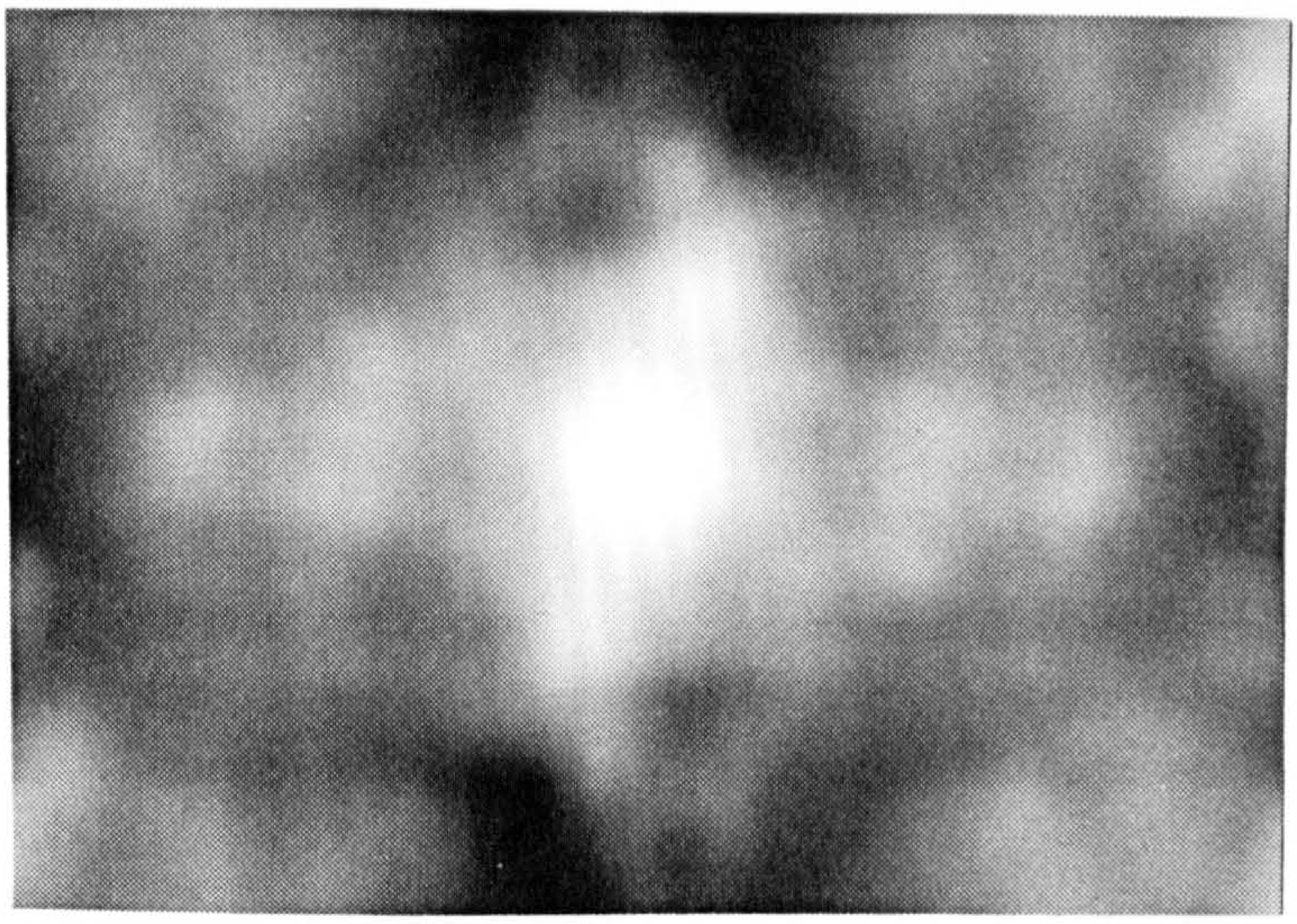

Figure 5.1b Autocorrelation of the above region showing broadened signal and self correlation peaks.

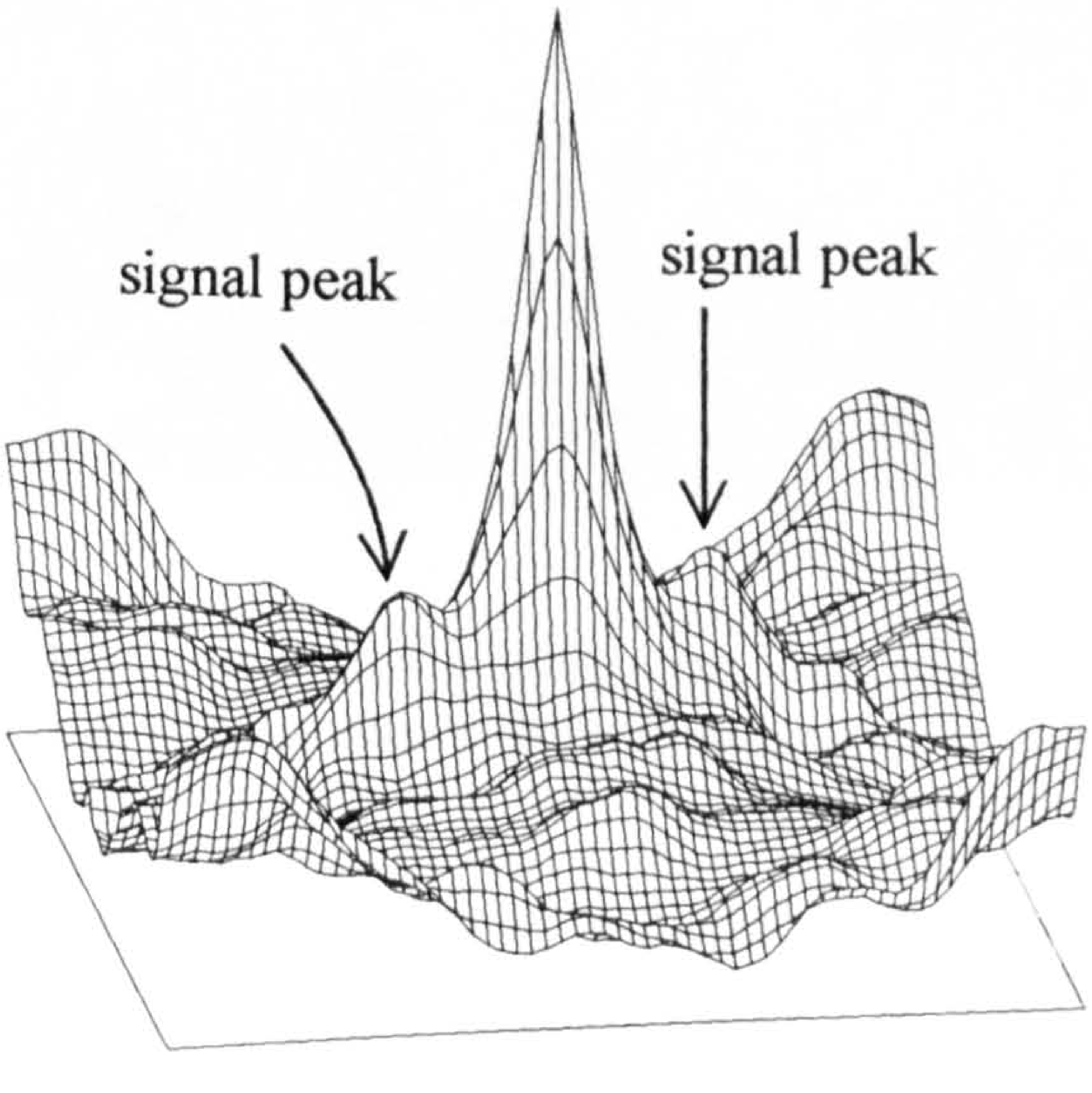

Figure 5.1c 3-D plot of above region indicating high noise floor and broad signal peaks of reduced height.

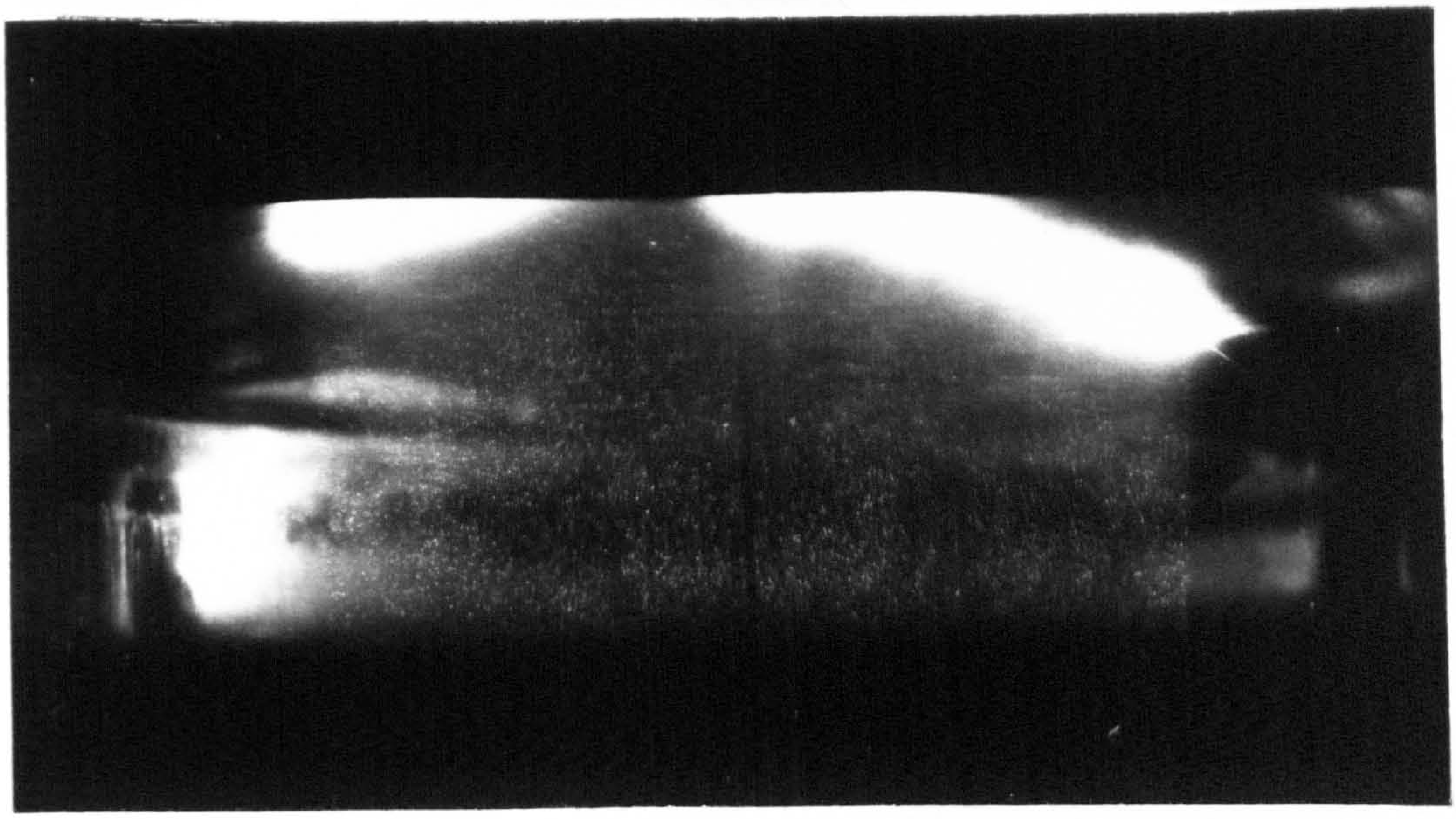

Figure 5.2a Induction PIV image, plane A-A, 45 degrees after TDC, 1.2 BSR Inlet valve to right. Note flare from open inlet valve and its reflection (lower left).

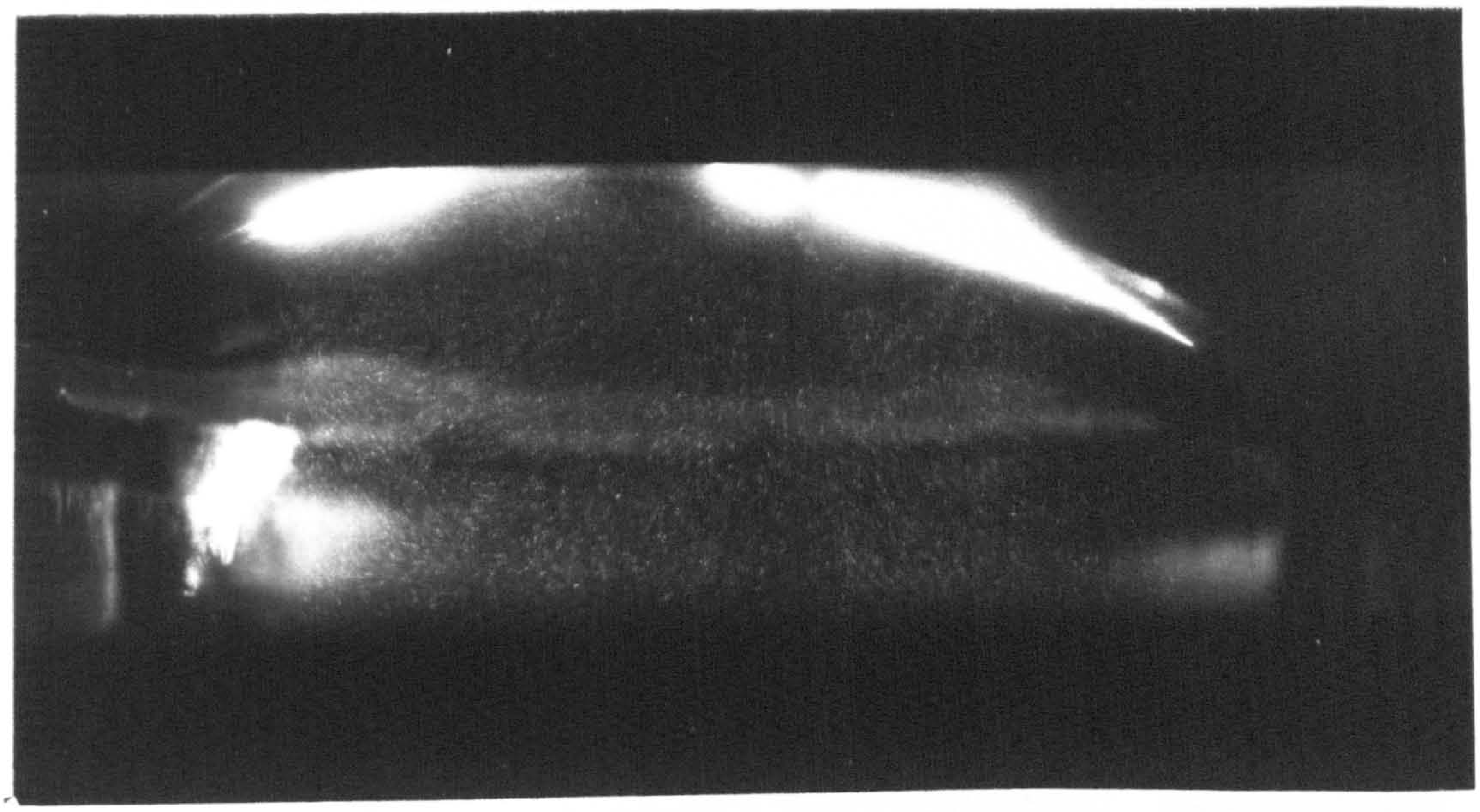

Figure 5.2b PIV image as above but with 1.8 BSR inlet. Note the dominant vortex beneath the exhaust valve (left of centre).

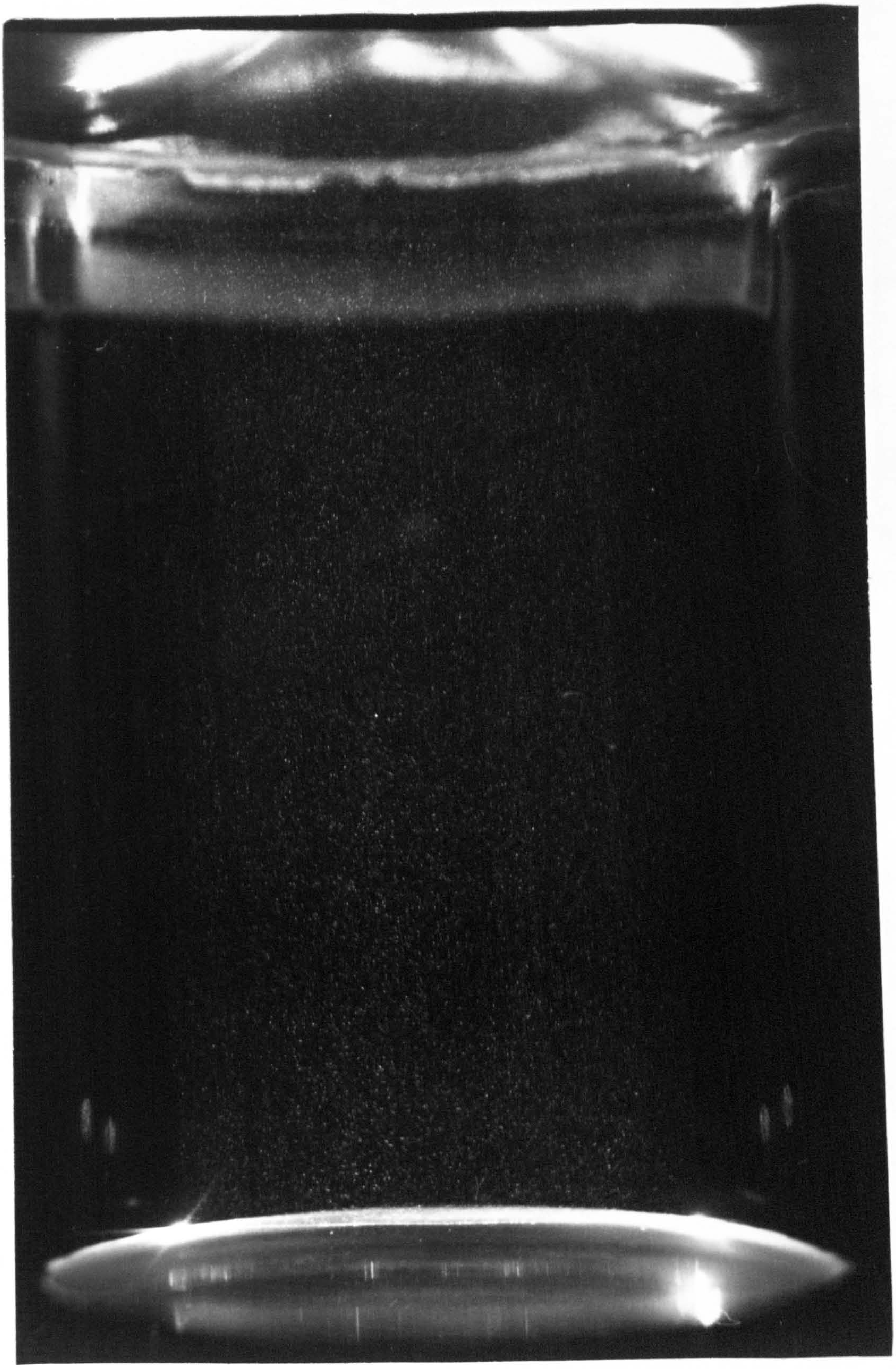

Figure 5.3 Typical PIV image at Inlet Valve Closure. Flare structure toward the cylinder head is due to flare from the combustion chamber surfaces and the cylinder head gasket.

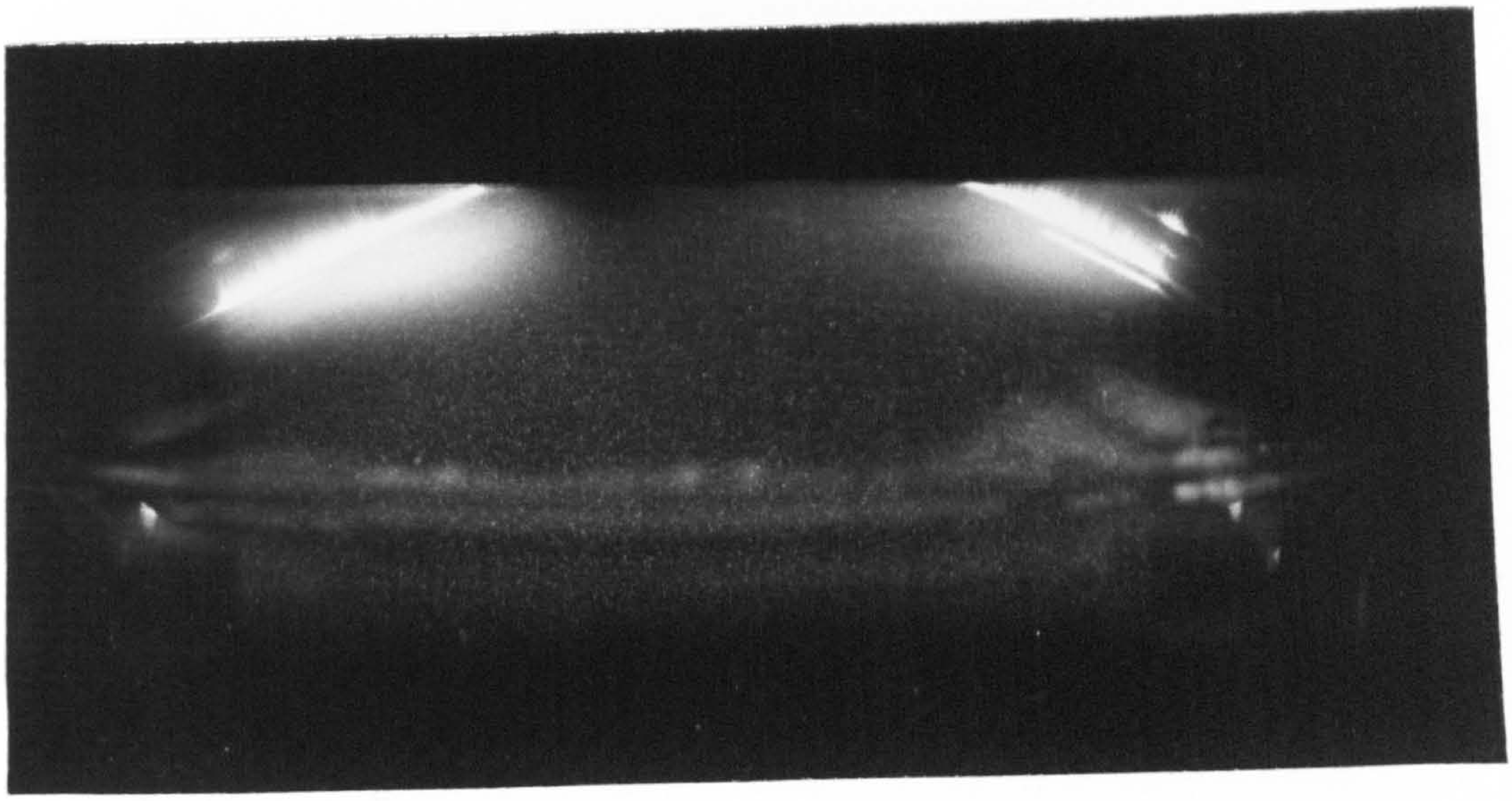

Figure 5.4 Compression PIV image, plane A-A, 320 degrees after TDC, 1.2 BSR Note vortex beneath inlet valve (lower right) and lack of particle pairs in out-of-plane flow beneath exhaust valve (top left).

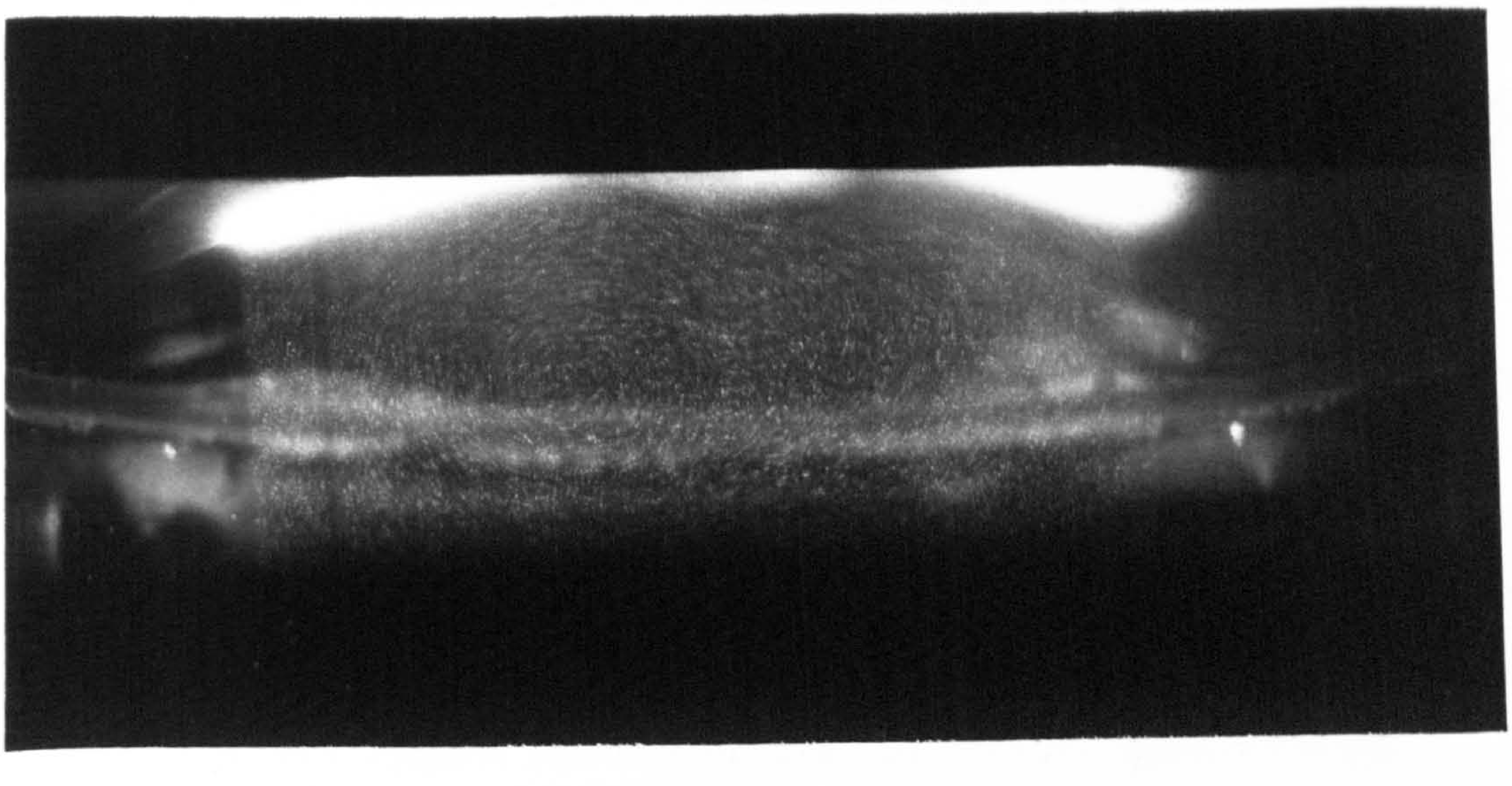

Figure 5.5 Compression PIV image as above but with 1.8 BSR inlet. Note the strong barrel vortex at this condition.

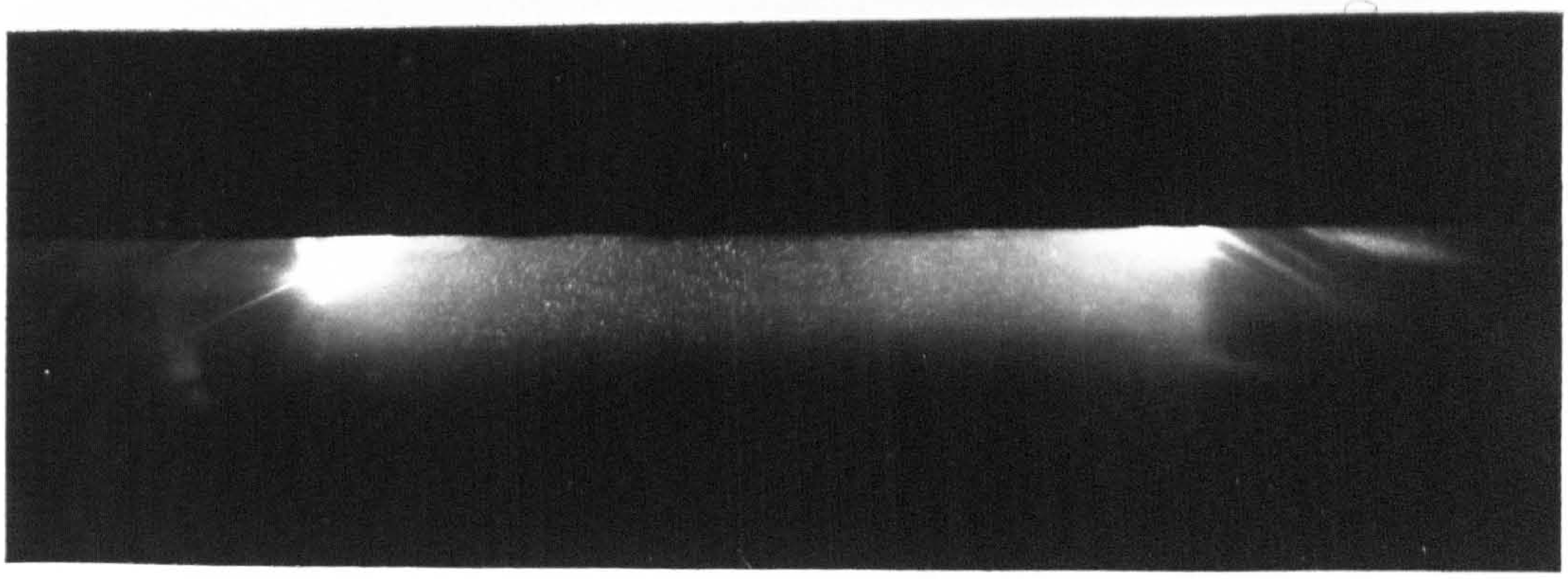

Figure 5.6a PIV image at 338 degrees after TDC (nominal ignition timing), Plane A-A. 1.2 BSR inlet

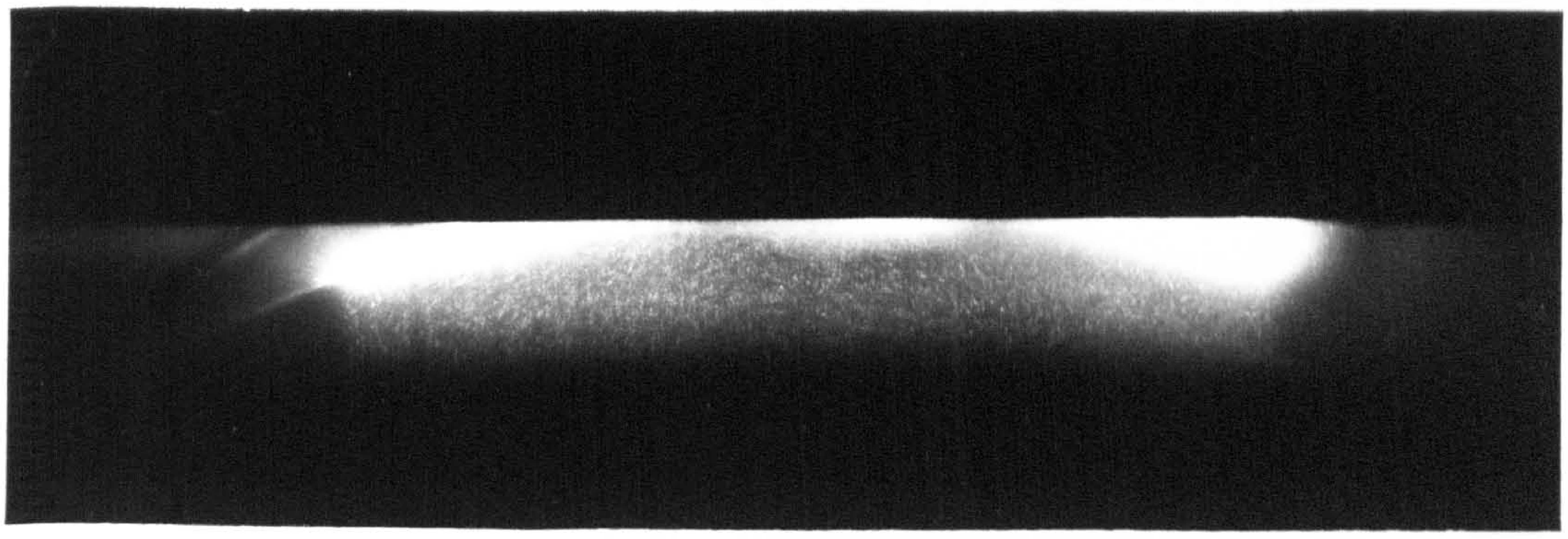

Figure 5.6b PIV image at 338 degrees after TDC (nominal ignition timing), Plane A-A. 1.8 BSR inlet.

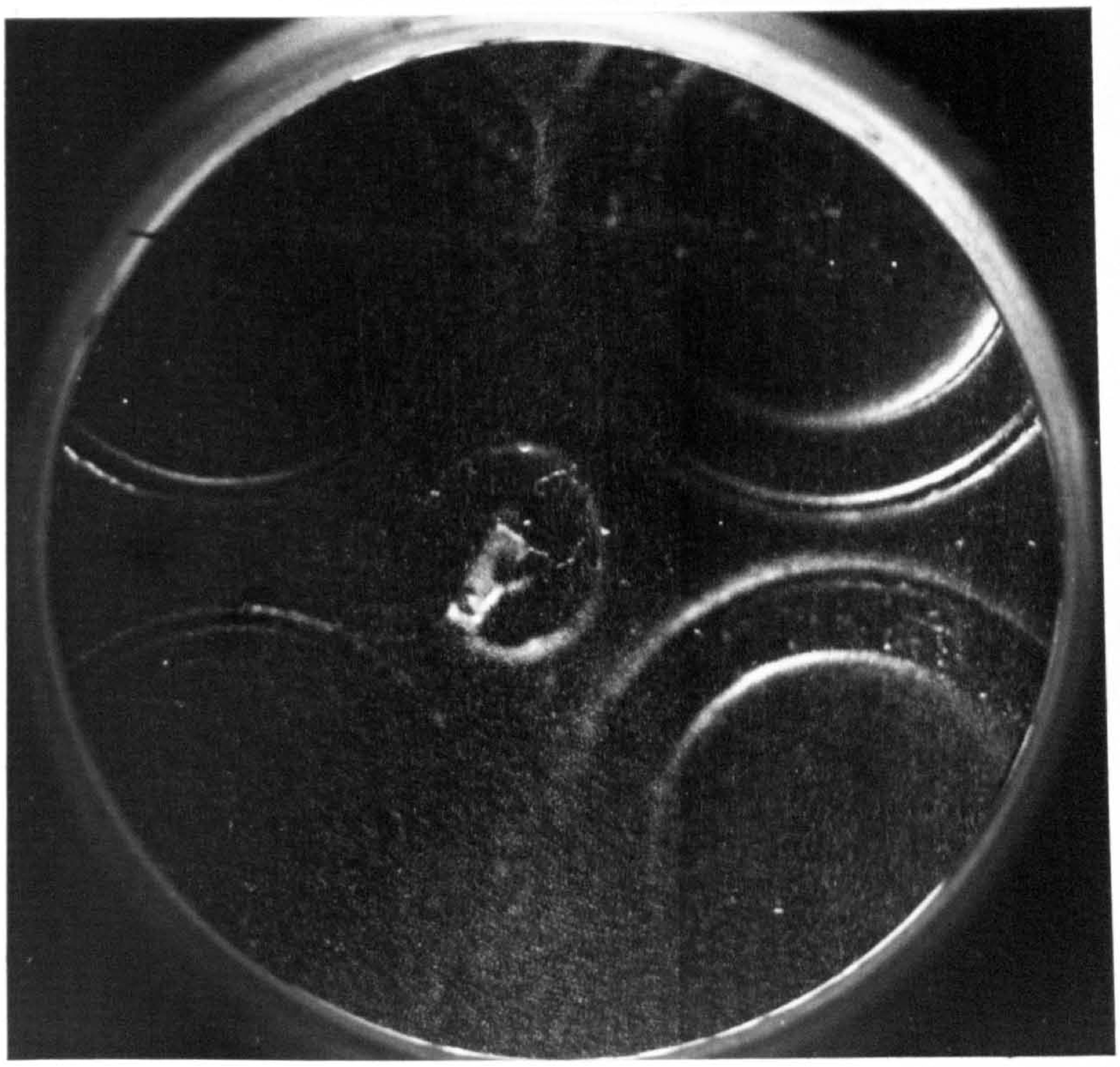

Figure 5.9 PIV image from horizontal plane H-H at the 1.8 BSR condition, 338 degrees after TDC (nominal ignition timing). View through piston crown window, inlet valves to right.

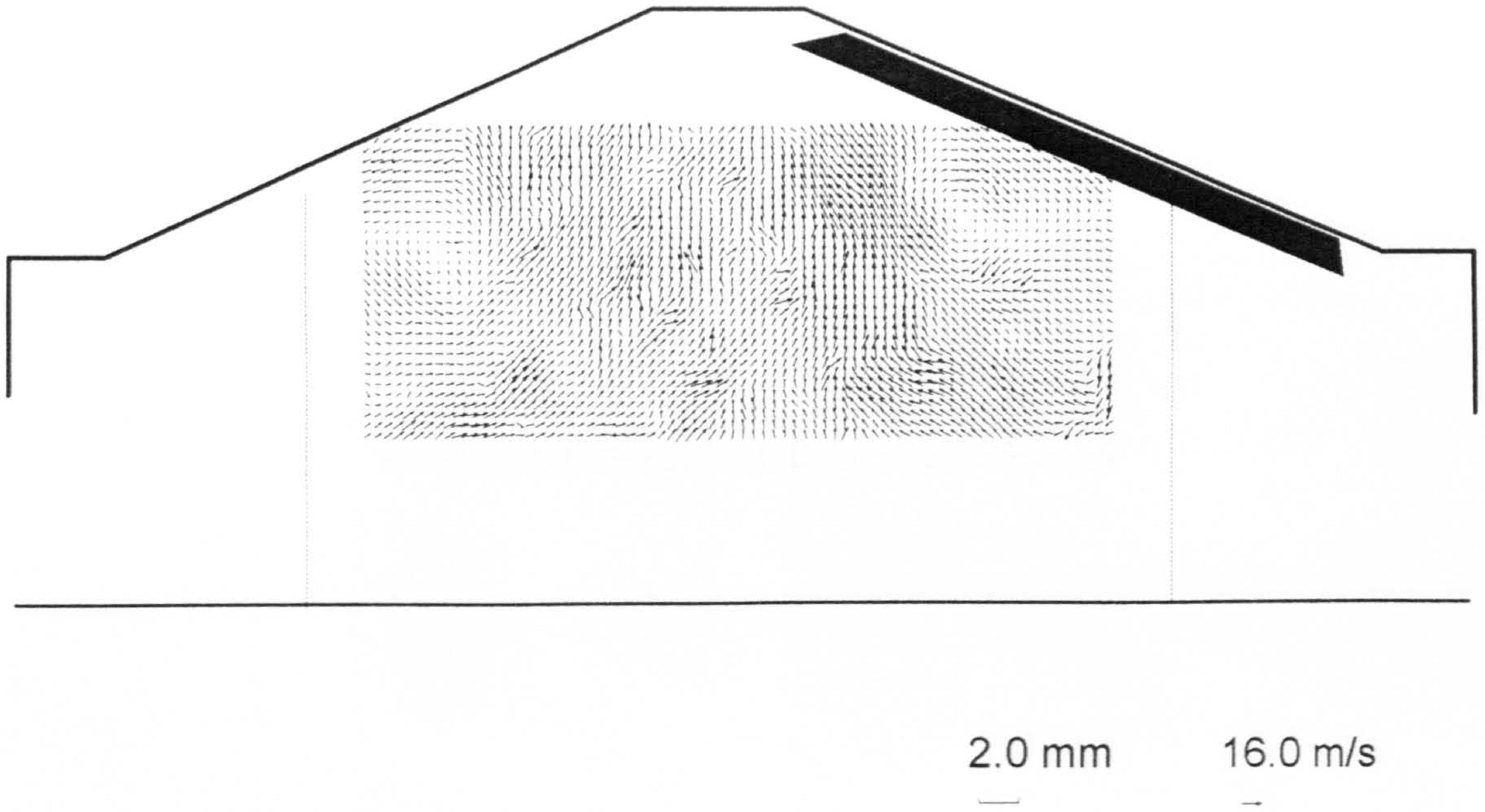

Figure 5.10 Plane A-A, 45 degrees induction, 1.2 BSR inlet.
Inlet valve to right. Note twin vortex structure.

T36#10.DRW

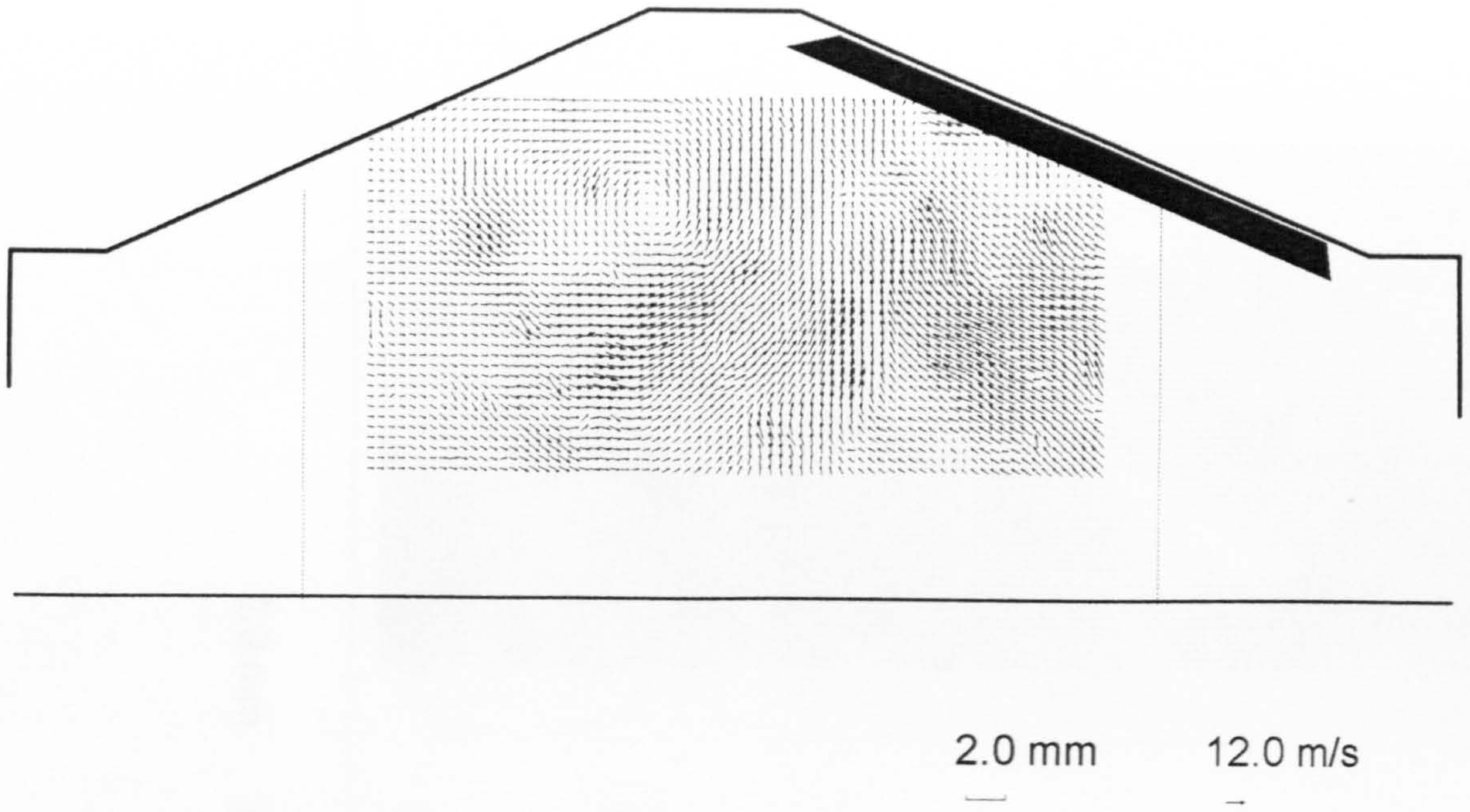

Figure 5.11 Plane A-A, 45 degrees induction, 1.8 BSR inlet.
Note dominant barrel vortex to left of centreline.

T31#1.DRW

Figure 5.12 Plane A-A, 222 degrees after TDC, 1.2 BSR inlet.

EN24#12.ASC

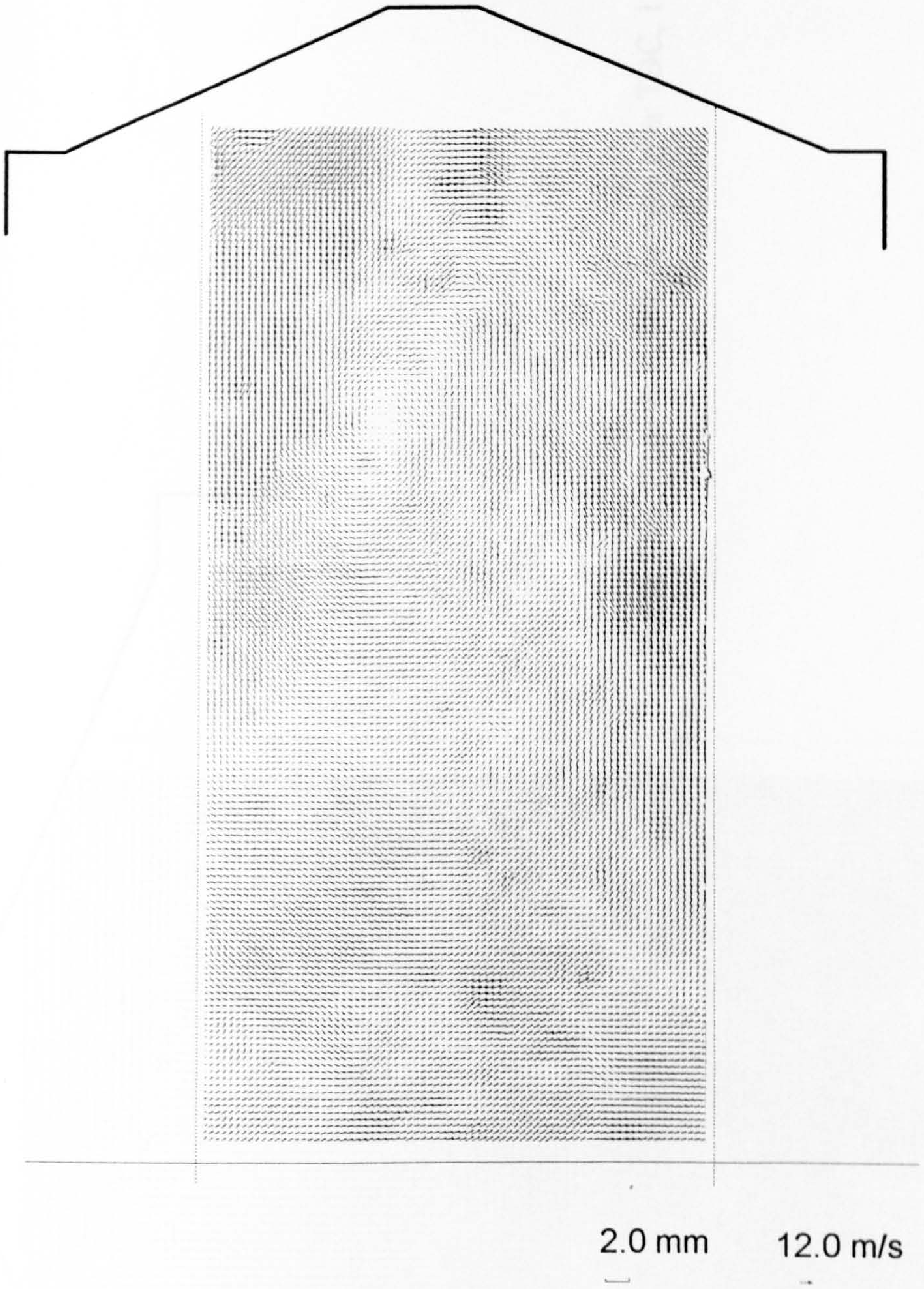

Figure 5.13 Plane A-A, 222 degrees after TDC, 1.8 BSR inlet.

EN31#8 ASC

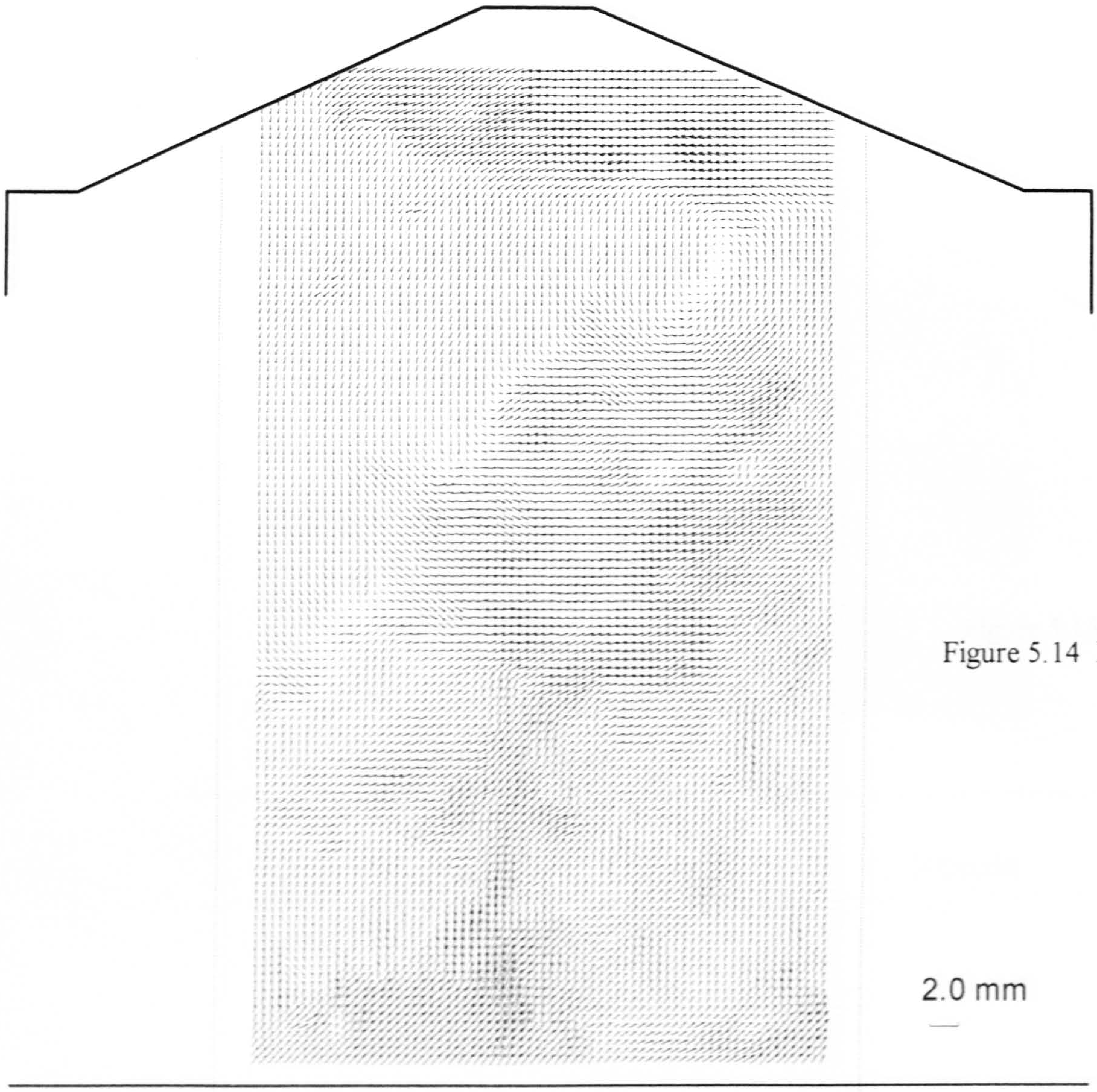

Figure 5.14 Plane A-A, 260 degrees after TDC, 1.2 BSR inlet.

T24#8.DRW

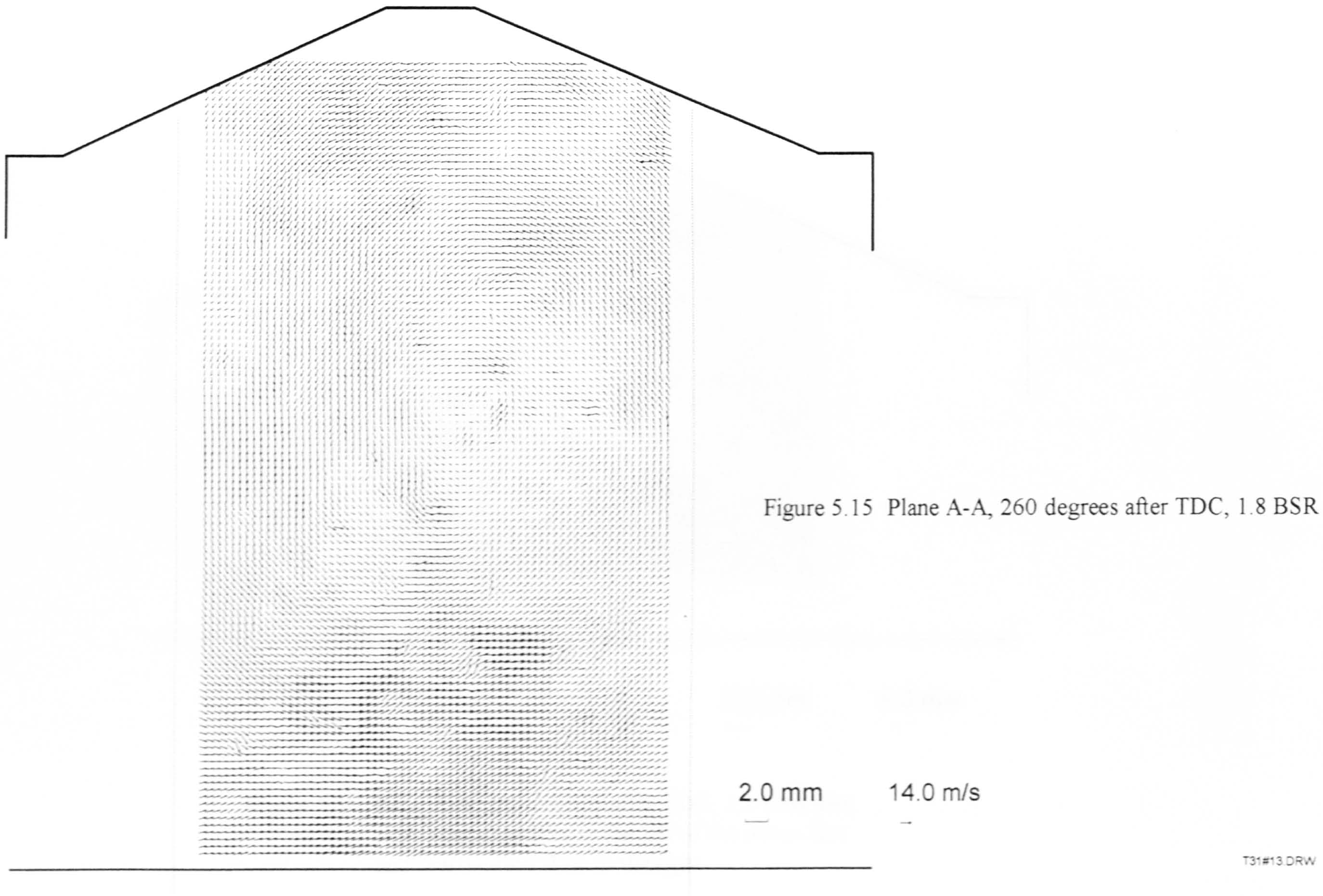

Figure 5.15 Plane A-A, 260 degrees after TDC, 1.8 BSR inlet.

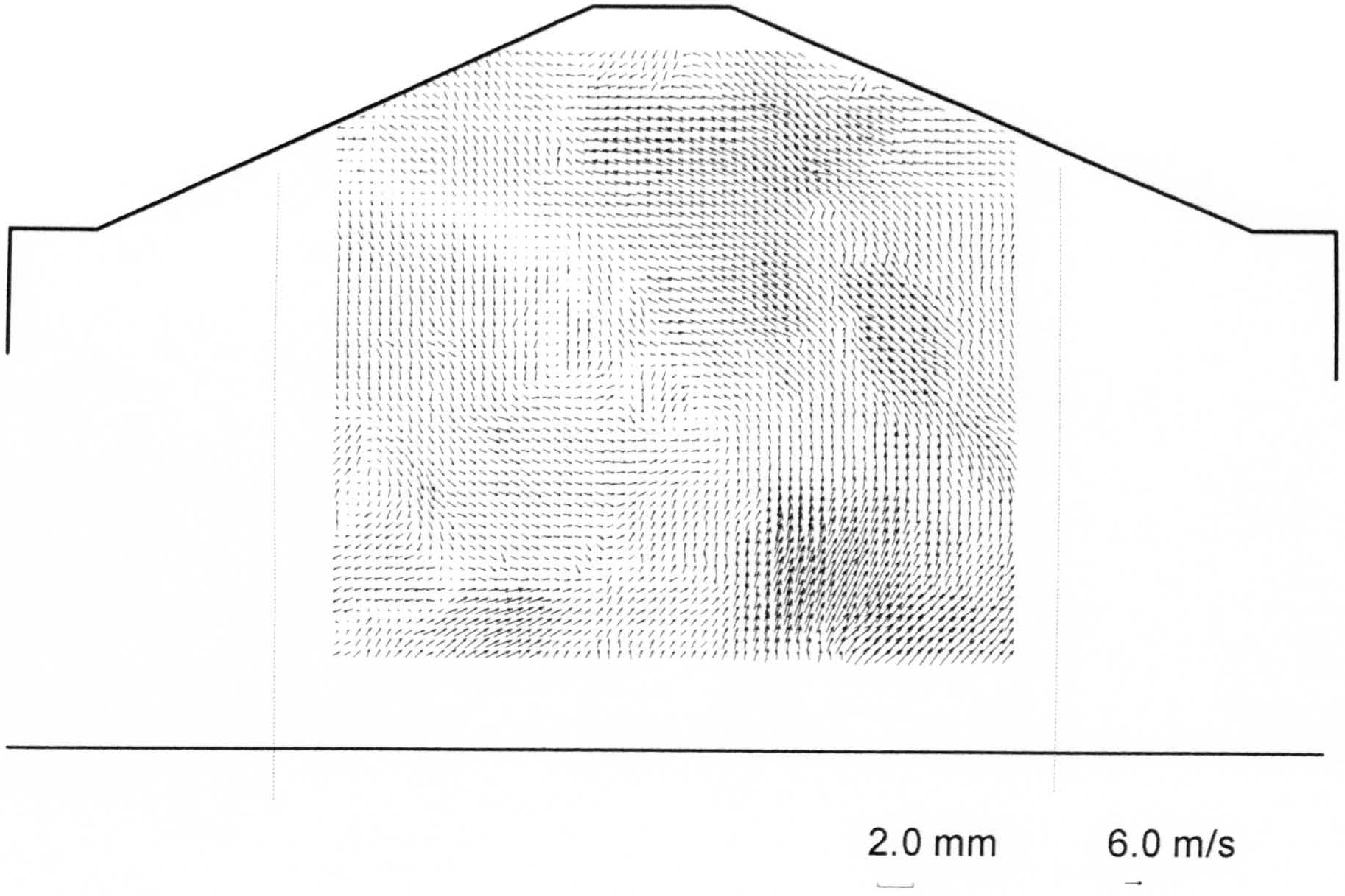

Figure 5.16 Plane A-A, 300 degrees after TDC, 1.2 BSR inlet. Note stagnated flow to the left of the piston face and near-vertical flow to the right.

T24#6.DRW

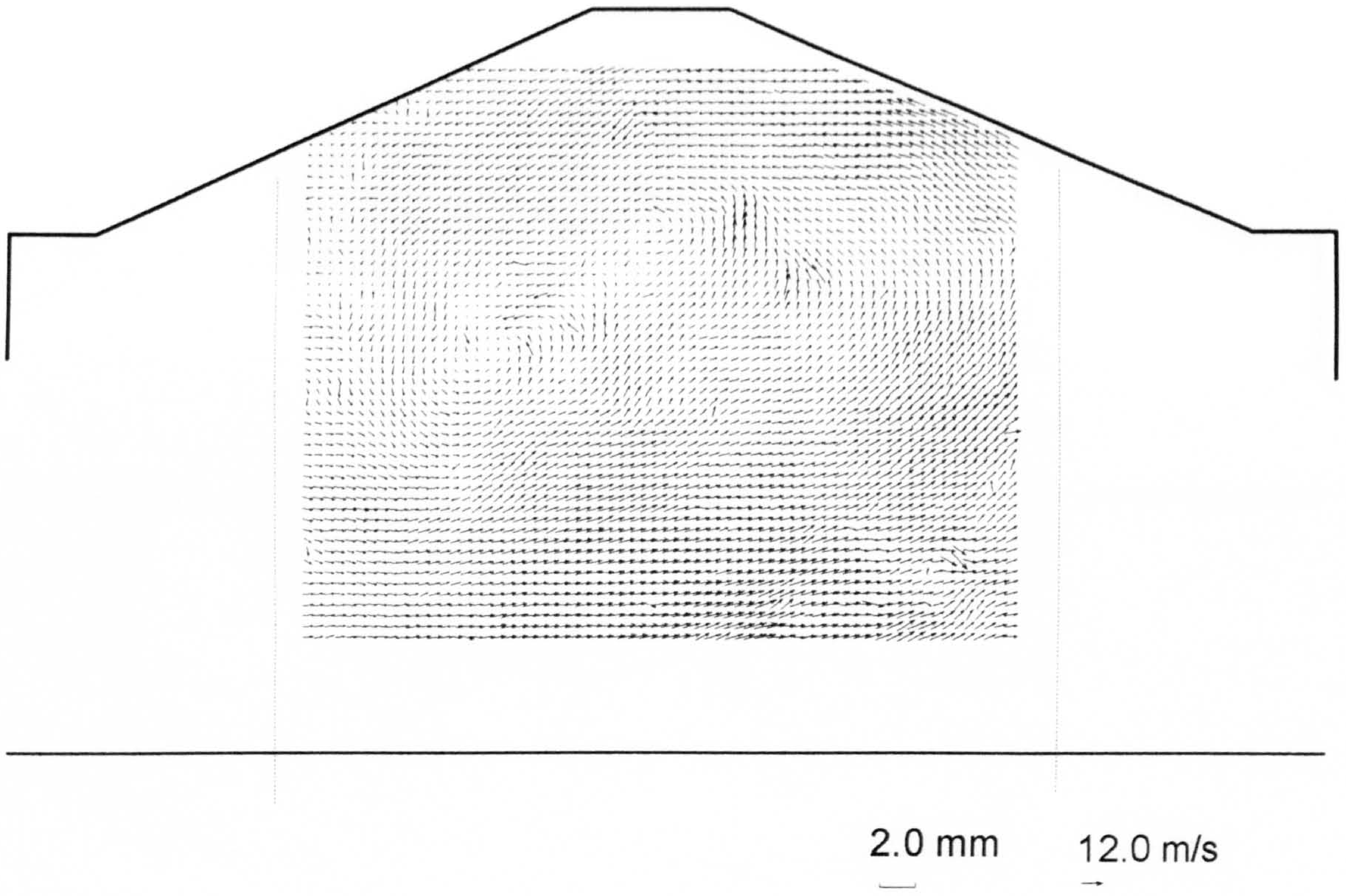

Figure 5.17 Plane A-A, 300 degrees after TDC, 1.8 BSR inlet.

T30#14.DRW

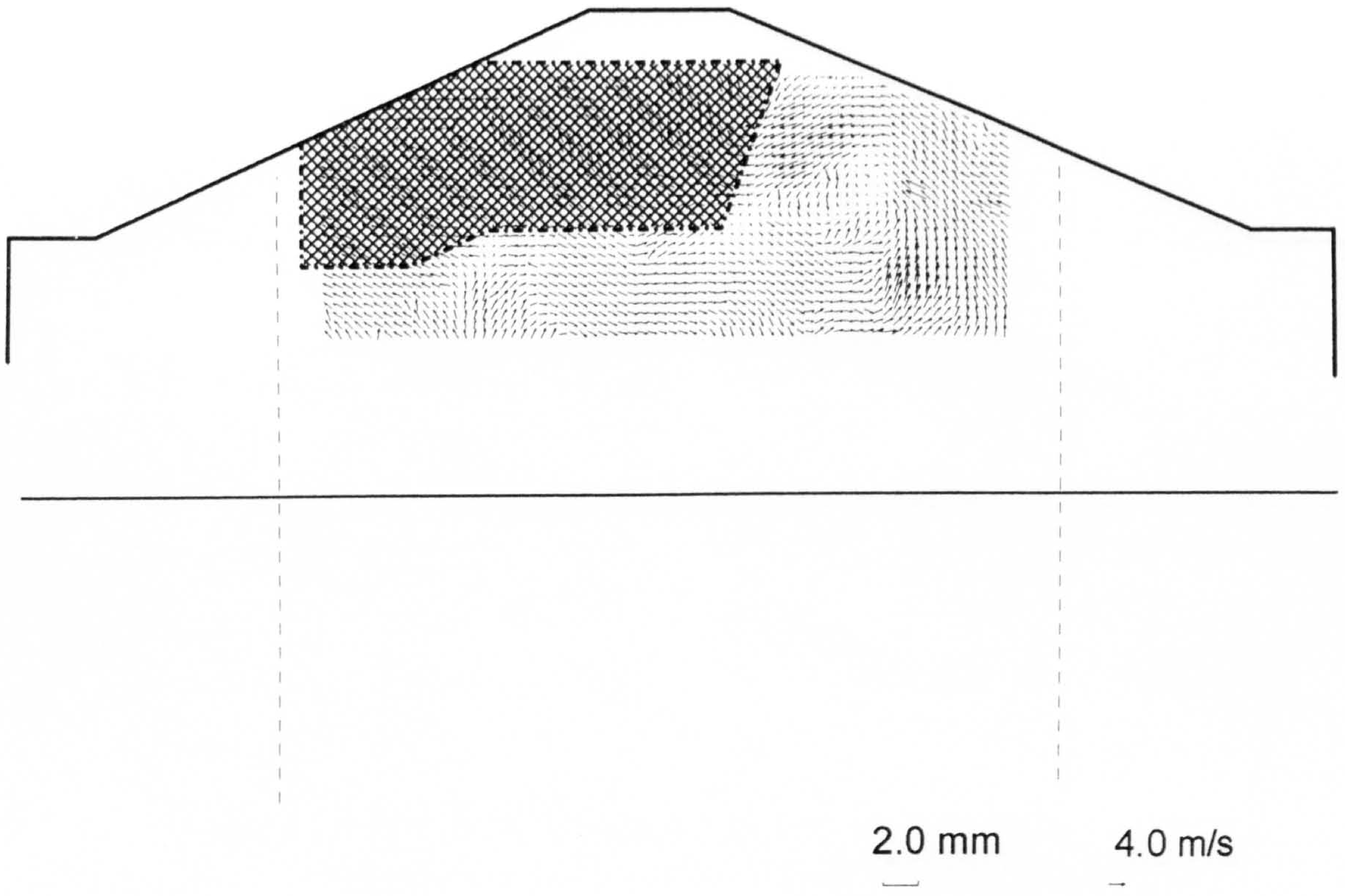

Figure 5.18 Plane A-A, 320 degrees after TDC, 1.2 BSR inlet. Note area of data loss beneath exhaust valve due to out-of-plane motion

T49#1.DRW

Figure 5.19 Plane A-A, 320 degrees after TDC, 1.8 BSR inlet.

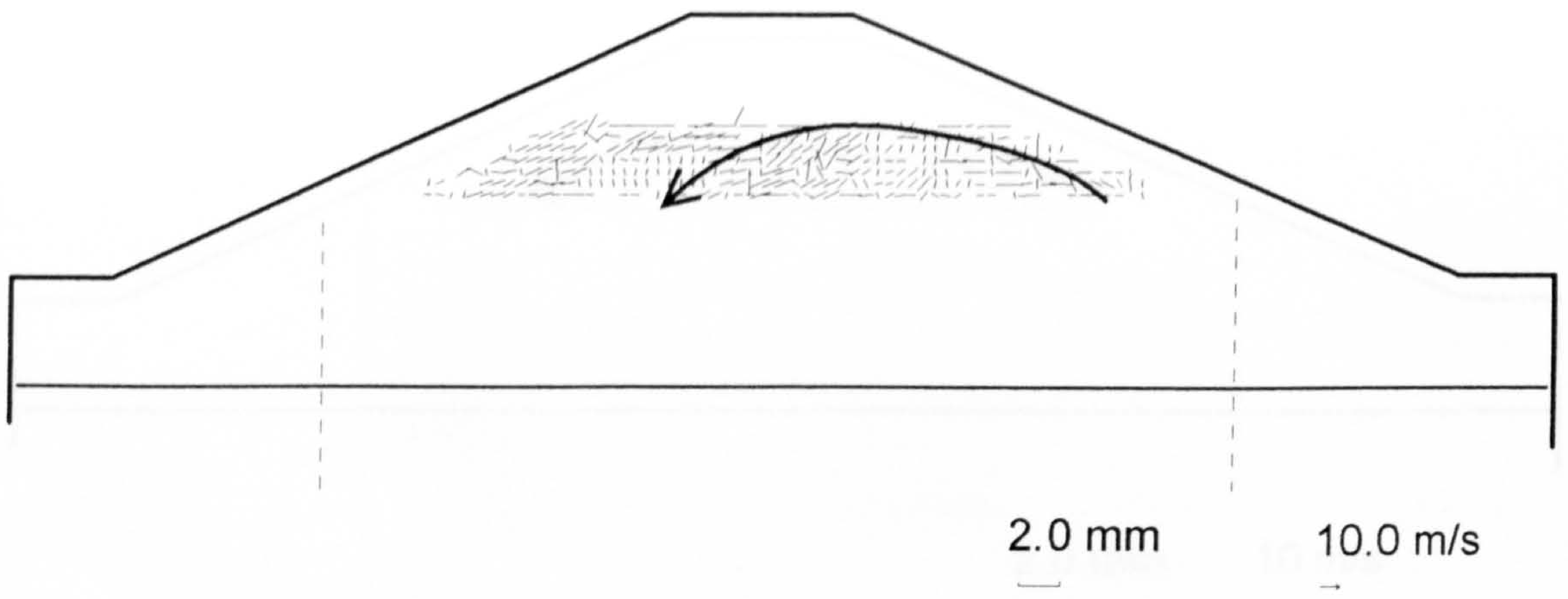

Figure 5.20 Plane A-A, 338 degrees after TDC, 1.2 BSR inlet.
Poor data quality due to flare and velocity gradients.

T24#3.DRW

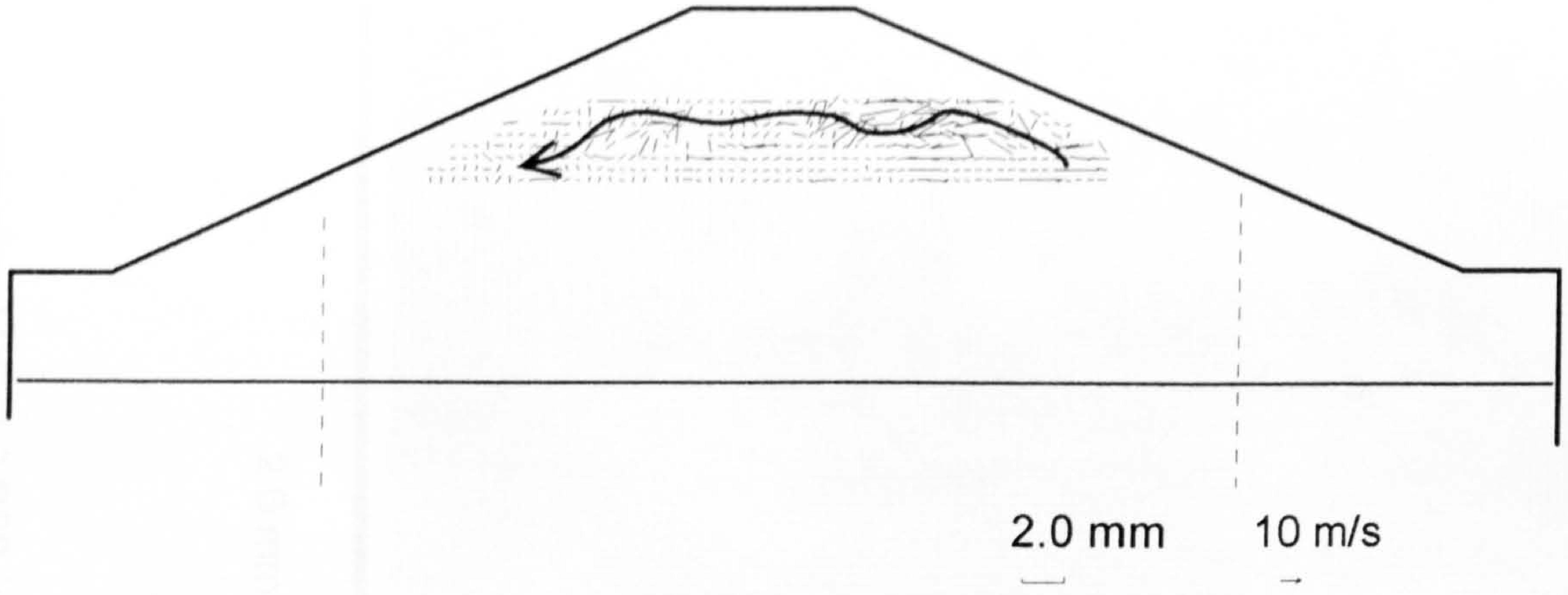

Figure 5.21 Plane A-A, 338 degrees after TDC, 1.8 BSR inlet.
Poor data quality due to flare and velocity gradients.

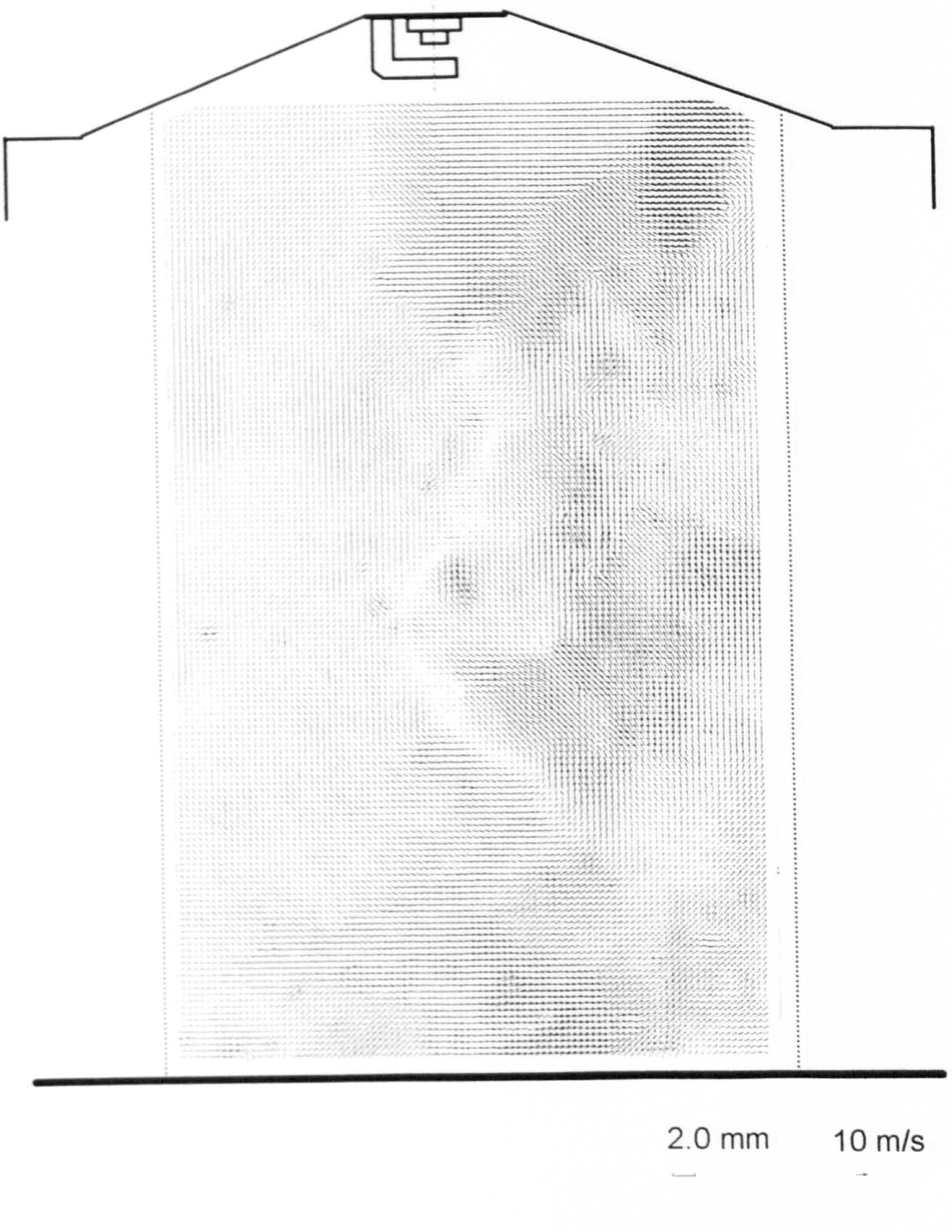

Figure 5.22 Plane B-B, 222 degrees after TDC, 1.2 BSR inlet.
Note shear layer close to cylinder axis.

EN22#10.ASC

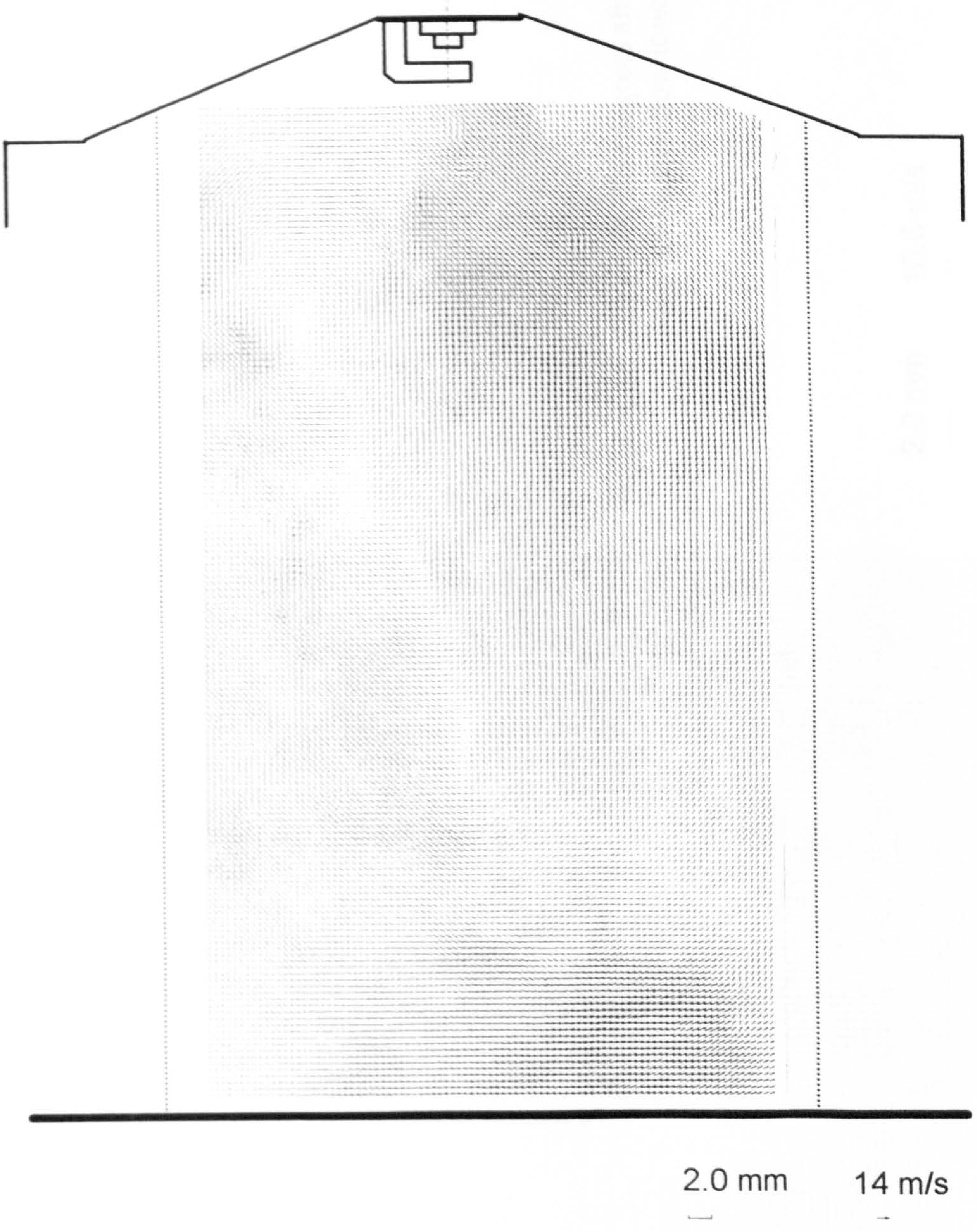

Figure 5.23 Plane B-B, 222 degrees after TDC, 1.8 BSR inlet.

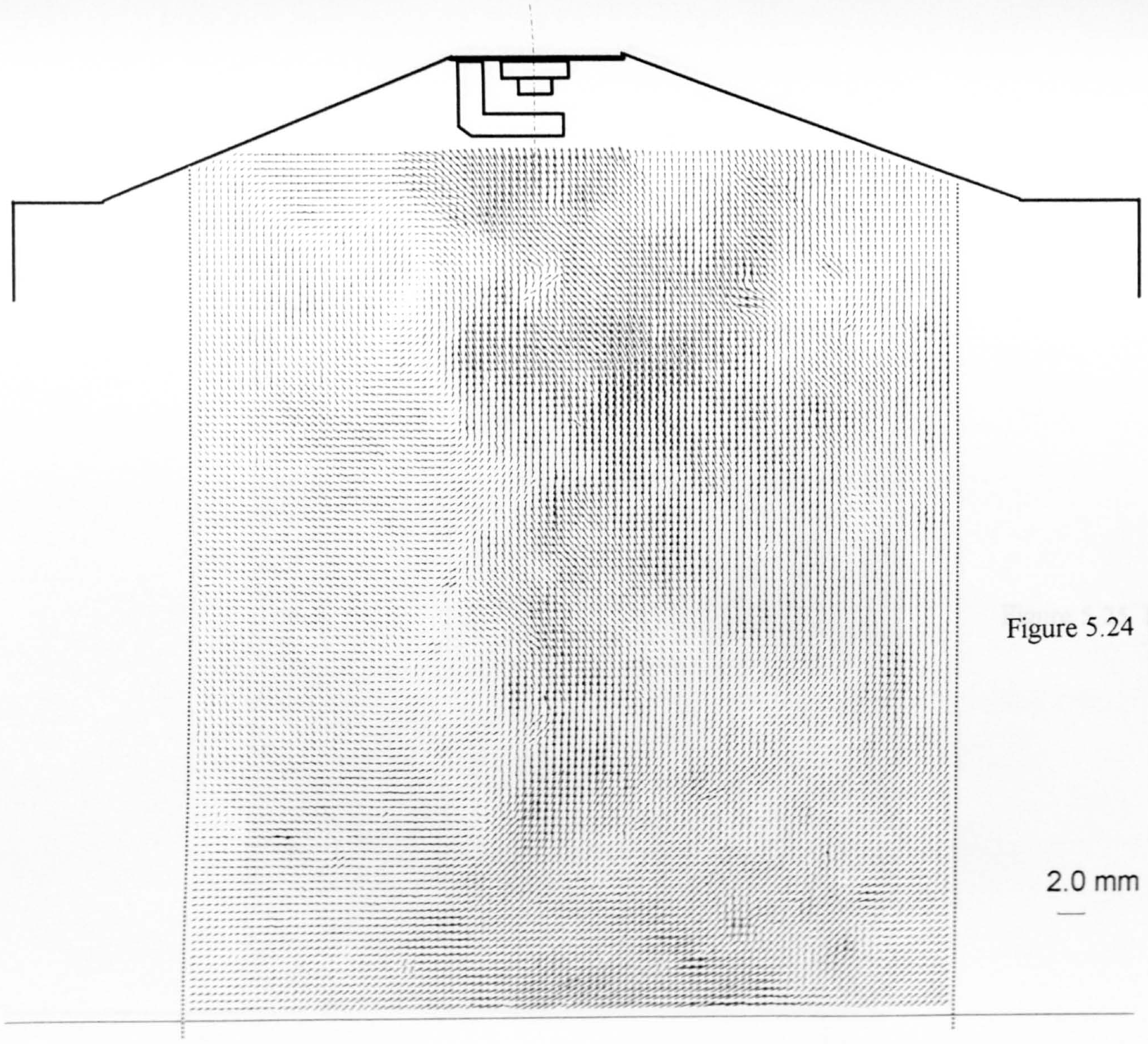

Figure 5.24 Plane B-B, 260 degrees after TDC, 1.2 BSR inlet. Note convective flow toward cylinder head.

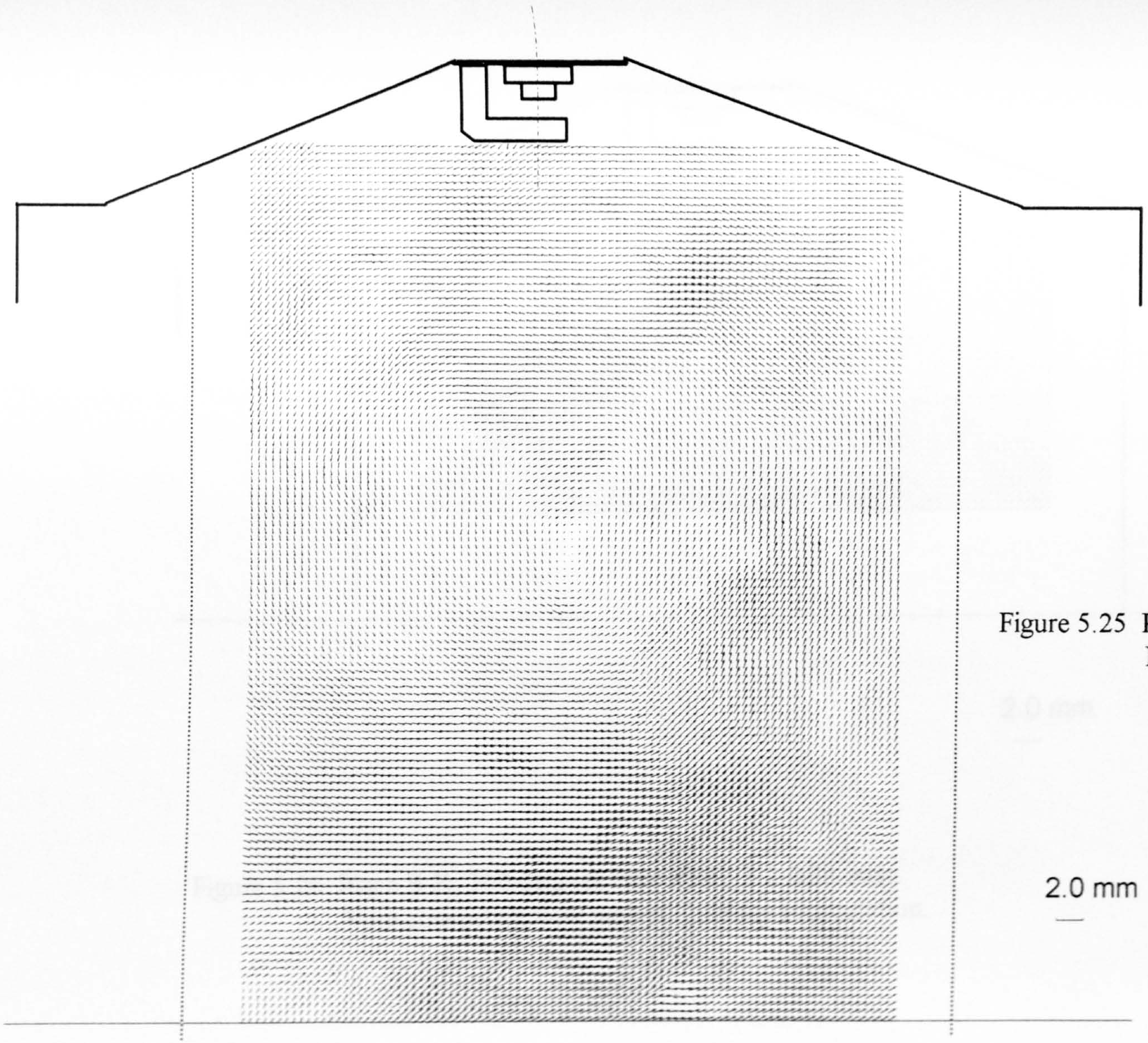

Figure 5.25 Plane B-B, 260 degrees after TDC, 1.8 BSR inlet. Note centrally located barrel vortex.

t50#12.drw

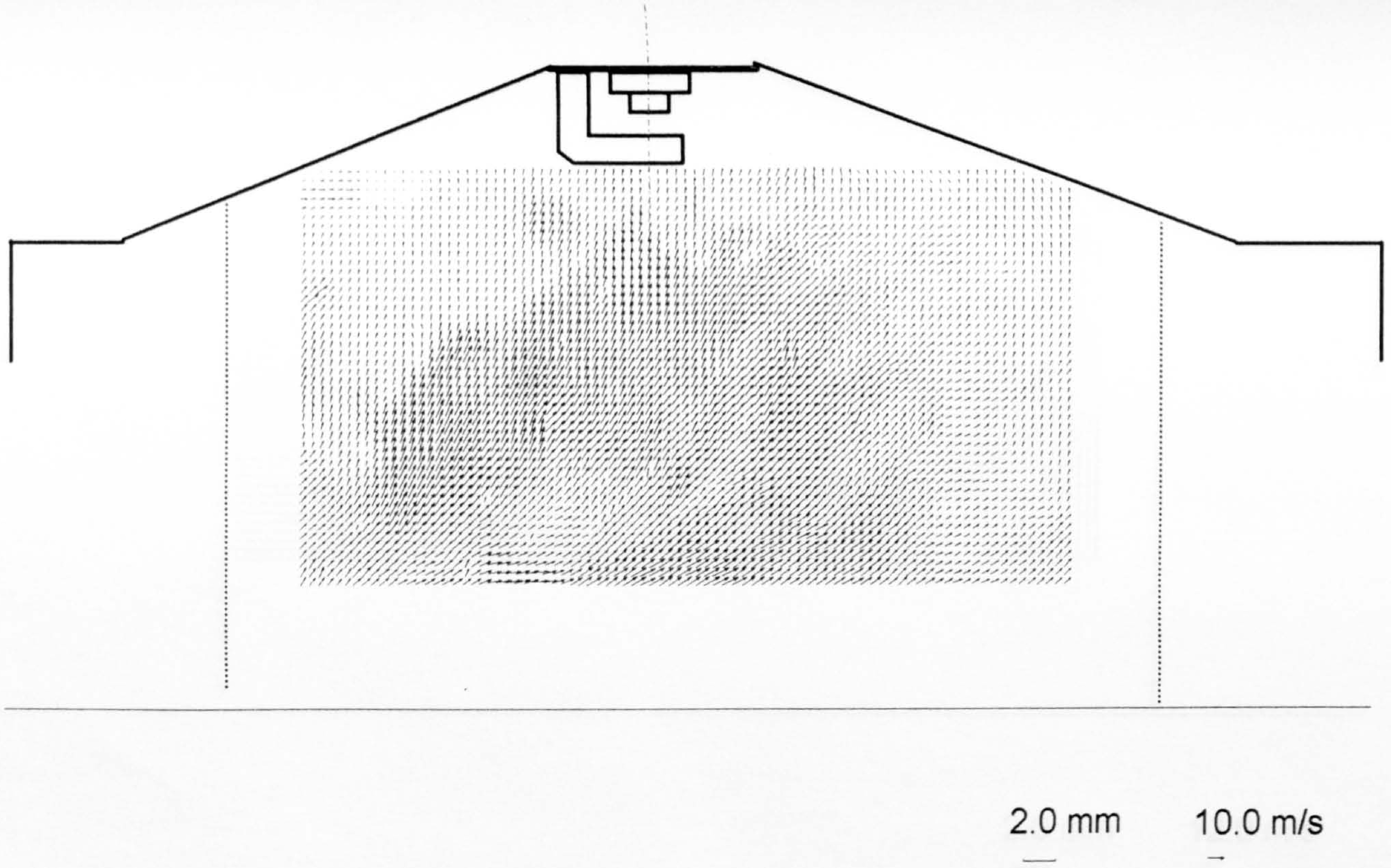

Figure 5.26 Plane B-B, 300 degrees after TDC, 1.2 BSR inlet.
Note convective flow with no in-plane recirculation.

t22#6.drw

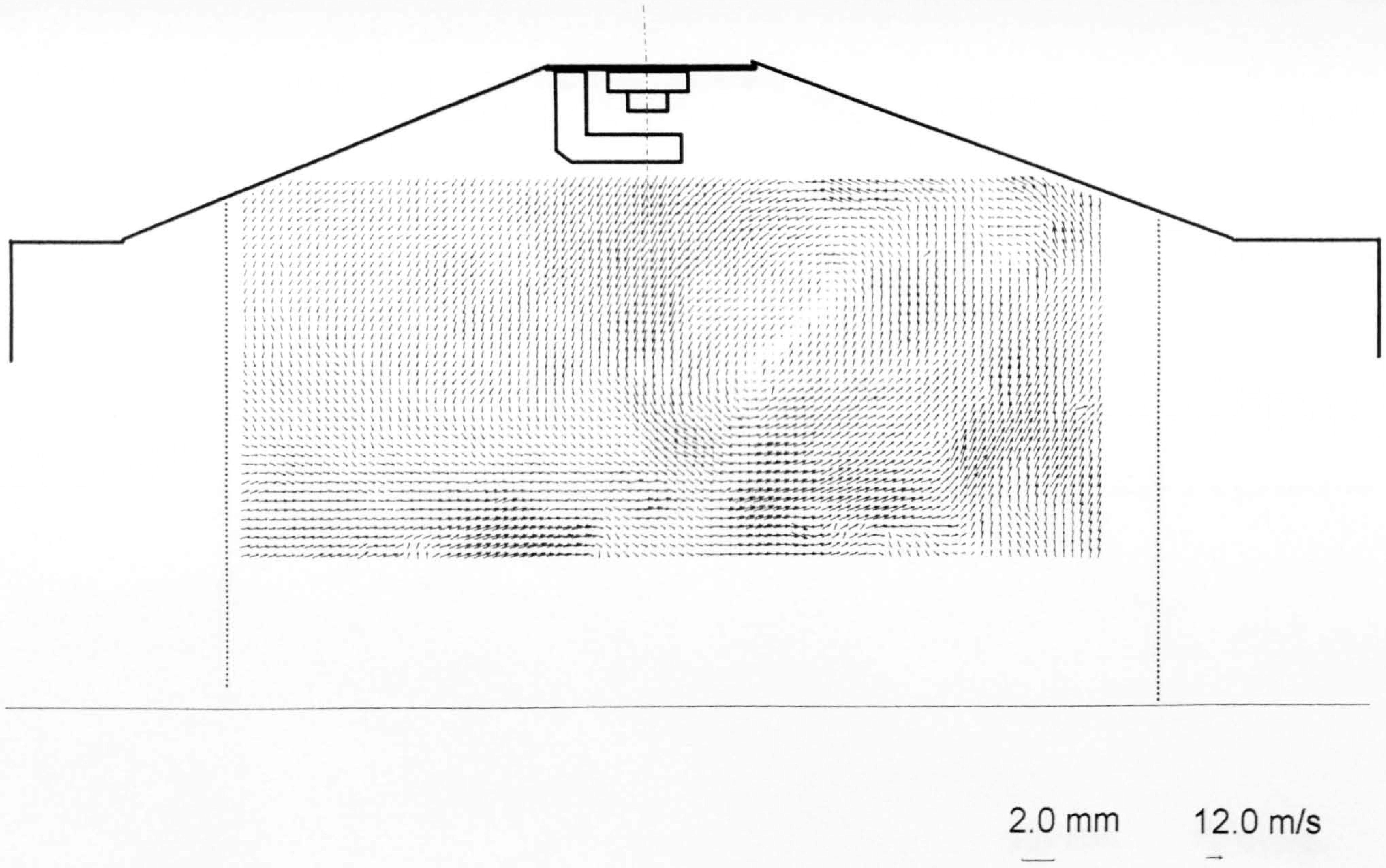

Figure 5.27 Plane B-B, 300 degrees after TDC, 1.8 BSR inlet.
Strong barrel vortex to right of centreline.

t50#7.drw

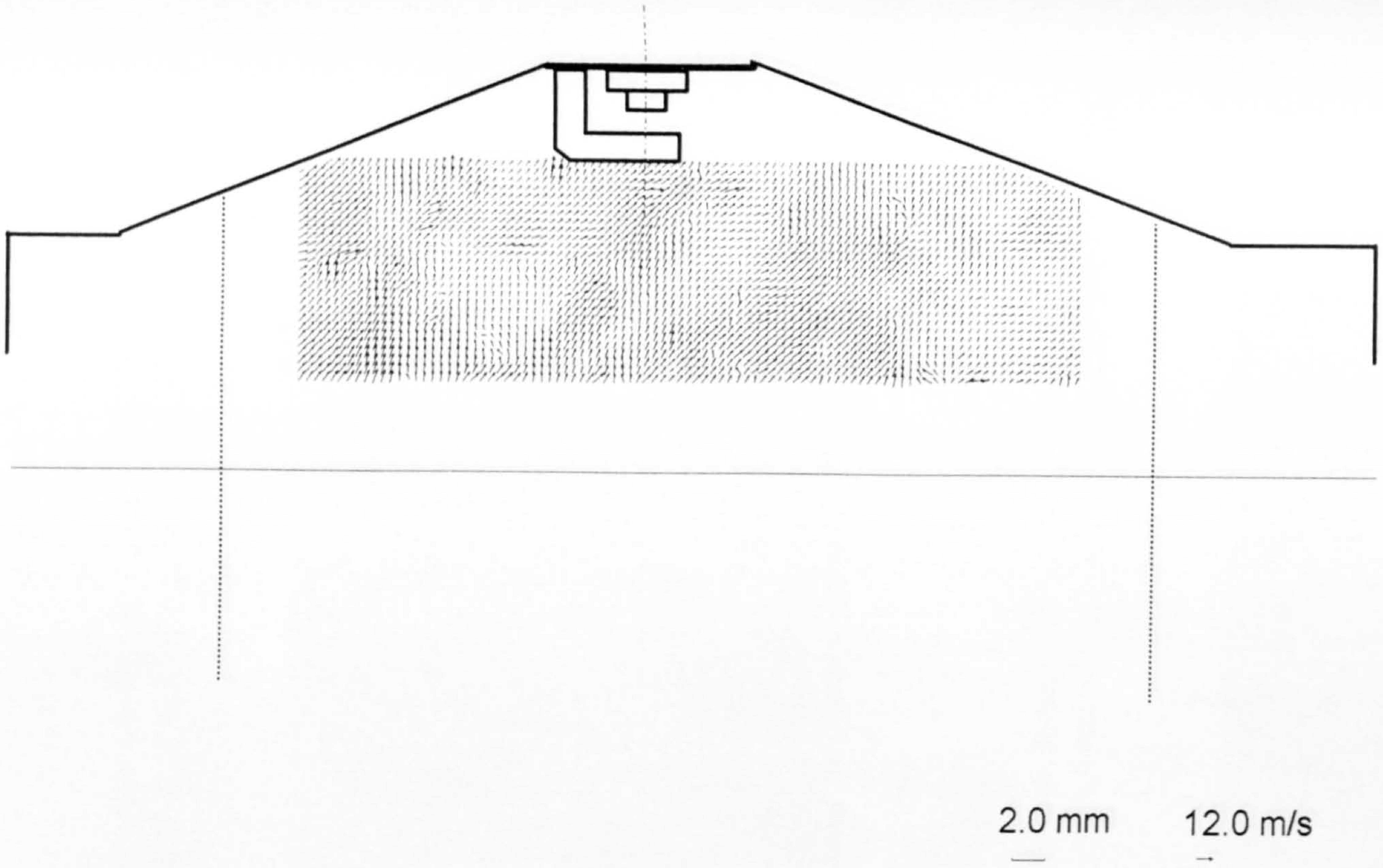

Figure 5.28 Plane B-B, 320 degrees after TDC, 1.2 BSR inlet.
Note lack of in-plane recirculation.

t51#7.drw

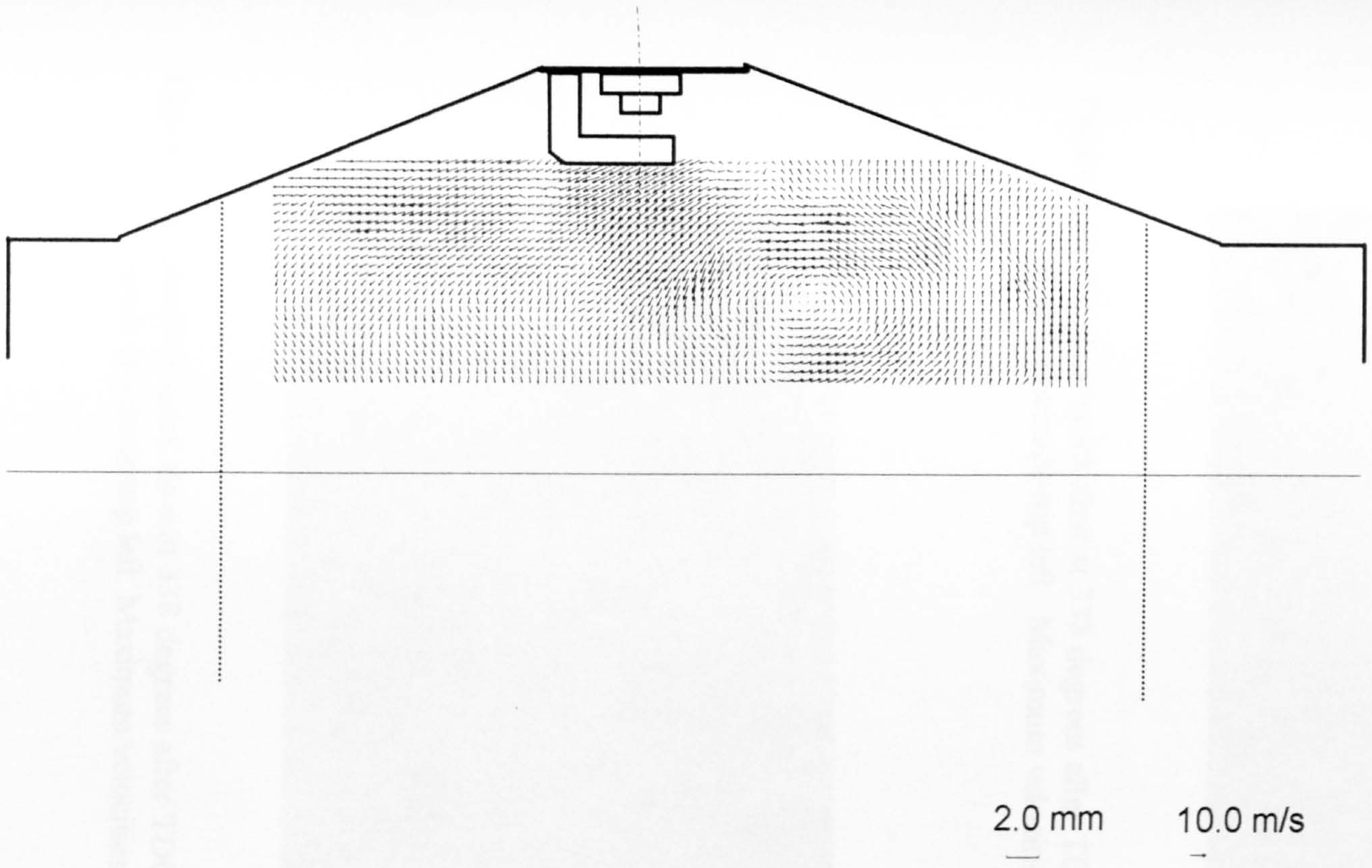

Figure 5.29 Plane B-B, 320 degrees after TDC, 1.8 BSR inlet. Note strong barrel vortex beneath inlet valve and high velocity cross-flow at the spark electrode. .

t50#6.drw

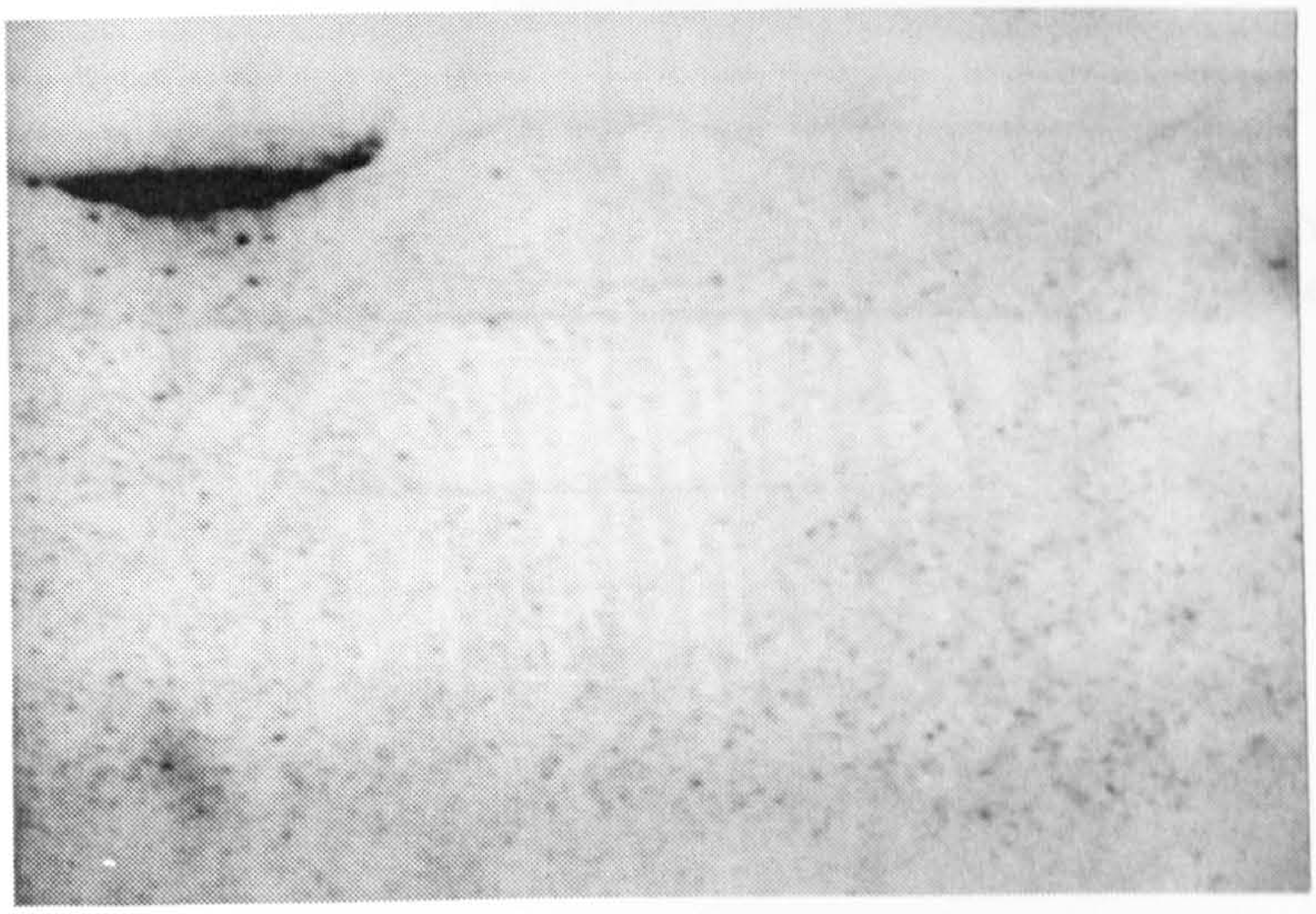

Figure 5.30 Detail of spark flow at 338 degrees after TDC. 1.2 BSR.. Spark electrode top left. Maximum velocities are 8-10m/s.

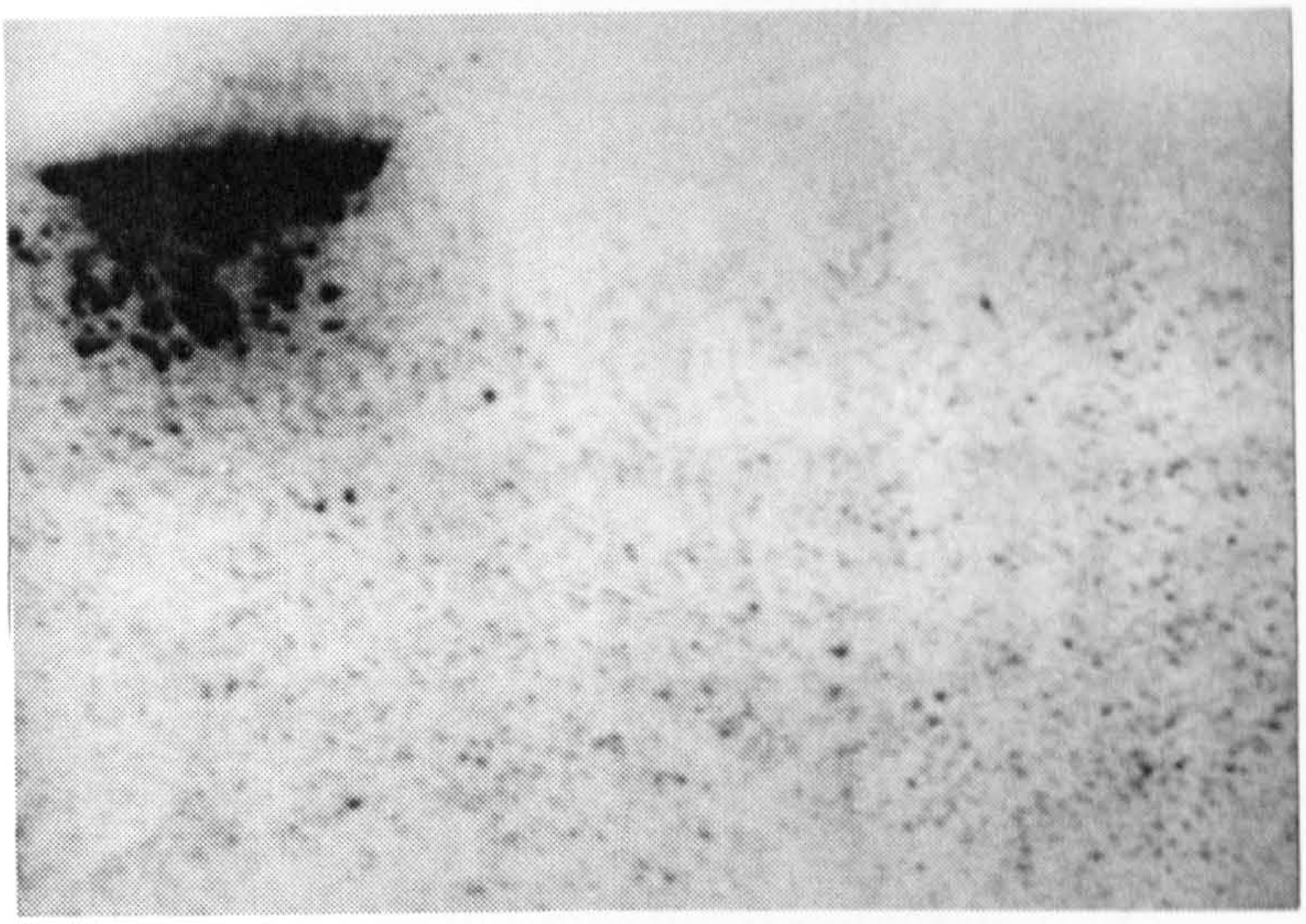

Figure 5.31 Detail of spark flow at 338 degrees after TDC. 1.8 BSR. Spark electrode top left. Maximum velocities are 12-14 m/s.

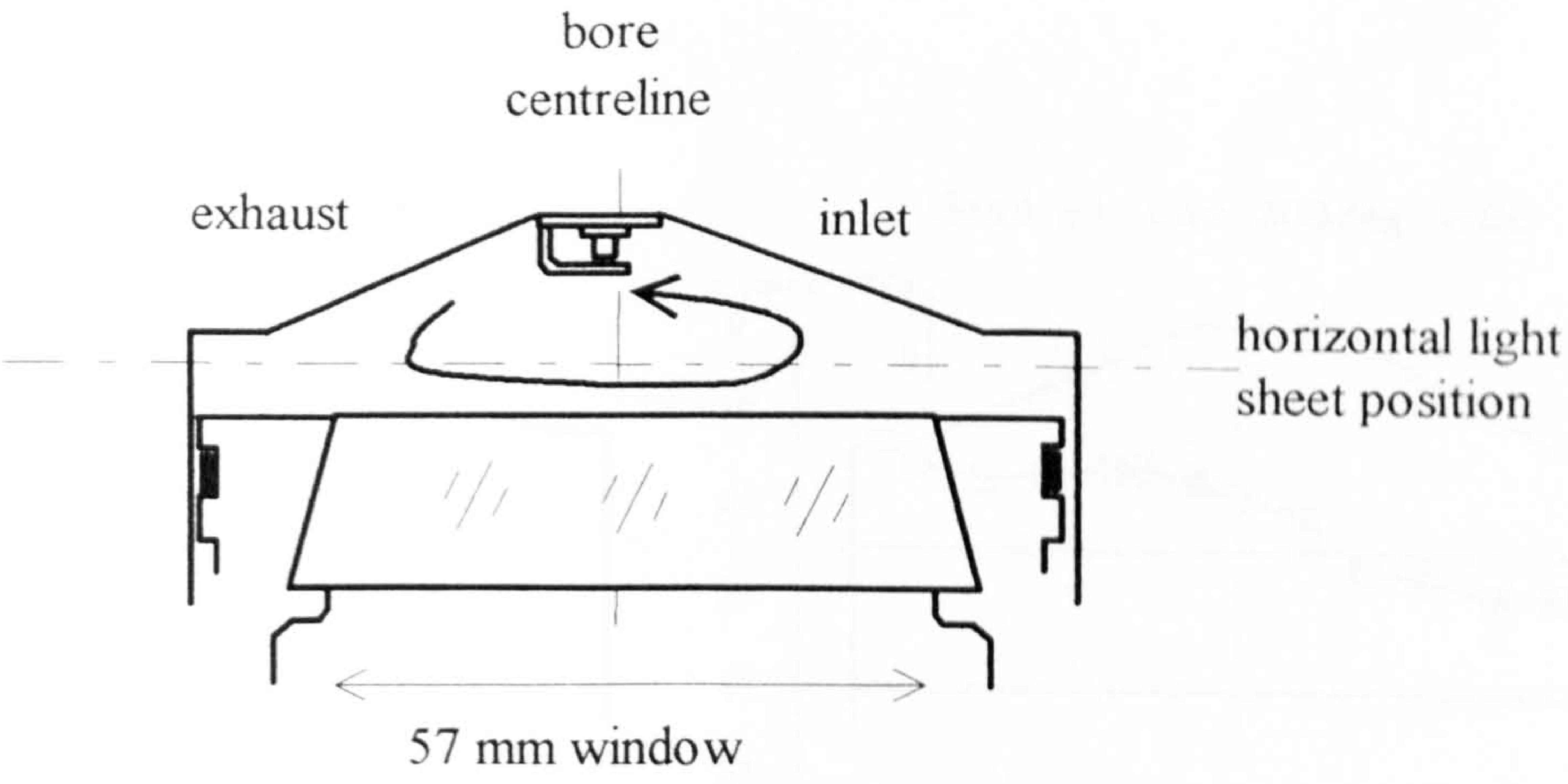

Figure 5.32a Orientation of plane H-H vector maps.

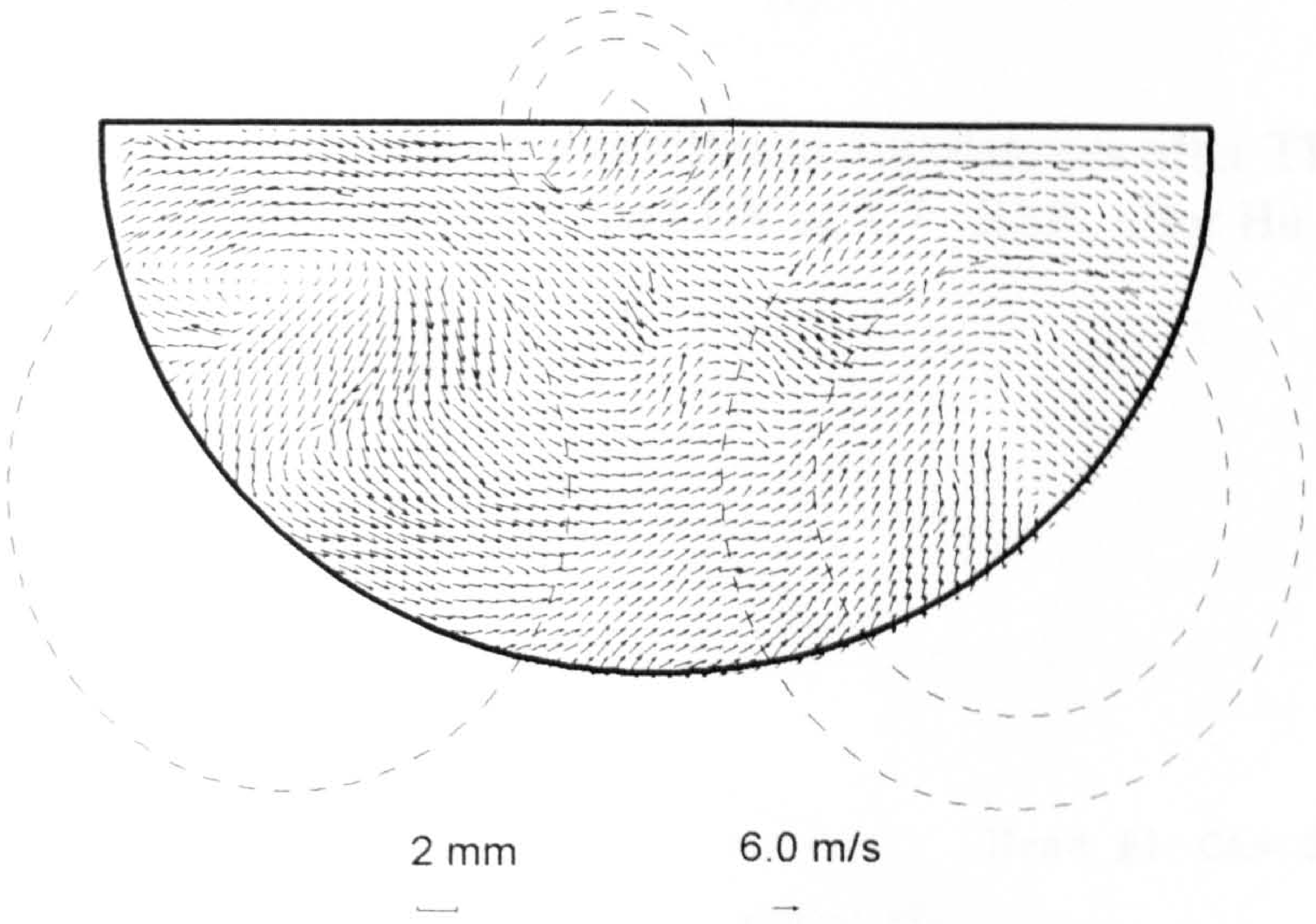

Figure 5.32b Plane H-H, 338 degrees after TDC, 1.2 BSR.

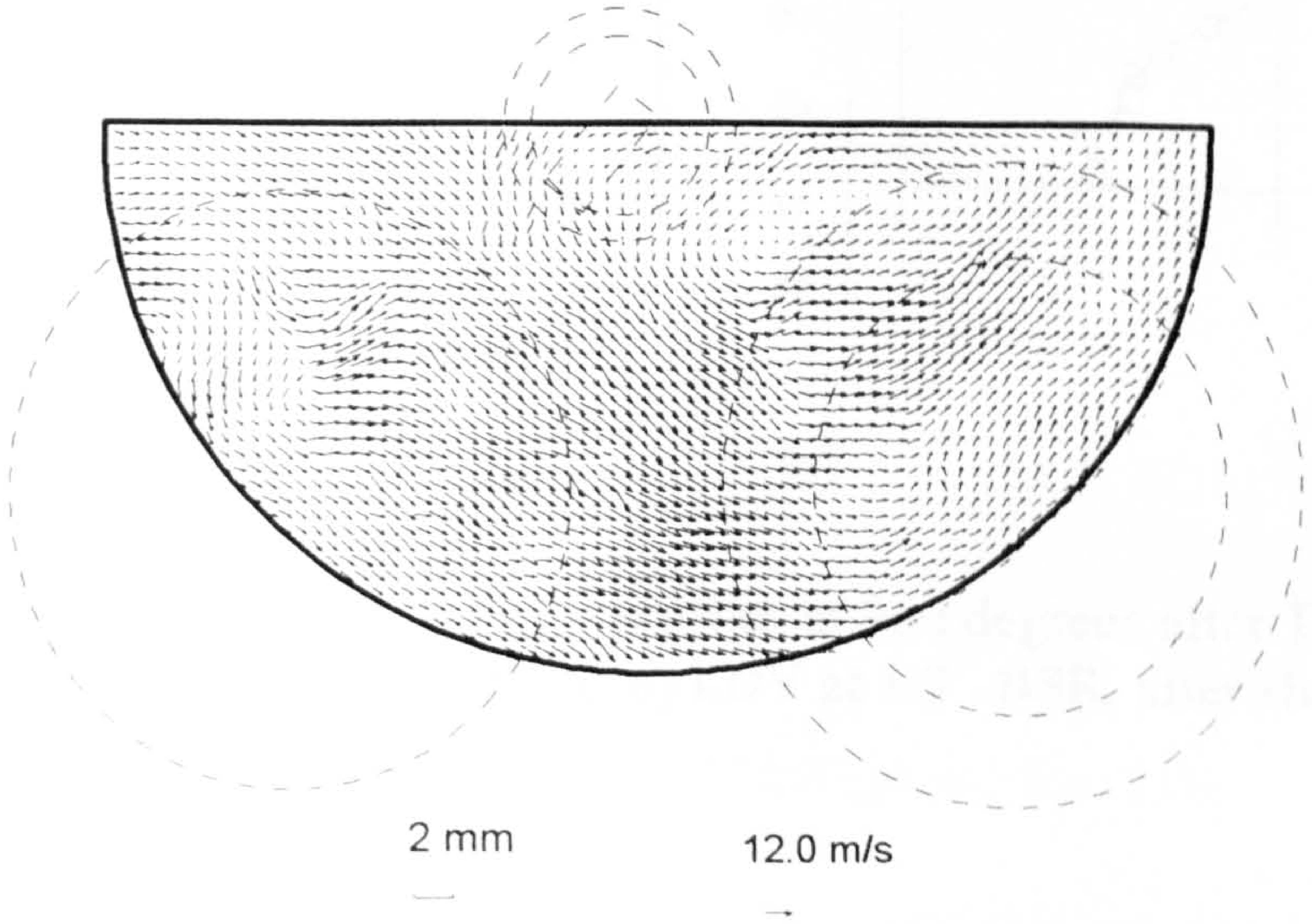

Figure 5.32c Plane H-H, 338 degrees after TDC, 1.8 BSR.

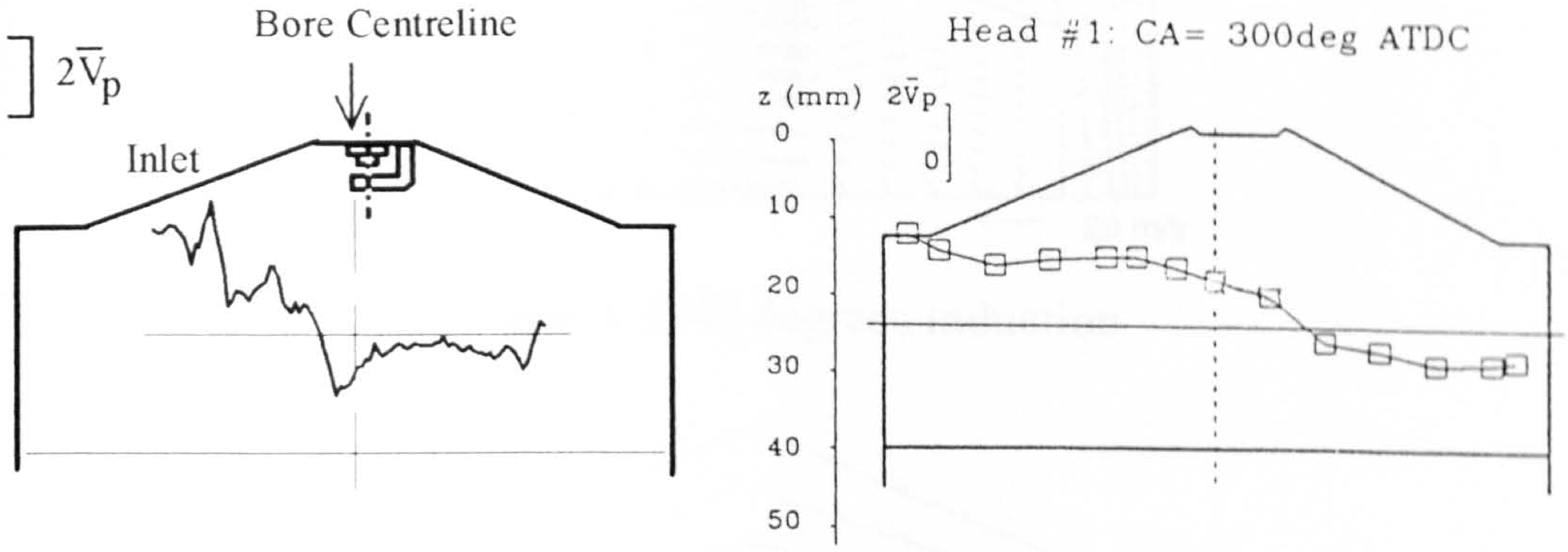

a)

b)

Figure 5.33 Comparison of *w* profiles at 300 degrees after TDC.
a) PIV at 1.8BSR b) LDV at 1.7 BSR, after Hu [5.2].

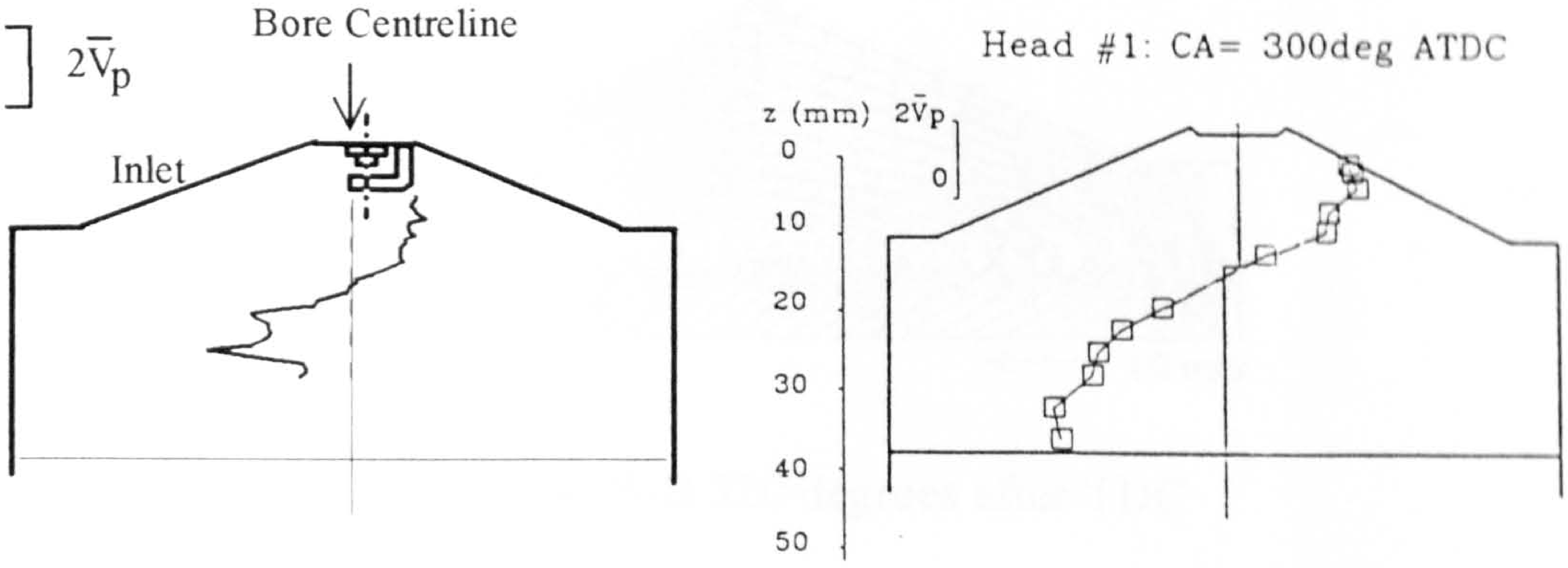

a)

b)

Figure 5.34 Comparison of *u* profiles at 300 degrees after TDC.
a) PIV at 1.8BSR b) LDV at 1.7 BSR, after Hu [5.2].

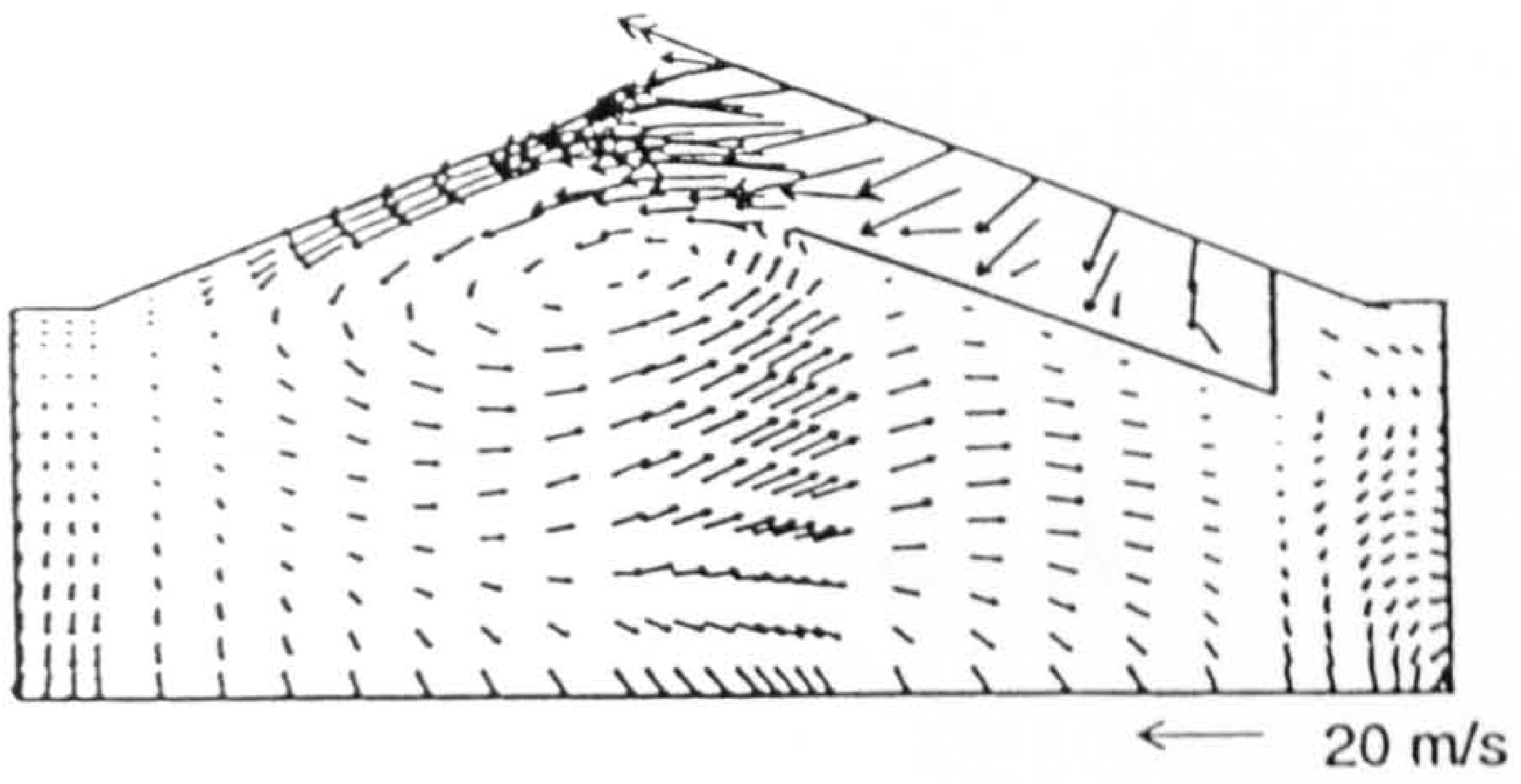

a) Plane A-A 45 degrees induction

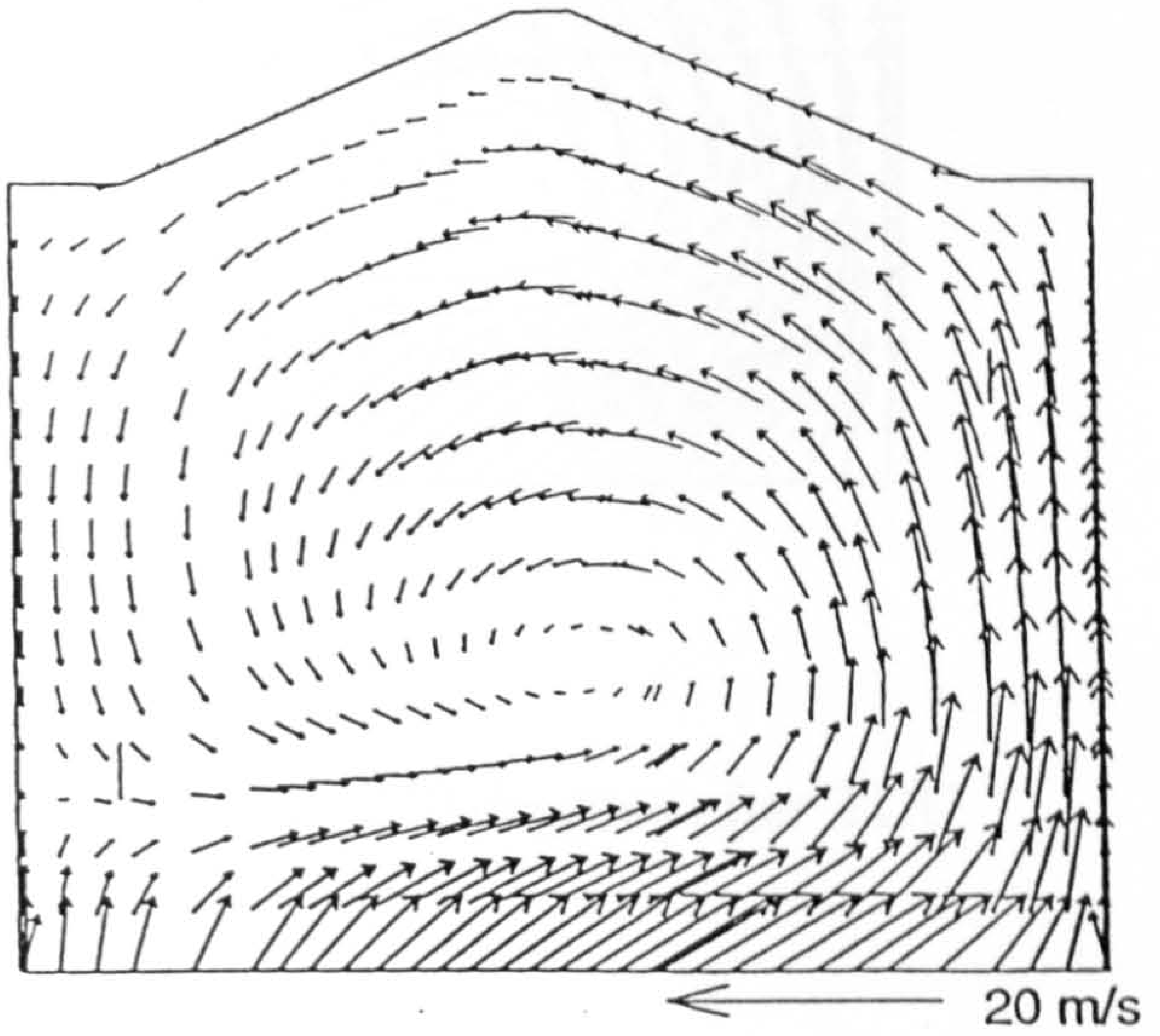

b) Plane B-B 260 degrees after TDC

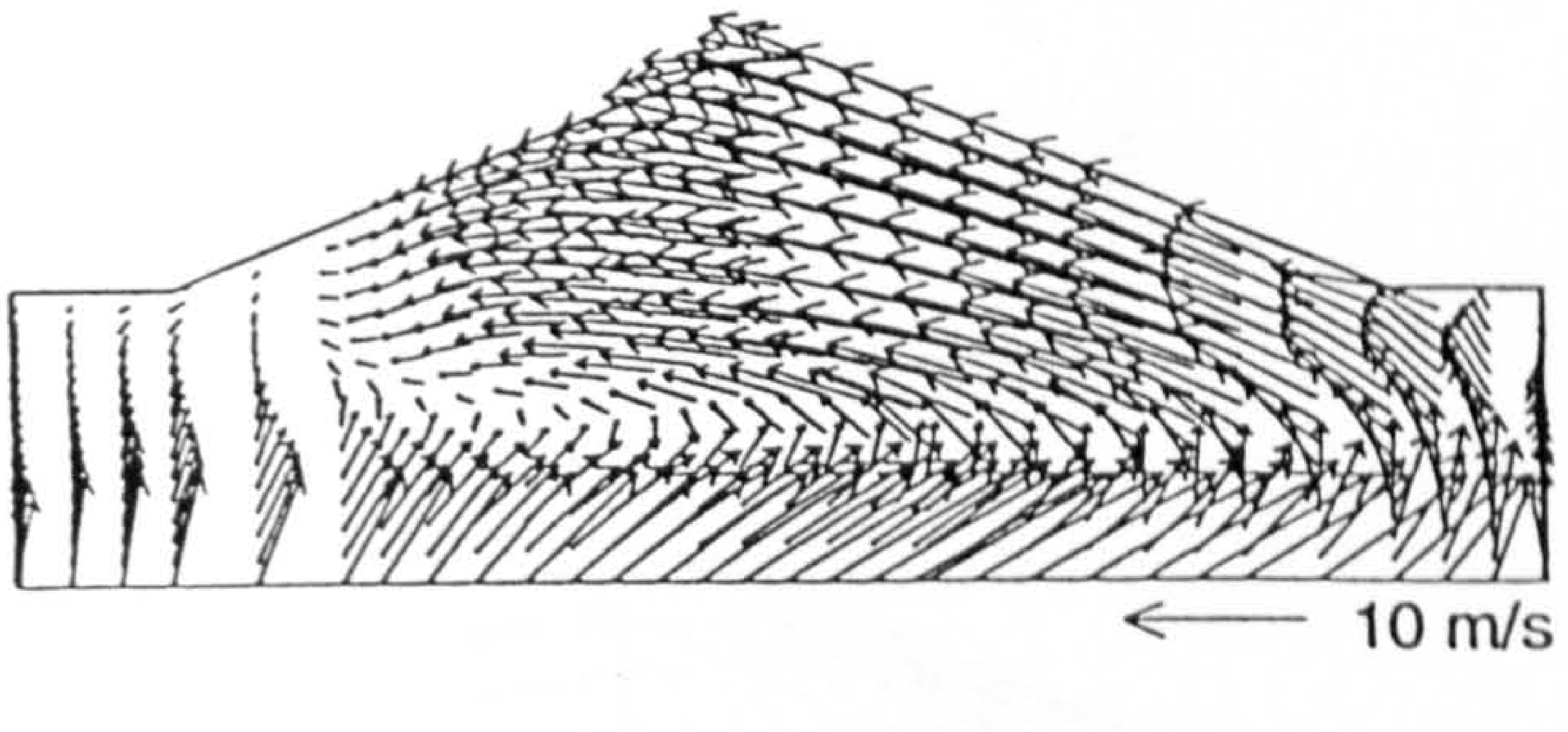

c) Plane B-B 320 degrees after TDC

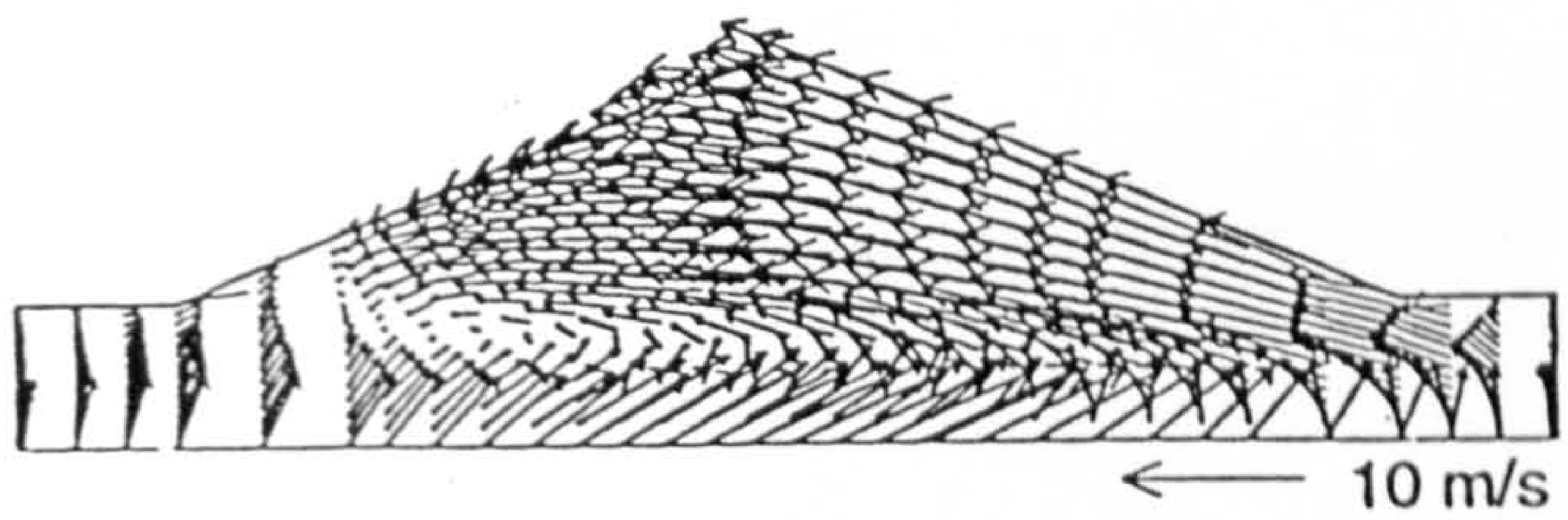

d) Plane B-B 338 degrees after TDC

Figure 5.35 Examples of flow simulation by Das and Dent [5.12]
Nominal BSR = 0.7.

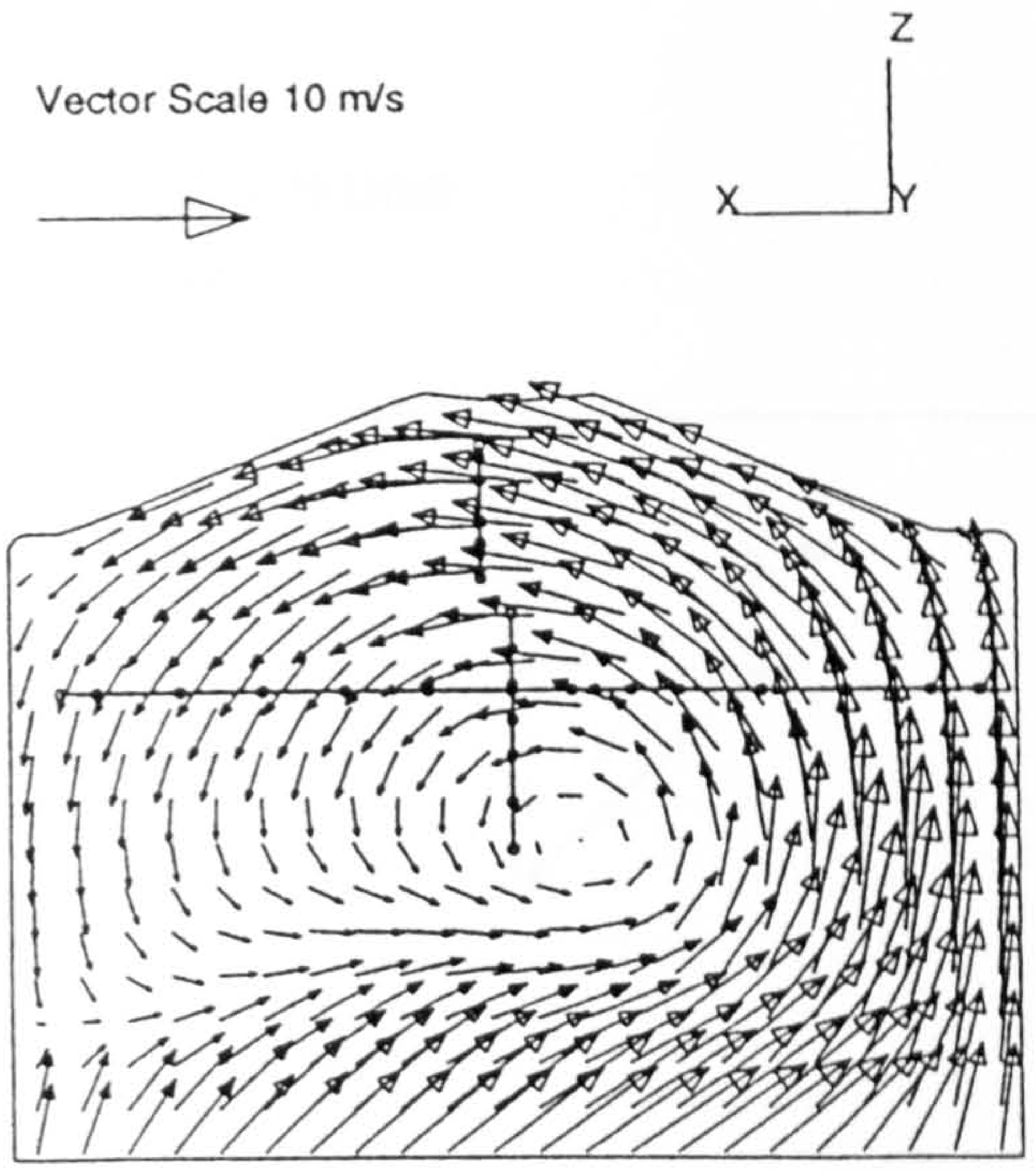

a) Plane B-B, 270 degrees after TDC

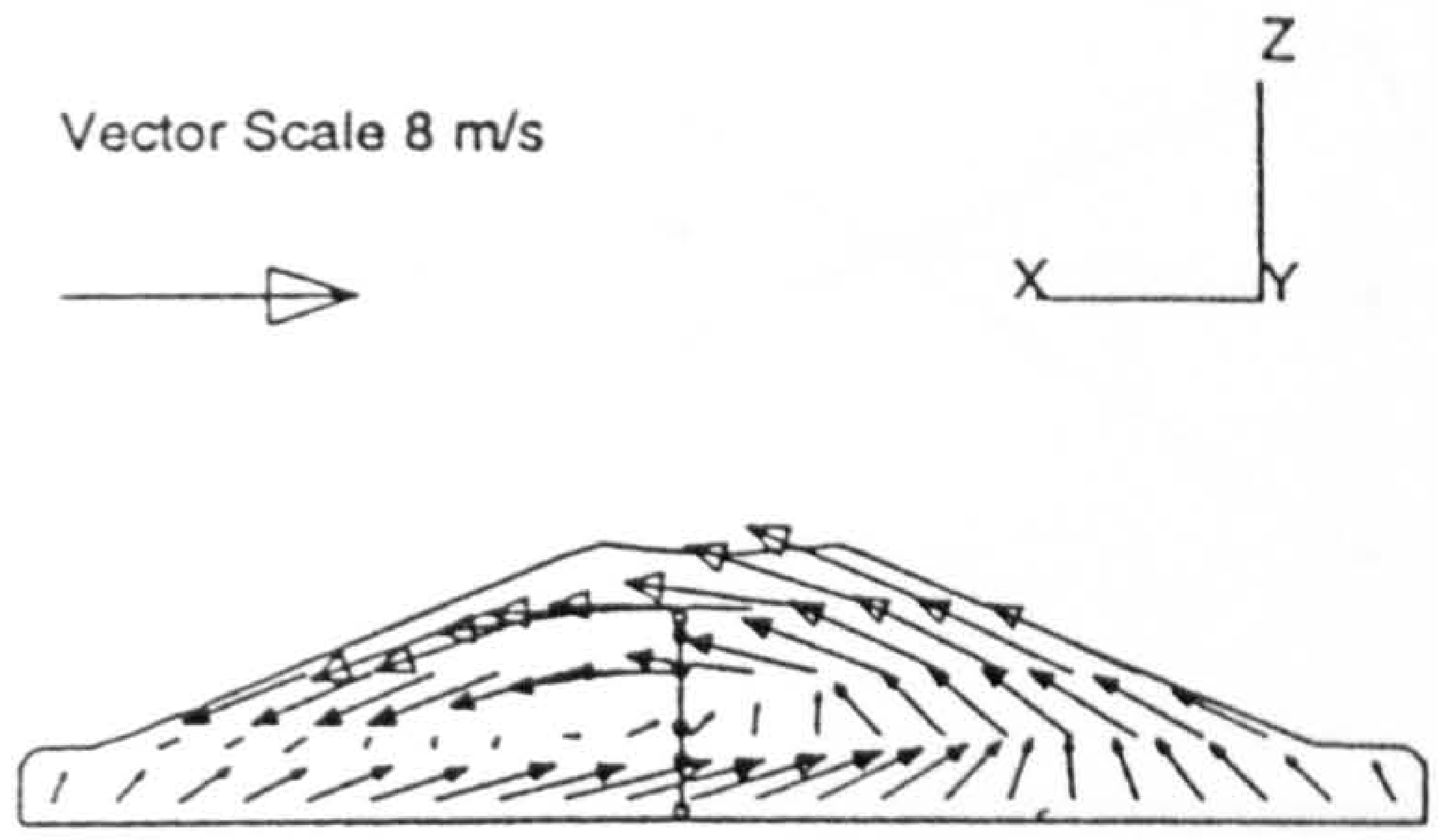

b) Plane B-B, 345 degrees after TDC

Figure 5.36 Examples of flow simulation by Jones and Junday [5.13]. Nominal BSR = 1.7.

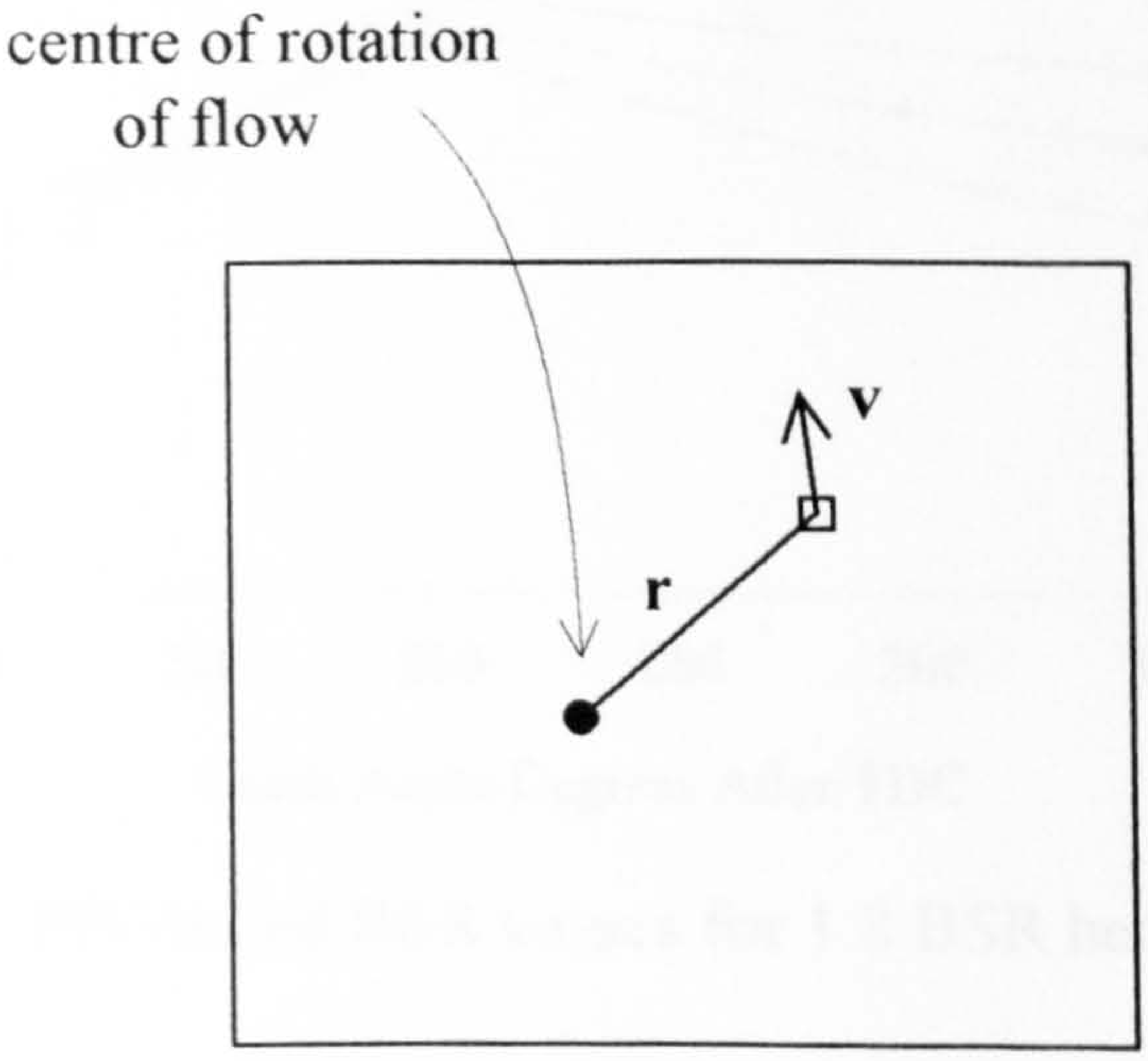

Figure 5.37 Geometry for calculation of dynamic
Barrel Swirl Ratio

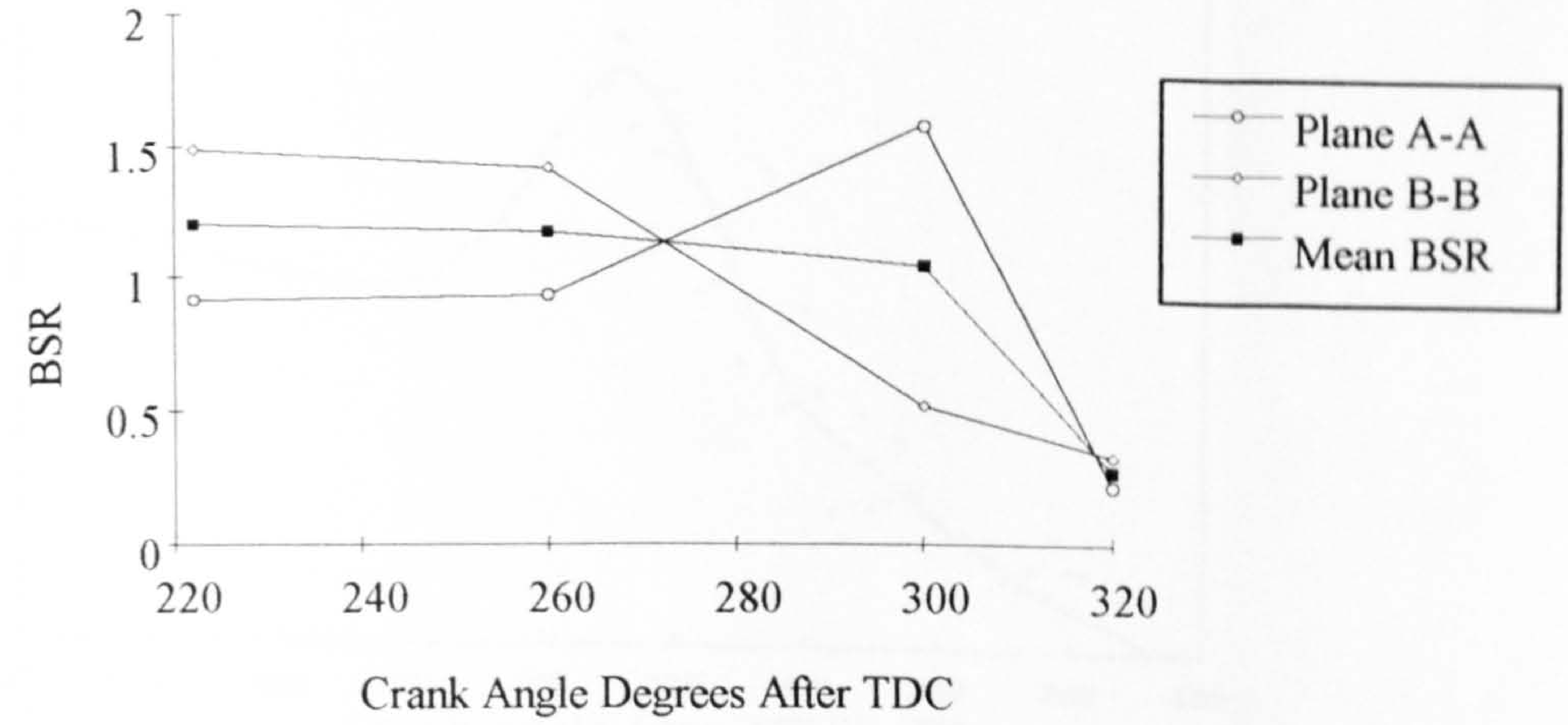

Figure 5.38 PIV-based BSR values for 1.2 BSR head.

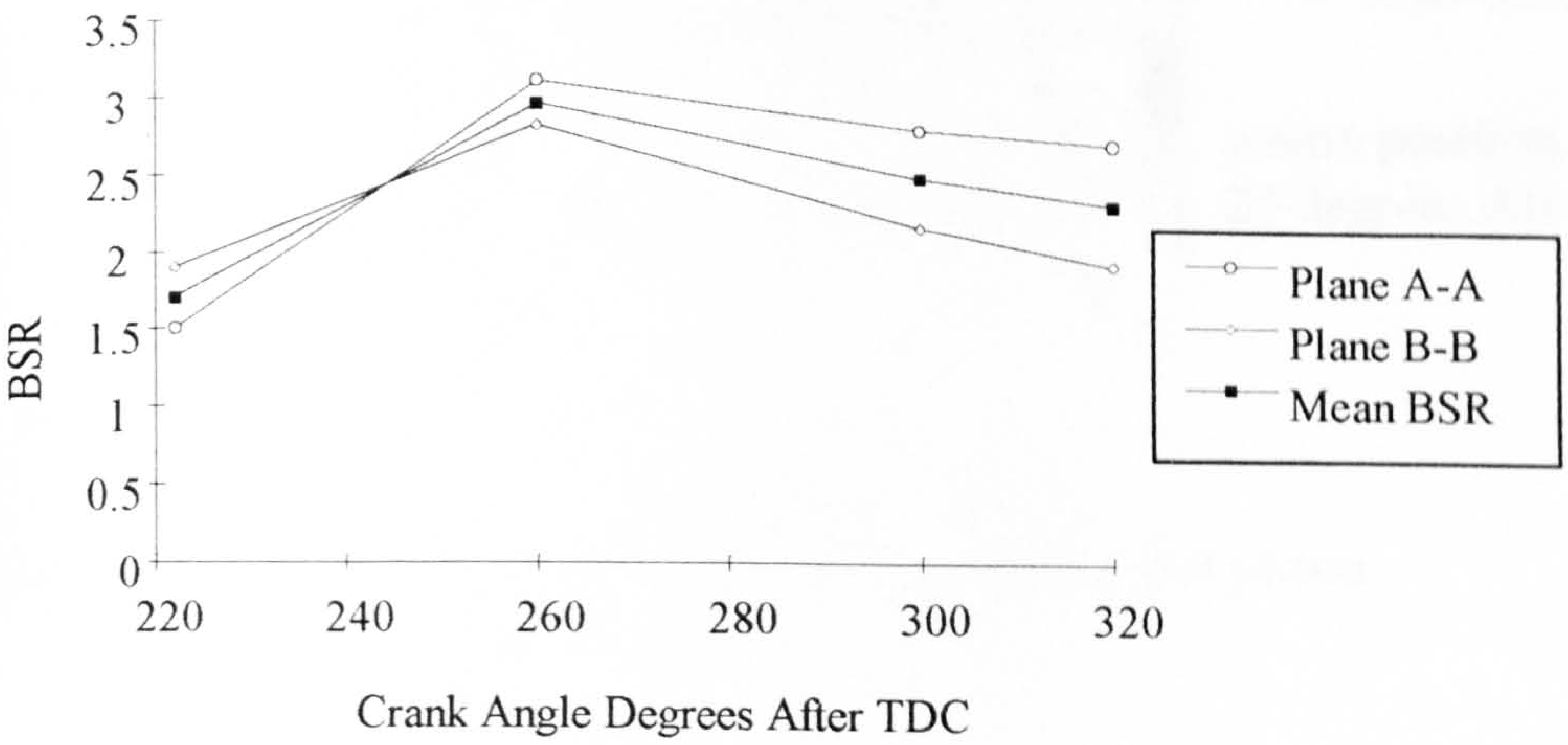

Figure 5.39 PIV-based BSR values for 1.8 BSR head.

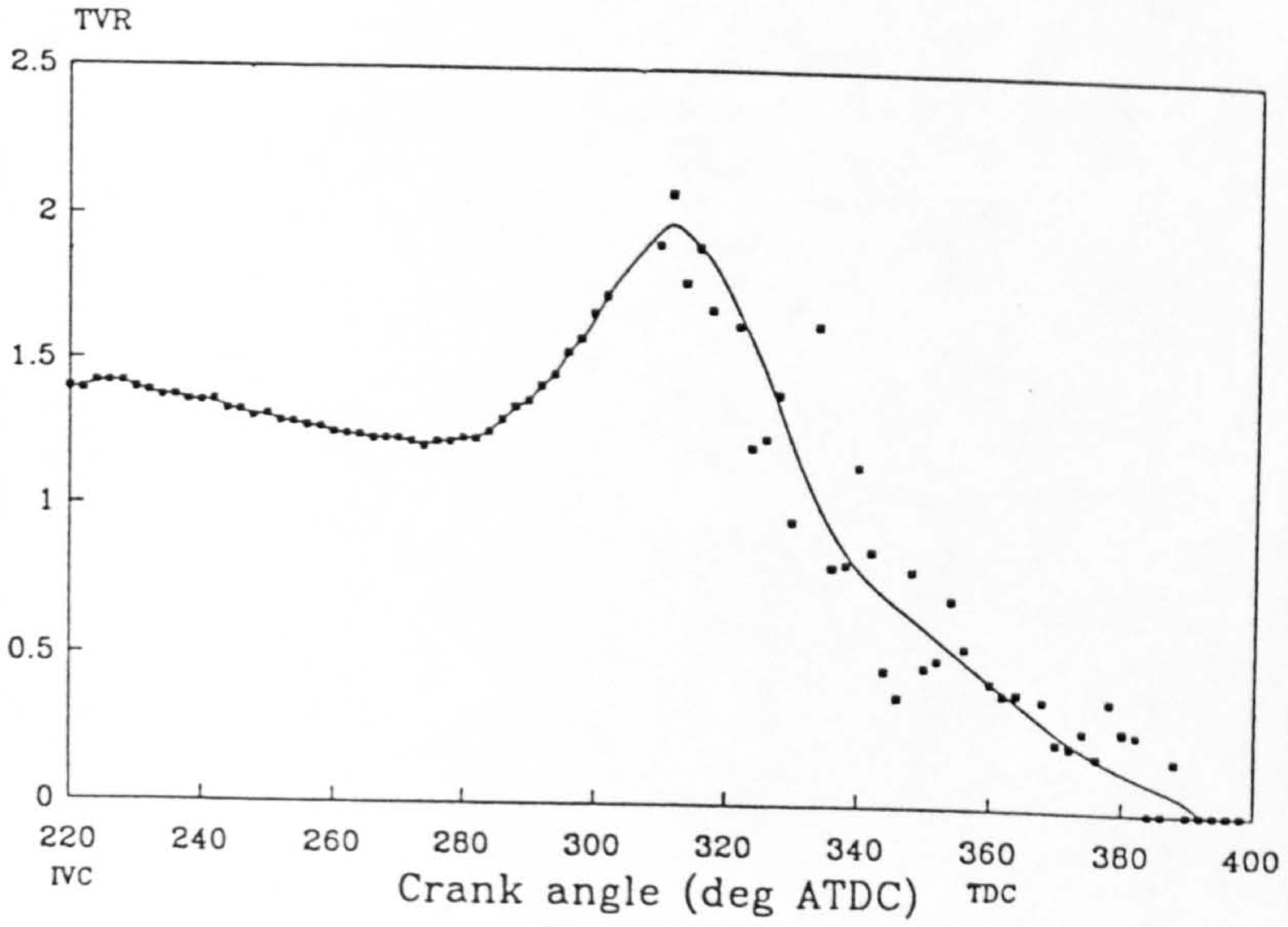

Figure 5.40 LDV-based TVR against crank angle during compression for a steady flow BSR of 1.7. After Hu [5.2].

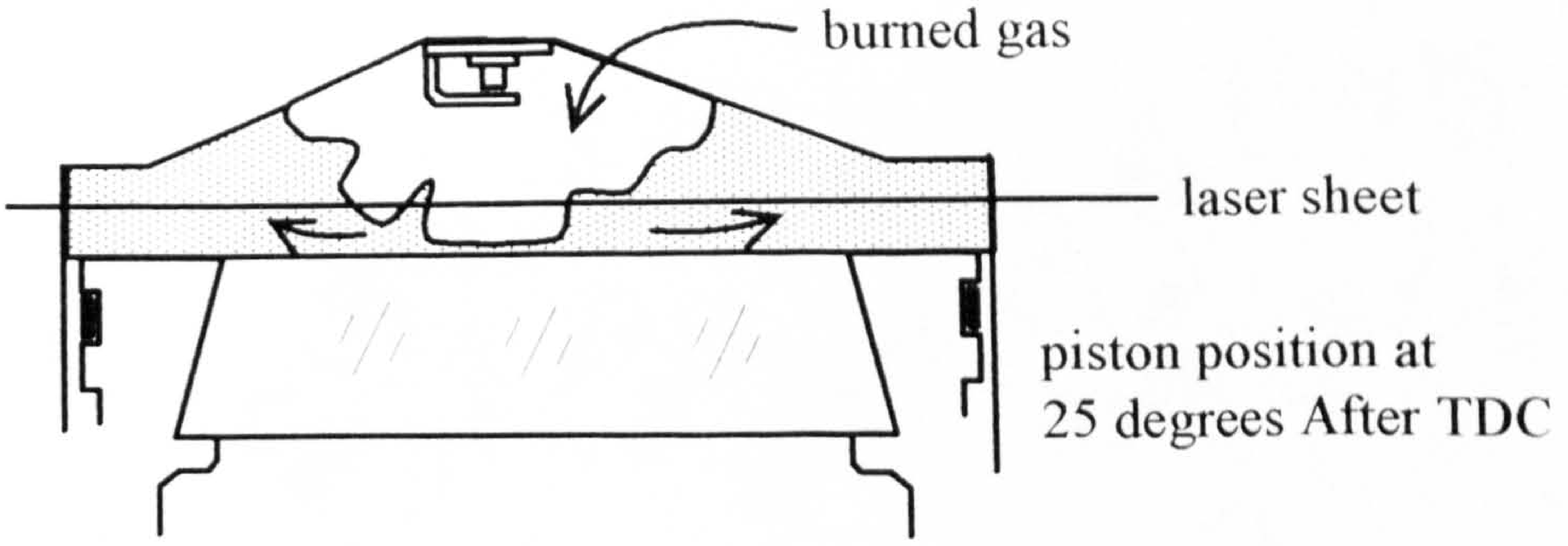

Figure 5.41 Geometry of light sheet, flame front and piston for fired PIV results.

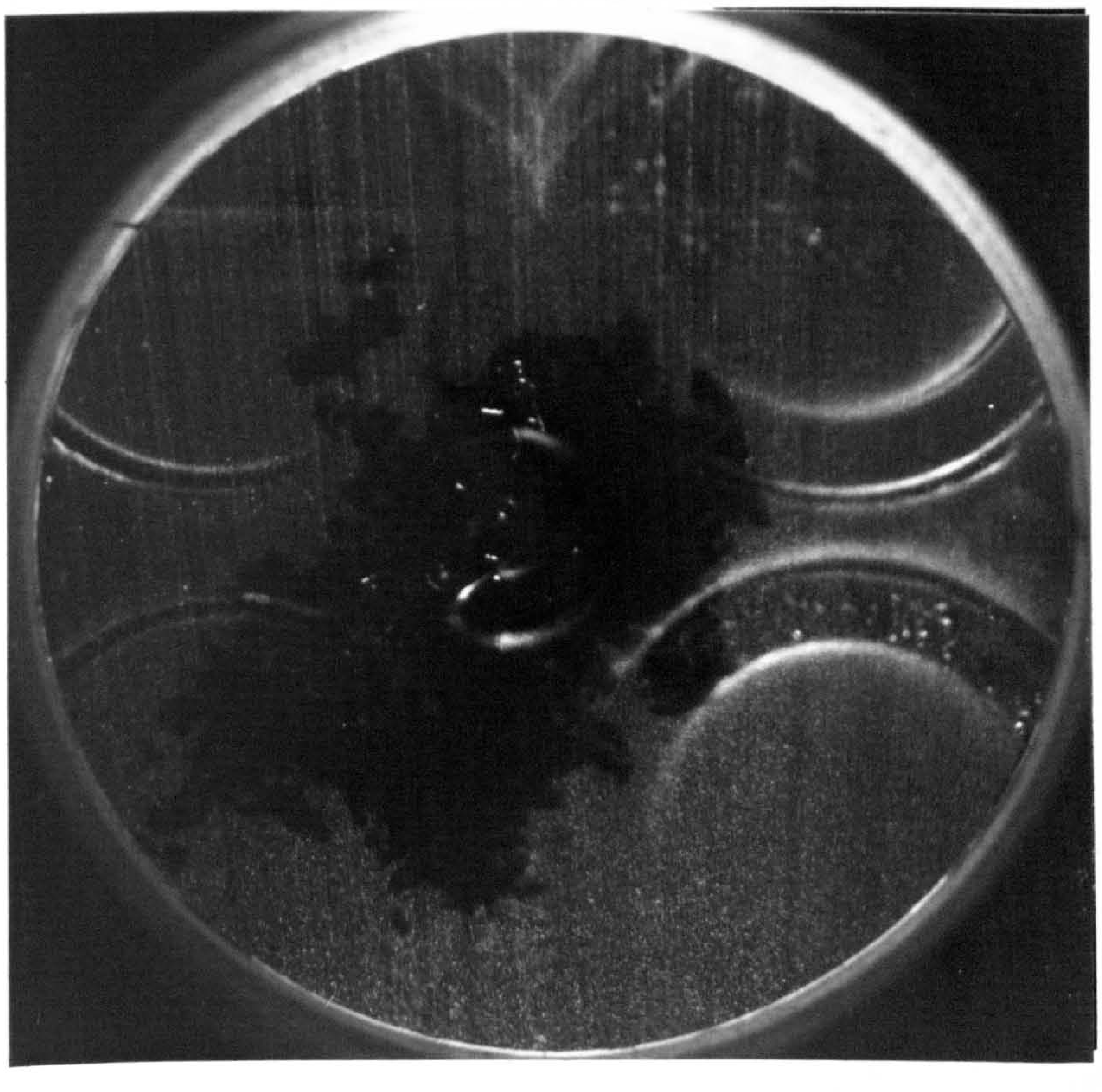

Figure 5.42 PIV image at 25 degrees after TDC showing irregular flame front. Dark region within irregular boundary is burned gas.

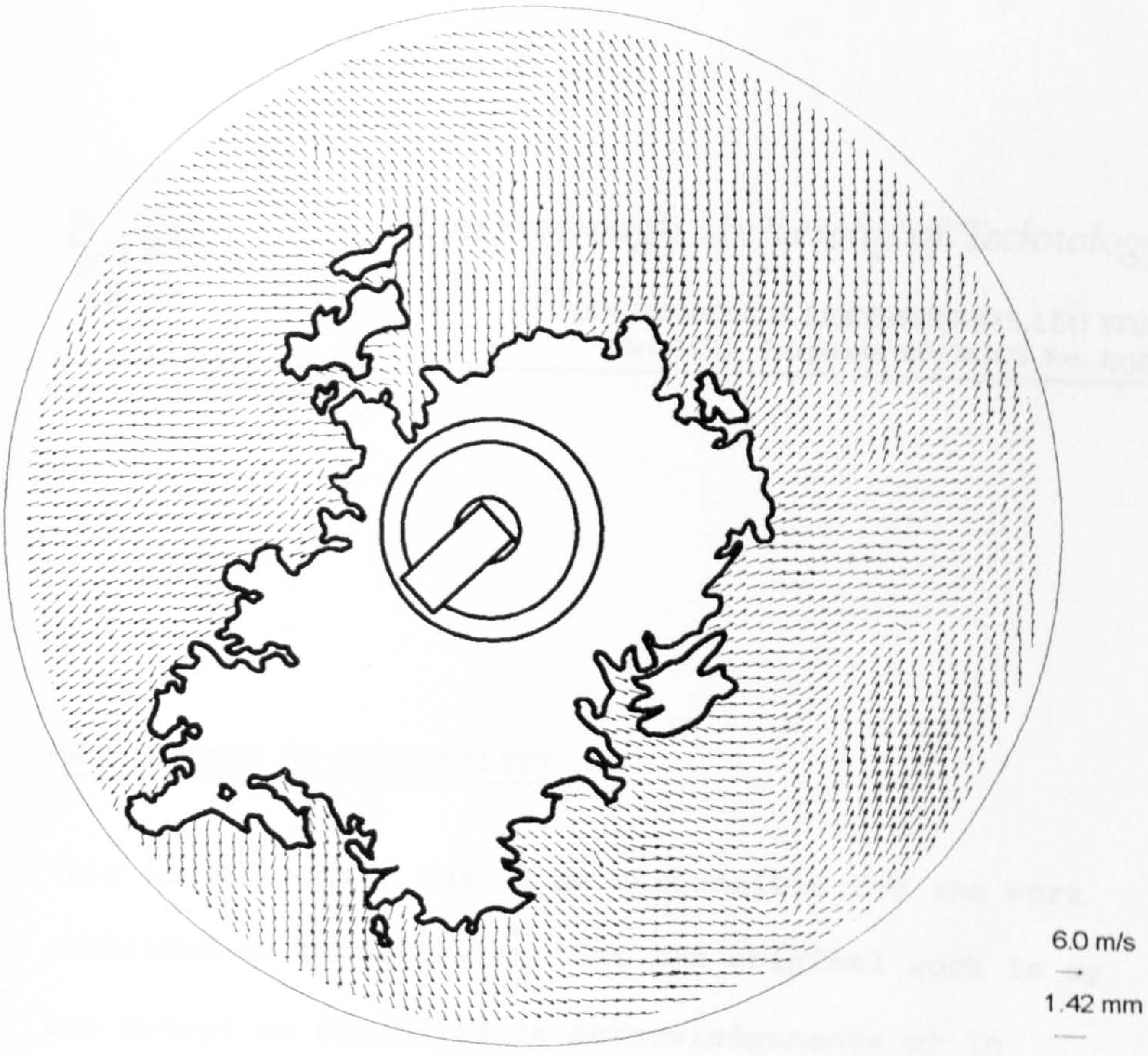

Figure 5.43 Flow field ahead of flame front in plane H-H
Ignition timing 5 degrees before TDC
Image recorded at 25 degrees after TDC.

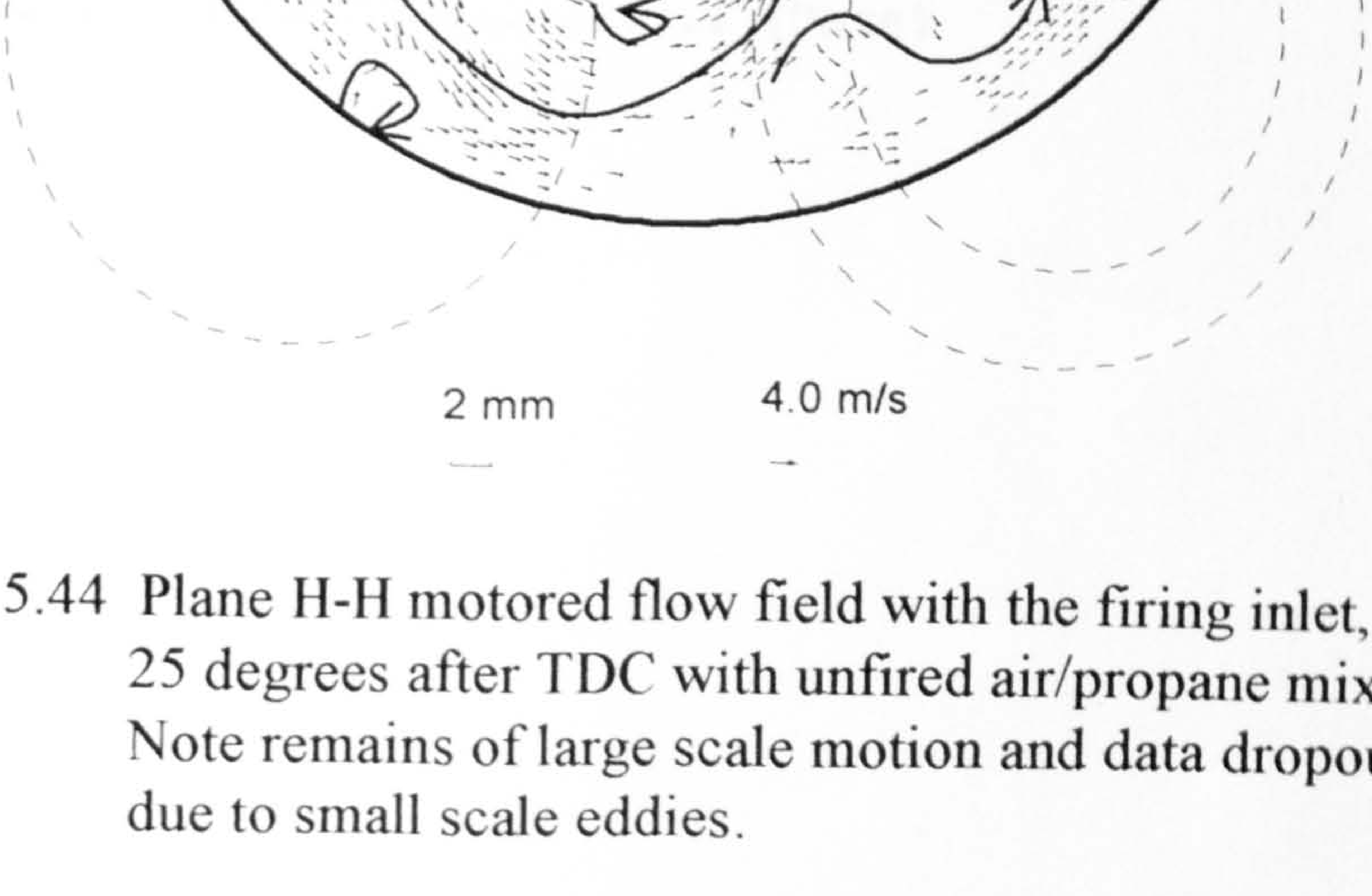

Figure 5.44 Plane H-H motored flow field with the firing inlet, at 25 degrees after TDC with unfired air/propane mixture. Note remains of large scale motion and data dropout due to small scale eddies.